Defense Nuclear Agency
Alexandria, VA 22310-3398

DNA-TR-93-69-V2

Tagging RDT&E
Volume 2—Appendices A-G

Gerald P. Alldredge, et al.
BDM Federal, Inc.
P.O. Box 9274
Albuquerque International
Albuquerque, NM 87119

March 1994

Technical Report

CONTRACT No. DNA 001-89-C-0189

Approved for public release;
distribution is unlimited.

Destroy this report when it is no longer needed. Do not return to sender.

PLEASE NOTIFY THE DEFENSE NUCLEAR AGENCY, ATTN: CSTI, 6801 TELEGRAPH ROAD, ALEXANDRIA, VA 22310-3398, IF YOUR ADDRESS IS INCORRECT, IF YOU WISH IT DELETED FROM THE DISTRIBUTION LIST, OR IF THE ADDRESSEE IS NO LONGER EMPLOYED BY YOUR ORGANIZATION.

DISTRIBUTION LIST UPDATE

This mailer is provided to enable DNA to maintain current distribution lists for reports. (We would appreciate your providing the requested information.)

NOTE:
Please return the mailing label from the document so that any additions, changes, corrections or deletions can be made easily.

☐ Add the individual listed to your distribution list.

☐ Delete the cited organization/individual.

☐ Change of address.

NAME: _____

ORGANIZATION: _____

OLD ADDRESS	CURRENT ADDRESS
_____	_____
_____	_____
_____	_____

TELEPHONE NUMBER: ( ) _____

DNA PUBLICATION NUMBER/TITLE	CHANGES/DELETIONS/ADDITIONS, etc.) *(Attach Sheet if more Space is Required)*
_____	_____
_____	_____
_____	_____

DNA OR OTHER GOVERNMENT CONTRACT NUMBER: _____

CERTIFICATION OF NEED-TO-KNOW BY GOVERNMENT SPONSOR (if other than DNA):

SPONSORING ORGANIZATION: _____

CONTRACTING OFFICER OR REPRESENTATIVE: _____

SIGNATURE: _____

CUT HERE AND RETURN

DEFENSE NUCLEAR AGENCY
ATTN: TITL
6801 TELEGRAPH ROAD
ALEXANDRIA, VA 22310-3398

DEFENSE NUCLEAR AGENCY
ATTN: TITL
6801 TELEGRAPH ROAD
ALEXANDRIA, VA 22310-3398

REPORT DOCUMENTATION PAGE

Form Approved OMB No. 0704-0188

1. AGENCY USE ONLY (Leave blank)	2. REPORT DATE	3. REPORT TYPE AND DATES COVERED
	940301	Technical 890915 – 930530

4. TITLE AND SUBTITLE

Tagging RDT&E
Volume 2—Appendices A-G

5. FUNDING NUMBERS

C - DNA 001-89-C-0189
PE - 62715H
PR - TA
TA - TA
WU - DH093030

6. AUTHOR(S)

Gerald P. Alldredge, Benny J. Hill, Earl M. Dressel, John J. Corcoran, Adam Wright, Russell C. Smith, and Robert A. Salazar

7. PERFORMING ORGANIZATION NAME(S) AND ADDRESS(ES)

BDM Federal, Inc.
P.O. Box 9274
Albuquerque International
Albuquerque, NM 87119

8. PERFORMING ORGANIZATION REPORT NUMBER

BDM/ABQ-93-0012-TR

9. SPONSORING/MONITORING AGENCY NAME(S) AND ADDRESS(ES)

Defense Nuclear Agency
6801 Telegraph Road
Alexandria, VA 22310-3398
FCPRC/Nelson

10. SPONSORING/MONITORING AGENCY REPORT NUMBER

DNA-TR-93-69-V2

11. SUPPLEMENTARY NOTES

This work was sponsored by the Defense Nuclear Agency under RDT&E RMC Code B4613D TA TA EA018 OPAC 2600A 25904D

12a. DISTRIBUTION/AVAILABILITY STATEMENT

Approved for public release; distribution is unlimited

12b. DISTRIBUTION CODE

13. ABSTRACT *(Maximum 200 words)*

Volume 2 - Appendices A-G contains comprehensive presentations of technical subjects considered too detailed for inclusion in the main body (Volume 1) of the Tagging RDT&E Draft Final Report. The topics included are:

Appendix A - Procedure for Annealing to Reduce Residual Stress in Injection-Molded Polycarbonate SLITS Joint Blocks
Appendix B - PTILS Software Utilities
Appendix C - SLOTS Optical Time Domain Reflectometry Measurements
Appendix D - Analysis of the Limits of Splice Detectability in Plastic Optical Fiber Using the OFM20-OTDR
Appendix E - Analysis of the Rayleigh Backscattered Power in a Multiwrap Glass SLOTS Optical Fiber with Bends and Splices
Appendix F - Creative Task Final Report - Innovative Tags
Appendix G - Utility Programs Used for Blink Comparator Process

14. SUBJECT TERMS

Optical Time Domain Reflectometry (OTDR) Passive Tamper Indicating Loop Seal (PTILS)
Secure Loop Inspectable Tag/Seal (SLITS) Secure Loop Optical Tag/Seal (SLOTS)

15. NUMBER OF PAGES

230

16. PRICE CODE

17. SECURITY CLASSIFICATION OF REPORT	18. SECURITY CLASSIFICATION OF THIS PAGE	19. SECURITY CLASSIFICATION OF ABSTRACT	20. LIMITATION OF ABSTRACT
UNCLASSIFIED	UNCLASSIFIED	UNCLASSIFIED	SAR

CLASSIFIED BY:

N/A since Unclassified.

DECLASSIFY ON:

N/A since Unclassified.

CONVERSION TABLE

Conversion factors for U.S. Customary to metric (SI) units of measurement.

MULTIPLY → / TO GET ←	BY → / BY ←	TO GET / DIVIDE
angstrom	1.000 000 X E -10	meters (m)
atmosphere (normal)	1.013 25 X E +2	kilo pascal (kPa)
bar	1.000 000 X E +2	kilo pascal (kPa)
barn	1.000 000 X E -28	meter^2 (m^2)
British thermal unit (thermochemical)	1.054 350 X E +3	joule (J)
calorie (thermochemical)	4.184 000	joule (J)
cal (thermochemical/cm^2)	4.184 000 X E -2	mega joule/m^2 (MJ/m^2)
curie	3.700 000 X E +1	*giga becquerel (GBq)
degree (angle)	1.745 329 X E -2	radian (rad)
degree Fahrenheit	$t_k = (t^oF + 459.67)/1.8$	degree kelvin (K)
electron volt	1.602 19 X E -19	joule (J)
erg	1.000 000 X E -7	joule (J)
erg/second	1.000 000 X E -7	watt (W)
foot	3.048 000 X E -1	meter (m)
foot-pound-force	1.355 818	joule (J)
gallon (U.S. liquid)	3.785 412 X E -3	meter^3 (m^3)
inch	2.540 000 X E -2	meter (m)
jerk	1.000 000 X E +9	joule (J)
joule/kilogram (J/kg) radiation dose absorbed	1.000 000	Gray (Gy)
kilotons	4.183	terajoules
kip (1000 lbf)	4.448 222 X E +3	newton (N)
kip/inch^2 (ksi)	6.894 757 X E +3	kilo pascal (kPa)
ktap	1.000 000 X E +2	newton-second/m^2 ($N-s/m^2$)
micron	1.000 000 X E -6	meter (m)
mil	2.540 000 X E -5	meter (m)
mile (international)	1.609 344 X E +3	meter (m)
ounce	2.834 952 X E -2	kilogram (kg)
pound-force (lbs avoirdupois)	4.448 222	newton (N)
pound-force inch	1.129 848 X E -1	newton-meter (N·m)
pound-force/inch	1.751 268 X E +2	newton/meter (N/m)
pound-force/foot^2	4.788 026 X E -2	kilo pascal (kPa)
pound-force/inch^2 (psi)	6.894 757	kilo pascal (kPa)
pound-mass (lbm avoirdupois)	4.535 924 X E -1	kilogram (kg)
pound-mass-foot^2 (moment of inertia)	4.214 011 X E -2	kilogram-meter^2 ($kg·m^2$)
pound-mass/foot^3	1.601 846 X E +1	kilogram/meter^3 (kg/m^3)
rad (radiation dose absorbed)	1.000 000 X E -2	**Gray (Gy)
roentgen	2.579 760 X E -4	coulomb/kilogram (C/kg)
shake	1.000 000 X E -8	second (s)
slug	1.459 390 X E +1	kilogram (kg)
torr (mm Hg, 0° C)	1.333 22 X E -1	kilo pascal (kPa)

*The becquerel (Bq) is the SI unit of radioactivity; 1 Bq = 1 event/s.
**The Gray (GY) is the SI unit of absorbed radiation.

TABLE OF CONTENTS

APPENDIX A
PROCEDURE FOR ANNEALING TO REDUCE RESIDUAL STRESS IN INJECTION-MOLDED POLYCARBONATE SLITS JOINT BLOCKS

A.1 OBJECTIVE.

The objective of annealing the joint block parts is to reduce the residual stress left from the molding process, so as to eliminate cracking due to the use of chemical coupling agents and other potential environmental influences.

Injection-molded polycarbonate joint blocks for SLITS (and possibly PTILS, formerly termed SLOTS) exhibit considerable stress inhomogeneity as indicated by fringes of high spatial frequency seen in a circular (mono-chromatic) polariscope. These high spatial frequency fringes appear in the corners of the well of the base part of the joint block, with the greatest stress indication appearing in the corners nearest the "tooth" separating the loop entryways.

Loop seals have cracked at the corners of the well, when they were assembled from injection-molded blocks with a coupling agent (consisting of a 5 percent solution of Union Carbide A-174 compound in methanol) brushed onto the surface of the base well before adding the epoxy/hematite mixture. Furthermore, joint block bases dosed with drops of the 5 % A-174 agent applied in the well have spontaneously cracked in all four corners of the well, with no external stress at all applied to the base. This experience suggests that the cracking is possibly due to stress corrosion. The high stress indication in the as-molded joint blocks suggests there may be susceptibilities to other environmental influences as well.

The procedure set forth here was developed after extensive testing of the effects of temperature treatment on the polariscopic stress indication in injection molded SLITS joint block bases and lids.

A.2 PREPARATION FOR ANNEALING.

The joint block bases and lids shall be cut from the molding runners neatly, so that no excess material from the runner remains on the bases and lids. Careful cutting with sharp diagonal cutters should suffice for this separation.

The joint block bases and lids shall be cleaned of any visible surface contamination (dust or other foreign particles, mold release, etc.) before the annealing process.

A.3 THE ANNEALING CHAMBER.

The annealing chamber shall be capable of attaining and holding (± 2°F or ± 1°C) internal temperatures in the range of 250 to 290°F (121 to 143°C) for periods of up to 2 hours. The chamber should have means of forced circulation of hot air or other means to ensure uniformity of temperatures (± 2°F or ± 1°C) in the volume used for annealing.

The actual temperature at the joint block parts being annealed is the controlling parameter; the chamber control temperature will have to be adjusted to obtain the joint block temperature described below, and the chamber shall accommodate means of directly measuring the temperature of the joint block parts or their carrier.

No control of relative humidity is required.

The annealing chamber shall be capable of cool-down from the annealing hold temperature to 220°F (105°C) at a rate no faster than 2°F per second (1°C per second); slower cool-down rates are acceptable.

The rate of cool-down from 220°F to room ambient is not critical, although extremely fast cool-down such as dumping the joint block parts into ambient temperature liquid should not be done. At or below 220°F (105°C), the "natural" cool-down of parts by removing them from the chamber on their carrier and allowing them to stand in ambient air is an acceptable procedure.

A.4 ANNEALING CARRIERS AND LOADING OF JOINT BLOCK PARTS ON CARRIER.

Carriers shall be provided to hold one or more joint block base/lid pairs while they are being annealed in the annealing chamber. The carriers shall have interior bottoms that are flat over sufficient area as to hold a number of joint block base and lid pairs. The bottom of the carrier shall be a smooth, low friction surface, such as the polished surface of glass or pyroceram (e.g., Corning Corelle) cookware or dishes, or the Teflon-coated surface of Teflon-coated aluminum cookware. The carrier shall be able to experience temperatures of up to 310°F (154°C) without any degradation, including distortion of the flatness of its bottom, and without any chemical contamination of the polycarbonate joint block items. The thermal conductivity and thickness of the carrier shall be such that, at the annealing "soak" temperature in an annealing chamber as specified above, the entire area of the carrier bottom that can contact annealing items shall be at the same temperature (±2°F or ±1°C).

The bases and the lids shall be loaded into the carrier so as to be in contact with the bottom of the carrier over the largest possible contact area of each base and each lid. Thus, the bases shall lie in the carrier with their backs in contact with the flat bottom of the carrier and the open well facing upward, and the lids shall lie with their outside surfaces in contact with the flat bottom of the carrier and the inside surface facing upward. No base or lid shall contact any non-horizontal part of the interior surface of the carrier. Bases and lids shall have sufficient space in the carrier that no base or lid shall have significant areas of contact with any other base or lid, and no incidental points or areas of inter-item contact shall experience pressure beyond what can be supported by the small frictional forces between the items being annealed and the bottom of the carrier.

A.5 CALIBRATION OF ANNEALING TEMPERATURE.

The actual temperature of the joint block items is the relevant temperature in the annealing process. With the joint block items having the greatest contact surface with the carrier bottom, and with the carrier material and thickness as specified in section A.4, the actual temperature of the carrier should be a very close surrogate for the actual temperature of the joint block items.

Experience has shown that neither the temperature indication of the controller in an automatic temperature-controlled chamber nor the temperature of the air in a chamber (even with forced air circulation) as measured with an independent, calibrated thermometer are good enough indications of the actual temperature of the carrier and annealing items. It is necessary to have an independent, calibrated thermometer to measure the actual temperature of the carrier. For example, the thermocouple bead of a K-type thermocouple thermometer (e.g., Fluke model 52 K/J thermometer) in firm contact with the surface of the carrier near where annealing items are placed has proven a satisfactory arrangement for measuring the actual temperature of the carrier.

Hence, it is necessary to determine what control temperature must be set for the annealing chamber in order to obtain the desired soak temperature at the carrier and annealing items. For the 2 hour soak described in section A.6 below, the target soak temperature at the carrier is 276°F (135.5°C). To find the necessary control temperature to obtain this soak temperature, follow the following procedure:

(1) Load all carriers that will be used in annealing runs with dry sand having the same weight per carrier as the weight of joint block items that will occupy that carrier in actual annealing runs.

(2) Provide an independent, calibrated thermometer for each carrier that will be used in the annealing chamber at a given time. These thermometers must have the capability of giving a temperature reading to an operator outside the chamber during a temperature soak period. These thermometers must be capable of accurately reporting temperature to within ±1°F (±.5°C).

(3) Pre-heat the annealing chamber to a control temperature of about 280°F (137.8°C).

(4) When the air temperature has stabilized so that the temperature over a 10 minute period does not drift either up or down, record the air temperature at one minute intervals for 10 minutes. Compute the average (mean) temperature and record it and the minimum and

maximum for the recording interval. Note the reading of the temperature control sensor (and its fluctuations) if this is available separately.

(5) Insert the sand-loaded carrier(s) into the chamber, and assure that the thermometer for each carrier used is in good contact with the carrier.

(6) Allow about 10 minutes after insertion of the sand-loaded carriers for the chamber to make a gross temperature recovery from the loss of hot air during the carrier insertion.

(7) Begin monitoring the air temperature and the carrier temperature(s).

When the air temperature has stabilized so that the temperature over a 10 minute period does not drift either up or down, record the air temperature at one minute intervals for 10 minutes. Compute the average (mean) temperature and record it and the minimum and maximum for the recording interval. Note the reading of the temperature control sensor (and its fluctuations) if this is available separately.

When the temperature of each carrier in the chamber has stabilized so that the temperature over a 10 minute period does not drift either up or down, record the carrier temperature at one minute intervals for 10 minutes. Compute the average (mean) temperature and record it and the minimum and maximum for the recording interval.

(8) If more than one carrier is used, verify that the carrier temperatures differ from one another by no more than 2°F (1°C). If the carrier temperatures differ by a greater amount, remove carriers until the carrier temperatures no longer differ by a greater amount. After each removal, execute steps (6) and (7).

(9) If the lowest mean (remaining) carrier temperature is less than 276°F (135.5°C), adjust the control temperature of the chamber upward by about 5°F (2.8°C).

If the lowest mean (remaining) carrier temperature is greater than 276°F (135.5°C), adjust the control temperature of the chamber downward by about 5°F (2.8°C).

Then repeat steps (6) - (9) until one has at least one lowest mean carrier temperature reading 5°F (2.8°C) above and below the target carrier soak temperature of 276°F (135.5°C).

(10) Use the table of temperature control settings and associated lowest mean carrier temperatures accumulated in the above steps to interpolate to the temperature control setting of the chamber required to produce a lowest mean carrier temperature of 276°F (135.5°C).

Three particular annealing runs in BDM's 24 cu. ft. Envirotronics chamber illustrate the rationale for a direct measurement of the actual carrier temperature. In one run, the air temperature measurements by the controller sensor indicator was 133.0 ±.1°C (271.4 ±.2°F) and by a Fluke 52 K/J thermometer was 132.1 ±.1°C (269.8 ±.2°F) over a 2 hour soak period. In the second run, the air temperature measurements by the controller sensor indicator was again 133.0 ±.1°C (271.4 ±.2°F), while the temperature of the carrier as measured by the Fluke 52 thermometer was 267°F average, with a low of 265°F 10 minutes after insertion of carrier and annealing parts to a high of 267.2°F over the last 30 minutes of the 2 hour soak period. Polariscopic examination of the joint block bases after both these anneals revealed significant stress remaining in the corners of the wells. In the third run, the temperature set point was higher, so that the air temperature measurement by the controller sensor indicator was 138.8 ±.1°C (281.8 ±.2°F), while the temperature of the carrier as measured by the Fluke 52 thermometer was 276.2 ±.2°F (135.7 ±.1°C) average, with a low of 274°F 10 minutes after insertion of carrier and annealing parts to a high of 276.4°F over the end of the 2 hour soak period. Polariscopic examination of the joint block bases after this third anneal revealed no significant stress remaining in the corners of the wells. Thus, with only about 9°F difference in carrier temperatures between run two and run three we moved from a mediocre anneal to a very good anneal, and there is about 4 to 5°F difference between air temperature and carrier temperature in such runs.

A.6 ANNEALING PROCEDURE.

(1) Pre-heat the annealing chamber to the temperature control setting required to produce a carrier temperature of 276°F (135.5°C) as determined in step (10) of section A.5 above. When the air temperature has stabilized so that the temperature over a 10 minute period does not drift either up or down, record the air temperature at one minute intervals for 10 minutes. Compute the average (mean) temperature and record it and the minimum and maximum for the recording interval. Note the reading of the temperature control sensor (and its fluctuations) if this is available separately.

(2) Load the joint block items (in base/lid pairs) to be annealed into the carrier(s) to be used in the annealing run as indicated in section A.4 above.

(3) When the chamber temperature has stabilized at the control temperature selected, insert the joint-block-loaded carrier(s) into the chamber, and assure that the thermometer for each carrier used is in good contact with the carrier.

(4) Allow 5 to 10 minutes after insertion of the joint-block loaded carriers for the chamber to make a gross temperature recovery from the loss of hot air during the carrier insertion. The faster the recovery, the shorter the wait time.

(5) Begin monitoring the air temperature and the carrier temperature(s). When the air temperature has stabilized so that the temperature over a 10 minute period does not drift either up or down, record the air temperature at one minute intervals for 10 minutes. Compute the average (mean) temperature and record it and the minimum and maximum for the recording interval. Note the reading of the temperature control sensor (and its fluctuations) if this is available separately.

When the temperature of each carrier in the chamber has stabilized so that the temperature over a 10 minute period does not drift either up or down, begin the 2 hour soak period.

For each carrier in use, record the carrier temperature at one minute intervals for 10 minutes. Compute the average (mean) temperature and record it and the minimum and maximum for the recording interval.

If the lowest mean carrier temperature is more than 1°F (0.5°C) lower or more than 5°F (2.8°C) higher than the target soak temperature of 276°F (135.5°C), adjust the chamber temperature control to bring the lowest mean carrier temperature (over a 10 minute interval) to 276 (-1, +5)°F (135.5 (-.5,+2.8)°C).

(6) If more than one carrier is used, verify that the carrier temperatures differ from one another by no more than 2°F (1°C). If the carrier temperatures differ by a greater amount, note which carriers and their locations differ by more than 2°F (1°C) from those carriers bearing the majority of base/lid pairs (the "majority" carriers). If these carriers differ in size and material from the majority carriers, do not use them or their locations in future annealing runs. If all carriers are the same, do not use the locations of those carriers whose carrier temperatures differ by more than 2°F (1°C) from the majority carriers.

(7) After a 2 hour soak at 276°F (135.5°C) carrier temperature, begin the cool-down phase. Do not exceed a carrier temperature cool-down rate of 2°F per second (1°C per second) from the soak temperature (276°F) to 220°F (105°C). Below 220°F (105°C), the cool-down rate can be accelerated, but not as fast as quenching in liquid at room ambient temperature. We recommend the simple procedure of removing the carriers from the chamber and allowing them to stand in room ambient air on insulated pads until the joint block items have equilibrated to room ambient temperature.

A.7. VERIFICATION OF ANNEAL.

For purposes of visually verifying the result of the annealing process, a circular polariscope can be constructed using elements from the Polarizer Experimenters Kit (part no. A38490, about $20) obtainable from Edmund Scientific Co., 101 E. Gloucester Pike, Barrington, NJ 08007-1380, phone (609)573-6250. This Kit contains two 2 x 2 inch square linear polarizers (gray) and two 2 x 2 inch square quarter-wave retarders (clear, with one corner tip cut off), which are needed for the assembly of a circular polariscope. We recommend obtaining a red filter such as that contained in Edmund Scientific's Book of 6 Filters (2 x 2 in.) (part no. A40676, about $5) to limit the range of wavelengths that pass through the polariscope.

In a piece of corrugated cardboard at least 4 x 2.5 inch with the long dimension parallel to the channels of the corrugations, make two parallel cuts about 1.5 inch long from one long edge across the corrugations. Make the cuts about 1 inch apart and located so that the cut closest to a short edge is about 1.5 inch from that short edge. The cuts should go all the way through the thickness of the cardboard.

Slip a gray polarizer square into each slit so that the squares stand up at right angles from the cardboard and parallel to each other with only about 1/16 inch protruding from the bottom of the slits. The top of the squares should be parallel to the surface of the cardboard. You want the polarizers to be "crossed," so if light appears to pass through both polarizers, remove one of the polarizers and replace it so that one of the formerly vertical edges (on the sides) is now horizontal (on top); now light should not appear to pass through both polarizers.

Next, place a quarter-wave retarder square in each slit adjacent to a polarizer square, with the quarter-wave squares (1) rotated 45 ° so that corners rather than edges are at top and bottom and (2) placed between the polarizer squares (so that the sequence of polarizers (P) and quarter-wave retarders (Q) is PQ-space-QP). Now, either light will appear to pass through both polarizer/quarter-wave pairs (the "bright field" arrangement), or light will appear not to pass through both polarizer/quarter-wave pairs (the "dark field" arrangement). If one wants a field arrangement other than that originally

assembled, just remove one quarter-wave square and replace it after a 90 ° rotation (so that one of the side corners is now at top). (Note: One must be certain to use the quarter-wave squares and not the half-wave squares, which are also clear, but do not have a corner clipped; the polariscope will not work if a half-wave square is inadvertently used.) If the recommended red filter has been obtained, it can be slipped between one of the polarizers and its adjacent quarter-wave plate; it does not matter where it is placed just so long as it limits the light passing through the polariscope to the very longest wavelength portion of the visible spectrum. This completes the assembly of the circular polariscope.

To use the circular polariscope, place a joint block base in the space between the PQ,QP pairs and look at it toward a fairly strong, diffuse light source; a high-pressure sodium lamp is ideal, but a strong white light source will work if the red filter is in place.

In a pre-annealed base, one should see multiple alternating bands of light and dark looping out from the corners of the well, with the number of bands and closeness of spacing greatest for the two corners furthest from the injection gate (and adjacent to the SLITS loop entry ways). (If white light without the red filter is used, these very closely spaced bands will be multicolored and so close together that by overlap of different colors they tend to wash out; this is the reason for recommending the red filter, so that only a small range of wavelengths are involved and the fringes are more distinct.) In a typical pre-annealed base, one might see 5 or 6 complete cycles from light to dark and back to light in the fringe pattern looping out from one of these corners.

After a successful anneal, one should not see even one complete cycle in a corner loop fringe; there should be only a few large, rather shapeless light and dark areas across the entire well floor.

APPENDIX B
PTILS SOFTWARE UTILITIES

This section gives a brief description of two PTILS software utility programs, the updated copy of the Universal Reader software (V6.0), and a set of batch files that execute them. OFM20TST is a program that controls the Opto-Electronics OFM20 Optical Time Domain Reflectometer (OTDR). This program uses the National Instruments GPIB control board and software drivers in the UR system computer to set up, acquire a fiber optic reading, and store that data in a disk file. The CLPLOT program is a utility to read the output file(s) from OFM20TST and display logarithmically scaled plots on the UR system computer screen. Each of these programs can be run independently or by using the PTILS.bat batch procedure file described below.

B.1 UR60.EXE (UNIVERSAL READER SOFTWARE V6.0).

This program is a modification of the Universal Reader software (V5.2) to read an additional tag type (PTILS). Wherever a choice was given to enter or edit a tag type, PTILS was added as a valid value. The PTILS tag signature area was designed to be the same in terms of size, location, fiducial structure, etc. as the SLITS tag. It does not directly call OFM20TST or CLPLOT.

To execute the program (stand-alone) enter:

```
UR60
```

B.2 OFM20TST.EXE (OFM20 TESTBED PROGRAM).

This is a program to control the Opto-Electronics OFM20 OTDR. The GPIB interface uses the National Instruments PC/XT IEEE-488.2 Controller (GPIB.PCII/IIA) board with the NI-488.2 MS-DOS software (Version 2.1.1). It sets up the OTDR and records data in two formats. OFM20TST accepts two filename arguments.

To execute the program (stand-alone) enter:

```
OFM20TST ofm20_parameter_filename ur60_parameter_filename
```

First is the OFM20 setup parameters file and second is the Universal Reader parameter file (used for compatibility with UR data annotation parameters found in UR tag signature files). If both file names are present, they are read during execution and no user interaction occurs. If the second filename is missing, the program will attempt to find the (default) file URD1.PRM and failing that will prompt for the missing values through the keyboard. If the first filename is missing, the program will attempt to find the default file OFM20.PRM and failing that will use internal default values for setup (see the documentation provided by Opto-Electronics for the OFM20 to obtain details about setup commands and values).

An example OFM20.PRM file is shown below:

```
* This is the parameter file for the OFM20 OTDR *
* values to be entered must be in the format cccccc=vvvvvv; *
* where cccccc is the OFM20 gpib command and vvvvvv is the value.  *
* Lines beginning with an asterisk in col. 1 are comments *
* 12/7/92 *
cursor=0.0;
index=1.492;
measure=x,2048;
origin=0.0;
sens=1;
snslev=-55.0;
units=m;
wpos=5.0;
wwidth=9.0;
```

Default values used in the OFM20 parameters in the OFM20TST program are:

cursor = 0.0	[set to left side of window]
index = 1.492	[for plastic fiber (PMMA)]
measure = x, 8192	["x" storage buffer, 8192 averages (scans)]
origin = 0.0	[Distance from the OFM20 bulkhead]
sens = 1	[Sensitivity mode, 0->low, 1->high]

snslev = -55.0	**[Sensitivity level (optical attenuation) in dB]**
units = m	**[Length (distance) units set to meters]**
wpos = 0.0	**[Window Position with respect to cursor]**
wwidth = 20.0	**[Window width in meters]**

An example URD1.PRM file is shown below:

```
* This is the universal reader parameter file for the OFM20TST program *
* values to be entered must be in the format cccccc=vvvvvv; *
* where cccccc is the Universal Reader parameter and vvvvvv is the value *
* lines beginning with an asterisk in this file are comments *
* 12/7/92 *
equipmentid=0005;
locationid=0000;
readdate=01-01-93;
readtime=00:00:01;
operatorid=5345;
tagid=9999;
fiducialid=1;
runnum=0001;
numraw=1;
numext=0;
codeversion=6.0;
tagtype=P;
filetype=PT;
snslev=-55.0;
```

OFM20TST Produces two types of output files, one in XDATA format and the second in the proposed UR6.0 format. Each file consists of a header block (XDATA) or Header Blocks (UR60) followed by a waveform. Both files are written in ASCII format. The waveform data is 256 amplitude elements in length. The UR60 format gives the data in "raw" (integer) counts as read from the OFM20. The XDATA format stores scaled data where the counts are divided by (# of scans * 25.6) to be compatible with the (floating point) output of the XDATA program supplied by Opto-Electronics and modified by BDM. The filename convention for the output is ttttrrrr.1xx where tttt is the Tag Id, rrrr is the Run Number, and xx

is XD for the XDATA format file, or PT for the UR60 compatible file. In the first example below (the XDATA output file) the name would be 90010004.1XD. The second example (the UR60 format file) would be named 90010004.1PT. To change the filenames, the Run Number and Tag ID fields in the UR60 parameter file should be edited.

An (edited) example XDATA file (with bracketed [] comments added for explanation) would look like:

Tag ID: 9001 Run #: 0004	[first comment line [up to 80 char.]
Comment line #2	[second comment line]
Comment line #3	[third comment line]
01-01-93	[date of measurement]
00:00:01	[time of measurement]
1.005000	[window width (meters)]
2.199000	[offset from bulkhead to window]
-53.950000	[sensitivity level (dB)]
128	[number of scans]
2.0935059E-01	[waveform element #1]
2.0568848E-01	[waveform element #2]
1.7150879E-01	[waveform element #3]
.	.
.	.
.	.
7.6293945E-02	[waveform element #254]
8.3007812E-02	[waveform element #255]
9.2163086E-02	[waveform element #256]

An (edited) example UR60 file (with [] comments added for explanation) would look like:

0005	[Equipment Id]
0000	[Location Id]
01-01-93	[ReadDate]
00:00:01	[ReadTime]
5345	[Operator Id]

9001	[Tag Id]
1	[Fiducial Id]
0004	[Run Number]
0001	[Number of "raw" (preview) images]
0000	[Universal Reader Code version]
6.000000	[Universal Reader Code version]
PTIL	[Tag Type]
PT	[File Type]
128	[Number of scans (OFM20)]
1	[Sensitivity Mode]
5.00153E-10	[Time per division (window = 10 div)]
2.1990	[Bulkhead to window delay (distance)]
1.492	[Refractive Index of fiber]
0	[Attenuation]
1	[Scaling Factor]
2.199	[Window Position]
	[DateTime_DataType]
0	[Checksum]
0	[Peak X Index]
0	[Peak Y Index]
0	[Pulse Energy]
0000000686	[waveform element #1]
0000000674	[waveform element #2]
0000000562	[waveform element #3]
.	.
.	.
.	.
0000000250	[waveform element #254]
0000000272	[waveform element #255]
0000000302	[waveform element #256]

B.3 CLPLOT.EXE (COMMAND LINE PLOT PROGRAM)

The plot program operates specifically for OFM20 data files. It plots one to nine files with autoscaling in solid line type (on color VGA display with different color for each trace) plus difference curves in dotted line style. It accepts files in

XDATA format. Difference curves are computed and displayed if two or more files are plotted. Each difference curve is computed by subtracting the "current" file (#2-10) from file #1 (considered the baseline). Waveforms are converted internally to logarithmic scale before plotting (element(i) = 5 * LOG10(element(i))). Data is scaled to five times the LOG (rather than 10 for standard power level) to account for the round trip in the fiber.

To execute the plot program (stand-alone) enter:

CLPLOT filename_1 filename_2 ...

B4 PTILS.BAT (DRIVER FOR SET OF BATCH FILES).

Batch control file to execute UR60, OFM20TST, and CLPLOT from a menu display for acquisition of PTILS related data. (Each of the programs is independent and can be executed in stand-alone mode as shown above.) This batch procedure calls a number of others:

(1) 1.bat - Runs Universal Reader version 6.0 (UR60) and returns to PTILS.bat

(2) 2.bat - Runs OFM20TST then returns to PTILS.bat.

(3) 3.bat - Runs CLPLOT or Reviews plot file list. Displays a menu and invokes two other batch files:

   (a) P.bat - Plots PTILS fiber data files (XDATA format) by calling C.bat which in turn calls CLPLOT with the specified file names and returns to PTILS.bat.

   (b) R.bat - Allows Review of PTILS fiber data file names by displaying a directory then returning to 3.bat.

(4) 4.bat - Exits to DOS

APPENDIX C
SLOTS OPTICAL TIME DOMAIN REFLECTOMETRY MEASUREMENTS

C.1 INTRODUCTION.

The SLOTS concept has been studied as a simple, low cost, reliable option for the tagging applications of relevance to the present contract. One key technical issue regarding the security of the SLOTS concept has to do with whether it is possible to make splices in polymethylmethacrylate (PMMA) fiber which are not subsequently detectable by a tag inspection team.

Plastic optical fibers have been widely used in short haul communication links, data transmission links and light delivery systems. Several authors have investigated the relevant loss characteristics[1] and transmission bandwidths[2,3] of plastic fibers for use in these applications. In most of these short haul transmission systems, relatively large splice losses can be tolerated. Therefore, little attention has been directed (prior to the work performed for the present contract) toward the development and characterization of low loss, low reflection signature plastic fiber splices.

We have recently shown that there is an "intrinsic" component in the reflection signature from plastic fibers.[4,5] This signature could prove to be useful in tagging applications since it could be used to identify attempts to sever or splice the plastic fiber tag. Therefore, it is important to characterize this intrinsic reflection component.

Optical time domain reflectometry (OTDR) is the usual technique used for fiber splice characterization and detection.[6,7,8] Since fusion splices are not feasible in plastic fibers[9] the most likely splicing technology that will lead to low OTDR reflection signatures in plastic fibers is a wet (index-matched) mechanical splice. The primary contributions to the reflection signature arise from Fresnel reflections due to imperfect index matching and fiber core misalignment. After these components are eliminated, the remaining reflectivity contribution is the "intrinsic" reflectivity of the fiber end. Through careful experimental procedures the Fresnel and alignment contributions can be eliminated under laboratory conditions and the intrinsic component of the OTDR reflection signature can be

measured. In this report we will discuss the results of detailed OTDR measurements which characterize this intrinsic reflection signature that is present in polished polymethylmethacrylate (PMMA) core plastic optical fibers.

In these experiments, Mitsubishi Eska Extra brand PMMA plastic test fibers were carefully end-polished using a variety of polishing conditions. For most of the experiments, the 0.5 mm fibers were then butted up against similar "energy dump" fibers (with a larger core to relax alignment requirements) such that the relative position and orientation of the two fibers could be adjusted. OTDR experiments were set up to map out the reflection characteristics of the fiber versus index matching fluid refractive index and fiber-dump alignment, in order to assure that the reflection signature was minimized. After these parameters were optimized, an intrinsic reflection signature which was clearly detectable above the Rayleigh noise floor was observed with all tested fibers. The properties of this intrinsic reflection signature were mapped out versus experimental parameters such as fiber surface roughness, fiber bevel angle, fiber dump characteristics, laser power, and laser wavelength. This intrinsic reflection signature may serve as a minimum intrinsic back reflection that can be used for reliable PMMA fiber splice detection in tagging applications.

C.2 EXPERIMENTS.

C.2.1 Experimental Setup.

The experimental setup was documented in detail in a previous report. A brief overview of this setup will be presented here, with particular emphasis on recent changes and improvements.

The experiments were designed with the purpose of measuring the minimum, intrinsic reflected signal from a fiber-fiber interface. To this end, a flexible, dye-laser based OTDR experiment was set up. A schematic diagram of the OTDR experiment for measuring the intrinsic reflection signature from these polished fiber ends is shown in Figure C-1. A frequency doubled Q-switched Nd:YAG laser is used to generate pulses at 530 nm with a full width at half maximum (FWHM) pulse width of 7 ns. These pulses are either directly used for OTDR experiments or they are used to pump a dye laser to generate pulses at

680 nm. These pulses are attenuated and aligned co-linearly with a continuous wave (CW) argon laser, which is used for optical alignment. A small part of the Nd:YAG beam is split off and directed to a joulemeter which provides a pulse energy reference. The remainder of the beam is focused by a f/30 lens into the fiber coupling optics which direct light into the fiber and collect the backscattered signal emitted from the fiber. This signal is focused onto a high speed photodiode which is connected to a digitizer.

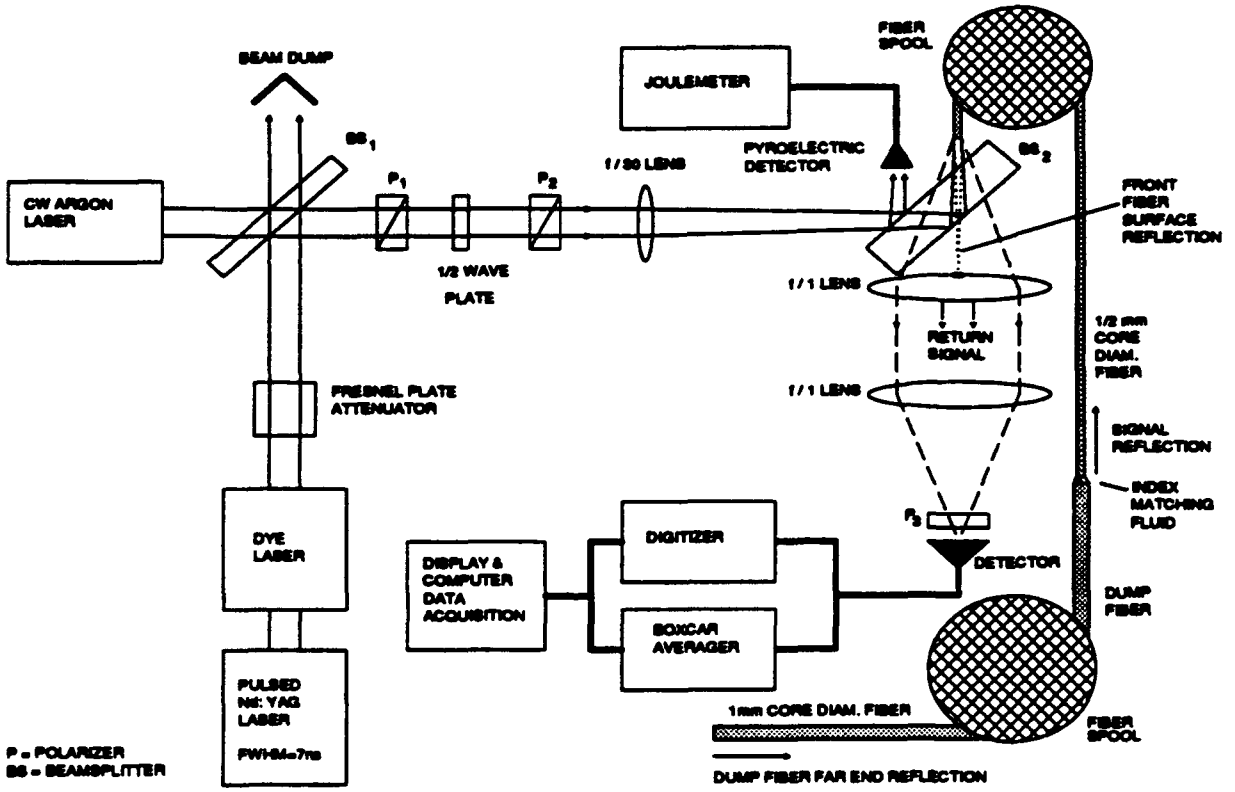

Figure C-1. Schematic of experimental test apparatus.

Using this experimental set-up, time domain reflectometry experiments were performed on polished PMMA fibers with a 0.5 mm core diameter. The test end of each 0.5 mm fiber was carefully cleaned and butted up against a similarly polished and cleaned dump fiber with a 1 mm core diameter. A dump fiber with a larger core diameter was used in order to relax alignment tolerances and avoid reflected signals due to fiber-fiber misalignment. Micropositioners were used to adjust the relative position and orientation of the two fiber ends to facilitate optimization of the fiber-dump alignment to minimize the backreflected signal. Additional measurements were also performed on 1 mm x 1 mm fiber splices.

The use of this laboratory based OTDR experiment enabled investigation of the splice reflectivity mechanisms and characteristics by variation of parameters such as input polarization, spatial input mode excitation, energy, detector sensitivity, and wavelength. In addition, the laboratory setup enabled the use of a combined spatial-polarization filtering technique that yielded a much superior dynamic range than that obtained with commercial OTDR's.

In order to assure that the signal measured is the minimum, intrinsic reflection signature from each fiber-dump fiber interface, attempts were made to eliminate any backscattered signals from the fiber surface due to spurious effects such as fiber-dump fiber misalignment or Fresnel reflection due to improper index matching.

C.2.2 Fiber-Dump Alignment Studies.

Experiments were conducted to investigate the dependence of the minimum signal on fiber-dump alignment, in order to assure that the alignment was properly optimized.[4] When a dump fiber with twice the core diameter of the signal fiber was used, the minimum reflected signal was relatively insensitive to transverse fiber-dump alignment, as expected. No variation in the reflected signal was observed when the transverse alignment was shifted by several tenths of a millimeter from the optimum position. Experiments were also performed to investigate the variation of the minimum reflected signal with fiber-dump separation, D. As is shown in figure C-2, for the index matched case, D can range from 0 to 2 mm with no variation in the minimum reflected signal. The signal varies with D when n_1 deviates significantly from the index matched case.

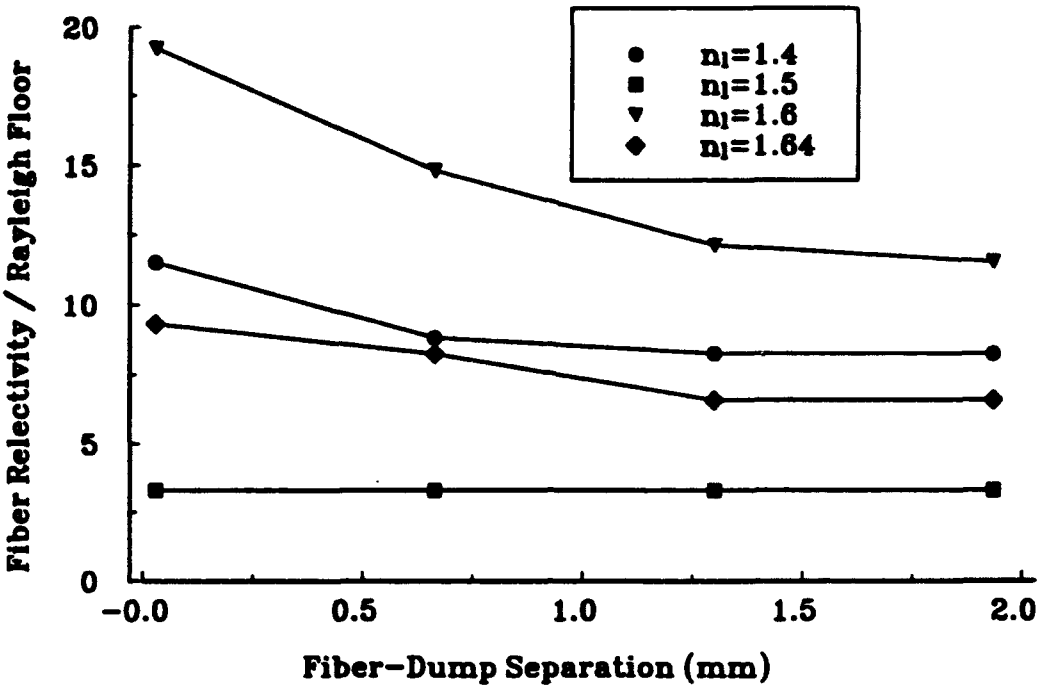

Figure C-2. Variation of minimum reflected signal with fiber-dump separation.

Hence, when index matching is performed, the reflected signal is insensitive to D and transverse alignment, which indicates that the minimum intrinsic signature is not a result of fiber-dump misalignment.

C.2.3 530 nm Index Studies.

To ensure that the fiber-dump interface is properly index matched, experiments were performed to investigate the variation of the minimum intrinsic signal with the refractive index, n_1, of the index matching fluid used for the fiber-dump interface.[5,10] For the particular laboratory conditions and fiber type used for this index measurement, the 1.496 fluid appeared to give the optimum index matching with 530 nm pulses. However, the reflectivity was seen to vary slowly with index close to the index matched condition, which indicates that either the 1.496 or 1.492 index fluids should provide excellent index matching for this wavelength.[5] It should also be noted that the optimum index fluid may be dependent on splice temperature, since the index fluid has a temperature dispersion of approximately 10^{-4}/°C.

C.2.4 680 nm Index Studies.

A variation of the index matching experiment was performed with 680 nm pulses. Figure C-3 shows a plot of the fiber reflectivity of a fiber finished with 5 mm de-agglomerated alumina (this fiber possessed a very small reflection signature). A Fresnel theory which sums over all transverse modes of the fiber and takes into account multiple reflections between the signal and dump fibers[5] was used to fit this data, with the effective fiber core index, n_c, used as a fitting parameter. The best fit to the data was obtained with n_c=1.492, and the resulting theoretical plot is shown as the solid line in figure C-3. Hence, at 680 nm, 1.492 index matching fluid provides the optimum index matching, and this fluid was used for all subsequent reflectivity measurements for fiber-dump systems at 680 nm. By comparing the experimental data to the theoretically generated plot which corresponds to optimum index matching, it can be seen that a non-index matchable y-offset exists which cannot be eliminated by careful index matching. One possible explanation for this intrinsic signal is a below-surface damage mechanism.[4,5] It is also possible that the intrinsic signal may be due to transverse inhomogeneities in the plastic fiber index profile.

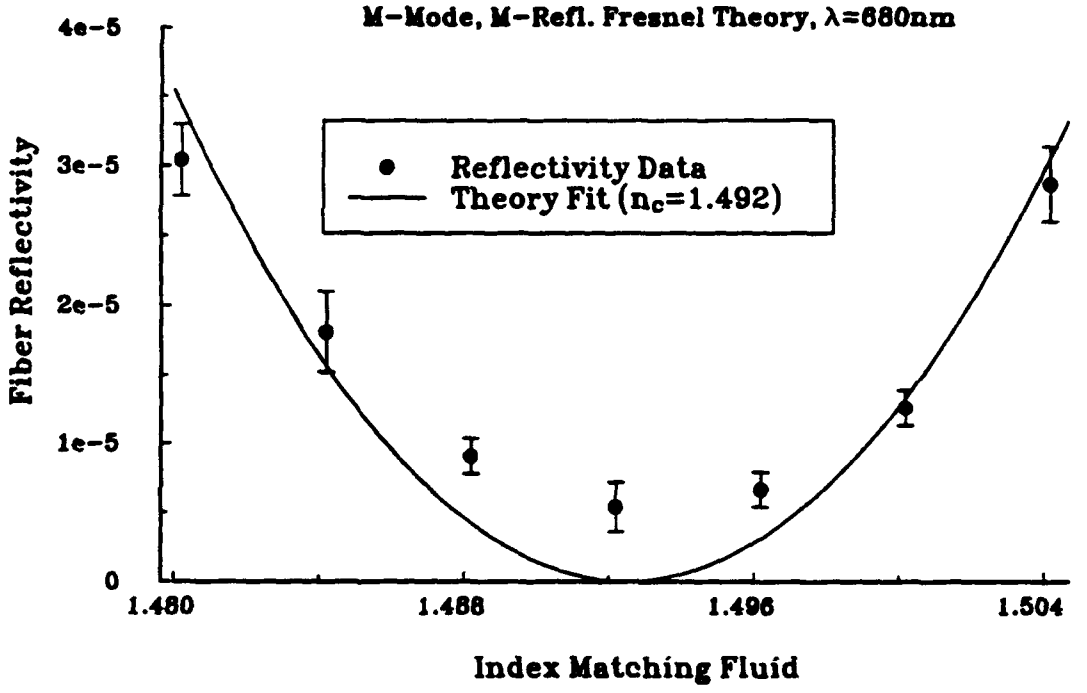

Figure C-3. Index Dependence Of Fiber Reflectivity at 680 nm.

C.2.5 Fiber Surface Finish Studies.

The dependence of this intrinsic signal with surface finish at wavelengths of 530 nm and 680 nm was investigated. In order to study the variation of the intrinsic signal with surface finish, another polishing "run" was performed. Fibers were removed at various stages of the polishing process to achieve different fiber surface finishes. Several 0.5 mm diameter signal fibers and 1 mm diameter dump fibers were cemented into plastic polishing pads and installed into the polishing apparatus described previously. The fiber ends were first simultaneously ground down with a wet 32 mm and 15 mm aluminum oxide paper. The fibers were then subsequently polished with a 5 mm, 1 mm, 0.3 mm, and 0.05 mm de-agglomerated alumina slurry. Test fibers were removed at each stage in this process.

The minimum, intrinsic reflectivity of each of these fibers was then measured at the two wavelengths of interest, 530 nm and 680 nm. The laser pulse width was measured to be 7 ns FWHM for the 530 ns pulses and 3.3 ns FWHM for the 680 nm pulses for this particular experiment (note that the pulse width depends on the detailed tuning of the dye laser). A single 1 mm diameter dump fiber which was finished with 0.05 mm de-agglomerated alumina was used for each fiber. The 1.496 index matching fluid was used for the 530 nm experiments and 1.492 index matching fluid was used for the 680 nm experiments. The minimum intrinsic reflectivity of fibers finished with 5 mm, 1 mm, 0.3 mm, and 0.05 mm de-agglomerated alumina oxide slurry at the two wavelengths is plotted in figure C-4. As shown in this plot, when the fiber surfaces are polished to successively finer finishes, the index matched minimum reflectivity does not decrease with decreasing surface roughness in any systematic way, since the roughest surface actually yields the minimum reflected signal. Instead, there is a variation in the reflected signal which appears to reflect the difference in the intrinsic reflection signal from fiber to fiber which has been observed previously.[4,5] It appears that any scattering due to surface roughness is eliminated by the very exact index matching which is performed in these experiments.

The error bars of the fiber reflectivity measurements for the two wavelengths overlap, so it is difficult to ascertain any wavelength dependence in

the fiber end reflectivity for the two wavelengths. Separate measurements of the spectral dependence of the fiber splice reflectivity will be examined in depth in section C.2.11. Although there is some indication that the fiber reflectivity for each surface at 530 nm is 1-2 db below those at 680 nm, this decrease may be due to measurement error since the error bars for data at the two wavelengths overlap (note that the error bars are much larger on the 530 nm data, since these signals are superimposed on a much larger Rayleigh floor). It will be shown in section C.2.11 that fiber reflectivity measurements performed on fiber-dump systems are insufficiently accurate to reliably determine reflectivity vs. wavelength, and it is necessary to use fiber-fiber splice systems where the core diameters are matched. The Rayleigh backscattering floor for the 530 nm, 7.3 ns FWHM pulses and the 680 nm, 3.3 ns FWHM pulses is also plotted in this figure. As shown in this plot the Rayleigh floor with the 680 nm, 3.3 ns pulses is approximately 6-7 times lower than that with the 530 nm, 7.3 ns pulses, as theoretically predicted by Rayleigh theory.

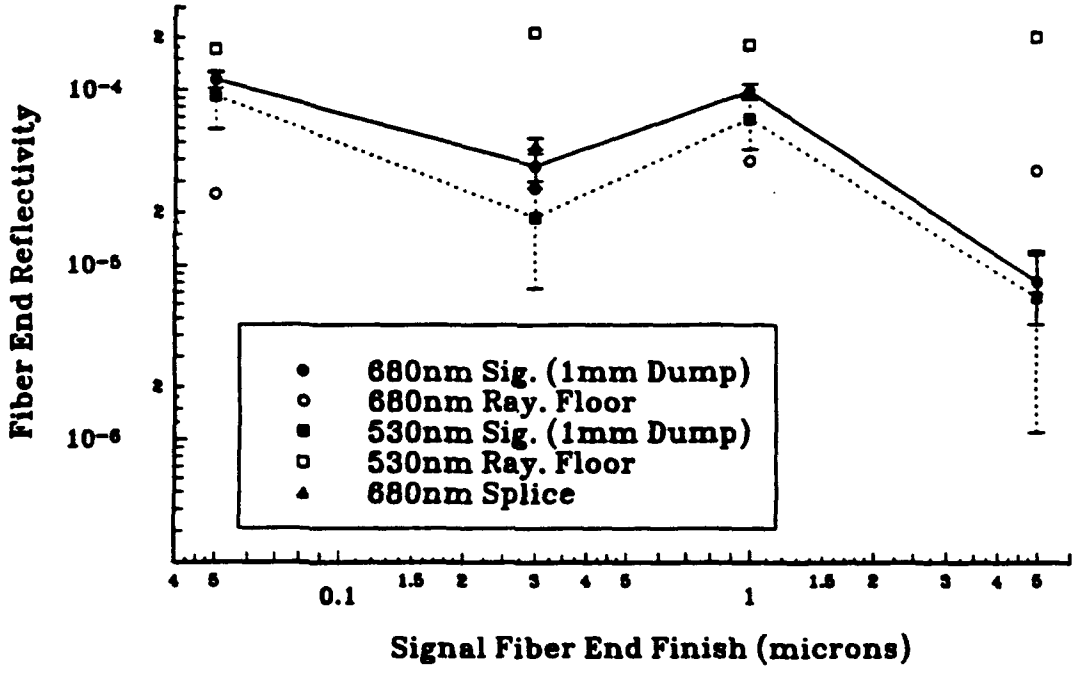

Figure C-4. Reflectivity vs. signal fiber finish.

C.2.6 Fiber Splice Measurement.

It is of interest to compare these intrinsic reflectivity measurements (which use a larger diameter dump fiber to eliminate spurious reflections due to fiber misalignment) to those obtained when the signal and dump fibers have the same diameter, as is the case with a fielded splice. To this end, OTDR reflectivity measurements were performed with 680 nm, 3.3 ns pulses on a splice made from the two fibers ends with the smallest intrinsic reflection signatures shown in figure C-4 (with a 0.3 mm finish and a 5 mm finish). The OTDR reflectivity of this splice is shown as the solid triangle in figure C-4. The measured splice reflectivity was approximately equal to the sum of the intrinsic reflectivities of the individual fibers which form the splice (note that any reflectivity contributions from the dump fiber will couple much more efficiently into the signal fiber when the core diameters are matched).

C.2.7 Reflectivity vs. Dump Fiber Characteristics.

Studies were also performed to analyze the splice reflectivity with respect to the dump fiber preparation. Previous studies[5] have shown that the contributions to the intrinsic splice reflectivity from a fiber-dump interface are dominated by contributions from the signal fiber. Measurements performed on different signal fibers prepared under similar polishing conditions show significant fiber to fiber variability in the intrinsic signature. Conversely, intrinsic reflectivity measurements performed on a given signal fiber appear to remain constant if different dump fibers (prepared under similar polishing conditions) are used.[5] The minimal dump fiber contribution to the intrinsic reflectivity may arise because only part of the backscattered reflection from the 1 mm diameter fiber is coupled into a 0.5 mm fiber. It was of interest to map out this small dump fiber contribution. A 0.5 mm diameter fiber with a small reflection signature was selected, and the resulting reflectivity was measured with the following 1 mm diameter dump fibers: (i) a smooth dump finished with 0.05 mm de-agglomerated alumina oxide; (ii) a dump fiber finished with 15 mm alumina oxide abrasion paper; (iii) a dump fiber finished with 32 mm alumina oxide abrasion paper; and (iv) a fiber cut with an unheated razor blade. The results of these measurements are shown in figure C-5. As can be seen from figure C-5, there is an observable variation in the splice reflectivity from the dump fibers prepared under radically

different surface preparation procedures. However, the change in reflectivities due to these different dump fibers is small compared to the intrinsic reflection signature of all but the lowest reflectivity splices.

C.2.8 Fiber Reflectivity vs. Pulse Fluence.

Measurements were also performed to determine the variation of the intrinsic fiber reflectivity with input pulse fluence. The reasons for this measurement were twofold: (i) in order to use the Nd: YAG pumped dye laser OTDR measurements to predict the performance of commercial OTDR systems (which typically use much smaller pulse powers than those available with the Nd: YAG pumped dye laser), it was important to show that the fiber reflectivity had no fluence dependence; (2) if the fiber reflectivity did exhibit a strong nonlinear component (i.e., the reflectivity varied with fluence), it might be possible to use this nonlinear phenomena as an additional mechanism for splice detection. Possible mechanisms for such a nonlinear phenomena include: nonlinear surface effects or nonlinear behavior in the index matching fluid.

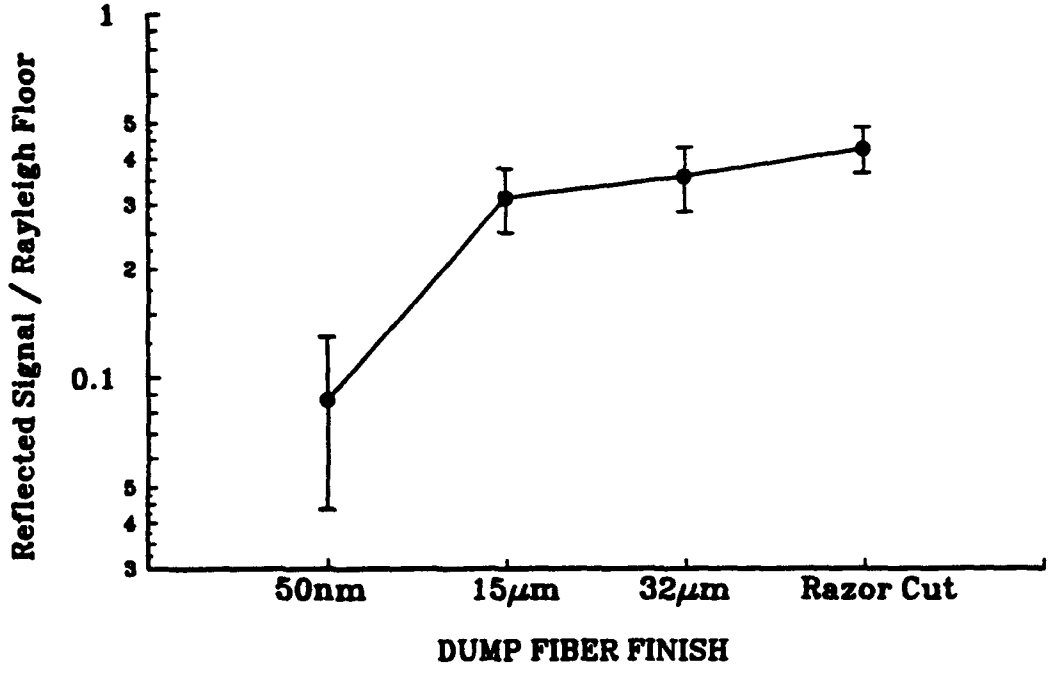

Figure C-5. Variation of fiber reflectivity with dump fiber finish (l=530nm, 0.3 mm Signal Fiber Finish).

Figure C-6 shows the variation of the ratio of the reflected signal to Rayleigh floor for input laser fluences which vary from approximately 0.002 J/cm^2 to 0.2 J/cm^2, where 7 ns, 530 nm laser pulses were used. The fiber labeled as Al-2 in figure C-6 was selected as the signal fiber because of its extremely low fiber reflectivity ($2x10^{-5}$). A low reflectivity fiber was used so that any nonlinear contributions would be easily visible on top of the small intrinsic reflection signal. As can be seen from this plot, any nonlinear contributions to the reflected signal are 13-14 db below the Rayleigh floor even at fluences as large as 0.25 J/cm^2, which is just below the fiber damage threshold. Some fiber damage (as exhibited by distortion in the temporal Rayleigh floor backscatter characteristics) was observed at 0.4 J/cm^2, and catastrophic self-focusing damage in the fiber was observed at 0.8 J/cm^2. Hence, it can be concluded that no significant nonlinear contributions to the fiber reflectivity exist for PMMA fiber when 7 ns, 530 nm laser pulses are used.

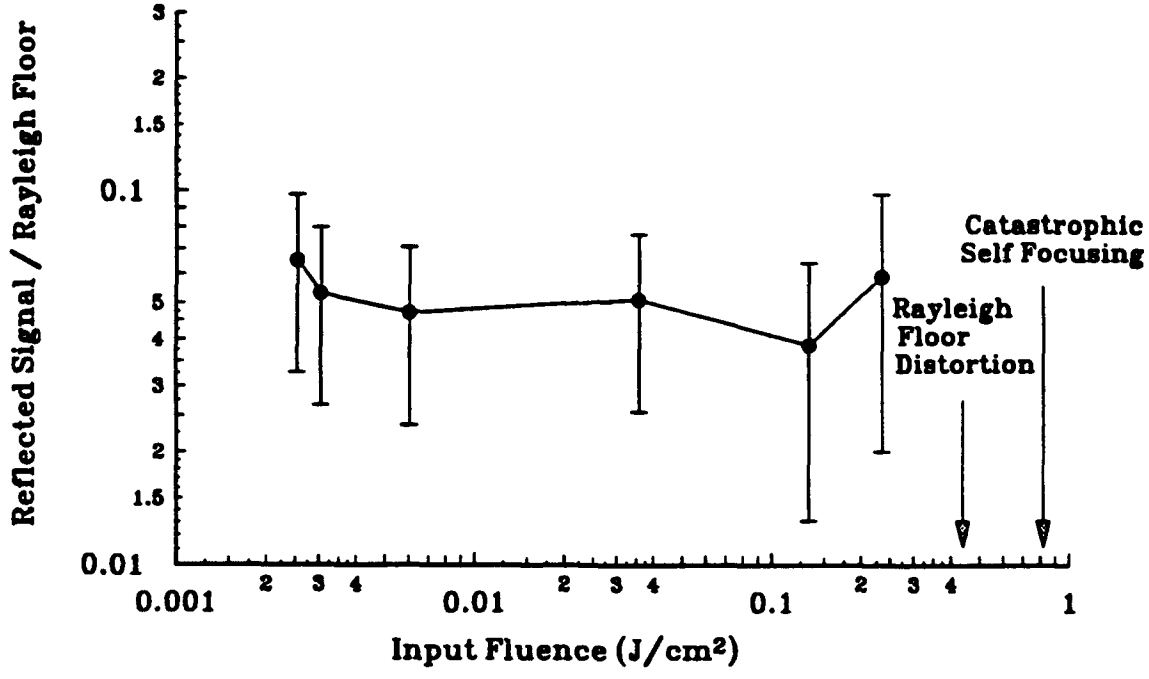

Figure C-6. Variation of fiber reflectivity with input pulse fluence (l=530 nm, t=7 ns),

C.2.9 Fiber Bevel Angle Measurements.

The technique of using beveled fiber ends for splices is commonly used to reduce or eliminate Fresnel reflections at the splice interface due to inexact index matching, since any reflections from the beveled surface occur at angles which are not propagated by the fiber. Investigations were performed of the variation of the intrinsic signal with fiber bevel angle, in order to verify that no significant decrease in the minimum intrinsic reflection signature occurs. In order to polish fiber ends at various bevel angles, a new polishing apparatus was fabricated which enables fibers to be polished at angles of 0°, 10°, 20°, 30°, and 40° with respect to the fiber axis. This polishing apparatus is pictured in figure C-7. In order to achieve flat fiber surfaces, a large area polishing apparatus was constructed from acrylic which has a hardness similar to that of the PMMA fiber core. For every 0.5 mm diameter signal fiber polished at a given bevel angle an opposing 1 mm diameter dump fiber was also polished at the same angle. Each fiber was polished with a combination of alumina oxide, cerium oxide, and de-agglomerated alumina oxide. OTDR experiments were performed on these fibers with 680 nm, 3.3 ns laser pulses, and the variation of the minimum intrinsic signal with bevel angle is shown in figure C-8. The primary result of these experiments is that the intrinsic signal did not appear to significantly decrease when beveled fibers were used, and the intrinsic reflection signatures were larger than those obtained with the previous fiber polishing "run." The reason that the use of beveled fibers did not lead to an observable decrease in intrinsic signal is probably because all Fresnel reflections have already been eliminated by careful index matching, so that no additional reduction is obtained from beveling the fibers. The exact functional dependence of the reflected signal with angle was difficult to ascertain. It should be noted that although each fiber was polished in the same polishing jig with identical polishing procedures, the separate fibers may have encountered unavoidably unique conditions due to the various tilt angles of the fibers, which may have introduced different polishing stresses.

Figure C-7. Angled fiber polishing apparatus.

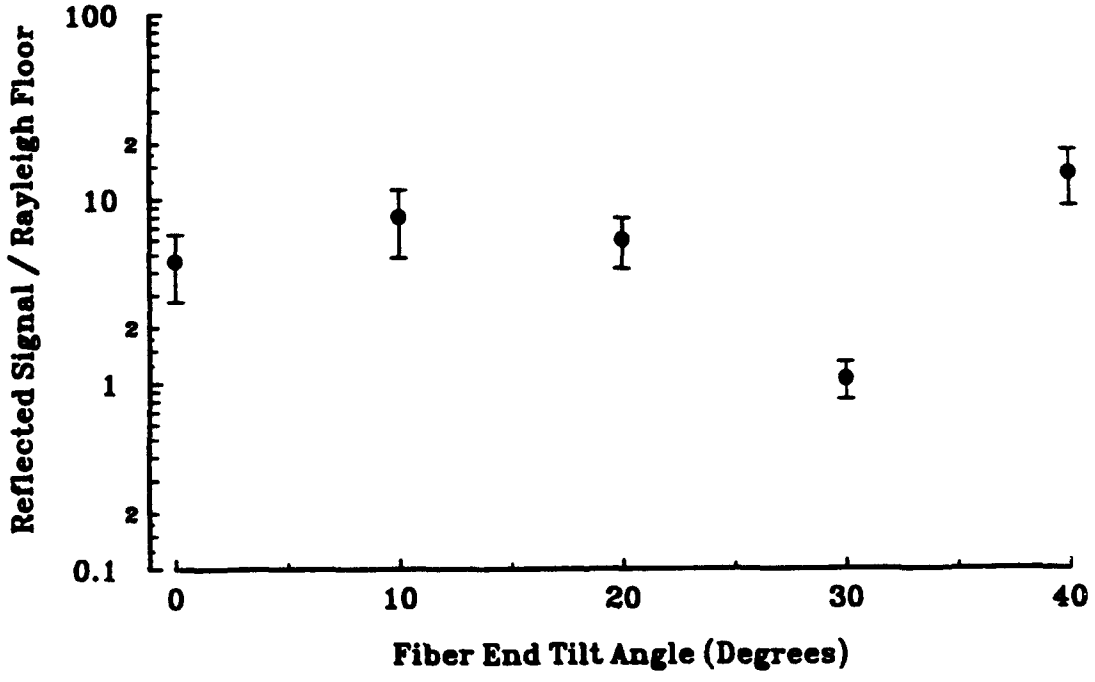

Figure C-8. Fiber reflectivity vs. bevel angle (l=680 nm, t=3.3ns).

C.2.10 Dependence Of Signature On Fiber Polishing Run.

Figure C-9 shows a compendium of the intrinsic reflectivity of all non-beveled fiber-dump systems tested. These fibers were prepared in three polishing runs. In the first run, fibers were polished with alumina oxide and finished with cerium oxide.[5] The fibers from this first run are labeled in figure C-9 as CeO-1 through CeO-5. In the second run, fibers were held in an acrylic lapping apparatus and finished with a combination of de-agglomerated alumina oxide and cerium oxide polishes. The non-beveled fiber from this polishing run is labeled as CeO/Al. The fibers prepared in the third run were finished with de-agglomerated alumina oxide with various lapping grit finishes. These fibers are labeled in figure C-9 as Al-1 (0.05 mm finish), Al-2 (0.3 mm finish), Al-3 (1 mm finish), and Al-4 (5 mm finish). The intrinsic minimum reflectivity of the fibers from these three polishing runs appear to show a dependence on the polishing procedure. The fibers from the first run show the largest intrinsic reflectivities, the fibers from the third run show the smallest intrinsic reflectivities, and the fiber from the second run appears to fall somewhere in between. Hence, these results indicate that any non-index matchable below-surface damage contribution which may cause the intrinsic signature appears to be dependent on the fiber preparation procedure.

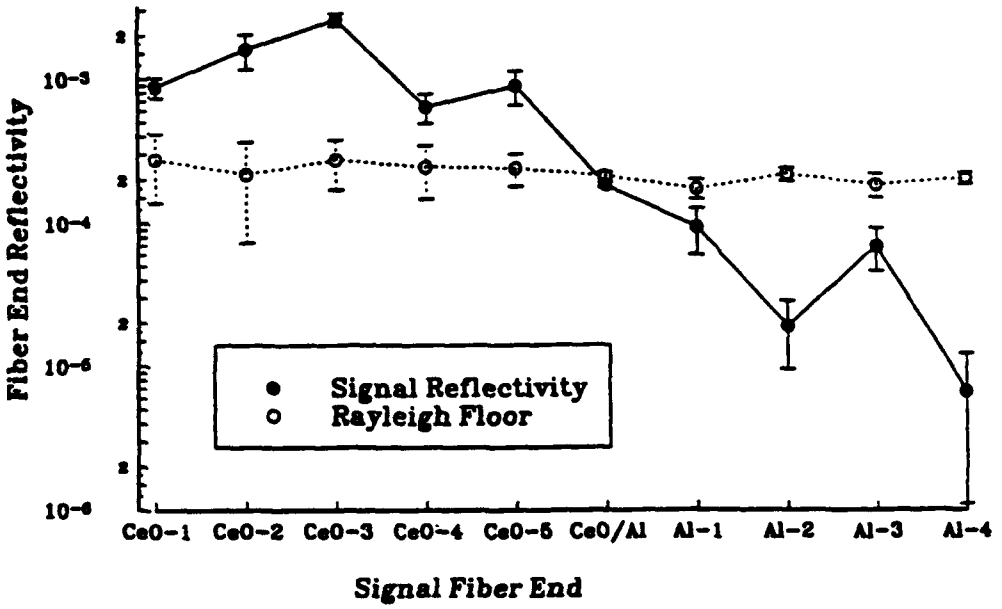

Figure C-9. Reflected Signal For Various Fiber Preparation Runs (l=530 nm, t=7.3ns).

Photographs of each of the signal fiber ends taken with a nomarsky polarimetric microscope with a magnification of 100x. Figures C-10 through C-13 show pictures of 0.5 mm fiber ends polished down to 5 micron grit, 1 micron grit, 0.3 micron grit, and 0.05 micron grit alumina oxide. As can be seen from these pictures, the 5 micron finished fiber end has the highest degree of flatness, and all fibers have uniform roughness across the fiber surface except for the 0.05 micron finish fiber which has a non-uniform region near the center of the fiber.

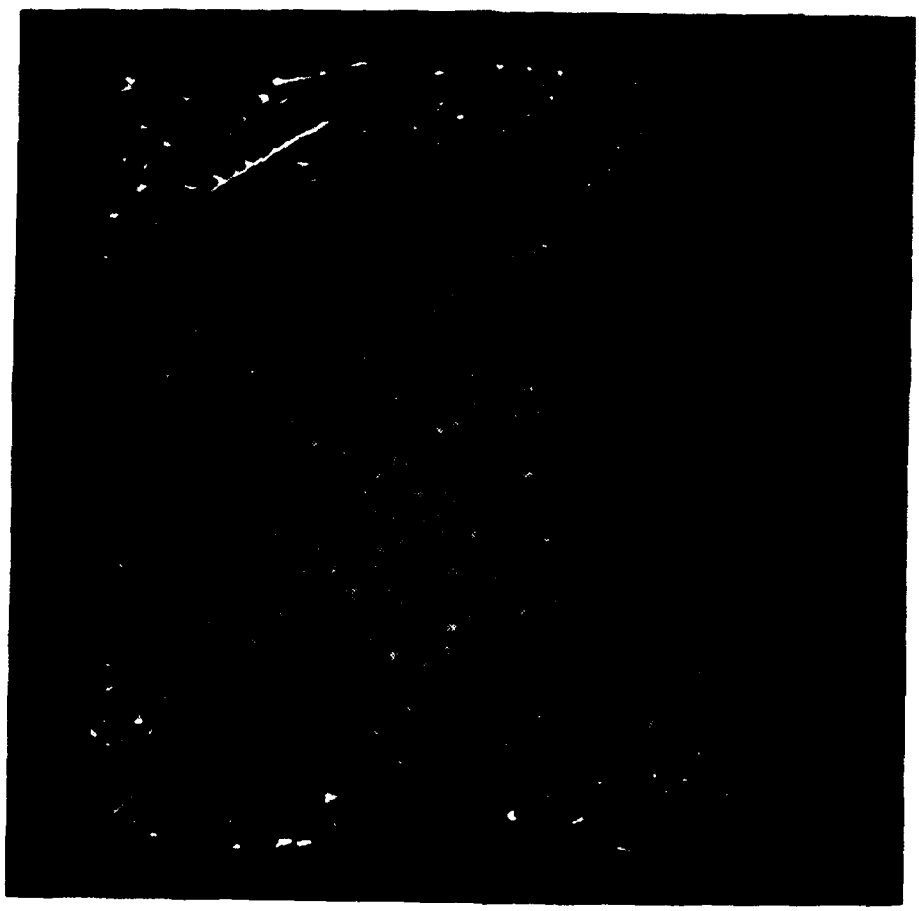

Figure C-10. PMMA fiber end (0.5 mm) finished with 5 mm grit (100x).

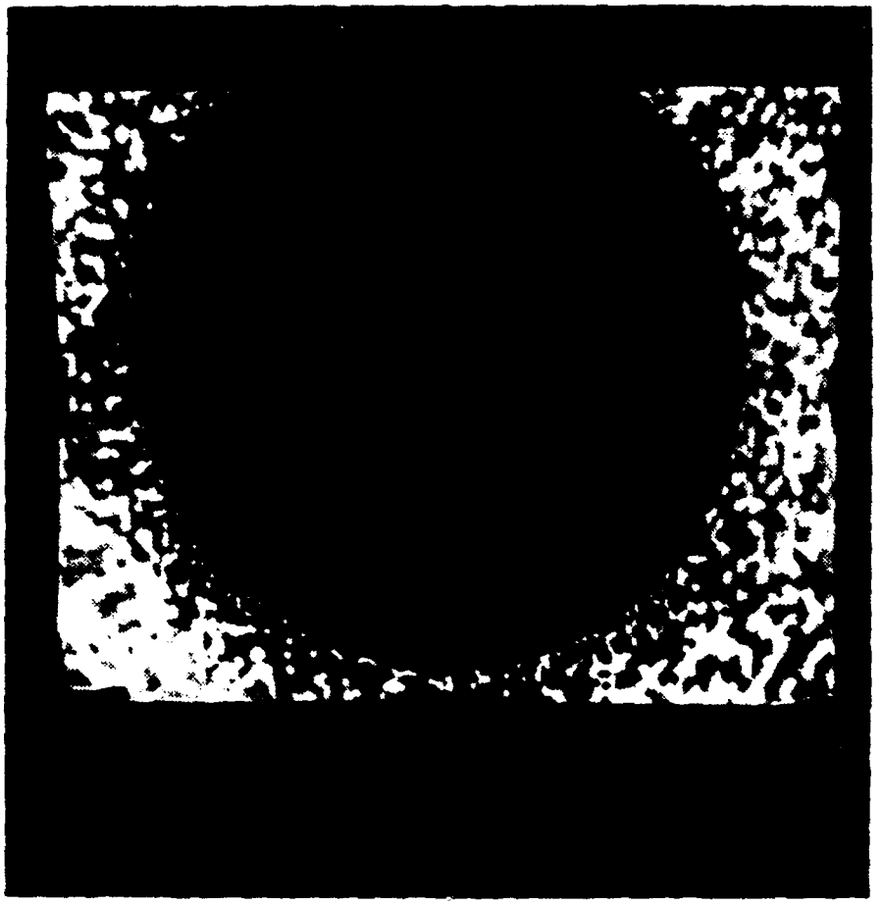

Figure C-11. PMMA fiber end (0.5 mm) finished with 1 mm grit (100x).

Figure C-12. PMMA fiber end (0.05 mm) finished with 0.3 mm grit (100x).

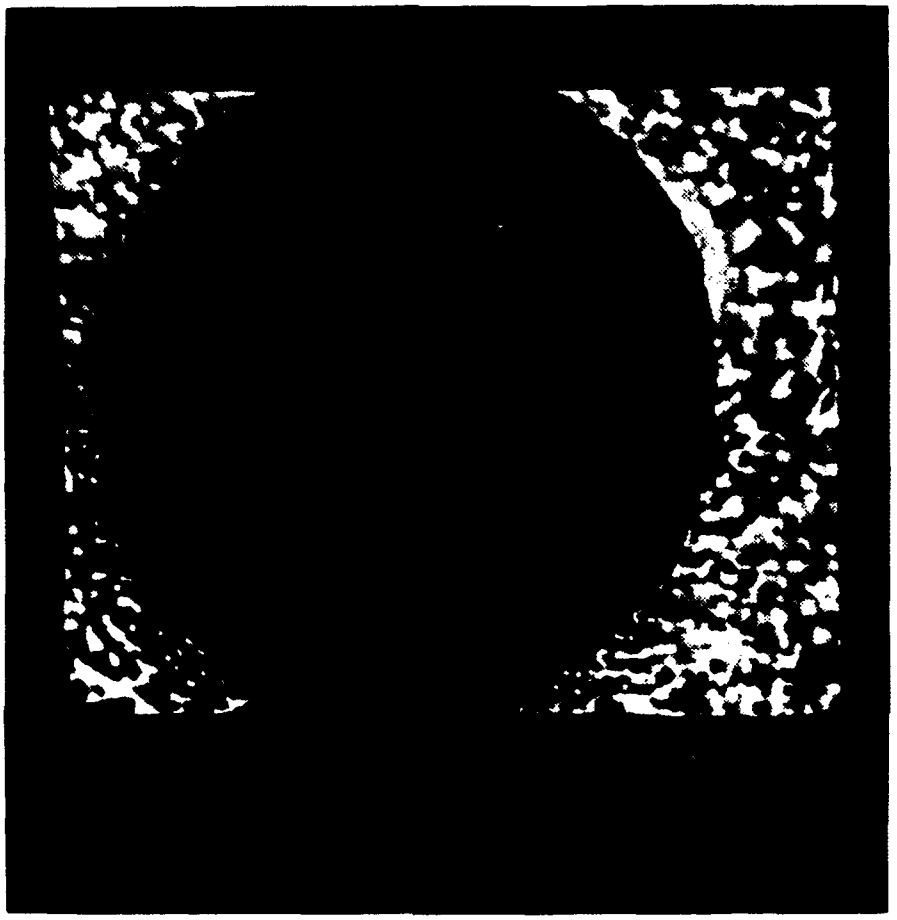

Figure C-13. PMMA fiber end (0.5 mm) finished with 0.05 mm grit (100x).

C.2.11 Wavelength Dependence of Fiber Reflectivity.

C.2.11.1 Introduction To Spectral Reflectivity Experiments. It has been shown that there is a nonvanishing, intrinsic component in the reflection signature of polished PMMA plastic optical fiber splices. This reflection signature is observed even when contributions from fiber core misalignment, refractive index mismatches and geometric imperfections in the fiber core at the fiber-fiber interface are experimentally eliminated. In this section, we will present experimental results which show the wavelength dependence of this intrinsic signature. These results will be fit with a Mie scattering model later in this report. This analysis is done in order to estimate the size of the scattering/reflection centers. This information is used to help understand the possible origins of the intrinsic signal.

C.2.11.2 Fiber Preparation. A large area polishing apparatus was constructed which incorporated 16 plastic polishing pads to hold the fibers during polishing. In order to obtain flat fiber surface profiles, polishing pads were selected with a hardness similar to that of the fibers, so that material was removed at a uniform rate from all surfaces being polished. Using this polishing apparatus, PMMA fiber ends were simultaneously ground down with 32 mm and 20 mm alumina oxide paper. A smooth finish was subsequently applied to the fibers by lapping them with wet slurries of de-agglomerated alumina oxide solution with particle sizes of 3 mm, 1 mm, 0.3 mm, and finally 0.05 mm.

The resultant finish on the fibers appeared to be very smooth, with few defects observable. Figures C-14 and C-15 show pictures of typical 250 mm PMMA fibers polished with this procedure taken through a nomarsky polarimetric microscope at 200x and 1000x magnification, respectively.

C.2.11.3 Experimental Setup. Measurements were performed to determine the functional dependence of the intrinsic fiber reflectivity on wavelength. A tunable dye laser (pumped by a frequency doubled or tripled Nd:YAG laser) was used to obtain laser light in the 450 nm to 700 nm spectral range.

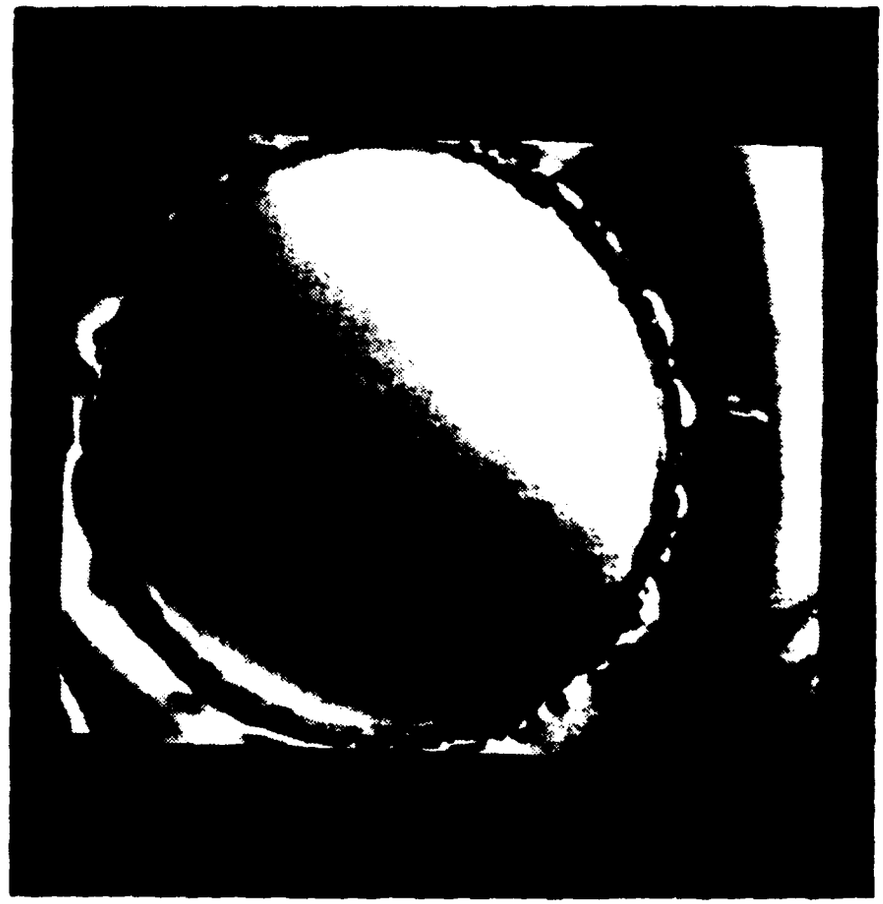

Figure C-14. PMMA fiber end (0.25 mm) finished with 0.05 micron grit (200x).

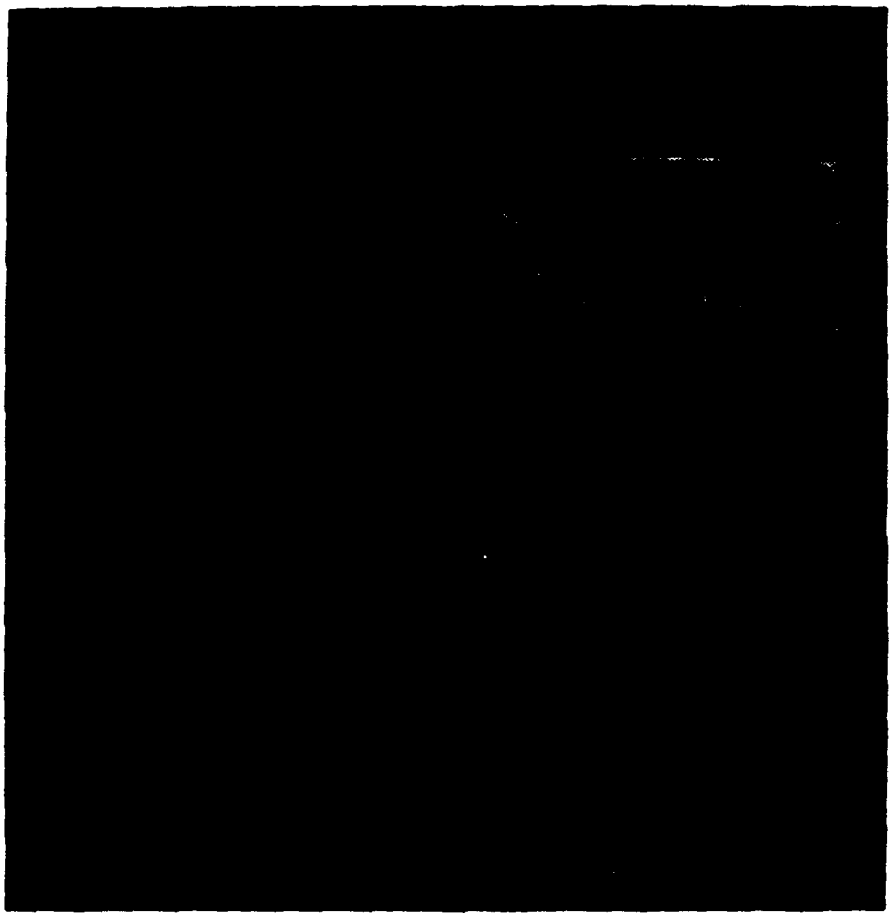

Figure C-15. PMMA fiber end (0.25 mm) finished with 0.05 micron grit (1000x).

Preliminary wavelength measurements, discussed in section C.2.5, showed that the fiber reflectivity does not vary strongly with wavelength, and the differences in fiber reflectivity at 680 nm and 530 nm were less than the data point error bars. Hence, in order to map out in detail the fiber reflectivity wavelength dependence, attempts were made at improving the accuracy of the fiber reflectivity measurements, by improving the OTDR experiment.

The first improvement involved the modification of the fiber coupling optics from those described in the last report to provide improved spatial and polarization filtering characteristics. Polarization filtering was improved by using a polarizer with an higher extinction ratio. Spatial filtering was improved by using micropositioners to achieve a much higher degree of control of the relative separations between the input lens and the spatial filter. Both spatial and polarization filtering were improved by using a micropositioner to more exactly control the laser spot size on the input fiber (too small of a spot can lead to fiber damage; too large of a spot can cause specular scattering and depolarization of the front surface reflection).

As a second improvement, careful electromagnetic shielding techniques were used to reduce electromagnetic interference (EMI) pickup in the cables, detectors, detector amplifiers, and digitizer. These techniques significantly reduced the background noise in the digitizer traces due to electromagnetic interference.

C.2.11.4 Laser Dye Analysis And Selection. An analysis was performed to select a complementary assortment of laser dyes that would yield dye laser tunability between 420 nm and 700 nm when pumped by a frequency doubled or tripled Nd:YAG laser. The optimum dye concentration in the selected solvent for the oscillator and amplifier dye laser stages was also determined. Table C-1 lists the selected dyes, along with the laser solvent, pump laser wavelength, and nominal dye molar concentration (for both the oscillator and amplifier dye cells). All of these dyes except for Stilbene 420 were successfully used for the OTDR experiment. Despite repeated efforts, use of Stilbene 420 in the dye laser yielded poor laser power and pulse stability, and data obtained with this dye was unreliable.

Table C-1. Laser dye analysis and selection.

LASER DYE	SOLVENT	PUMP (nm)	LASER RANGE (nm)	CONCENTRATION (molar)
Stilbene 420	CH_3OH	355	420-459	$5.3x10^{-4}$(osc) / $9.1x10^{-5}$(amp)
Coumarin 460	CH_3OH	355	442-490	$1.6x10^{-3}$(osc) / $5.6x10^{-4}$(amp)
Coumarin 500	CH_3OH	355	483-559	$5x10^{-3}$(osc) / $2x10^{-3}$(amp)
Rhodamine 590	CH_3OH	532	552-584	120mg/l(osc) / 51mg/l(amp)
Kiton Red 620	CH_3OH	532	578-606	$2.2x10^{-4}$(osc) / $2.8x10^{-5}$(amp)
DCM	CH_3OH	532	607-676	not available
LDS 698	CH_3OH	532	661-740	$2x10^{-4}$(osc) / $5x10^{-5}$(amp)

C.2.11.5 Index Matching Studies. In order to map out the wavelength dependence of the *intrinsic* fiber reflectivity, any spurious variations in the OTDR reflectivity due to wavelength variations must be eliminated. One possible mechanism for such a spurious spectral reflectivity variation arises from imperfect index matching at the splice due to the differential spectral dispersion between the PMMA fiber and the index matching fluid. To avoid these spurious effects, it is essential to verify that index matching is achieved at each wavelength of interest for the plastic fiber splice. To this end, measurements were made of the variation of the OTDR signal with index fluid at two wavelength extremes, 470 nm and 680 nm. Previous measurements have been made which mapped out the OTDR signal vs. index fluid for the fiber-fiber interface,[5,10] but these previous, more qualitative measurements were performed with no effort made to control the temperature of the fiber splice. Hence, small errors in these previous measurements could have arisen due to thermally induced differential shifts in the index of the fluid relative to that of the fiber. In the present measurements, the OTDR signals from two similar 1 mm PMMA fiber splices (made with the same fibers) were mapped out vs. index matching fluid at 470 nm and 680 nm. The splice temperature was nearly identical (to within 0.5°C) for the two

experiments, which should eliminate any thermally induced spurious effects. It should be noted that measurements were performed on a fiber-fiber splice rather than the fiber-dump system described before, to provide more accurate characterization of the Rayleigh floor. Rather than butting the two fibers together, the fiber-fiber separation was set to approximately 0.5 mm, to facilitate easy addition and removal of the different index fluids.

Results from experiments performed with 470 nm laser pulses are shown in figure C-16. In this plot, the solid round points are the splice reflectivity data. The minimum, intrinsic reflectivity (i.e., the minimum of the curve) for this particular splice is seen to be 6×10^{-5}. The open circles in figure C-16 show points where this constant value of the intrinsic reflectivity has been subtracted from the data, to displace the curve downward.

A Fresnel theory which sums over all transverse modes of the fiber and takes into account multiple reflections between the signal and dump fibers[5] was used to fit this data, with the effective fiber core index, n_c, used as a fitting parameter. The best fit to the data was obtained with $n_c = 1.491$, and the resulting theoretical plot is shown as the solid line in figure C-16. It can be seen that there is excellent agreement between the down-shifted data and the multimode Fresnel theory corresponding to optimum index matching. Hence, it can be seen that a non-index matchable constant y-offset exists which cannot be eliminated by careful index matching.

The corresponding measurements at 680 nm are shown in figure C-17, with the splice reflectivity data again plotted as solid round points. The minimum, intrinsic reflectivity (i.e., the minimum of the curve) for this particular splice is seen to be 4×10^{-5}. The constant value is again subtracted from all of the data points to obtain the downwardly displaced data curve which is plotted as open circles. The same Fresnel theory[5] was fitted to the data with n_c

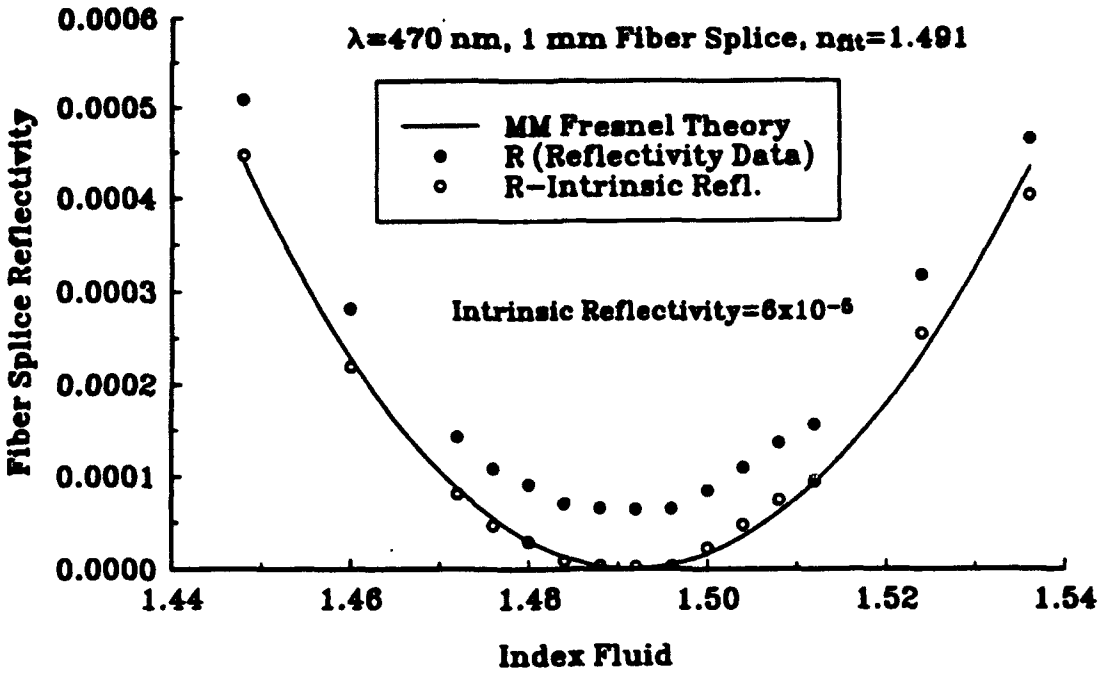

Figure C-16 . Fiber splice reflectivity at 470 nm vs. index fluid with multimode fresnel theoretical fit.

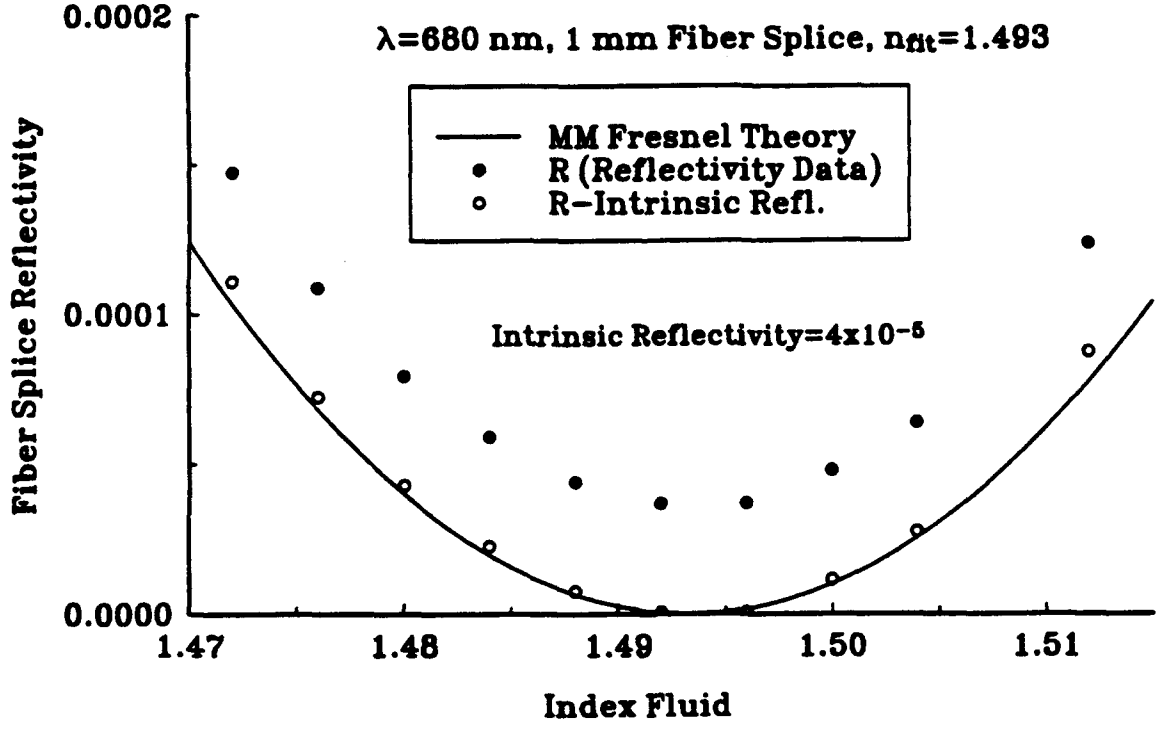

Figure C-17. Fiber splice reflectivity at 680 nm vs. index fluid with multimode fresnel theoretical fit.

used as a fitting parameter. The best fit to the data was obtained with n_c=1.493 for this wavelength, and the resulting theoretical plot is shown as the solid line in figure C-17. It can be seen that there is again excellent agreement between the down-shifted data and the multimode Fresnel theory corresponding to optimum index matching, which is again consistent with a non-index matchable constant y-offset.

Since the best index matching was found to be 1.491 at 470 nm and 1.493 at 680 nm, it has been shown that there is indeed a small differential dispersion between the index matching fluid and the fiber. However, this shift is found to be insignificant compared to the index resolution (0.004) provided by the set of index matching fluids. Therefore, 1.492 index matching fluid will provide optimum index matching over the entire spectral range of interest.

C.2.11.6 Experimental Result Of Reflectivity Vs. Wavelength. Measurements were performed on a conventional fiber-dump setup which utilized a 0.5 mm diameter signal fiber and a 1 mm diameter dump fiber. As in previous measurements, the minimum, "intrinsic" reflected signal at each wavelength is measured after the fiber-dump alignment is optimized and the dump fiber is index matched to the signal fiber. This data is plotted in figure C-18. As with the fiber-dump data, there is some suggestion of a decrease in the fiber-dump reflectivity at lower wavelengths. However, because of the very large scatter in this data, it is not possible to reliably determine the spectral dependence of the intrinsic fiber-dump reflectivity.

The reason for the large error in this fiber-dump reflectivity data is because of errors in measuring the Rayleigh floor in the exact vicinity of the splice, since the Rayleigh floor undergoes a discontinuous drop at this point due to the large diameter of the dump fiber compared to the signal fiber. These errors are exacerbated at low wavelengths where the Rayleigh floor is very large compared to the intrinsic signal. Hence, it was determined that an improvement was required in the experimental procedure in order to reliably ascertain the functional dependence of the intrinsic reflectivity vs. wavelength.

To this end, a 1 mm x 1 mm plastic fiber splice was incorporated into a second, duplicate micropositioner-based fiber-fiber splice apparatus. This

enabled much more accurate measurement of the Rayleigh floor, since the fiber diameter of the signal and dump fibers was identical. Once the fiber-fiber position was optimized for the 1 mm x 1 mm splice, the fibers were index matched with 1.492 fluid and fixed in place so that no variations would occur in the fiber-fiber alignment for different data acquisition runs at different wavelengths. The reason for fixing these fibers in place was that the fiber splice is much more sensitive to alignment when the dump fiber has the same diameter as the signal fiber.

Measurements were then performed of the intrinsic fiber splice reflectivity vs. wavelength. However, since the fiber-fiber position was fixed (to avoid alignment variations), it was not possible to directly measure the Fresnel reflection at each wavelength, which was previously used to calibrate the signal. Hence, an alternative calibration technique was used, as described in the following paragraph.

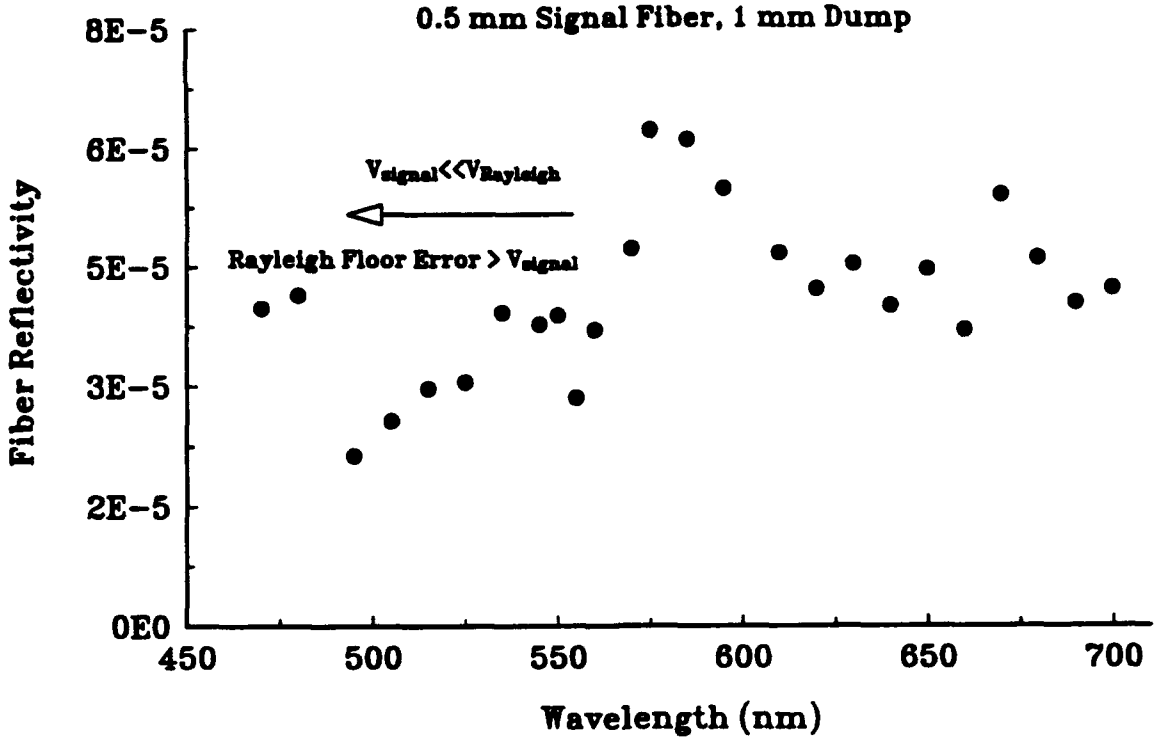

Figure C-18. Fiber-dump reflectivity vs. wavelength.

The ratio of the Fresnel reflectivity to the Rayleigh floor at the splice interface should be a constant if it is assumed that the laser pulse width does not vary (this assumption shall be examined presently). This ratio of the Fresnel reflectivity to the Rayleigh floor will be independent of variations in the fiber transmission or detector sensitivity with wavelength. In addition, this ratio should also be independent of the variations in the laser-fiber coupling efficiency. Hence, for each data point, the splice reflectivity data was calibrated with the associated measurement of the Rayleigh floor. In addition, pulse-to-pulse variations in the integrated laser pulse energy were also accounted for.

The resultant intrinsic fiber splice reflectivity is plotted vs wavelength in figure C-19. As can be seen from this figure, the scatter in the data has been significantly improved for the fiber splice measurements compared to the previous fiber-dump measurements. However, it can be seen that the measured splice reflectivity seems to increase at the end points of each dye curve, particularly with the Rhodamine 590 and Kitton Red 620 dyes.

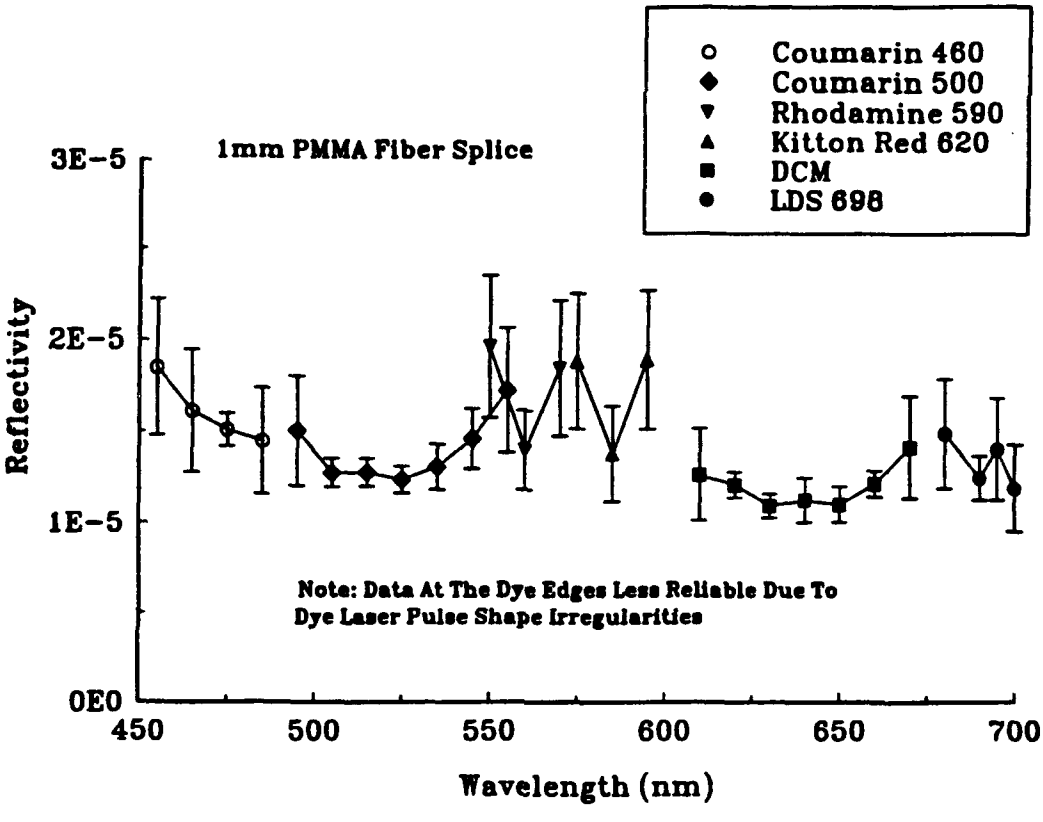

Figure C-19. Fiber splice reflectivity vs. wavelength.

In order to understand this increase in the fiber reflectivity at the dye edges, it must be remembered that the ratio of the Fresnel reflectivity to the Rayleigh floor will be constant at the splice interface only if the laser pulse shape and width is constant, since the Fresnel reflectivity signal will scale as the peak laser power and the Rayleigh floor scales as the laser energy (integrated over the relevant time window). Hence, measurements were performed of the variation of the dye laser pulse width with wavelength, as shown in figure C-20. As can be seen from figure C-20, the laser pulse width significantly decreases near the dye edges, which will lead to an apparent increase in the measured reflectivity compared to the Rayleigh floor. However, the pulse width of the various laser dyes is relatively constant (ranging between 5 and 6 ns) in the middle regions of the laser dye gain profiles. Hence, the intrinsic splice reflectivity data taken at the edges of the various laser dyes was deleted from the set shown in figure C-19, with the resulting data subset shown in figure C-21. This data exhibits a much better consistency (i.e., small data scatter) than that plotted previously (note that most previous reflectivity plots shown in this report were plotted logarithmically). As can be seen from this plot, the intrinsic fiber splice reflectivity is relatively constant over the measured wavelength range (470 nm to 700 nm). A very slight decrease in the reflectivity with increasing wavelength is evident, but this decrease is within the error bars of the data.

C.2.11.4 Summary And Conclusions Of Wavelength Experiments. Hence, the wavelength dependence of the splice reflectivity has been successfully mapped out in figure C-21. It can be seen that this wavelength dependence is much flatter than might have been expected from theoretical considerations alone. Fitting this wavelength plot with a Mie scattering model will provide invaluable information regarding the mechanisms which cause the intrinsic reflection signature. The first important piece of information that this Mie scattering model will provide will be whether the fundamental mechanism for the intrinsic signature is due to below surface scattering, surface damage, or inhomogeneities in the transverse index profile of the PMMA fiber core index. If the intrinsic signature is due to a scattering mechanism, the Mie scattering model should provide definitive information about the type and size of the scattering centers. If the intrinsic signature is due to inhomogeneities in the fiber index profile, additional experiments will have to be performed to explore and verify this mechanism. Establishing the fundamental mechanism for the intrinsic reflection signature

will provide important assurance that no fiber preparation techniques exist, or can be developed, which will cause the intrinsic signature to vanish.

C.3 SUMMARY.

In summary, OTDR measurements have been performed on polished PMMA fibers. After the dominant splice reflection sources due to inexact index matching, and fiber core misalignment were eliminated, an intrinsic reflection signature which was clearly detectable above the Rayleigh noise floor was observed with all tested fibers. One possible explanation for this intrinsic signal is a below-surface damage mechanism.[4,5] It is also possible that the intrinsic signal may be due to transverse inhomogeneities in the plastic fiber index profile. Mie scattering results to be discussed later in this report may resolve this question.

The properties of this intrinsic reflection signature were mapped out versus experimental parameters such as fiber surface roughness, bevel angle, fiber separation and alignment, index matching fluid, dump fiber characteristics, laser fluence, and laser wavelength.

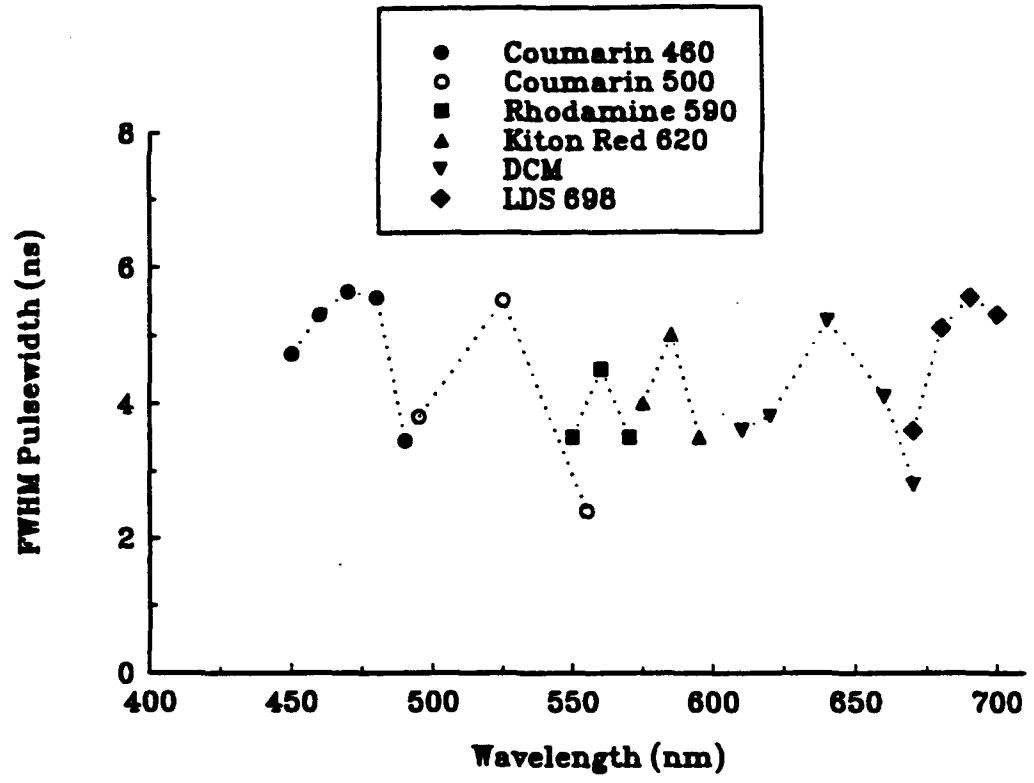

Figure C-20. Dye laser pulsewidth vs. wavelength.

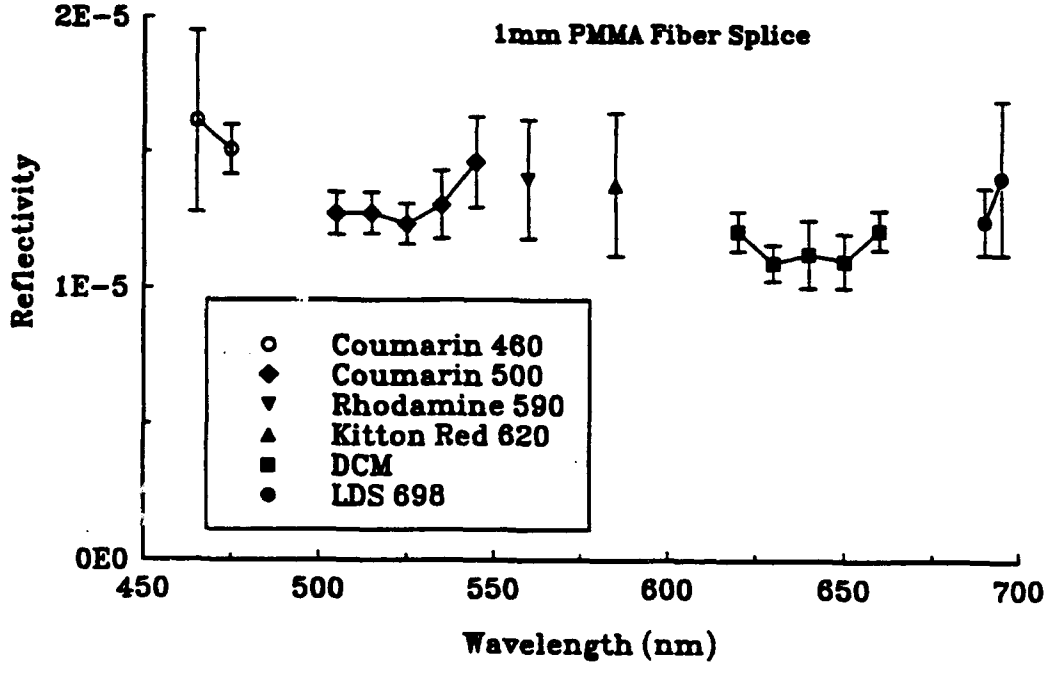

Figure C-21. Fiber splice reflectivity vs. wavelength (dye edge data points removed).

1 Spectral fiber loss measurements provided by Mitsubishi Cable America, Inc.

2 J. Meier, W. Lieber, W. Heinlein, W. Groh, P. Herbrechtsmeier, and J. Theis, "Time-Domain Bandwidth Measurements Of Step-Index Plastic Optical Fibres," Electron. Lett. vol. 23, pp. 1208-1209 (1987).

3 S. Takahashi and K. Ichimura, "Time Domain Measurements Of Launching-Condition-Dependent Bandwidth Of All-Plastic Optical Fibres," Electron. Lett., vol. 27, pp. 217-219, 1991.

4 C.M. Lawson, R.R. Michael, G.M. Finn, E.M. Dressel, and D.W. Harmony, "Measurements Of The Minimum Reflection Signature Of PMMA Fiber Splices," To Be Published.

5 C.M. Lawson, R.R. Michael, E.M. Dressel, and D.W. Harmony, "Nd: YAG Laser Based Time Domain Reflectometry Measurements Of The "Intrinsic" Reflection Signature From PMMA Fiber Splices," SPIE Proc. Vol. 1592, pp. 73-83 (1991).

6 S.D. Personik, "Photon Probe - An Optical Fiber Time-Domain Reflectometer," Bell Sys. Tech. J. vol. 56, pp. 355 (1977).

7 M.K. Barnoski, M.D. Rourke, S.M. Jensen, and R.T. Melville, "An Optical Time-Domain Reflectometer," Appl. Opt. vol. 16, pp. 2375 (1977).

8 S.D. Personik, *Fiber Optics, Technology And Applications*, Chapter 13, Plenum Press, New York, 1985.

9 S. Carson and R. Salazar, "Splicing Plastic Optical Fibers," to be published in SPIE Proceedings, vol. 1592 (1991).

10 These Results Were Discussed In Detail In A Previous Report.

APPENDIX D
ANALYSIS OF THE LIMITS OF SPLICE DETECTABILITY IN PLASTIC OPTICAL FIBER USING THE OFM20 OTDR

D.1 INTRODUCTION.

Establishing the limits of splice detectability with the Opto-Electronics OFM20 Optical Fiber Monitor, the optical time domain reflectometer (OTDR) selected for the PTILS tamper detection system, was an integral part of establishing proof-of-principle for PTILS. The physics of OTDR backscattering and the phenomenology of the OFM20 detector characteristics were simulated to allow artificial generation of OFM20 traces displaying hypothetical splices of very high quality–splice qualities that would be very difficult or impossible to achieve in the laboratory. This modeling effort also allowed quantitative evaluation of the throughput losses and reflectivities of actual splices prepared in the laboratory, so that the relationship between the current state-of-the-art in splicing plastic optical fiber to the limits of splice detectability with the OFM20 could be assessed. Finally, insights gained from analyzing OFM20 traces in the context of a descriptive model provided the requisite understanding necessary to select credible algorithms for pursuing automated "red light/green light" tamper assessment in the fielded PTILS system.

D.2 QUALITATIVE DESCRIPTION OF THE PHOTON COUNTING OFM20 OTDR.

The OFM20 OTDR used in PTILS is a photon counting instrument that uses a different principle of detection of backscattered light than is used in an ordinary OTDR. The type of analysis necessary to model the performance of the OFM20 is complicated by this difference. In particular, nonlinearities associated with the detector design introduce modeling difficulties that require special techniques to unravel meaningful quantitative interpretations from the traces. Before entering into a mathematical description of OFM20 trace generation, it is helpful to digress for a moment to qualitatively describe the detection principles used in a photon counting OTDR.

D.2.1 Description of the Photon Counting Detection Method.

To generate a trace, the OFM20 samples light backscattered from the fiber at 256 discrete time nodes corresponding to 256 discrete, evenly spaced spatial locations spanning the particular spatial window on the fiber that has been selected for the trace display. Instead of registering an analog voltage in linear proportion to the light power returned at each point in each sample as in a normal OTDR, the photon counting OFM20 has only a binary (2 bit) signal/no signal counter as a receiver. The 8 bit digital amplitude assigned to the returned light intensity is accrued by summing repeated binary samples (each from a different laser pulse firing) at each discrete spatial location: 256 2-bit numbers are added up in each of the 256 channels to form one 8 bit amplitude assignment for each channel. Thus, 256x256 laser firings are needed to completely sample an entire OFM20 trace one time. Noise in the trace is then reduced by averaging thousands of individual trace acquisitions in each channel.

The photon counting receiver, which uses an avalanche photodiode (APD) for its detector, has a non-zero probability of triggering with backscattered energies as low as one to three individual photons within a given sampling interval. The higher the backscattered light intensity becomes, the higher the probability that the APD will trigger and register a count during that sample. If the backscattered light intensity becomes too high, then the APD will always trigger, and the trace will saturate. Since the laser diode always fires at maximum brightness, the intensity of the backscattered light reaching the detector in any given fiber-OTDR configuration must be controlled by the operator though the digitally stepped neutral density filter in series with the OFM20's laser diode light source. The setting of this neutral density filter is referred to as the *sensitivity* setting associated with the particular trace acquisition. In normal OFM20 operation, the backscattered light intensity is diminished sufficiently using the sensitivity setting so that the probability of triggering the APD in any given sample is between 10^{-6} and 10^{-1}. With very low light levels, most of the 256 binary addends contributing to the amplitude assignment will be zero, so that the sum over one trace generation cycle is far from saturated. Under these conditions the OTDR response amplitude approaches linearity in the backscattered light power received, but the signal-to-noise ratio is relatively low. For sensitivity

settings allowing higher backscattered light intensities, the signal-to-noise ratio improves, but the probabilistic accuracy of the photon counting detector is diminished, leading to marked nonlinearity in the trace response.

The light pulse generated in each firing of the laser diode source has a peak power of about 100 mW and a full width at half maximum (FWHM) of about 40 ps. In addition to the nominal Gaussian shape of the main pulse, the overall light pulse shape includes a low amplitude, slowly decaying exponential tail that extends for several microseconds. Most of the energy in the pulse is contained in the Gaussian shaped part of the pulse; however, the extended tail significantly raises the apparent backscattered response for several meters beyond any high amplitude Fresnel event in the trace. Spurious elevation of the Rayleigh floor after a Fresnel event due to the pulse tail is an important effect to take into account in modeling, if false interpretations of the trace amplitude are to be avoided.

By its nature, photon counting requires the light collection time of each binary sample to be finite, not infinitesimal. That is, the detector must "open its eye" to receive photons for a finite time duration if it is to collect enough photons to trigger the APD with sufficient probability to form a trace. The effect of collecting light over a finite time interval associated with each spatial node in the trace is to integrate the light power received over the duration of the sampling time window. Thus, the OFM20 trace indicates the light *energy* backscattered from each point on the fiber in contrast to indicating the light *power* backscattered as in a normal OTDR. The technique of cumulative time window sampling with a photon counting receiver replaces the function of an analog receiver amplifier; therefore, effectively eliminating concerns with receiver bandwidth as a modeling parameter. However, the effect of the sampling window on the trace, that of smearing the time history of the backscattered power by convolution with a detector function, is an effect that is very similar to that produced by bandwidth limitation. For example, an artifact of the photon counting detection technique is that the finite sampling time window of photon collection (corresponding to a finite spatial interval of photon backscatter events in the fiber) must be assigned to an instantaneous time (or spatial position) on the trace. The exact mapping of when (or where) on the trace that each sampling window interval is assigned is an arbitrary assignment that leads either to precursor or trailing deflection in the

OFM20 trace that does not exactly temporally (or spatially) correspond to the instantaneous backscattered light power events.

The OFM20 offers sampling widows in two different widths. The wider of these sampling windows achieves greater overall sensitivity by allowing more backscattered energy to be received in each sample, and thus allows a greater maximum detection sensitivity of the instrument. With the narrower window, the amplitude of the Rayleigh backscatter floor is reduced, but the spatial resolution of Fresnel-like events is better preserved, given the very short width of the laser pulse. Since the amplitude of the Fresnel-like deflection relative to the amplitude of the Rayleigh backscatter floor determines the splice detection sensitivity of the OTDR, only the narrower sampling window was used in the PTILS application.

The time duration of the sampling window is precisely controlled for each sample in the OFM20 by a free running time delay generator which according to Opto-Electronics has a 5 ps step resolution with less than 1 ps rms jitter. Although the on/off switching of the APD is controlled in time very precisely relative to the width of the sampling window through the time delay generator, the rate of change in the detection sensitivity of the APD when switched on or off is limited by the overall time constants of the detector circuit. Thus, the sampling window does not have sharp, rectangular edges, but rather has a rapid but finite rise time and a more slowly decaying fall time of detection sensitivity. To complicate matters further, the detection sensitivity of the probabilistic photon counting detection method is a nonlinear function of the instantaneous light power received, which has the effect of making the apparent sampling window shape change for different amplitudes and time histories of backscattered power. The problem of characterizing the sampling window sensitivity dependence on the backscattered power is a complication that makes mathematical description of the sampling window difficult.

D.2.2 The Effective Dead Zone in an OFM20 Trace.

If a Fresnel reflection is large, the OFM20 detector may become saturated at the particular spatial positions spanned by the reflection. However, since the detector is turned off at all times except for its very brief time window of sampling,

there is no residual dead zone due to saturation of the preceding spatial sample. According to Opto-Electronics, the actual saturation time of the OFM20 detector is approximately 10 times the pulse width (10 x 40 ps = 0.4 ns), which is much shorter than the period between samples (~1000 ns). In contrast, an ordinary OTDR with an analog receiver has its detector and amplifier turned on at all times, so that once saturated, it takes the receiver circuitry several to tens of nanoseconds to come out of saturation, resulting in an extended dead zone after a strong Fresnel event. The OFM20 does have a significant *effective* dead zone (4 to 5 meters), however, that arises from an echo train of light pulses (from reflections internal to the OTDR) launched into the fiber in addition to the primary light pulse launched directly from the laser diode. An OFM20 trace showing the echo train is shown in Figure D-1. The ordinate in this trace, as in all OTDR traces, has been divided by two so that the Rayleigh floor appears to have the correct slope for the lossiness of the fiber. In other words, the dB scale in OTDR trace displays is defined to be $5 \log_{10}[backscattered\ response]$ instead of the normal dB definition. Note that the echo train of pulses launched into the fiber, which is visible in the trace following every Fresnel event occurring in the fiber beyond the bulkhead, is different from the echo train within the OTDR, which is seen only at the bulkhead.

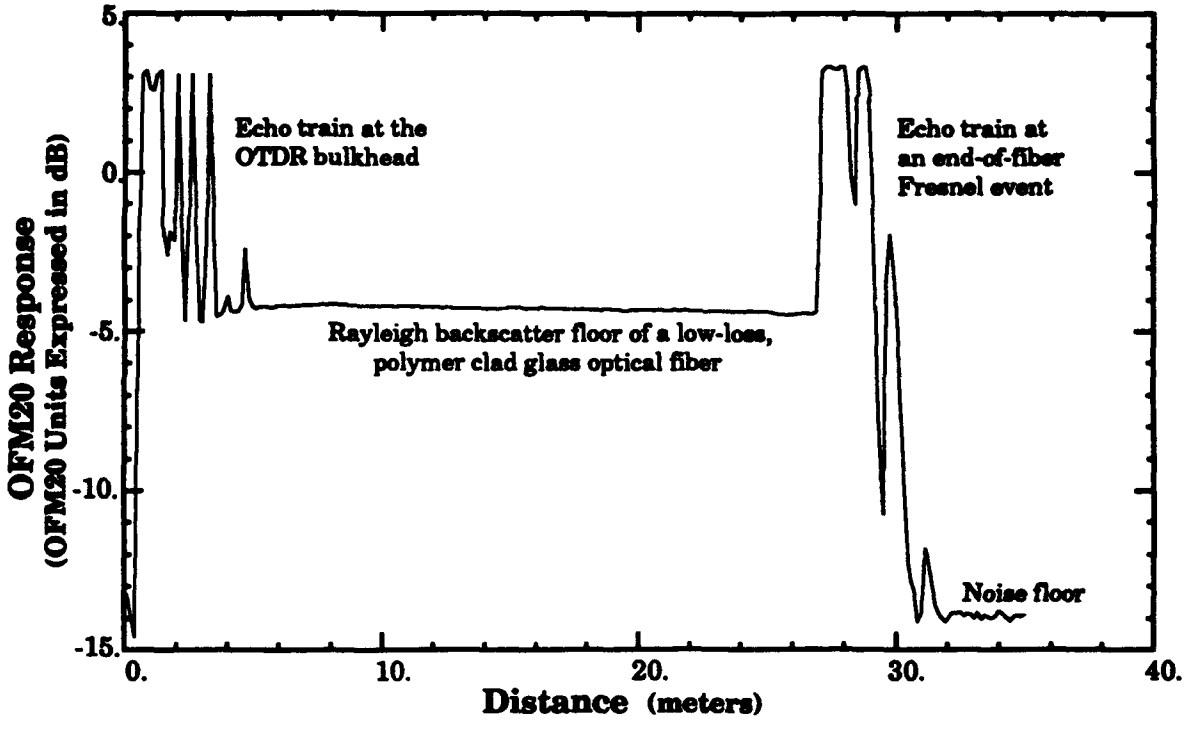

Figure D-1. OFM20 trace showing the echo train following fresnel events.

This echo train, which presumably is present but unnoticeable in ordinary OTDRs, is a nontrivial effect in OFM20 traces because the extreme narrowness of the laser pulse results in a Rayleigh backscatter floor of extremely low amplitude–low enough to easily reveal the weak Fresnel signals echoing within the OTDR. The monotonically decreasing train of echo pulses launched with each laser firing makes discrimination of a covert splice in the trace region following any strong Fresnel event risky or impossible. The practical workaround is to treat the echo region of the trace as if it were a dead zone, and simply avoid attempting to make trace interpretations in regions of the fiber following strong Fresnel events.

D.3 TREATMENT OF THE OFM20 NONLINEARITY.

As discussed in section D.2, the OFM20 trace response can be described as a convolution of the backscattered power with the sampling window. The mathematical formulation of this statement is:

$$\tilde{E}(t_i) = A_c \int_{t_i - (1-\eta)\tau_w}^{t_i + \eta\tau_w} \tilde{W}(t_i + \eta\tau_w - \tau; P_{bs}) P_{bs}(\tau)\, d\tau + \delta\tilde{E}(P_{bs}) \ , \qquad \text{(D-1)}$$

where

$\tilde{E}(t_i)$ is the time-based nonlinear OTDR trace response in OFM20 units at node i in the 256 node trace,

t_i is the time elapsed since the time of arrival at time node i of the forward-propagating light pulse from some reference position x_0 within the fiber,

$P_{bs}(t)$ is the backscattered power returning to reference location x_0 at time t from all points on the fiber downstream from location x_0,

A_c is the attenuation factor resulting from all fiber connectivity conditions upstream from x_0 to the detector (i.e., connector losses and fiber attenuation, including those inside the OTDR),

$\tilde{W}(\tau; P_{bs})$ is the nonlinear sampling window function whose sensitivity is a function of the backscattered power $P_{bs}(t)$,

τ_w is the *extreme* width of the sampling window; i.e.,

$$\widetilde{W}(\tau \leq 0; P_{bs}) = \widetilde{W}(\tau \geq \tau_w; P_{bs}) = 0 \quad ,$$

η is a fraction between 0 and 1 biasing the placement of the finite width result of the definite integral on the instantaneous time line, and

$\delta\widetilde{E}(P_{bs})$ is a random variable describing the trace noise associated with random fluctuations in the photon counting detector response.

In equation D-1, the units of $\widetilde{E}(t_i)$ are defined by the units of $\widetilde{W}(\tau; P_{bs})$ (OFM20 units/joule). The limits of the integral in equation D-1 are written in a general form so that the placement of the sampling window relative to the time axis can be varied by selection of the biasing parameter η. The argument of the window function simply ensures that the integral spans the entire sampling window at all times t_i and for any choice of η. Trace noise is denoted as a function of the backscattered light power because, based on the photon counting method of data acquisition, the (unknown) probability density distribution associated with probability of the detector triggering will depend in some sense on the light power striking the detector. Formally, the dependence of $\delta\widetilde{E}$ on P_{bs} probably should also include reference to the finite time of exposure of the detector through the sampling window function $\widetilde{W}(\tau; P_{bs})$. Fortunately, however, detailed theoretical description of $\delta\widetilde{E}$ was not necessary in this analysis; a phenomenological approach to the treatment of the noise term was sufficient.

Conversion of equation D-1 to the more familiar distance argument normally displayed by the OTDR is accomplished through the relation

$$\widetilde{E}_x(x_i) = \widetilde{E}(vt_i/2) \, , \qquad \text{(D-2)}$$

where

v is the group velocity of light propagating in the optical fiber,

x_i is the position of node i within the optical fiber relative to the reference position x_0, and

$\widetilde{E}_x(x_i)$ is the distance-based nonlinear OTDR trace response in OFM20 units at node i in the 256 node trace.

The factor of two in equation D-2 accounts for the out-and-back propagation distance traversed by the detected light in any given time t. The velocity of light in the fiber is given by $v = c/n_{core}$, where c is the speed of light in vacuum and n_{core}= 1.492 is the index of refraction of the polymethylmethacrylate (PMMA) optical fiber core.

The fundamental dilemma faced in attempting to use equation D-1 to model the OFM20 is that the function $\widetilde{W}(\tau; P_{bs})$ is not known. Since all trace information obtainable from the OFM20 reports only the integrated function $\widetilde{E}_x(x_i)$, the shape of $\widetilde{W}(\tau; P_{bs})$, which is a factor in the integrand, must be deduced inferentially. Insight into the variability of the shape of $\widetilde{W}(\tau; P_{bs})$ can be obtained by examining at the OFM20 response to a simple Fresnel reflection at different sensitivity settings, as depicted in figure D-2. The distortion of the OFM20 response to the Fresnel event, even before the onset of saturation in the trace, is apparent. The narrow spikes in the traces depicted in figure D-2 are the result of a error in the OFM20 software, and do not correspond to any physical events. This software error has been fixed by Opto-Electronics but the software update had not yet been incorporated in the particular OTDR owned by DNA when these traces were produced.

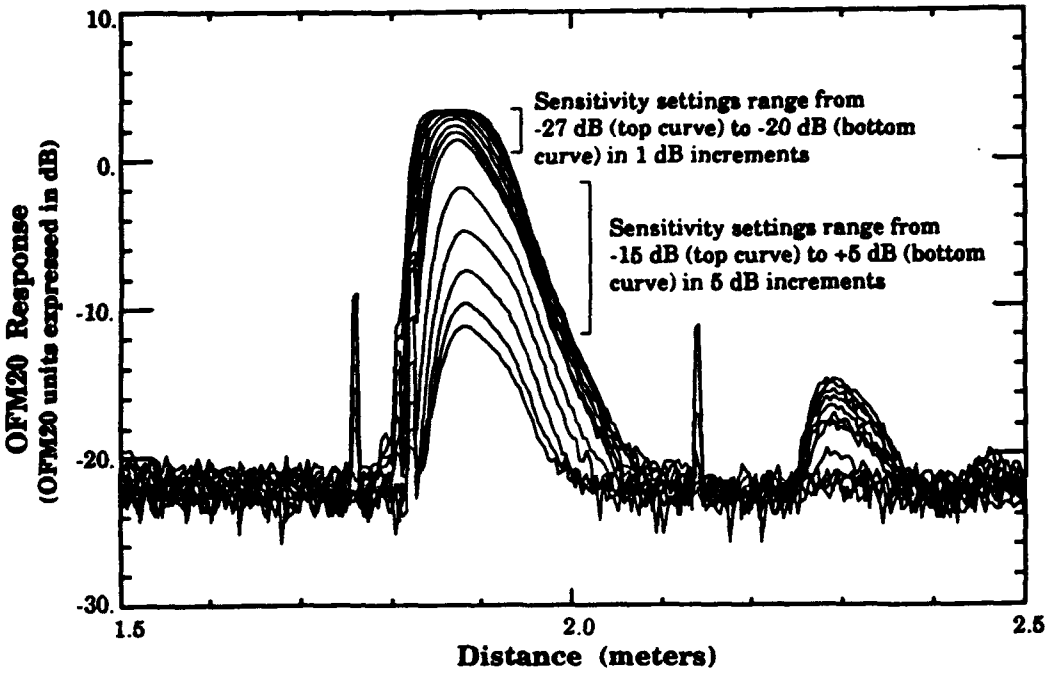

Figure D-2. OFM20 response to a simple Fresnel reflection at different sensitivity settings.

D.3.1 Decomposition of the Nonlinear Sampling Window.

To attempt to generate a full bivariate description of the sampling window function $\widetilde{W}(\tau; P_{bs})$ from sets of traces such as those depicted in figure D-2 would be a time consuming numerical task, particularly with the presence of trace noise. As a more expedient alternative, the following approximate but much simpler approach was pursued. It is observed in figure D-2 and in other similar trace data sets that OTDR traces of reasonably low amplitude appear to maintain a fairly constant window shape. In view of this observation, assert that the nonlinear window function can be decomposed as

$$\widetilde{W}(\tau; P_{bs}) \approx D(E)W(\tau) \tag{D-3}$$

where

$W(\tau)$ is a dimensionless, power-independent sampling *window shape* function approximating the shape of $\widetilde{W}(\tau; P_{bs})$, and

$D(E)$ is a *detector sensitivity* function that accounts for the nonlinear amplitude deviation of the OTDR from variations in backscattered light power.

By construction, the dimensionless window shape function is normalized so that $\max\{W(\tau)\} = 1$ and the units conversion of the detector (OFM20 units/joule) is assigned to the detector sensitivity function. The detector sensitivity function $D(E)$ is cast as a function of energy (not power) in this approximation because power integrated over the sampling window is the only quantity accessible through the OFM20 traces. The energy argument in $D(E)$ is related to the backscattered power driving the detector by the linear convolution

$$E(t) = A_c \int_{t-(1-\eta)\tau_w}^{t+\eta\tau_w} W(t+\eta\tau_w - \tau) P_{bs}(\tau)\, d\tau \tag{D-4}$$

and represents the backscattered energy available to drive the detector within the sampling window at any instant of time t.

The simplification to equation D-1 that results from the decomposition expressed in equations D-3 and D-4 is seen by substituting equation D-3 into D-1:

$$\tilde{E}(t_i) = D(E)\, A_c \int_{t_i - (1-\eta)\tau_w}^{t_i + \eta\tau_w} W(t_i + \eta\tau_w - \tau)\, P_{bs}(\tau)\, d\tau + \delta\tilde{E}(P_{bs}) , \qquad \text{(D-5)}$$

and, using the energy definition of equation D-4,

$$\tilde{E}(t_i) = D(E)\, E(t_i) + \delta\tilde{E}(P_{bs}) . \qquad \text{(D-6)}$$

The form of equation D-6 shows that the effect of separating the nonlinearity of the OFM20 trace response from the sampling window shape is to create a simple proportionality between the nonlinear OFM20 response and the linear backscattered energy available to drive the detector through the univariate detector function D(E). Simulation of $E(t_i)$ is accomplished by modeling the linear physics of backscattered *power*, as would be done in an ordinary OTDR, and feeding these backscattered power results into equation D-4. Although there is no data yet to confirm whether the detector function D(E) is unique to each machine, it is presumed that D(E) must be determined experimentally for each individual OFM20 OTDR.

D.3.2 Determination of the OFM20 Detector Sensitivity Function.

Conceptually, the experimental approach to determining the detector sensitivity function D(E) would be to vary E in a known manner while measuring the OFM20 response $\tilde{E}$, holding all other parameters constant. This measurement format is made conveniently straightforward in the OFM20 through use of the neutral density filter that attenuates the light power launched into the fiber by accurately known increments. The relationship between the sensitivity setting controlling the neutral density filter and the independent variable, the backscattered energy E, must first be specified.

Let $P_{bs0}(t)$ be the light power that would be backscattered to the reference location x_0 without the neutral density filter present. The power backscattered to x_0 with the filter present is then

$$P_{bs}(t) = A_{filter}\, P_{bs0}(t) , \qquad \text{(D-7)}$$

where A_{filter} is the attenuation factor introduced by the neutral density filter. Substituting equation D-7 into equation D-4 establishes the relationship between the filter attenuation and the backscattered energy available to drive the detector:

$$E(t) = A_c A_{filter} \int_{t-(1-\eta)\tau_w}^{t+\eta\tau_w} W(t+\eta\tau_w - \tau) P_{bs0}(\tau)\, d\tau \,. \qquad \text{(D-8)}$$

For a specific trace event occurring at time t_{event} in a static fiber-OTDR setup, the detector function can be evaluated as

$$D(E) = \frac{\tilde{E}(t_{event}; A_{filter})}{E(t_{event}; A_{filter})} \,, \qquad \text{(D-9)}$$

where the trace noise has been ignored (that is, has been smoothed or averaged in some sense as an feature irrelevant to the definition of the function D(E)). The notation in equation D-9 calls attention to the fact that it is the neutral density filter attenuation (hence power received hence energy received) that is being varied. Substituting equation D-8 into D-9 gives

$$D[E(A_{filter})] = \frac{\tilde{E}(t_{event}; A_{filter})}{E_{max} A_{filter}} \,, \qquad \text{(D-10)}$$

where

$$E_{max} \triangleq A_c \int_{t_{event}-(1-\eta)\tau_w}^{t_{event}+\eta\tau_w} W(t_{event} + \eta\tau_w - \tau) P_{bs0}(\tau)\, d\tau \qquad \text{(D-11)}$$

is the backscattered energy that would be available to drive the detector with no filter present (i.e., $A_{filter} = 1$).

The absolute attenuation factor provided by the neutral density filter in the OFM20 is unknown; only a sensitivity setting S_{dB} on a seemingly arbitrary dB scale is given. Therefore, if

$$S_{dB} = 10 \log_{10}\left(\frac{A_{ref}}{A_{filter}}\right) \qquad \text{(D-12)}$$

is the sensitivity setting in dB, where A_{ref} is the unknown reference attenuation calibrating the sensitivity scale, then solving for A_{filter} and inserting the result into equation D-10 gives

$$D[E(S_{dB})] = \frac{\tilde{E}(t_{event};S_{dB})}{E_{max} A_{ref} 10^{-S_{dB}/10}} \quad . \tag{D-13}$$

Equation D-13 describes the detector sensitivity in terms of the OFM20 trace magnitude $\tilde{E}$ for a given sensitivity setting S_{dB} at any given trace event, up to an unknown constant $K = 1/E_{max}A_{ref}$. In the OFM20, as in all OTDRs, the absolute magnitude of the OTDR trace is of no consequence; only the relative magnitudes of points on a given trace are of interest. Thus, the fact that K is unknown is immaterial to the analysis or interpretation of the results. In this analysis, the magnitude of K was arbitrarily selected so that D(E) (in units of OFM20 units/joule) was unity at low trace amplitudes.

To generate a reasonably densely discretized representation of $D[E(S_{dB})]$ useful for subsequent modeling, a series of OFM20 traces of a Fresnel event was generated in which the sensitivity setting S_{dB} alone was varied by 0.5 dB and 1 dB increments. An overlay plot of these traces is shown in figure D-3.

Although in principle any particular time (corresponding to a particular distance) on the traces in figure D-3 could be selected for t_{event} to generate the functional form of D(E), in practice it was found that, because of distortion in the shape of the sampling window as a function of amplitude, the shape of the function D(E) changed significantly with different choices of t_{event}. The fact that D(E) is not an invariant of position on the trace points out the approximate nature of the decomposition asserted in equation D-3 that defined D(E). In an OFM20 trace deflected in response to a covert splice, it is the amplitude of the peak relative to the amplitude of the Rayleigh backscatter floor that is the critical quantitative piece of information. Therefore, the particular t_{event} chosen to define D(E) corresponded to the *peaks* of the traces in figure D-3.

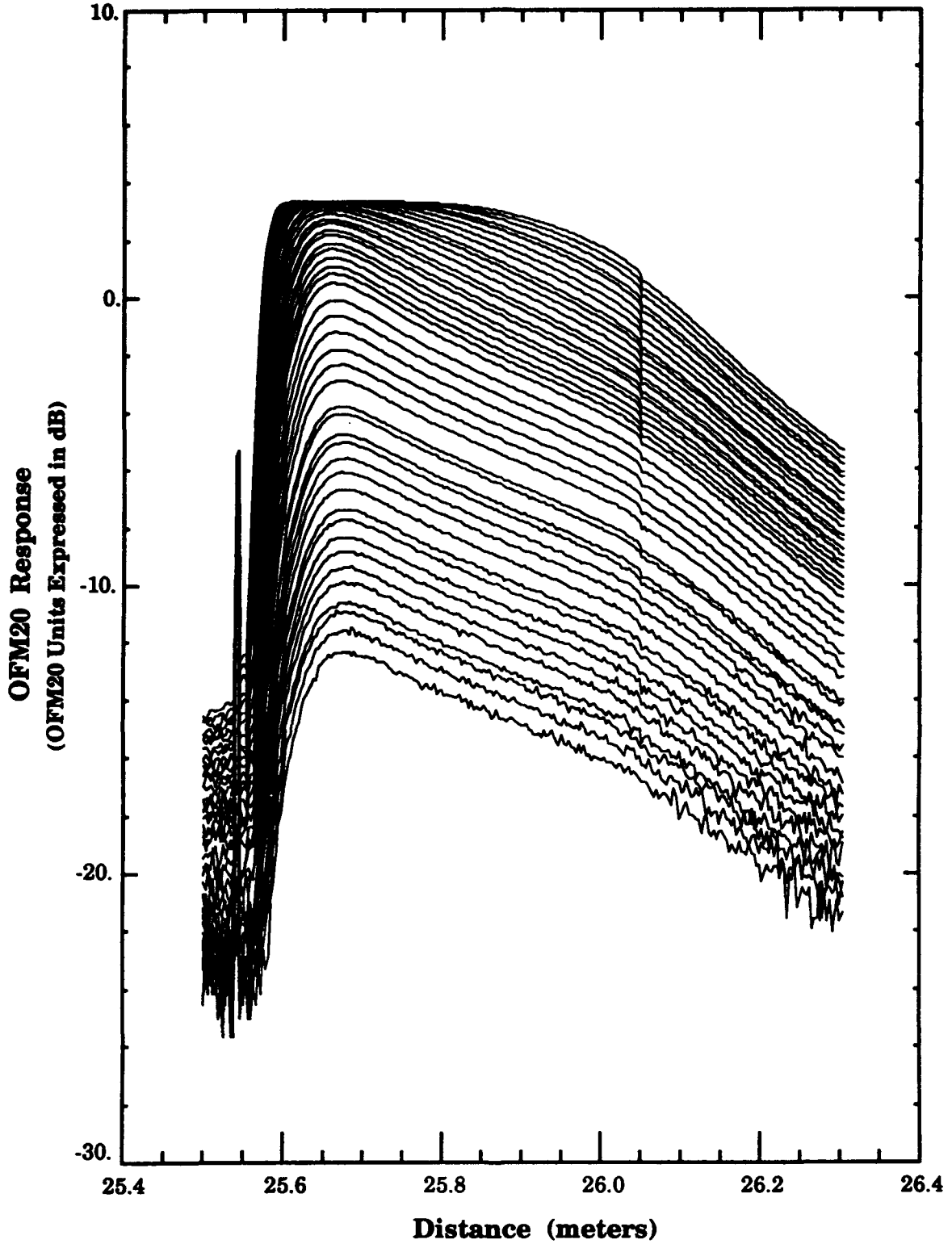

Figure D-3. OFM20 traces used to determine the detector sensitivity D(E).

Figure D-4 shows the nonlinearity of the OFM20 response at the trace peaks taken from the traces in figure D-3 as a function of backscattered energy available to drive the detector, defined in equation D-8. A curious feature of OFM20 nonlinearity revealed in this plot is the superlinear response sensitivity preceding the sublinear response near saturation as the backscattered energy increases. Note that the ordinate is defined as $10\log_{10}(\tilde{E})$ rather than the $5\log_{10}(\tilde{E})$ definition used in OTDR trace displays so that the scaling of the ordinate and the abscissa is the same in this plot.

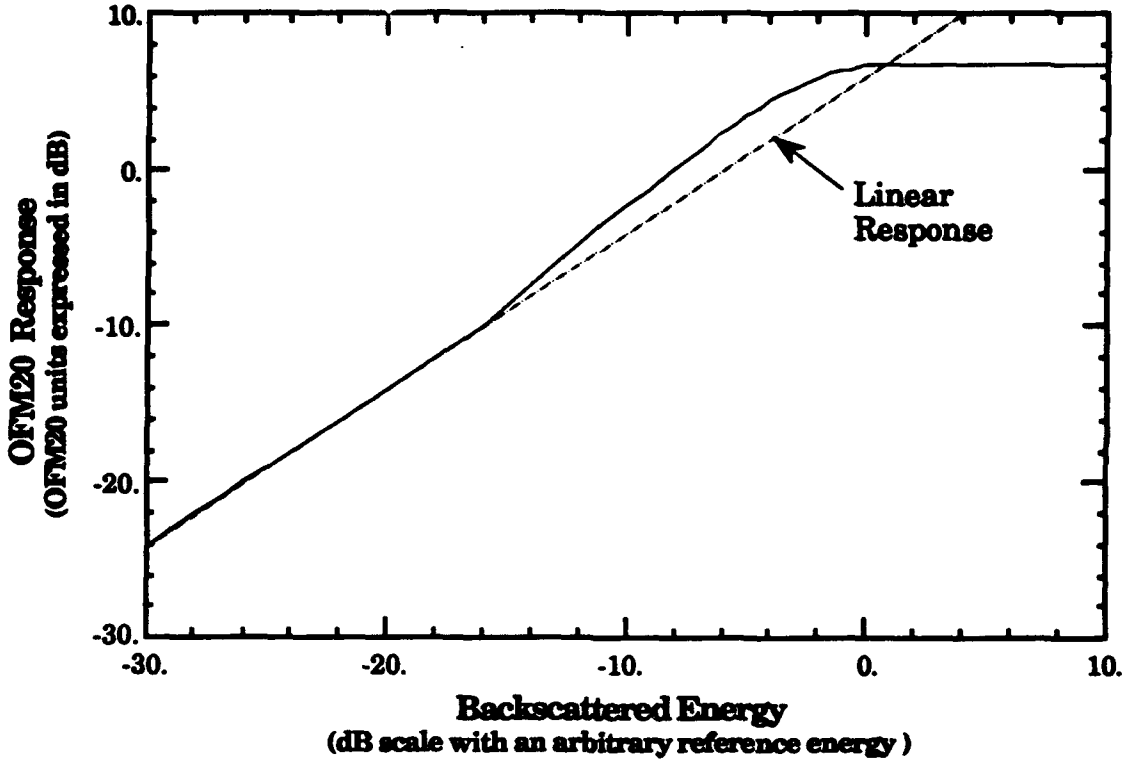

Figure D-4. Peak response of the OFM20 traces as a function of the backscattered energy available to drive the detector.

Figure D-5 plots D(E) (as calculated via equation D-13 from the trace peak data in figure D-3) directly on the dB scale so that the magnitude of the nonlinearity correction can be seen. In both figures D-4 and D-5, the raw data were smoothed so that numerical usage of D(E) would not introduce irrelevant noise in the simulation results. Formal introduction of realistic noise in the model is deferred until section D.8.

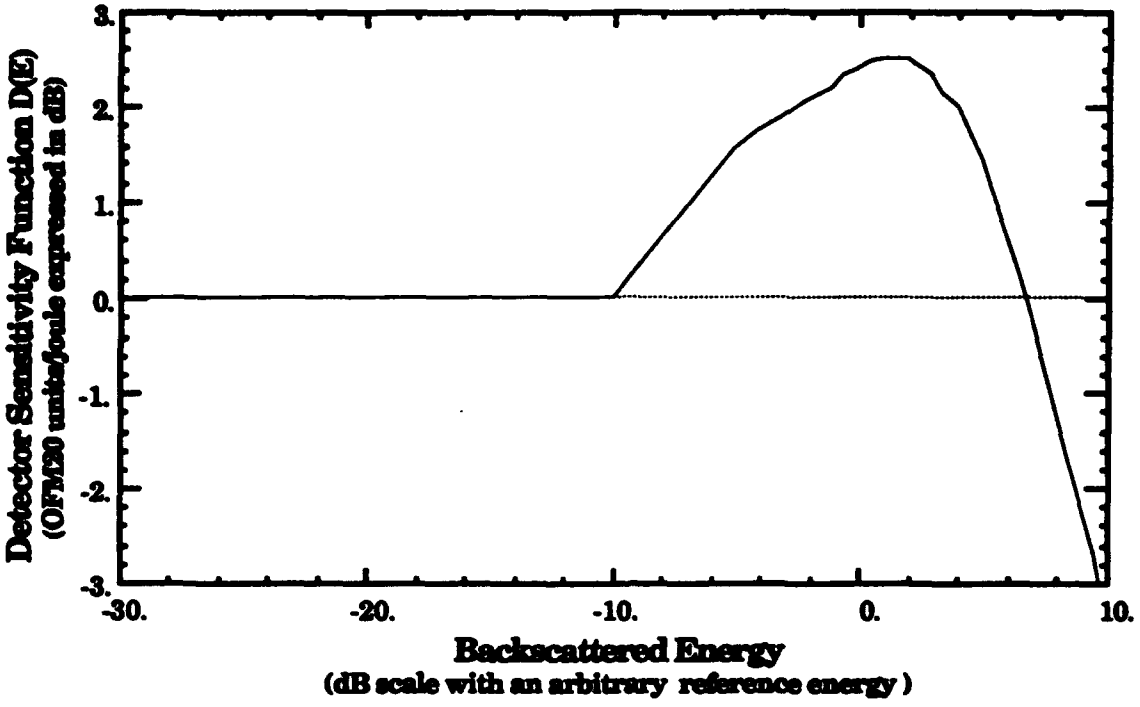

Figure D-5. Detector sensitivity function D(E) of the OFM20 based on trace peaks.

It should be noted that in practice, the function

$$D^{-1}(\tilde{E}) = \frac{E_{max} A_{ref} 10^{-S_{dB}/10}}{\tilde{E}(t_{event}; S_{dB})} = \frac{1}{D(E)} \quad , \tag{D-14}$$

is the useful form for *removing* the nonlinearity from an OFM20 trace to prepare it for linear analysis. The form D(E) is useful for *restoring* the nonlinear OFM20 trace appearance from linear backscatter analysis or simulation. Although mathematically the two functions are simply reciprocals of one another, the two forms are not equivalent computationally because they require use of different abscissas (E or $\tilde{E}$) when interpolating the ordinate of the discretely defined detector function.

D.4 DETERMINATION OF THE POWER-INDEPENDENT SAMPLING WINDOW.

In a strong Fresnel return, the time history of the backscattered power $P_{bs}(t)$ closely mimics the shape of the forward launched pulse because the contribution from Rayleigh backscatter is relatively small. Thus, if the shape of the laser pulse were known, then the backscattered power $P_{bs}(t)$ causing the OFM20 trace deflection (associated with the Fresnel event) could be treated as an isolated pulse of known shape. Knowledge of the pulse shape would then allow the shape of the sampling window to be deduced by deconvolution of the OFM20 trace.

D.4.1 Direct Deconvolution of the OFM20 Trace.

The initial approach used to determine the sampling window $W(\tau)$ in equation D-4 was to deconvolve the window shape from measured traces and knowledge of the light pulse emitted from the laser diode. Because the BDM/Albuquerque laboratory did not have at its disposal measurement equipment of sufficient bandwidth to measure the light pulse shape directly, various plausible pulse shapes were asserted based on verbal descriptions of typical laser pulse shapes provided by Opto-Electronics.

Two major problems were encountered with the deconvolution approach. First, noise in all the OFM20 traces used in this analysis was significant enough to introduce unacceptable, nonphysical artifacts in every numerical deconvolution method attempted. The numerical approaches used included direct iterative refinement of the window function from an initial guess of the window shape using forward convolution, Monte Carlo synthesis of the window function by successive approximation using forward convolution, a matrix technique of recovering the unknown portion of the integrand in the forward convolution by singular value decomposition of the overdetermined system of numerical integration equations, and numerical deconvolution using spectral methods. Although crude representations of a sampling window could be recovered by any of these techniques, none of them produced a digitally represented function smooth enough to be used as a credible window function for trace analysis.

The second major problem was that the shape of the laser pulse, particularly the details of the extended tail, was not known well enough to arrive at a defensible deconvolution result. It was observed that reasonable looking sampling windows could be deconvolved if the tail of the pulse was essentially negligible, so that the pulse was very short compared to the convolved trace deflection. However, when a slowly decaying tail was extended from the pulse, the deconvolved sampling window shape became increasingly meaningless physically. Given the lack of knowledge of the actual pulse shape and the unsatisfactory physical implications on the window shape that resulted from trying to guess the pulse shape, the following approximate analysis approach was pursued instead.

D.4.2 Impulse Response Approximation of the Sampling Window Shape.

As mentioned at the beginning of this section, the time history of the backscattered power $P_{bs}(t)$ closely mimics the time history of the light power in the launched pulse in a strong Fresnel reflection except at amplitudes near to or below the Rayleigh backscatter floor. Therefore, if $T(\tau)$ represents the time history of the laser pulse, normalized so that

$$\int_{-\infty}^{\infty} T(\tau)\, d\tau = 1 \ , \tag{D-15}$$

then to an almost exact approximation in a *strong* Fresnel event,

$$P_{bs}(t - t_F) \approx \mathcal{E}_F T(t) \ , \tag{D-16}$$

where t_F is the time when the pulse first encounters that fiber feature causing the Fresnel event and $\mathcal{E}_F$ is the total light energy reflected in the Fresnel event (measured at reference location x_0). The script form $\mathcal{E}$ is used to distinguish the total energy contained in the pulse from the convolved energy E available to drive the detector, as defined in equations D-4 and D-8. Inserting the representation of $P_{bs}(t)$ of equation D-16 into equation D-5 gives the trace interpretation:

$$\tilde{E}(t_i) = D(E)\, A_c\, \mathcal{E}_F \int_{t_i - t_F - (1-\eta)\tau_w}^{t_i - t_F + \eta\tau_w} W(t_i - t_F + \eta\tau_w - \tau)\, T(\tau)\, d\tau + \delta\tilde{E}(\mathcal{E}_F T(\tau)) \,. \quad \text{(D-17)}$$

Since the main part of the pulse is very narrow compared to the sampling window, the pulse was approximated as $T(\tau) \approx \delta(\tau)$, where $\delta(\tau)$ is the Dirac delta function. With the delta function approximation, equation D-17 evaluates analytically to

$$\tilde{E}(t_i) = \begin{cases} 0 & , t_i \le t_F - \eta\tau_w \\ D(E)\, A_c\, \mathcal{E}_F W(t_i - t_F + \eta\tau_w) + \delta\tilde{E}(P_{bs}) & , t_F - \eta\tau_w < t_i < t_F + (1-\eta)\tau_w \\ 0 & , t_i \ge t_F + (1-\eta)\tau_w \end{cases} \quad \text{(D-18)}$$

In words, equation D-18 states that the shape of the trace deflection due to a *strong* Fresnel event seen in the OFM20 trace (ignoring the Rayleigh backscatter floor as negligible) is the same as the sampling window shape, except for nonlinearity distortion introduced by the detector sensitivity function D(E) and perturbations introduced by trace noise.

The strong Fresnel event selected for defining W(τ) via equation D-18 was the end-of-fiber reflection trace depicted in figure D-6. The traces in figure D-6 show two discrepant, nonlinear OFM20 responses to the same Fresnel event at two different sensitivity settings of the neutral density filter. The traces have been scaled in amplitude to compensate for the different attenuations implied by the sensitivity settings.

If the nonlinearity correction model described in equation D-6 were completely accurate, then when represented in the linear form $E(t_i)$, the curves in figure D-6 should exactly overlay (except for trace noise). It is seen in figure D-7 that the peak amplitudes of the two curves do correspond very closely when linearized, which is expected since D(E) was defined using only trace peaks, but that the shapes of the linearized curves are still somewhat discrepant, particularly at the leading edges of the deflection. It is also noted that that the amplitude of the Rayleigh backscatter floor is not the same for both traces, which is particularly troublesome since the ratio of the peak value of the trace to the

Rayleigh floor is of interest in the subsequent analysis. The amount and character of the discrepancy between the two curves gives insight into the limitations of the approximation introduced by equation D-3.

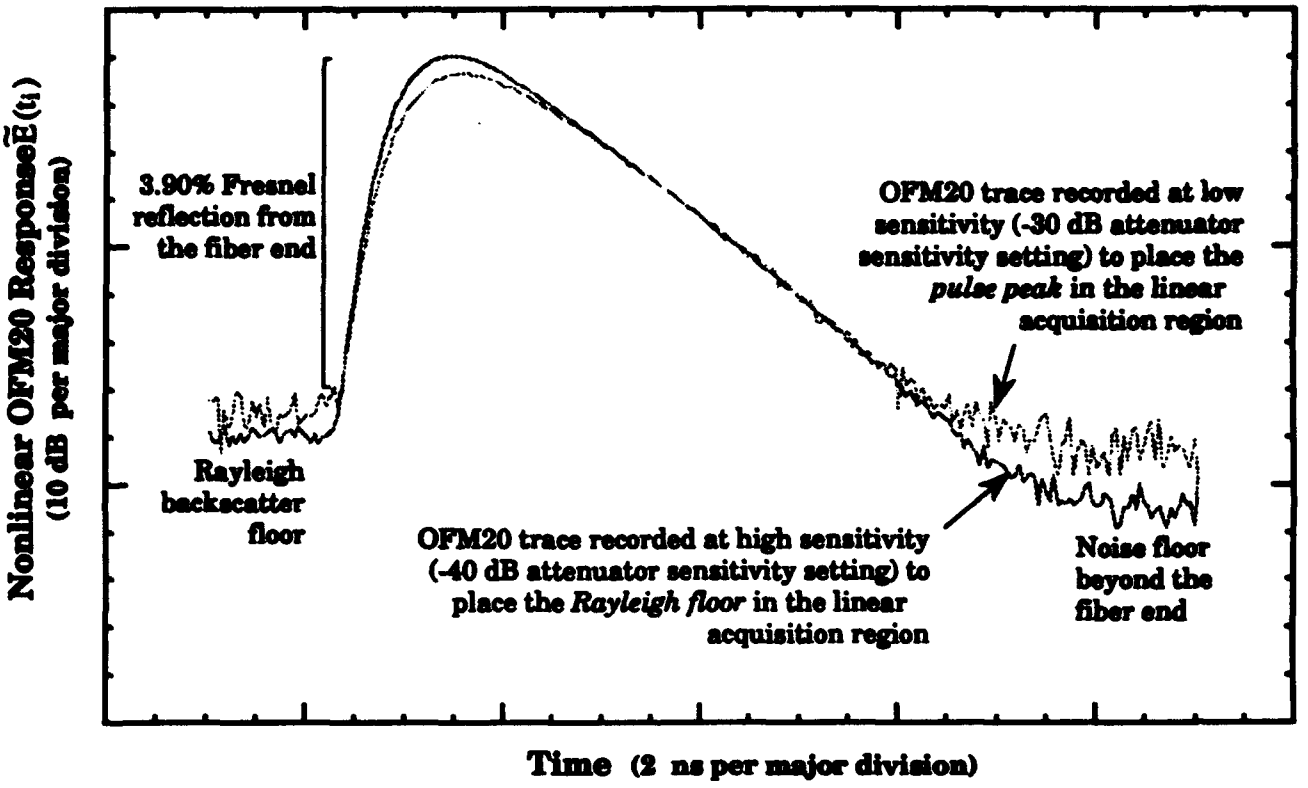

Figure D-6. OFM20 traces on which the sampling window shape was based.

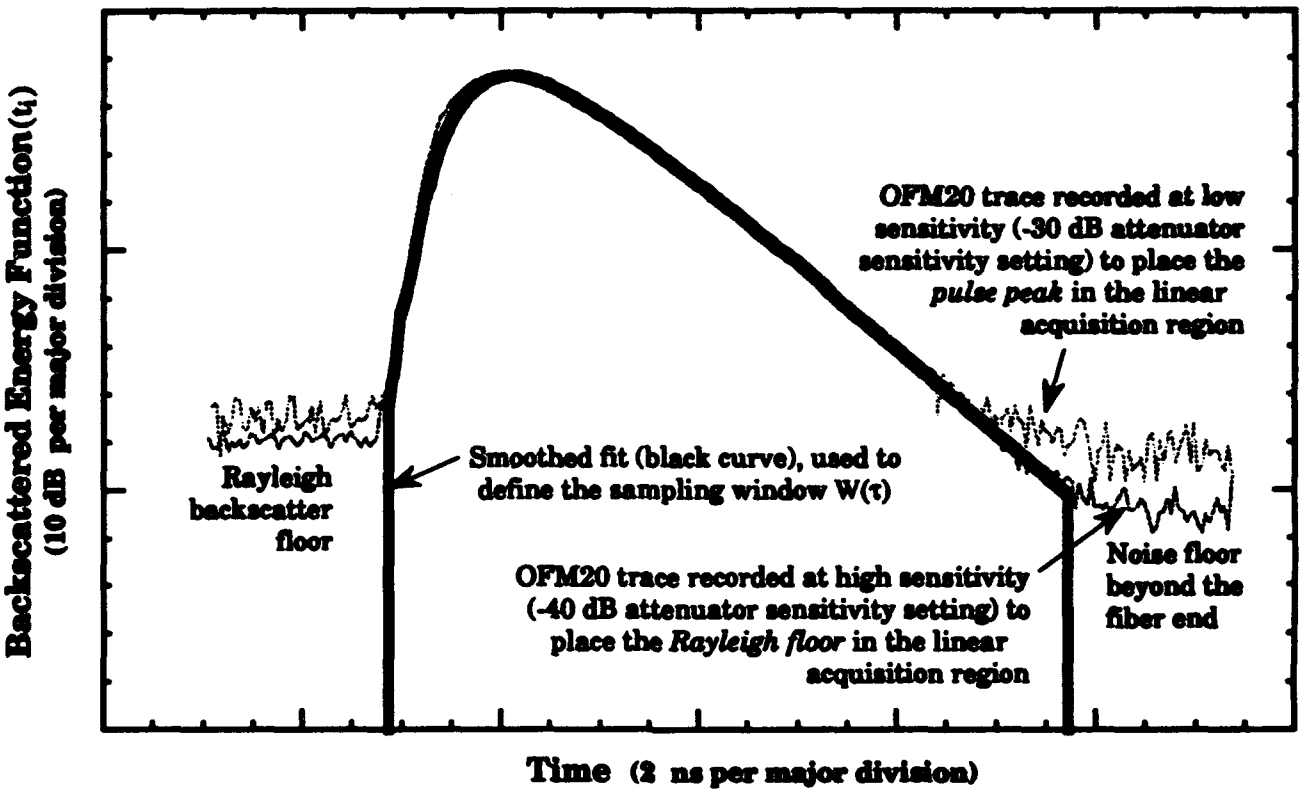

Figure D-7. Linearized OFM20 traces overlaid with the sampling window fit.

Instead of selecting one curve or the other in figure D-7 to define the sampling window shape, a "compromise" window shape was synthesized using the best information from both curves. The argument for using some information from each trace is that the traces are least distorted by nonlinearities at low amplitudes but are also most representative of the sampling window shape when they minimize both noise and the influence of the Rayleigh backscatter floor. Therefore, the trace recorded at low sensitivity was used to define the window shape near the peak of the curve, and the trace recorded at high sensitivity was used to define the window shape near the base of the curve. The solid black line defines the synthesized sampling window function $W(\tau)$ used in this analysis. Note that the full width at half maximum (FWHM) of the sampling window function is about 1.5 nanoseconds.

D.5 INCLUSION OF BACKSCATTERED POWER IN THE OFM20 MODEL.

Now that the nonlinear behavior of the OFM20 has been described and the sampling window shape has been identified, the remaining task prerequisite to evaluating equation D-1 is to describe the power $P_{bs}(t)$ backscattered from all points in the fiber in a form useful for trace analysis.

D.5.1 General Formulation of the Backscattered Power.

The instantaneous light power moving forward from the laser source at reference point x_0 in the fiber is a pulse described by

$$P_0(t) = \mathcal{E}_0 T(t) \tag{D-19}$$

With the normalization of the pulse shape $T(\tau)$ specified in equation D-15, then $\mathcal{E}_0$ must be interpreted as the total light energy contained in the forward moving light pulse at location x_0. Again, the script form $\mathcal{E}$ is used to distinguish the total energy contained in the pulse from the convolved energy E available to drive the detector, as defined in equations D-4 and D-8.

The light power backscattered to reference location x_0 from a fiber containing a splice, in the local region surrounding the splice (that is, ignoring reflections from connectors and from the end of the fiber) is,

$$P_{bs}(t) = \begin{cases} \frac{1}{2} v \mathcal{E}_0 f_{bs} \sigma_s \int_0^{\tau_{pulse}} e^{-\sigma v (t-\tau)} T(\tau) d\tau & , t \le \frac{2x_s}{v} \\ \frac{1}{2} v \mathcal{E}_0 f_{bs} \sigma_s \int_{t-\frac{2x_s}{v}}^{t} e^{-\sigma v (t-\tau)} T(\tau) d\tau & \\ \quad + \mathcal{E}_0 e^{-2\sigma x_s} R_s T(t - \frac{2x_s}{v}) & \\ \quad + \frac{1}{2} v A_s^2 \mathcal{E}_0 f_{bs} \sigma_s \int_0^{t-\frac{2x_s}{v}} e^{-\sigma v (t-\tau)} T(\tau) d\tau & , t > \frac{2x_s}{v} \end{cases} \tag{D-20}$$

where

x_s is the location of the splice on the fiber,

τ_{pulse} is the *extreme* width of the light pulse (i.e., $T(0) = T(\tau_{pulse}) = 0$),

A_s is the one-way throughput attenuation of the splice,

R_s is the reflectivity of the splice, and

σ is the total linear attenuation cross section of the fiber (1/cm), which is constant for a uniform fiber,

σ_s is the total linear cross section for Rayleigh scattering in the fiber (1/cm), which is also constant for a uniform optical fiber.

f_{bs} is the fraction of Rayleigh scattered light that is backscattered within the aperture of the fiber, and is therefore captured as backward-propagating light power.

The upper condition in equation D-20 describes the Rayleigh backscatter floor at points on the fiber upstream from the splice. The lower condition describes the trace region downstream from the splice transitioning between Rayleigh floors preceding and following the splice, as well as the Fresnel-like[1] reflection from the splice itself. In an actual fiber, σ and σ_s are not entirely constant, but contain small perturbations about some average value. These perturbations cause trace deflections that have an appearance similar to noise, but unlike random noise, the cross section perturbation-caused trace features are reproducible from trace to trace. Fiber uniformity perturbations of this nature are ignored in this portion of the model, but are discussed in section D.8 in connection with modeling of trace noise taken from actual OFM20 datD.

D.5.2 Determination of the Total Linear Attenuation Cross Section of Plastic Optical Fiber From OFM20 Traces.

In a region of optical fiber free from backscatter sources other than normal Rayleigh backscatter, the backscattered power (from equation D-20) is

$$P_{bs}(t) = P_R e^{-\sigma v t}. \qquad \text{(D-21)}$$

[1] The term "Fresnel-like" is used to describe the spatially localized backscattering of covert splices. The trace appearance of the localized backscatter from a splice in an OTDR trace is identical to that of a fiber event producing a Fresnel reflection, but the optical mechanism of backscatter in a splice may or may not be related to Fresnel reflection in a formal optical sense.

where the Rayleigh backscatter power constant is defined here as

$$P_R \triangleq \frac{1}{2} v \mathcal{E}_0 f_{bs} \sigma_s \int_0^{\tau_{pulse}} e^{-\sigma v t} T(\tau) d\tau \,. \qquad \text{(D-22)}$$

The backscattered energy available to drive the OFM20 detector in trace regions of Rayleigh backscatter floor is obtained by substituting the backscattered power from equation D-21 into equation D-4:

$$E(t) = A_c P_R \int_{t-(1-\eta)\tau_w}^{t+\eta\tau_w} W(t + \eta\tau_w - \tau) e^{-\sigma v t} d\tau \,. \qquad \text{(D-23)}$$

With the variable transformation $\tau = \tau' - t$, the integral in equation D-23 simplifies as

$$\int_{t-(1-\eta)\tau_w}^{t+\eta\tau_w} W(t + \eta\tau_w - \tau') e^{-\sigma v \tau'} d\tau' = e^{-\sigma v t} \int_{-(1-\eta)\tau_w}^{\eta\tau_w} W(\eta\tau_w - \tau) e^{-\sigma v \tau} d\tau \,, \qquad \text{(D-24)}$$

which removes all reference to the time variable t from the integration. For notational simplicity, define

$$\zeta \triangleq \int_{-(1-\eta)\tau_w}^{\eta\tau_w} W(\eta\tau_w - \tau) e^{-\sigma v \tau} d\tau \qquad \text{(D-25)}$$

as a constant that is obtained from convolving the sampling window function with the exponential slope of the Rayleigh backscatter floor. Substituting the forms expressed in equations D-24 and D-25 into equation D-23 yields the simple exponential form

$$E(t) = A_c P_R \zeta e^{-\sigma v t} \,. \qquad \text{(D-26)}$$

Equation D-26 shows that the energy available to drive the OFM20 detector in trace regions of Rayleigh backscatter floor decreases exponentially at a rate that is independent of both the laser pulse shape and the sampling window shape.

On the other hand, the amplitude of the Rayleigh backscatter floor depends on both the laser pulse shape and amplitude through the constant P_R and on the sampling window shape through the constant ζ.

The simple form of equation D-26 allows the total linear attenuation cross section σ to be determined directly from the slope of OFM20 traces. By restoring the nonlinearity of the OFM20 traces via equations D-6 and D-14, and converting to a spatial functional dependence via equation D-2, then equation D-26 can be recast as

$$D^{-1}(\tilde{E}_x)\tilde{E}_x(x) = A_c P_R \zeta e^{-2\sigma x} \quad . \tag{D-27}$$

Taking the natural logarithm of both sides yields

$$\ln\left[D^{-1}(\tilde{E}_x)\tilde{E}_x(x)\right] = -2\sigma x + \ln\left[A_c P_R \zeta\right] \quad , \tag{D-28}$$

which is the equation of a line in the slope-intercept form $y = mx + b$. Therefore, the total linear attenuation cross section σ can be calculated as negative one-half of the slope of the least squares fit to the natural log of the linearized OFM20 trace. This was the computational method used to evaluate σ in all traces used in this analysis. Although it was not used this analysis, it is noted here that the fiber attenuation rate in units of dB per unit length is calculable from knowledge of the total linear attenuation cross section σ through the relation

$$\frac{dA_{dB}}{dx} = -10\sigma \log_{10}(e) \quad . \tag{D-29}$$

Typical values for the fiber attenuation rates measured from OFM20 traces were in the range of -230 to -360 dB/km, depending on the particular sample of optical fiber selected. These attenuation rates are consistent with vendor data for plastic optical fiber at 680 nm wavelength.

D.5.3 Assignment of the Total Linear Scattering Cross Section for Plastic Optical Fiber.

Unlike the total linear attenuation cross section σ, total linear *scattering* cross section σ_s for plastic optical fiber cannot be obtained easily from OFM20

traces. Instead, the scaling relation cited by Kaino[3] was used:

$$\sigma_s = -\left(\frac{\lambda_{ref}}{\lambda}\right)^4 \frac{\left[\frac{dA_{s\,dB}}{dx}\right]_{ref}}{10\log_{10}(e)}\ , \qquad \text{(D-30)}$$

where

λ = 680 nm is the wavelength of the laser in the OFM20 OTDR,

λ_{ref} = 633 nm is the reference wavelength of the scaling relation, and

$[dA_{s\,dB}/dx]_{ref}$ = -13.5 dB/km is the attenuation in dB per unit length of plastic optical fiber *due to scattering* at the reference wavelength.

Evaluating equation D-30 and expressing the result in a form calculated analogously to equation D-29 gives an attenuation rate due to scattering of $dA_{s\,dB}/dx$ = -10.1 dB/km.

D.5.4 Approximation of the Backscattered Power Function in the Limit of Short Pulses.

If the pulse shape $T(\tau)$ were known, then an accurate representation of the backscattered light power $P_{bs}(t)$ could be computed using equation D-20 without approximation. The actual pulse shape in the OFM20 is not known, however, as discussed in section D.4. Furthermore, the sampling window function $W(\tau)$ was constructed in section D.4.2 under the assumption that $T(\tau)$ could be reasonably approximated by a Dirac delta function. Therefore, for self-consistency in the overall model, the pulse shape was also approximated in this backscattered power portion of the model as $T(\tau) \approx \delta(\tau)$. With this approximation, then equation D-20 simplifies to

$$P_{bs}(t) = \begin{cases} \frac{1}{2} v \mathcal{E}_0 f_{bs} \sigma_s e^{-\sigma v t} & , t \le \frac{2x_s}{v} \\ \mathcal{E}_0 e^{-2\sigma x_s} R_s \delta(t - \frac{2x_s}{v}) & \\ \quad + \frac{1}{2} v A_s^2 \mathcal{E}_0 f_{bs} \sigma_s e^{-\sigma v t} & , t > \frac{2x_s}{v} \end{cases} . \qquad \text{(D-31)}$$

[3] Kaino, T., M. Fujiki, and S. Oikawa, "Low-loss plastic optical fibers," **Applied Optics**, Vol. 20, No. 17, September 1, 1981.

Inserting this expression for backscattered power into equation D-4, which describes the linear energy available to drive the detector within the linearized window approximation, gives

$$E(t) = A_c \begin{cases} \frac{1}{2} v \mathcal{E}_0 f_{bs} \sigma_s \int_{t-(1-\eta)\tau_w}^{t+\eta\tau_w} W(t+\eta\tau_w-\tau) e^{-\sigma v \tau} d\tau & , t \le \frac{2x_s}{v} - \eta\tau_w \\ \frac{1}{2} v \mathcal{E}_0 f_{bs} \sigma_s \int_{t-(1-\eta)\tau_w}^{\frac{2x_s}{v}} W(t+\eta\tau_w-\tau) e^{-\sigma v \tau} d\tau & \\ \quad + \mathcal{E}_0 e^{-2\sigma x_s} R_s W\left(t+\eta\tau_w-\frac{2x_s}{v}\right) & \\ \quad + \frac{1}{2} v A_s^2 \mathcal{E}_0 f_{bs} \sigma_s \int_{\frac{2x_s}{v}}^{t+\eta\tau_w} W(t+\eta\tau_w-\tau) e^{-\sigma v \tau} d\tau & , \frac{2x_s}{v} - \eta\tau_w < t < \frac{2x_s}{v} + (1-\eta)\tau_w \\ \frac{1}{2} v A_s^2 \mathcal{E}_0 f_{bs} \sigma_s \int_{t-(1-\eta)\tau_w}^{t+\eta\tau_w} W(t+\eta\tau_w-\tau) e^{-\sigma v \tau} d\tau & , t \ge \frac{2x_s}{v} + (1-\eta)\tau_w \end{cases} \quad \text{(D-32)}$$

The form of equation D-32 can be simplified using the variable transformation of equation D-24 and the variable definition of equation D-25. With these simplifications equation D-32 becomes:

$$E(t_i) = A_c \cdot \begin{cases} \frac{1}{2} v \mathcal{E}_0 f_{bs} \sigma_s \zeta e^{-\sigma v t_i} & , t_i \le \frac{2x_s}{v} - \eta\tau_w \\ \frac{1}{2} v \mathcal{E}_0 f_{bs} \sigma_s e^{-\sigma v t_i} \int_{-(1-\eta)\tau_w}^{\frac{2x_s}{v} - t_i} W(\eta\tau_w - \tau) e^{-\sigma v \tau} d\tau & \\ \quad + \mathcal{E}_0 e^{-2\sigma x_s} R_s W\left(t_i - \frac{2x_s}{v} + \eta\tau_w\right) & \\ \quad + \frac{1}{2} v A_s^2 \mathcal{E}_0 f_{bs} \sigma_s e^{-\sigma v t_i} \int_{\frac{2x_s}{v} - t_i}^{\eta\tau_w} W(\eta\tau_w - \tau) e^{-\sigma v \tau} d\tau & \\ & , \frac{2x_s}{v} - \eta\tau_w < t_i < \frac{2x_s}{v} + (1-\eta)\tau_w \\ \frac{1}{2} v A_s^2 \mathcal{E}_0 f_{bs} \sigma_s \zeta e^{-\sigma v t_i} & , t_i \ge \frac{2x_s}{v} + (1-\eta)\tau_w \end{cases} \quad . \qquad \text{(D-33)}$$

The discretized form of the time variable has been reintroduced in equation D-33 for modeling realism. The nonlinear OFM20 response is computed from equation D-6 using $E(t_i)$ as described in equation D-33 and the digital representation of D(E) as defined in figure D-7.

The complicated form of equation D-33 arises from description of the transition region between the Rayleigh backscatter floor preceding and following the trace deflection caused by the splice. In the special circumstance that the throughput loss of the splice is negligibly small, then $A_s \approx 1$ and equation D-33 simplifies to

$$E(t_i) = A_c \Big[\underbrace{\frac{1}{2} v \mathcal{E}_0 f_{bs} \sigma_s \zeta e^{-\sigma v t_i}}_{\textit{Rayleigh contribution}} + \underbrace{\mathcal{E}_0 e^{-2\sigma x_s} R_s W\left(t_i - \frac{2x_s}{v} + \eta\tau_w\right)}_{\textit{Fresnel-like contribution}} \Big] \quad . \qquad \text{(D-34)}$$

When the backscattered energy available to drive the detector is expressed in the form of equation D-34, it is easily seen how the detectability of the splice in the OFM20 trace depends on the magnitude of the Fresnel-like contribution

revealing the presence of the splice relative to the magnitude of the background of the Rayleigh backscatter contribution.

D.6 DETERMINATION OF THE BACKSCATTER FRACTION FOR PLASTIC OPTICAL FIBER.

It is evident in equations D-33 and D-34 that the Rayleigh backscatter contribution to the total trace amplitude is directly proportional to the backscatter fraction f_{bs}. Although formulas for computing this fraction have been developed for various configurations of glass optical fiber,[3] whether these formulas correctly predict the backscatter fraction in plastic optical fiber is not clear. Furthermore, it is possible that the backscatter fraction varies with the launch conditions of the OTDR. Therefore, a method was developed to quantify the backscatter fraction directly from measured traces using a Fresnel event of known reflectivity as a calibration point.

For the purposes of analyzing f_{bs}, if the splice is replaced by an end-of-fiber condition in equation D-33, then $\sigma_s = 0$ for all points beyond the location of the fiber end at x_{end} (corresponding to all time nodes $t_i > t_{end} \triangleq 2x_{end}/v$). Also, since the end-of-fiber reflection is orders of magnitude larger in light power than the Rayleigh backscatter floor, then to an excellent approximation, equation D-33 simplifies under these conditions to

$$\widetilde{E}(t_i) = \frac{A_c}{D^{-1}(\widetilde{E})} \cdot \begin{cases} \frac{1}{2} v \mathcal{E}_0 f_{bs} \sigma_s \zeta e^{-\sigma v t_i} & , t_i \le \frac{2x_{end}}{v} - \eta\tau_w \\ \mathcal{E}_0 e^{-2\sigma x_{end}} R_{end} W\left(t_i - \frac{2x_{end}}{v} + \eta\tau_w\right) & , t_i > \frac{2x_{end}}{v} - \eta\tau_w \end{cases} , \quad \text{(D-35)}$$

where R_{end} is the reflectivity of the polished, optically flat fiber end. Trace noise has been ignored in equation D-35. The inverse form of equation D-6, discussed in the context of equation D-14, has been used in equation D-35 because unraveling of the trace nonlinearity (as opposed to restoring the trace nonlinearity) is the operation required to recover f_{bs} from actual OFM20 traces. It was assumed in this analysis that because of the large core size of multimode plastic optical fiber,

[3] Hentschel, Christian, **Fiber Optics Handbook**, Hewlett Packard GmbH, Boeblingen Instruments Division, Federal Republic of Germany, March 1989.

the end-of-fiber reflectivity could be accurately approximated by the expression for the reflectivity of plane wave at normal incidence at a dielectric interface:

$$R_{end} = \left(\frac{n_{core} - n_{air}}{n_{core} + n_{air}}\right)^2 .$$

where $n_{air} = 1$ is the index of refraction of air. Separate analysis has shown that a composite reflectivity that accounts for the distribution of directions of incidence to the fiber end arising from all propagation modes within the aperture of the optical fiber is negligibly different from a simple reflectivity calculated with the assumption of normal incidence.

The ratio of the trace amplitude at the peak of the deflection, $\widetilde{E}(t_{peak})$, to the Rayleigh backscatter floor at some point just upstream from the onset of the trace deflection due to the end reflection, $\widetilde{E}(t_{floor})$, is

$$\frac{\widetilde{E}(t_{peak})}{\widetilde{E}(t_{floor})} = \frac{2D^{-1}\left[\widetilde{E}(t_{floor})\right] e^{-2\sigma x_{end}} R_{end}\, W\left(t_{peak} - \frac{2x_{end}}{v} + \eta\tau_w\right)}{D^{-1}\left[\widetilde{E}(t_{peak})\right] v\, f_{bs}\, \sigma_s\, \zeta\, e^{-\sigma v t_{floor}}} . \qquad \text{(D-36)}$$

The unknown constants A_c and $\mathcal{E}_0$ cancel in the ratio. Solving for f_{bs} and consolidating the exponentials gives

$$f_{bs} = \frac{2R_{end} e^{-\sigma v(2x_{end}/v - t_{floor})} W\left(t_{peak} - \frac{2x_{end}}{v} + \eta\tau_w\right)}{v\,\sigma_s\,\zeta} \frac{D^{-1}\left[\widetilde{E}(t_{floor})\right]\widetilde{E}(t_{floor})}{D^{-1}\left[\widetilde{E}(t_{peak})\right]\widetilde{E}(t_{peak})} . \qquad \text{(D-37)}$$

Before equation D-37 can be evaluated numerically, the position x_{end} must be expressed in terms of an event identifiable on the OFM20 trace. Since in the approximation of laser pulse as a Dirac delta function the shape of the sampling window is identical to the shape of the trace deflection in the strong Fresnel event (c.f., equation D-8), then the time on the trace at which the forward-moving pulse arrives at the end of the fiber is

$$t_{peak} = \frac{2x_{end}}{v} - \eta\tau_w + \tau_{peak} , \qquad \text{(D-38)}$$

where τ_{peak} is the time when the window function $W(\tau)$ peaks. Solving for $2x_{end}/v$ and substituting this expression into equation D-37 gives

$$f_{bs} = \frac{2R_{end}\, e^{-\sigma v(t_{peak} - t_{floor} + \eta\tau_w - \tau_{peak})}}{v\,\sigma_s\,\zeta} \; \frac{D^{-1}\left[\tilde{E}(t_{floor})\right]\tilde{E}(t_{floor})}{D^{-1}\left[\tilde{E}(t_{peak})\right]\tilde{E}(t_{peak})} \quad . \qquad \text{(D-39)}$$

where it is noted that $W[t_{peak} - (t_{peak} + \eta\,\tau_w - \tau_{peak}) + \eta\,\tau_w] = W(\tau_{peak}) = 1$ by definition of the linear window function (c.f., equation D-3).

To establish an accurate measurement of f_{bs} using equation D-39, several OFM20 traces were recorded using two different end-of-fiber reflectivity conditions. A 200 μm core polymer clad glass optical fiber was carefully cleaved to create an optically flat end surface very closely perpendicular to the fiber axis. The fiber end was then left in air for one reflectivity condition and in deionized water for the other reflectivity condition. The nonlinear OFM20 traces generated under these conditions are shown in figure D-8.

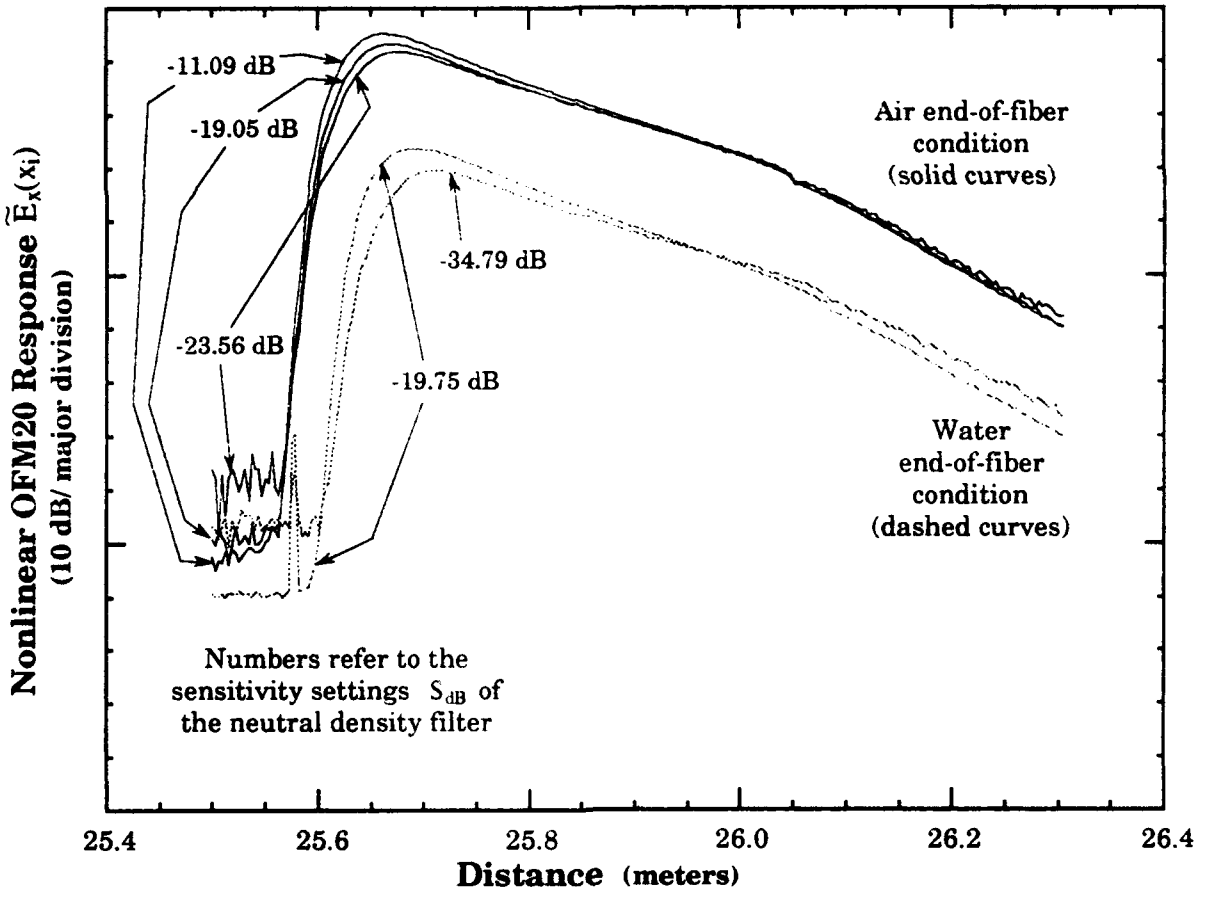

Figure D-8. OFM20 traces showing air and water end-of-fiber Fresnel events at different sensitivity settings in polymer coated glass optical fiber.

It is apparent in figure D-8 that the amplitude ratio of the Rayleigh backscatter floor to the trace peak is not at all constant in the nonlinear OFM20 traces. Unfortunately, the ratio is not very constant in the *linear* energy available to drive the detector either. Table D-1 lists the ratio

$$\frac{E(t_{floor})}{E(t_{peak})} = \frac{D^{-1}\left[\widetilde{E}(t_{floor})\right]\widetilde{E}(t_{floor})}{D^{-1}\left[\widetilde{E}(t_{peak})\right]\widetilde{E}(t_{peak})} \qquad \text{(D-40)}$$

and the backscatter fraction f_{bs} (computed via equation D-39) for each trace in figure D-8 as a function of the OFM20 sensitivity setting.

Table D-1. Backscatter fractions predicted by the traces in figure D-8.

	S_{dB}	$\frac{E(t_{floor})}{E(t_{peak})}$	f_{bs}
Air	-23.56 dB	-32.2 dB	5.45 %
	-19.05 dB	-35.4 dB	2.62 %
	-11.09 dB	-36.4 dB	2.09 %
Water	-34.79 dB	-30.8 dB	0.45 %
	-19.75 dB	-26.5 dB	1.22 %

The data in table D-1 show that even after nonlinearity correction with the model developed above, OFM20 traces are not linear enough to obtain an accurate estimate of the backscatter fraction. It is conjectured, based on qualitative observation of curve behavior but without any quantitative evidence to support or refute the conjecture, that if two separate detector functions–the one already developed for trace peaks and another similar one for Rayleigh backscatter floors–were developed, that a reasonably accurate backscatter fraction could be computed. Although the shape of the Rayleigh backscatter floor detector functions would be straightforward to synthesize, the amplitude relationship between these two different detector functions will take some thought, because this relationship (unlike the absolute amplitude) cannot be assigned arbitrarily.

The backscatter fractions for air traces in table D-1 bracket the backscatter fraction for step index glass optical fiber computed from the HP handbook (f_{bs}=3.7 ± 0.5 %), using the numerical aperture (N.D. = 0.47 ± 0.3) and core index of refraction (n_{core} = 1.492) for plastic optical fiber. Since no one trace could be

recommended over any another in table D-1 as the "correct" backscatter fraction (particularly for plastic optical fiber), the HP handbook number was used as a reasonable default for this analysis. If further work is performed on PTILS to better quantify the backscatter fraction, then backscatter fraction measurements should be performed on plastic optical fiber, not polymer coated glass optical fiber.

It should be noted that part of the difficulty in obtaining stable results in these measurements is that the dynamic range spanned by the trace is so large (25 to 35 dB). Given a reasonably accurate estimate of the backscatter fraction, the following analysis of real splices and prediction of traces for various stipulated splice reflectivities should be reasonably accurate because the dynamic range of the trace deflection in these situations is significantly smaller.

D.7 DETERMINATION OF SPLICE REFLECTIVITY FROM ACTUAL OFM20 TRACES OF LABORATORY PREPARED "SPLICES."

As discussed in the main report, several laboratory "splices" were prepared to attempt to establish the limits of splice quality in plastic optical fiber. Some of these "splices" were prepared with 250 μm core fiber, and traces showing the splice reflectivity characteristics were generated using the OFM20 as part of proof-of-concept demonstration of the PTILS tamper detection system. It was of interest to quantify the reflectivity and throughput loss characteristics of the splices in these traces so that quantitative assessments could be made of how close these attempts came to the limit of detectability with the OFM20.

At the peak of the OFM20 trace deflection from a "splice", the energy available to drive the detector is, from equation D-33,

$$E(t_{peak}) = A_c\left[\frac{1}{2} v \mathcal{E}_0 f_{bs} \sigma_s \zeta_{peak} e^{-\sigma v t_{peak}} + \mathcal{E}_0 e^{-2\sigma x_s} R_s W\left(t_{peak} - \frac{2x_s}{v} + \eta\tau_w\right)\right]. \quad \text{(D-41)}$$

where for notational compactness the integral terms are represented by the constant

$$\zeta_{peak} \triangleq \int_{-(1-\eta)\tau_w}^{\frac{2x_s}{v} - t_{peak}} W(\eta\tau_w - \tau) e^{-\sigma v \tau} d\tau + A_s^2 \int_{\frac{2x_s}{v} - t_{peak}}^{\eta\tau_w} W(\eta\tau_w - \tau) e^{-\sigma v \tau} d\tau . \quad \text{(D-42)}$$

Note that in the special case of a lossless splice (i.e., $A_s = 1$) then the transition region between Rayleigh backscatter floor levels is nonexistent, and $\zeta_{peak} \equiv \zeta$ as defined in equation D-25. Solving for the splice reflectivity R_s in equation D-41 gives

$$R_s = \frac{\dfrac{E(t_{peak})}{A_c \mathcal{E}_0} - \frac{1}{2} v f_{bs} \sigma_s \zeta_{peak} e^{-\sigma v t_{peak}}}{e^{-2\sigma x_s} W\left(t_{peak} - \frac{2x_s}{v} + \eta\tau_w\right)} . \qquad \text{(D-43)}$$

The constant $A_c\mathcal{E}_0$ in equation D-43 is unknown, but can be deduced from the magnitude of the Rayleigh backscatter floor on the same trace. At some point on the Rayleigh backscatter floor just preceding the splice deflection, the energy available to drive the detector, again from equation D-33, is

$$E(t_{floor}) = \frac{1}{2} v A_c \mathcal{E}_0 f_{bs} \sigma_s \zeta e^{-\sigma v t_{floor}} . \qquad \text{(D-44)}$$

Solving for $A_c\mathcal{E}_0$ in equation D-44 and substituting this result into equation D-43 yields

$$R_s = \frac{1}{2} v f_{bs} \sigma_s \left\{ \frac{\zeta e^{-\sigma v t_{floor}} \dfrac{D^{-1}\left[\tilde{E}_t(t_{peak})\right]\tilde{E}_t(t_{peak})}{D^{-1}\left[\tilde{E}_t(t_{floor})\right]\tilde{E}_t(t_{floor})} - \zeta_{peak} e^{-\sigma v t_{peak}}}{e^{-2\sigma x_s} W\left(t_{peak} - \frac{2x_s}{v} + \eta\tau_w\right)} \right\} . \qquad \text{(D-45)}$$

where the linear energy available to drive the detector has been expressed in terms of the raw trace magnitudes via equation D-40.

Because the shape of the trace described in equation D-41 involves a Rayleigh floor transition term in addition to the Fresnel-like window-shaped term, the observed peak of the trace does not exactly coincide with the peak of the window function in the Fresnel-like term. In other words, the argument of the window function $W(\tau)$ in equation D-41 does not evaluate exactly to τ_{peak} as was approximated in the discussion following equation D-39 in section D.6. Through numerical evaluation, it was found that the magnitude of R_s computed from equation D-45 can be extremely sensitive to the placement of the splice relative to the time assignment of the measured trace peak (i.e., R_s can be very sensitive to the difference $2x_s/v - t_{peak}$). The splice reflectivity is affected only weakly through the window function explicitly shown in the denominator of equation D-45, but is

affected very strongly through the integral limits implicit in the constant ζ_{speak} (c.f., equation D-42) if the splice attenuation is large (i.e., $A_s << 1$). Therefore, proper evaluation of equation D-45 requires iterative refinement of the splice position assignment $2x_s/v$ relative to the measured trace abscissa so that the time of the peak in the trace model (described by equation D-41) is self-consistent with the measured time of the peak t_{peak} in the trace.

The above discussion will be made more clear by reviewing splice reflectivity and throughput loss analysis of an OFM20 trace of an actual "splice." Figure D-9 shows various partial trace contributions and the total simulated OFM20 trace predicted by equation D-41 (multiplied by D(E) to restore the nonlinearity) overlaid on on OFM20 trace of a 250 μm to 1000 μm "splice." The "splice" characteristics are summarized in the upper right hand corner of the plot. The indicated "splice" location on the plot is a conclusion based on iterating on x_s until the position of the peak of the simulated curve predicted by equation D-41 matched the position of the peak of the original trace on the distance axis. The discrepancy on the distance axis between the peak of the Fresnel-like contribution and the total OFM20 trace peak is indicated by the quantity Δx.

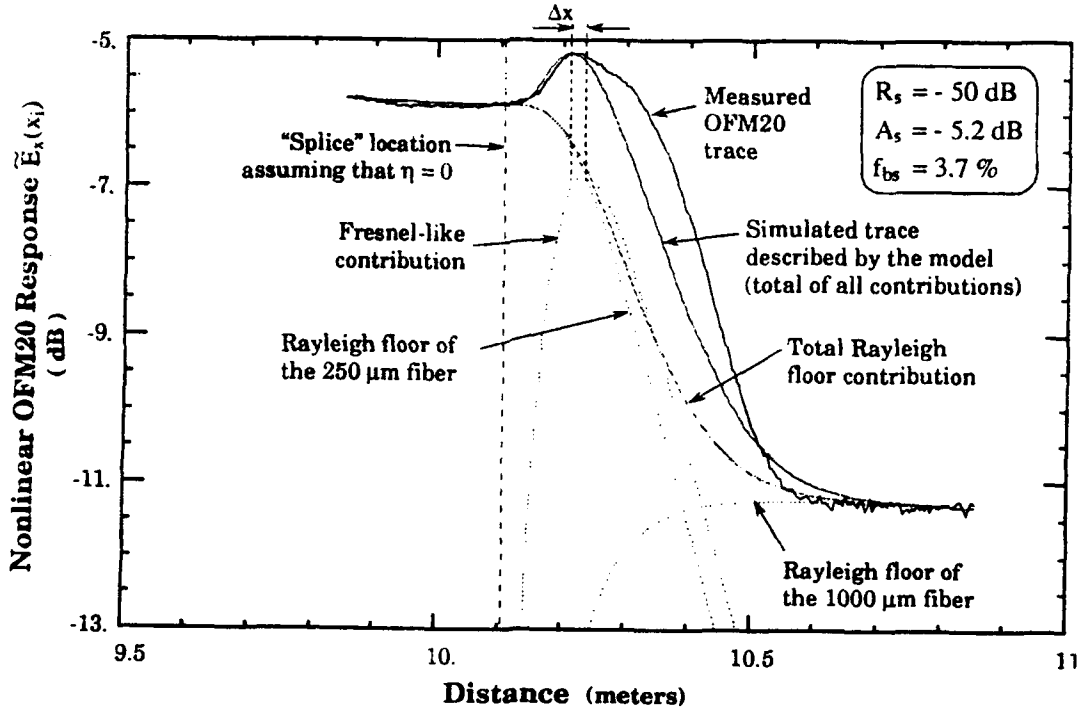

Figure D-9. Analysis of an OFM20 trace showing an index matched, butt "splice" between 250 μm and 1000 μm plastic optical fibers.

The agreement between the simulated trace and the measured trace in figure D-9 is not excellent. The shape of the simulated trace is based on the sampling window shape depicted in figure D-7, which was developed directly from other OFM20 trace shapes as described in section D.4.2. The cause of the distorted shape of the measured trace compared to the simulated trace shape in figure D-9 is not well understood. Whether the shape discrepancy between measured and simulated traces introduces error in the "splice" reflectivity calculated in this analysis is unclear.

Figure D-10 shows a overlay of analysis results on a 250 μm into 250 μm fiber "splice" prepared at BDM/McLean. Because the spatial extent of the trace is so much wider than the trace in figure D-9, the annotations have been left out for clarity. The meaning of each of the curves remains the same. As described in the main report, this particular "splice" was optimized to minimize reflectivity at the expense of increasing throughput loss; as a result, the throughput loss is quite noticeable.

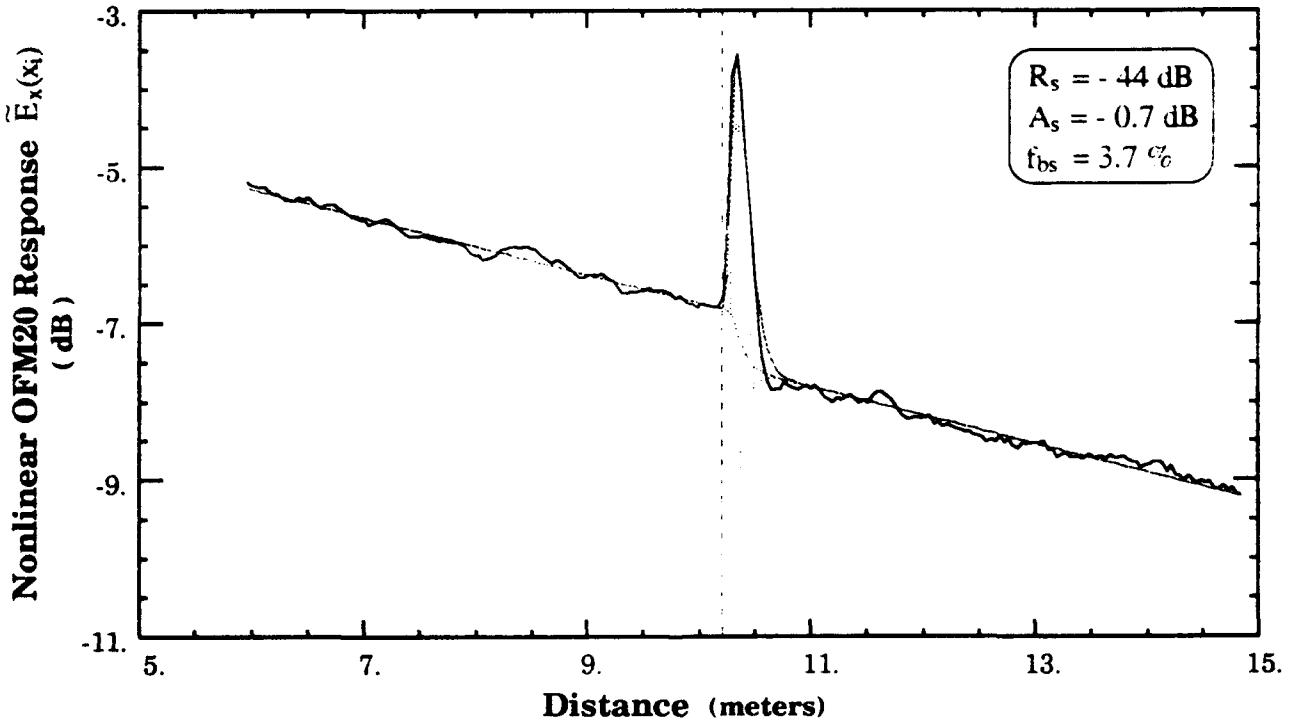

Figure D-10. Analysis of an OFM20 trace showing a 250 μm to 250 μm "splice" prepared in BDM/McLean.

Figure D-11 shows a overlay of analysis results on a 250 μm into 250 μm fiber "splice" prepared at BDM/Albuquerque. The amplitude of the trace in figure D-11 is well into the nonlinear region (c.f., figure D-4), and the effect of the nonlinearity can be seen in the curvature of the slope of the Rayleigh backscatter floor. The second Fresnel event in the trace, which is irrelevant to this analysis, is the saturated trace deflection from the fiber-air interface at the far end of the optical fiber. It should be noted that both the reflected signal and the throughput loss could be used as indicators of the "splices" in the OFM20 traces in figures D-10 and D-11.

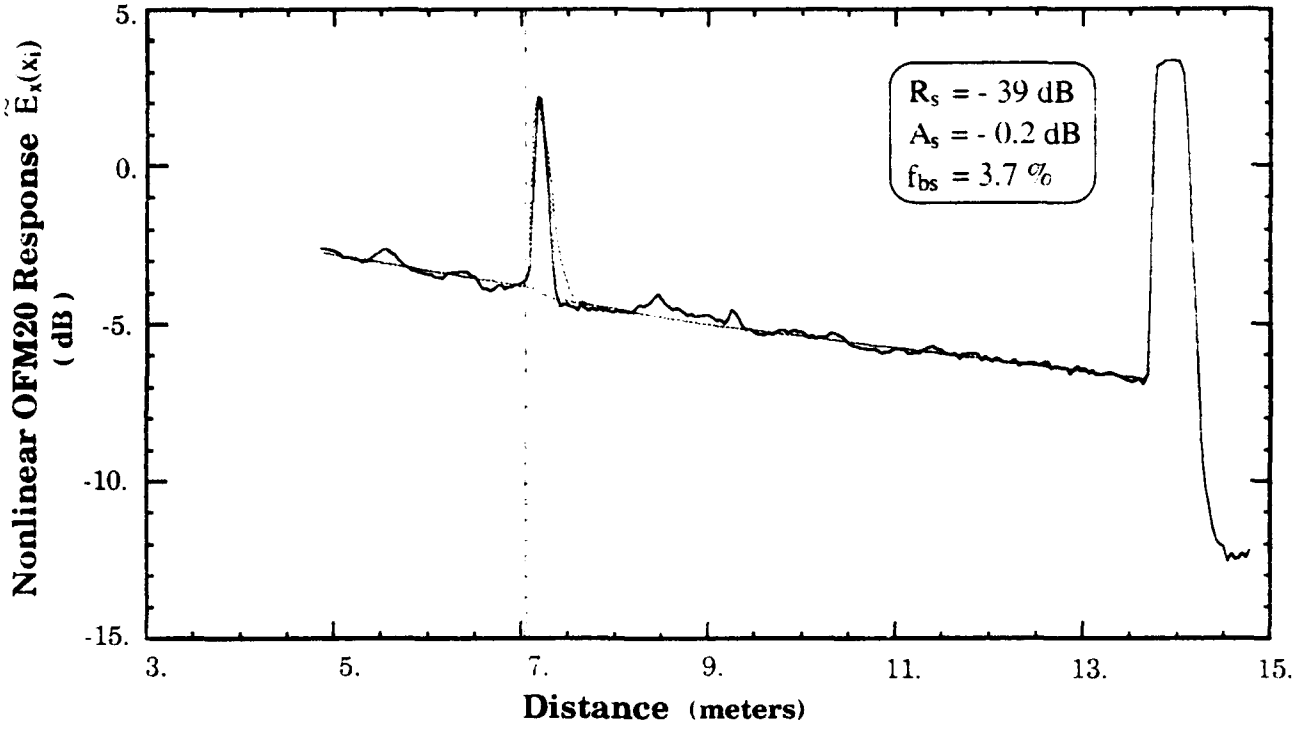

Figure D-11. Analysis of an OFM20 trace showing a 250 μm to 1000 μm "splice" prepared in BDM/Albuquerque.

The trace analysis presented in this section can and should be checked against experiment. Model confirmation could be accomplished by comparing model predictions against end-of-fiber trace events of known reflectivity. The reflectivity of end-of-fiber events can be controlled by immersing the fiber end into fluids of known index instead of air, and computing the reflectivity according to

$$R_{end} = \left(\frac{n_{core} - n_{fluid}}{n_{core} + n_{fluid}} \right)^2 .$$

D.8 SIMULATION OF OFM20 TRACES WITH MULTIPLE, HYPOTHETICAL SPLICE REFLECTIVITIES.

All of the pieces necessary to simulate the performance of the OFM20 have been assembled, except for evaluation of the trace noise. Because small reflectivity splices could be confused with or lost in trace noise, realistic quantification of the trace nose is critically important if conclusions regarding the limits of splice detectability with this instrument are to be valid.

D.8.1 Quantification of Trace Noise.

As was mentioned in connection with equation D-20 in section D.5.1, the apparent noise in OFM20 traces is actually a combination of random detector noise and small perturbations in the uniformity of the fiber. In the notation presented in this model, detector noise is described by the random variable $\delta\tilde{E}(P_{b_s})$, whereas fiber perturbation would be described (if it were pursued mathematically) as small deviations in σ and σ_s. For the purpose of splice detection in a given tag/seal, the distinction between the two effects is very important because the fiber perturbations should be reproducible from trace to trace, whereas the random detector noise should be uncorrelated between traces. Thus, differencing a verification trace and a reference trace should leave only the random detector noise component in addition to the splice deflection (if a splice is present) as a residual because the physically invariant fiber perturbation effects should subtract out.

For the purposes of splice simulation, on the other hand, the distinction between random detector noise and fiber perturbation effects could be ignored because a common noise signature could be used for all trace simulations. Lumping random detector noise and fiber perturbation into a single "noise" effect greatly simplified the analysis because σ and σ_s could then be treated as constants. A full characterization of the fiber perturbations would have required replacement of σ and σ_s in equation D-20 by $\sigma + \delta\sigma(x)$ and $\sigma_s + \delta\sigma_s(x)$, respectively, where $\delta\sigma(x)$ and $\delta\sigma_s(x)$ are spatially dependent perturbation functions that

describe subtle nonuniformities in fiber manufacture leading to the observed trace signature.

It was found, for a given OTDR setup on a given section of optical fiber, that the random component of noise relative to the trace amplitude varies with the sensitivity setting S_{dB}. Figure D-12 shows traces of a 2 m length of Rayleigh backscatter floor in plastic optical fiber at 10 different sensitivity settings. The top trace in figure D-12 (S_{dB}= -60 dB) is the most sensitive setting available in the OFM20. Clearly, the effect of the random component of trace noise becomes less significant as the sensitivity is increased. The control of trace noise by adjustment of the sensitivity setting has strong implications in relation to setting up OFM20 measurements to maximize splice detectability in a verification inspection.

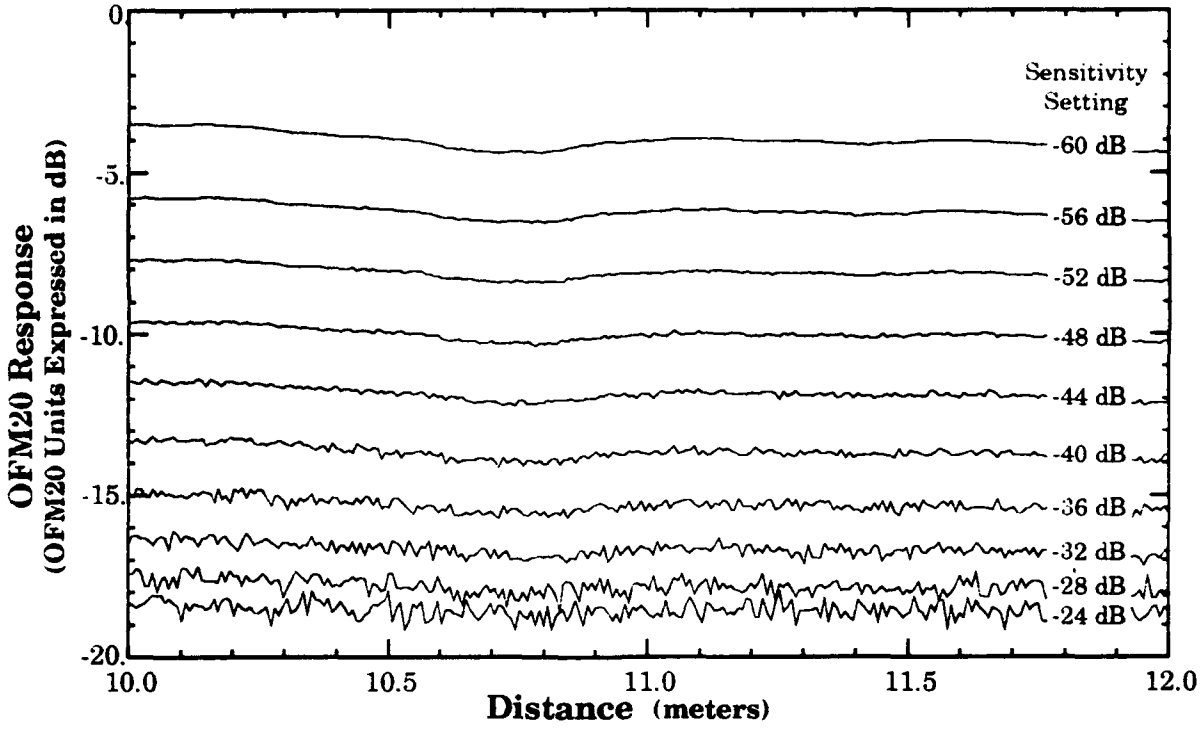

Figure D-12. OFM20 traces of a 2 m section of Rayleigh backscatter floor in plastic optical fiber at different sensitivity settings.

The undulations common to all of the traces in figure D-12 are perturbations in the uniformity of the optical fiber. They appear in these traces to be a low frequency component that is easily distinguishable from the higher frequency random noise. This low frequency appearance is an artifact of the

narrow (2 m) display window of the trace; a wider display window would cause the appearance of the the fiber perturbations to be as dense or more dense than the random noise component, whose 256 independent data acquisition channels are independent of the display window width.

The following approach was used to include lumped "noise" in the trace. "Noise" is set in quotations to signify that reproducible perturbation effects were included, even though these effects would not be treated as noise in verification trace comparisons. First, an actual trace of a section of Rayleigh backscatter floor at a given sensitivity setting was converted to linear energy form via

$$E_R(t_i; S_{dB}) = D^{-1}(\tilde{E})\tilde{E}(t_i; S_{dB}) , \qquad \text{(D-46)}$$

where S_{dB} is the sensitivity setting of the neutral density filter associated with the trace. Next, the least squares fit (a straight line on dB scale) to $E_R(t_i; S_{dB})$, call it $\hat{E}_R(t)$, was determined. The deviation of the least squares fit from the original trace function was used to define a linear "noise" function $\delta E(t_i; S_{dB})$:

$$\delta E(t_i; S_{dB}) = E_R(t_i; S_{dB}) - \hat{E}_R(t_i) . \qquad \text{(D-47)}$$

A noise-free trace containing an lossless splice of some specified reflectivity was then simulated using equation D-34. The amplitude of the Rayleigh backscatter floor in the simulated trace was scaled to exactly match the amplitude of the least squares fit $\hat{E}_R(t)$. "Noise" was then included in the simulated trace, and the nonlinear appearance of the trace was restored as

$$\tilde{E}_{sim}(t_i; S_{dB}) = D(E)\left[E_{sim}(t_i; S_{dB}) + \delta E(t_i; S_{dB})\right] , \qquad \text{(D-48)}$$

where $E_{sim}(t_i; S_{dB})$ denotes the properly scaled simulated trace computed using equation D-34. This approach of including trace noise is consistent with equation D-6 (with the understanding that fiber perturbations were included in the noise term) and ensured that the amplitude of the "noise" for a given sensitivity setting was realistic because the "noise" was taken directly from an actual OFM20 trace.

D.8.2 Simulation of OFM20 Traces.

The tactic used to reveal the limits of splice detectability with the OFM20 OTDR was to simulate attenuation-free splices of successively smaller reflectivities, using the method described in section D.8.1, until the deflection in the trace indicating the presence of a splice became visually indistinguishable from a splice-free Rayleigh backscatter floor. Establishing exactly where the actual limit of detectability falls as a tampering decision statistic requires a separate study that must consider reader-to-reader variation, temperature variation, tag/seal aging and environmental degradation, etc.

Figure D-13 shows the result of simulating OFM20 traces at a sensitivity setting of -40 dB of a splice, varying the reflectivity from -30 to -60 dB in 5 dB increments, on the same optical fiber used to generate the traces in figure D-12. This sensitivity setting places the amplitude of the trace in the linear regime of the OFM20, and is consistent with the normal usage of the OFM20 recommended by the manufacturer. It is seen that a splice with a -50 dB reflectivity splice is probably easily distinguishable above the noise, but that the detectability verdict for a -55 dB reflectivity splice would be less certain.

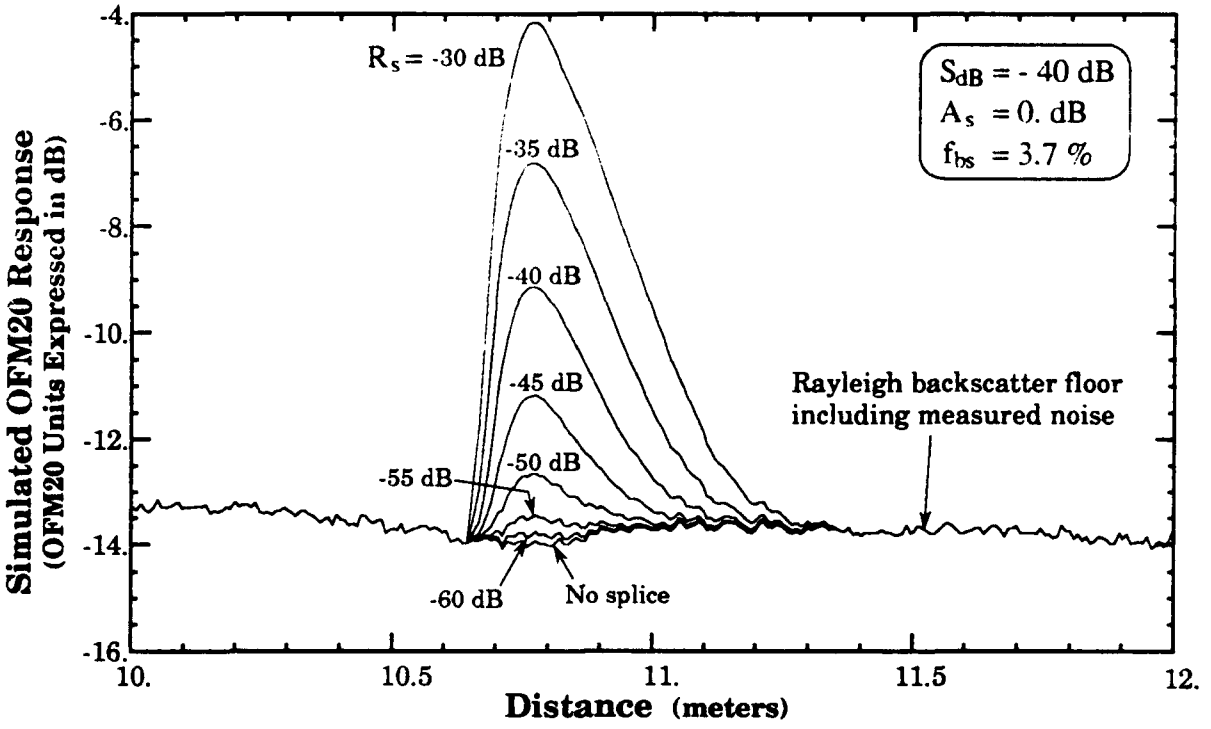

Figure D-13. Simulation of nonlinear OFM20 traces at a -40 dB sensitivity setting showing a splice with various reflectivities.

The backscatter fraction, which was shown to be uncertain in section D.6, was asserted to be 3.7 % in these simulations. If the real backscatter fraction is larger than this, then the Rayleigh backscatter floor rises relative to the splice reflection signal, and detectability is diminished. Conversely, if the real backscatter fraction is smaller than 3.7 %, then the Rayleigh backscatter floor would be lowered relative to the splice reflection signal, and detectability would be enhanced. To show this effect, simulations of a -55 dB splice were run for excursion backscatter fraction assertions of 2 % and 6 %. Figure D-14 shows these simulations overlaid on the 3.7 % backscatter fraction reference case. It is seen that even with variation in f_{bs} by almost a factor of two from the asserted backscatter fraction of 3.7 %, the ultimate distinguishability of a -55 dB reflectivity splice with a sensitivity setting of -40 dB is only marginally affected.

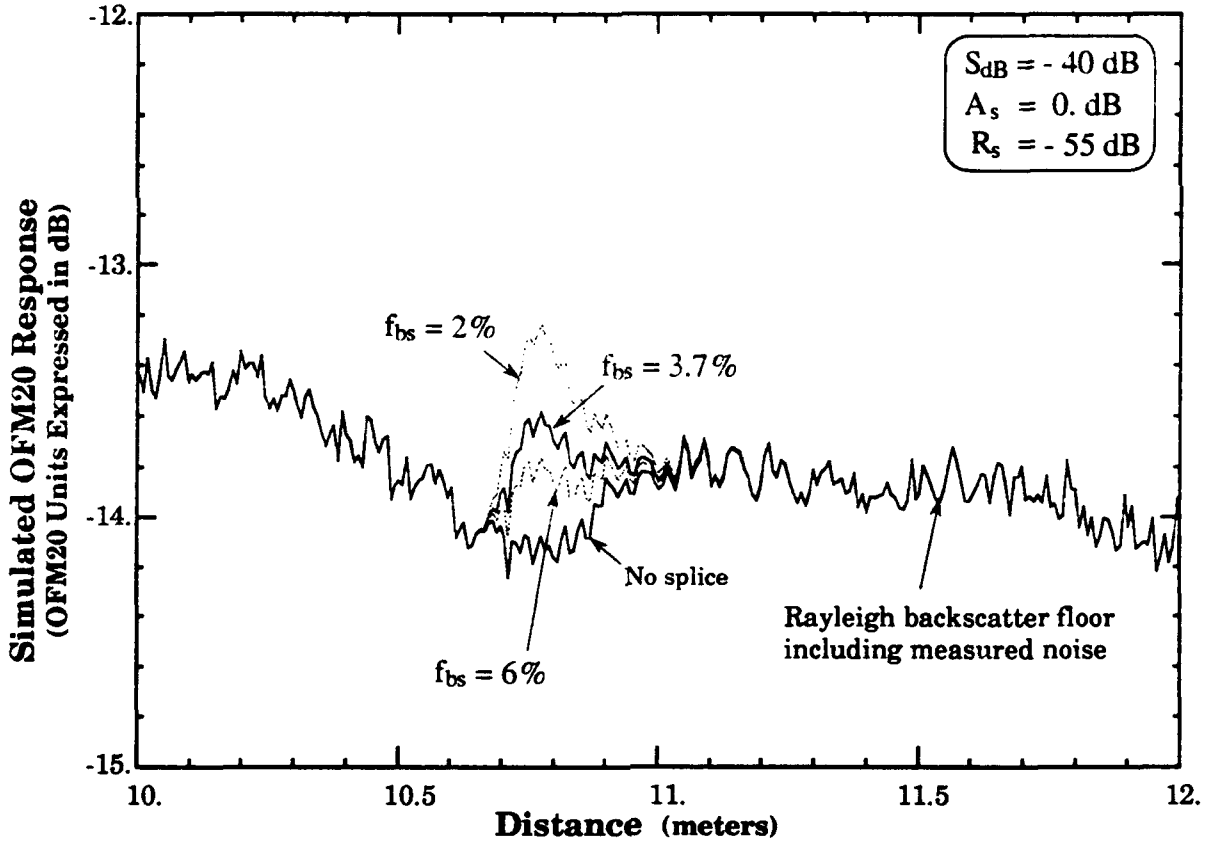

Figure D-14. Simulation of nonlinear OFM20 traces at a -40 dB sensitivity setting showing a -55 dB reflectivity splice with three different asserted backscatter fractions.

Figure D-15 shows an OFM20 simulation similar to that in figure D-13 (with f_{bs} = 3.7%), but with the sensitivity maximized at S_{dB} = -60 dB. In this case, a -55 dB reflectivity splice is easily distinguishable above the noise, but the detectability of a -60 dB reflectivity splice is questionable. Thus, it is seen that maximizing the sensitivity of the OFM20 does indeed enhance splice detectability, provided that maximum sensitivity does not saturate any portions of the trace that must not be saturated to be meaningfully interpreted. The fact that the trace showing a -30 dB reflectivity splice in figure D-15 is saturated is inconsequential because the existence of the splice would obviously be detected. Usage of the OFM20 at maximum sensitivity is unusual for normal, investigative applications envisioned by the manufacturer, but would seem to be the appropriate mode for tamper detection in the PTILS application. It should be noted that the display window in this simulation is the same as that of the noise traces–10 to 12 meters into the plastic optical fiber. At further distances, fiber attenuation would diminish the strength of the Rayleigh backscatter floor signal relative to random noise, but as can be seen from figure D-12, there is sufficient dynamic range remaining to retain a large signal-to-noise ratio for PTILS loop lengths of at least 30 m, the maximum fiber length that can be interrogated by the OFM20 with its 1 MHz sampling rate.

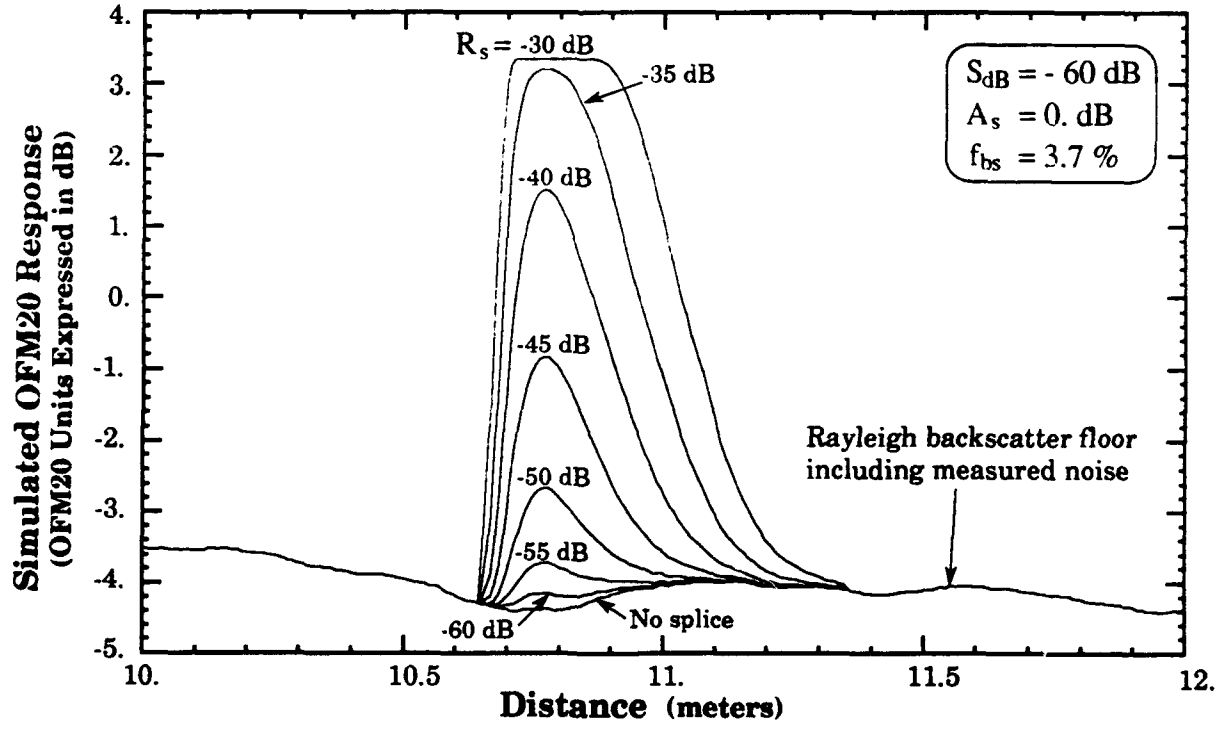

Figure D-15. Simulation of nonlinear OFM20 traces at a -60 dB sensitivity setting showing a splice with various reflectivities.

D.9 CONCLUSIONS.

A body of theory allowing the OFM20 to be successfully modeled has been developed. With this theory, the two laboratory "splices" prepared by BDM were analyzed, and their reflectivities were determined to be approximately -39 and -44 dB. Simulations probing the limits of detectability showed that even with significant trace noise, splices of -50 dB reflectivity should be visually detectable in a reference-to-verification trace overlay comparison, and a -55 dB reflectivity splice may be detectable with a differencing algorithm. Thus, it appears that there is a significant safety margin between the observed detectability of laboratory "splices" and the simulated limits of splice detectability. The safety margin between the detectability of real world splices and the simulated limits of splice detectability is expected to be even greater.

Several weaknesses in this OFM20 simulation model have been identified. The detector sensitivity function appears to be adequate to describe the nonlinear behavior of trace peaks, but is inaccurate in describing the nonlinear behavior of the Rayleigh backscatter floor. This inaccuracy is manifested in the calculation of the Rayleigh backscatter fraction, which is proportional to the ratio of the peak to the floor in a calibration trace of known reflectivity. Thus, refinement of the detector sensitivity function to include proper treatment of the Rayleigh backscatter floor, for the purpose of stabilizing the backscatter fraction analysis, is a critical area of focus for model improvement. Plastic optical fiber, not polymer coated glass optical fiber, should be used to determine the backscatter fraction when these model improvements are accomplished. Also, it would be wise to set up a laboratory test case to compare the model prediction on a low amplitude Fresnel event of known reflectivity. Such an experimental benchmark would greatly enhance the model credibility in predicting the limits of splice detectability in the verification community.

Another less critical area of research is to understand the inconsistent trace shapes associated with Fresnel events. The sampling window function that was developed in this analysis appears to be one window shape that is regularly observed in traces, but it is not the only shape that arises in traces containing simple Fresnel reflections. The cause of these inconsistencies, and whether they significantly affect the conclusions presented here, remains to be determined.

APPENDIX E

ANALYSIS OF THE RAYLEIGH BACKSCATTERED POWER IN A MULTIWRAP GLASS SLOTS OPTICAL FIBER WITH BENDS AND SPLICES

E.1 INTRODUCTION.

This appendix develops a mathematical theory of Rayleigh backscatter for glass optical fibers that are physically configured as multiwrap glass (MWG) tags. Results are plotted for extreme cases of bend loss and covert splice loss to show the behavior of fiber in the MWG configuration with and without covert splices, as seen by an optical time domain reflectometer (OTDR). Plots of OTDR trace simulations using this model, incorporating more realistic bend loss and splice loss information based on measured data, are also provided.

E.2 MODEL DERIVATION.

The light power moving forward down the fiber and arriving at distance x in the optical fiber is

$$P_f(x,t) = P_0 \prod_{i=1}^{N-1} \left[1 - \left(1 - A^+_{b,i}\right) \Theta(x - x_{b,i})\right] \prod_{j=1}^{N} \left[1 - (1 - A_{s,j}) \Theta(x - x_{s,j})\right] \times \exp\left[-\int_{x_0}^{x} \sigma(x')dx'\right] f_t\left(t - \frac{x - x_0}{v}\right) \Theta\left(t - \frac{x - x_0}{v}\right), \quad \text{(E-1)}$$

where

P_0 is the peak forward-propagating light power at a reference position x_0, which in this analysis is located at the leading end connector of the tag (inside the tag fiber),

t is the time elapsed since the time of arrival of the forward-propagating light pulse at reference position x_0,

v is the mean velocity of the light pulse in the fiber ignoring modal dispersion,

$\sigma(x) = \sigma$ is the total linear attenuation cross section of the fiber (cm^{-1}), which is constant for a uniform fiber,

$f_t(\tau)$ is the time history of the light pulse, normalized so that $\max[f_t(\tau)] = 1$,

$A^+_{b,i}$ is the attenuation of forward-propagating (+) light due to the i^{th} bend at bend location $x_{b,i}$,

$A_{s,j}$ is the splice attenuation due to the j^{th} covert splice at splice location $x_{s,j}$,

N is the total number of wraps in the tag, where a wrap is defined as a single fiber transit around the tag loop, and

$\Theta(x)$ is the Heaviside unit step function.

In the light propagation model expressed by equation E-1, the losses due to bends and splices are accumulated by the product factors, which gain new non-unity factors as x increases. Light power loss in a bend is loss due to leakage of higher order propagating modes. Therefore, it is expected that the loss per bend will monotonically decrease with traversal of successive bends, because a decreasing amount of energy remains in higher order modes after each bend traversal. That is, $A^+_{b,1} \leq A^+_{b,2} \leq \ldots \leq A^+_{b,N} < 1$. The energy in lower order modes should be unaffected by the presence of the macrobends at the relatively large bend radius inside the joint block of the tag. The use of step functions to model the onset of loss at each bend implies that all of the loss occurs instantaneously at a single point $x_{b,i}$ for each bend index i.

Traversal of a splice is also modeled as light leakage loss localized at a point, and is assumed in this model to leave the modal distribution incident on the splice unaffected. In fact, it is known that splices do tend to populate higher order modes in multimode optical fiber.[1] Therefore, ignoring splice perturbation on the modal distribution is a conservative assumption that minimizes the detectability of the splice in the model (that is, real splices should produce larger, more detectable losses than the benign, idealized splices in this model).

It is assumed that the quality of covert fusion splices is high enough so that no splice will create a detectable Fresnel reflection in the OTDR trace. With this assumption, the only backscatter mechanism (except for Fresnel reflections at the front and back end connectors) is Rayleigh scattering. The differential light power reflected by Rayleigh scattering in the length interval dx about location x in the fiber is

$$dS(x,t) = f_{bs}\, \sigma_s(x)\, P_f(x,t)\, dx\,, \qquad \text{(E-2)}$$

where

f_{bs} is the fraction of Rayleigh scattered light that is backscattered within the aperture of the fiber, and is therefore captured as backward-propagating light power, and

---

[1] Ikeda, M., Y. Murakami, and K. Kitayama, "Mode scrambler for optical fibers," **Applied Optics**, 16:4, April 1977.

$\sigma_s(x) = \sigma_s$ is the total linear cross section for Rayleigh scattering in the fiber (cm^{-1}), which is constant for a uniform optical fiber.

The contribution to the backward-propagating power returning to the reference location x_0 that was produced in the length increment dx' at $x' > x_0$ is

$$dP(x',t)\Big|_{x=x_0} = \prod_{i=1}^{N-1}\left[1-\left(1-A^{-}_{b,k-i+1}\right)\Theta(x'-x_{b,i})\right]\prod_{j=1}^{N}\left[1-(1-A_{s,j})\Theta(x'-x_{s,j})\right] \times \exp\left[-\int_{x_0}^{x'}\sigma(x'')dx''\right] dS\left(x', t-\frac{x'-x_0}{v}\right), \quad \text{(E-3)}$$

where

$E^{-}_{b,k-i+1}$ is the attenuation of backward-propagating (-) light due to the i^{th} bend encountered at $x_{b,i}$ and

$k = \text{int}[(x'-x_0)/L_{tag}]$ is a position-dependent starting index, where L_{tag} is the tag length (which is also the fiber length per wrap) and int[ ] means the integer part of the quantity in brackets.

The index k-i+1 in the bend attenuation factor references all bend indices to the location of the scattering event at position x'. This is done so that, as in the forward-propagating case, the loss per bend can be assigned to monotonically decrease with traversal of successive bends for backward-propagating light. That is, $E^{-}_{b,1} \le E^{-}_{b,2} \le \ldots \le E^{-}_{b,N} < 1$. The backward-propagating attenuation factors $E^{-}_{b,i}$ are expected to differ from the forward-propagating attenuation factors $A^{+}_{b,i}$ only insofar as the modal structure generated by Rayleigh backscatter differs from that of the forward-propagating light launched into the tag fiber.

The total power returned to the reference location x_0 in the fiber from all backscattered contributions between x_0 and some field point x is the integral of the differential backscattered power contributions given in equation E-3:

$$P(x_0,t) = \int_{x_0}^{x}\prod_{i=1}^{N-1}\left[1-\left(1-A^{-}_{b,k-i+1}\right)\Theta(x'-x_{b,i})\right]\prod_{j=1}^{N}\left[1-(1-A_{s,j})\Theta(x'-x_{s,j})\right] \times e^{-\sigma\cdot(x'-x_0)}\left[\int_{4\pi}\sigma_s P_f\left(x', t-\frac{x'-x_0}{v}\right)dx'\right], \quad \text{(E-4)}$$

where the last bracket is the result of incorporating equation E-2 for the source

term dS at the retarded time of arrival of the light pulse at position x′. Substituting equation E-1 for forward-propagating light power P_f into equation E-4 and rearranging terms yields

$$P(x_0,t) = f_{bs}\,\sigma_s P_0 \int_{x_0}^{x} \prod_{i=1}^{N-1}\left[1-\left(1-A_{b,i}^{+}\right)\Theta(x'-x_{b,i})\right]\left\{\prod_{j=1}^{N}\left[1-(1-A_{s,j})\Theta(x'-x_{s,j})\right]\right\}^2 \tag{E-5}$$
$$\times \prod_{i'=1}^{N-1}\left[1-\left(1-A_{b,k-i'+1}^{-}\right)\Theta(x'-x_{b,i'})\right] e^{-2\sigma\cdot(x'-x_0)}\; f_t\left(t-\frac{2(x'-x_0)}{v}\right)\Theta\left(t-\frac{2(x'-x_0)}{v}\right)dx'.$$

With the aid of of the mathematical identity

$$\prod_{i=1}^{N}\left[1-(1-g_i)\Theta(x'-x_i)\right]\prod_{j=1}^{N}\left[1-(1-h_j)\Theta(x'-x_j)\right]$$
$$= \prod_{i=1}^{N}\left[1-(1-g_ih_i)\Theta(x'-x_i)\right]$$

equation E-5 simplifies to

$$P(x_0,t) = f_{bs}\,\sigma_s P_0 \int_{x_0}^{x} \prod_{i=1}^{N-1}\left[1-\left(1-A_{b,i}^{+}A_{b,k-i+1}^{-}\right)\Theta(x'-x_{b,i})\right]\prod_{j=1}^{N}\left[1-\left(1-A_{s,j}^{2}\right)\Theta(x'-x_{s,j})\right] \tag{E-6}$$
$$\times\; e^{-2\sigma\cdot(x'-x_0)}\; f_t\left(t-\frac{2(x'-x_0)}{v}\right)\Theta\left(t-\frac{2(x'-x_0)}{v}\right)dx'.$$

The final step function with respect to time in equation E-6 requires that $2(x - x_0)/v \le t$ if the integrand is to be non-zero; therefore, all contributions to the backscattered light power observed at time t have occurred by distance $x = x_0 + vt/2$ down the fiber. Observing this, the upper limit to the integral in equation E-6 can be truncated and the equation cast in the equivalent simplified form

$$P(x_0,t) = f_{bs}\,\sigma_s P_0 \int_{x_0}^{x_0+x_{max}} \prod_{i=1}^{N-1}\left[1-\left(1-A_{b,i}^{+}A_{b,k-i+1}^{-}\right)\Theta(x'-x_{b,i})\right] \tag{E-7}$$
$$\times \prod_{j=1}^{N}\left[1-\left(1-A_{s,j}^{2}\right)\Theta(x'-x_{s,j})\right] e^{-2\sigma\cdot(x'-x_0)}\; f_t\left(t-\frac{2(x'-x_0)}{v}\right)dx',$$

where $x_{max} = vt/2$ is the maximum distance of light propagation down the fiber from x_0 in time t/2.

With appropriate variable substitutions, the spatial integral can be simplified by transforming to retarded time:

$$P(x_o,t) = \frac{1}{2} v f_{bs} \sigma_s P_o e^{-\sigma v t} \int_0^t \prod_{i=1}^{N-1} \left[1 - \left(1 - A^+_{b,i} A^-_{b,k-i+1}\right) \Theta\left(x_0 + \tfrac{1}{2} v(t-\tau) - x_{b,i}\right)\right] \times \prod_{j=1}^{N} \left[1 - \left(1 - A^2_{s,j}\right) \Theta\left(x_0 + \tfrac{1}{2} v(t-\tau) - x_{s,j}\right)\right] e^{\sigma v \tau} f_t(\tau)\, d\tau \,. \tag{E-8}$$

The OTDR trace shape specified by equation E-8 is very difficult to visualize from the mathematical form, and is equally difficult to evaluate on the computer. The next step is to expand this form bend by bend and splice by splice so that the mathematical operations that must be performed in its evaluation can be seen explicitly. In expanded form, equation E-8 becomes

$$P(x_o,t) = \frac{1}{2} v f_{bs} \sigma_s P_o e^{-\sigma v t} \begin{cases} \displaystyle\int_0^t e^{\sigma v \tau} f_t(\tau)\, d\tau, & \boxed{1a} \quad 0 \le t \le \frac{2(x_{s,1} - x_0)}{v} \\[2ex] \displaystyle\int_{t - \frac{2(x_{s,1} - x_0)}{v}}^{t} e^{\sigma v \tau} f_t(\tau)\, d\tau + A^2_{s,1} \int_0^{t - \frac{2(x_{s,1} - x_0)}{v}} e^{\sigma v \tau} f_t(\tau)\, d\tau, & \boxed{1b} \quad \frac{2(x_{s,1} - x_0)}{v} \le t \le \frac{2(x_{b,1} - x_0)}{v} \\[2ex] \displaystyle\int_{t - \frac{2(x_{s,1} - x_0)}{v}}^{t} e^{\sigma v \tau} f_t(\tau)\, d\tau + A^2_{s,1} \int_{t - \frac{2(x_{b,1} - x_0)}{v}}^{t - \frac{2(x_{s,1} - x_0)}{v}} e^{\sigma v \tau} f_t(\tau)\, d\tau \\ \quad + A^2_{s,1} A^+_{b,1} A^-_{b,1} \displaystyle\int_0^{t - \frac{2(x_{b,1} - x_0)}{v}} e^{\sigma v \tau} f_t(\tau)\, d\tau, & \boxed{2a} \quad \frac{2(x_{b,1} - x_0)}{v} \le t \le \frac{2(x_{s,2} - x_0)}{v} \\[2ex] \displaystyle\int_{t - \frac{2(x_{s,1} - x_0)}{v}}^{t} e^{\sigma v \tau} f_t(\tau)\, d\tau + A^2_{s,1} \int_{t - \frac{2(x_{b,1} - x_0)}{v}}^{t - \frac{2(x_{s,1} - x_0)}{v}} e^{\sigma v \tau} f_t(\tau)\, d\tau \\ \quad + A^2_{s,1} A^+_{b,1} A^-_{b,1} \displaystyle\int_{t - \frac{2(x_{s,2} - x_0)}{v}}^{t - \frac{2(x_{b,1} - x_0)}{v}} e^{\sigma v \tau} f_t(\tau)\, d\tau \\ \quad + A^2_{s,1} A^2_{s,2} A^+_{b,1} A^-_{b,1} \displaystyle\int_0^{t - \frac{2(x_{s,2} - x_0)}{v}} e^{\sigma v \tau} f_t(\tau)\, d\tau, & \boxed{2b} \quad \frac{2(x_{s,2} - x_0)}{v} \le t \le \frac{2(x_{b,2} - x_0)}{v} \\ \quad \vdots \end{cases} \tag{E-9}$$

The labeled boxes in equation E-9 refer to temporal intervals that correspond to the spatial regions between bends and splices in the fiber, as shown in figure E-1.

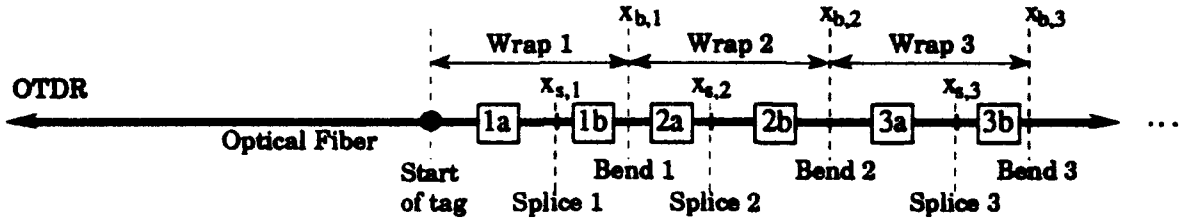

Figure E-1. Key to labels denoting regions between bends and splices.

To simplify the notation, define the integral function

$$I(t; x_\alpha, x_\beta) \triangleq \int_{\max\left[0,\, t - \frac{2(x_\alpha - x_0)}{v}\right]}^{t - \frac{2(x_\beta - x_0)}{v}} e^{\sigma v \tau} f_t(\tau) d\tau \quad . \tag{E-10}$$

In this notation, equation E-9 becomes

$$P(x_0,t) = \frac{1}{2} v f_{bs} \sigma_s P_0 e^{-\sigma v t} \begin{cases} I(t; x_{s,1}, x_0), & \boxed{1a} \\ I(t; x_{s,1}, x_0) + A_{s,1}^2 I(t; x_{b,1}, x_{s,1}), & \boxed{1b} \\ I(t; x_{s,1}, x_0) + A_{s,1}^2 I(t; x_{b,1}, x_{s,1}) \\ \quad + A_{s,1}^2 A_{b,1}^+ A_{b,1}^- I(t; x_{s,2}, x_{b,1}), & \boxed{2a} \\ I(t; x_{s,1}, x_0) + A_{s,1}^2 I(t; x_{b,1}, x_{s,1}) \\ \quad + A_{s,1}^2 A_{b,1}^+ A_{b,1}^- I(t; x_{s,2}, x_{b,1}) \\ \quad + A_{s,1}^2 A_{s,2}^2 A_{b,1}^+ A_{b,1}^- I(t; x_{b,2}, x_{s,2}), & \boxed{2b} \\ \quad \vdots \end{cases} \tag{E-11}$$

Cast in the form of equation E-11, a recursion pattern becomes evident. Through examination of this pattern, it is seen that equation E-11 can be written in a computationally tractable, nested form as

$$
\begin{aligned}
P(x_o,t) = \tfrac{1}{2} v f_{bs} \sigma_s P_o e^{-\sigma v t} \quad & \left[I(t; x_{s,1}, x_0) \right. \quad + A_{s,1}^2 \left[I(t; x_{b,1}, x_{s,1}) \right. \\
+ A_{b,1}^+ A_{b,1}^- \quad & \left[I(t; x_{s,2}, x_{b,1}) \right. \quad + A_{s,2}^2 \left[I(t; x_{b,2}, x_{s,2}) \right. \\
+ A_{b,2}^+ A_{b,2}^- \quad & \left[I(t; x_{s,3}, x_{b,2}) \right. \quad + A_{s,3}^2 \left[I(t; x_{b,3}, x_{s,3}) \right. \qquad \text{(E-12)} \\
& \qquad\qquad \vdots \\
+ A_{b,n-1}^+ A_{b,n-1}^- & \left[I(t; x_{s,n}, x_{b,n-1}) \right. + A_{s,n}^2 \left[I(t; x_{b,n}, x_{s,n}) \right] \left] \cdots \right] \left] \right] \left] \right] \left] \right]
\end{aligned}
$$

where the time dependent wrap-launch index n, given by

$$
n = \min\left[N, \operatorname{int}\left(\frac{\frac{1}{2} v t}{L_{tag}} \right) + 1 \right], \qquad \text{(E-13)}
$$

automatically accounts for all of the boxed partition conditions specified in equation E-11 for $n > 1$. At early time when $n = 1$ (i.e., the backscattered launch occurs in the first wrap), the computational form of equation E-12 defaults to

$$
P(x_o,t) = \tfrac{1}{2} v f_{bs} \sigma_s P_o e^{-\sigma v t} \left[I(t; x_{s,1}, x_0) + A_{s,1}^2 I(t; x_{b,1}, x_{s,1}) \right] \quad . \qquad \text{(E-14)}
$$

Equations E-12 and E-14 are the forms that were used to generate the OTDR trace simulations shown below.

E.3 MODEL SIMULATIONS.

The appearance of trace perturbations due to bends and splices depends on the pulse shape $f_t(t)$ launched by the OTDR, as specified in equation E-10. Figure E-2 shows the shapes of three different pulse widths used in these simulations. The 10 ns and 50 ns full width at half maximum (FWHM) pulse widths are available in the Antel LANprobe 850 nm OTDR board, although the actual pulse shape may be somewhat different. The 1 ns FWHM pulse is included in the simulations to give insight into the effect of pulse width on the detectability of individual bends and splices in the OTDR trace.

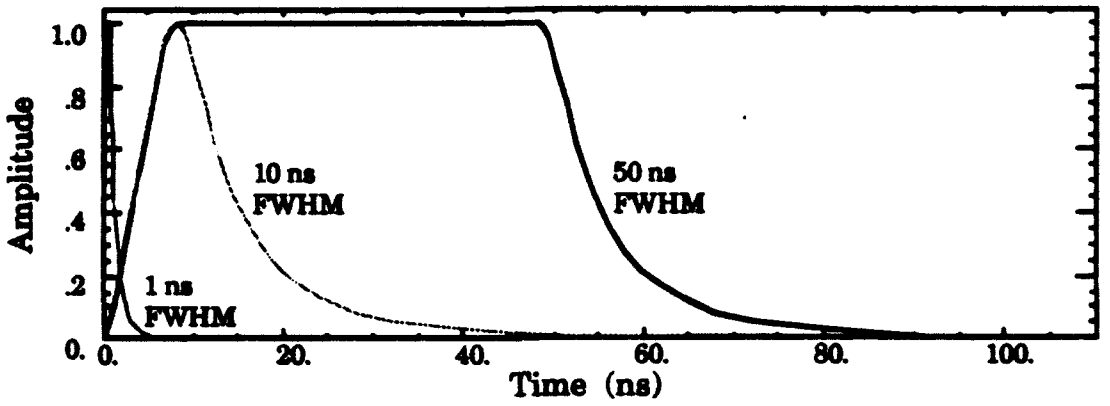

Figure E-2. Pulse shapes used in the simulations.

Figure E-3 is a bar chart showing the bend loss assignments that were selected for the first round of simulations. These bend losses, in which $A^{+}_{b,i} = E_{-b,i}$ for i = 1, 2, ..., N, were deliberately chosen to be artificially large so that the qualitative effect of successive bends could be easily observed in the trace.

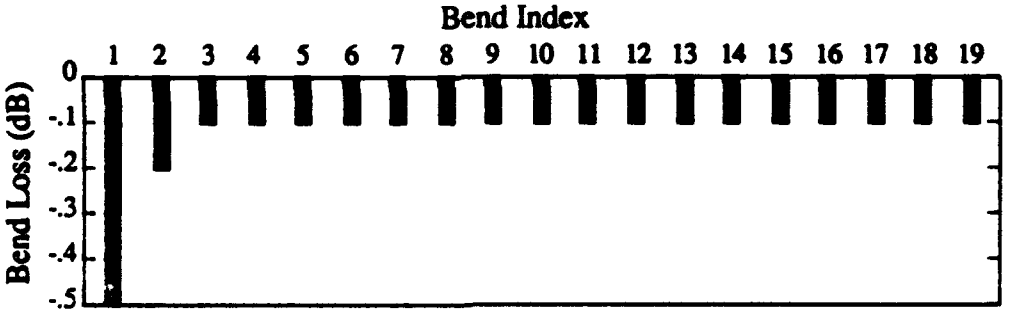

Figure E-3. Assigned loss in each bend for the first round of simulations.

Figures E-4 through E-6 plot the OTDR traces predicted by equations E-12 and E-14 for three different pulse widths, assuming that no splices are present ($A_{s,i} = 1$, i = 1, 2, ..., N) and using the bend losses specified in figure E-3. It is seen in these traces that the individual bends are more easily distinguished with shorter pulse widths, but that the aggregate loss per length is independent of pulse width. Figure E-7 displays these same traces in lower resolution on the same plot so that the relative amplitudes, resulting from differences in total backscattered power due to pulse width differences for a constant peak amplitude laser source, can be compared.

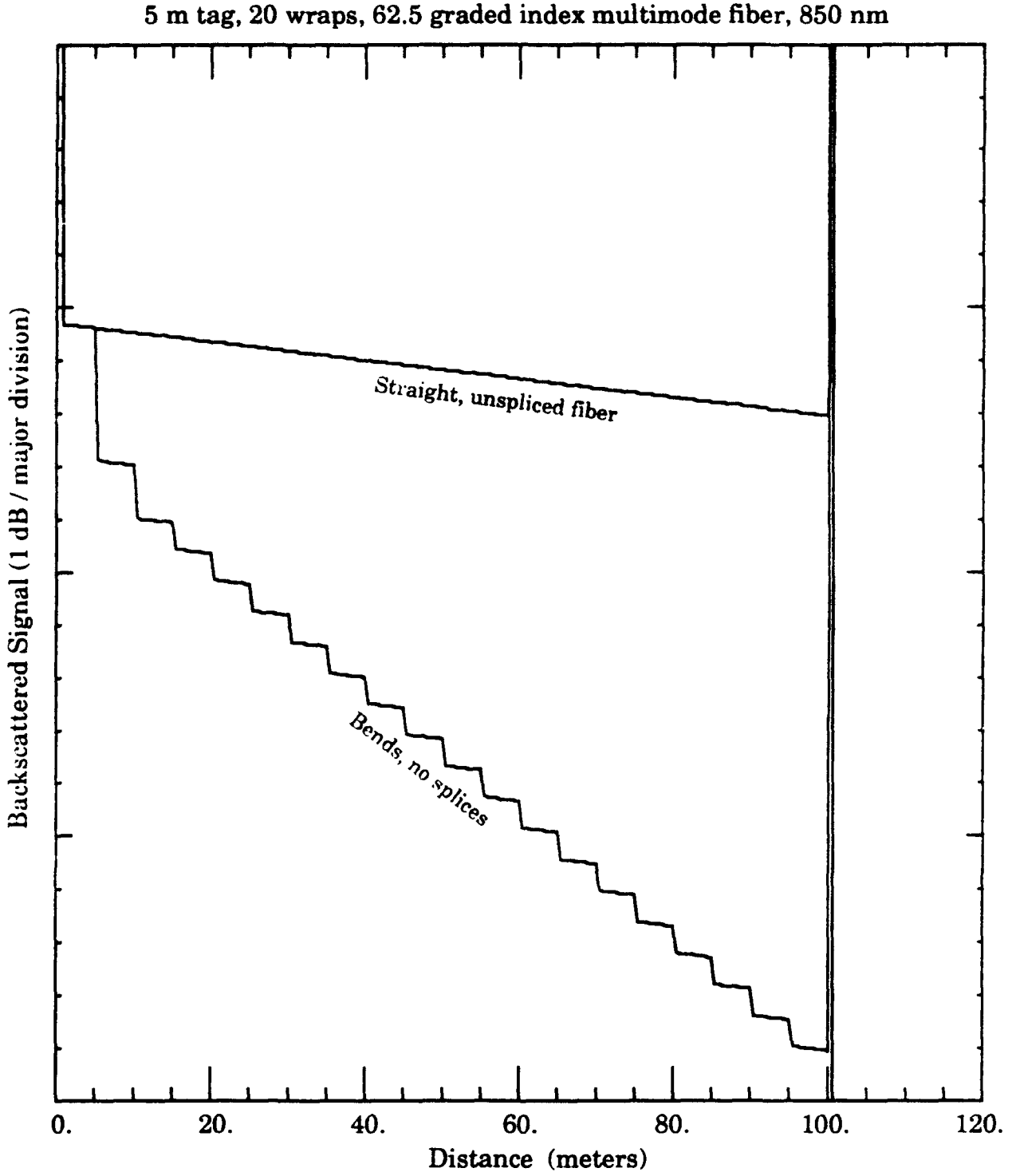

Figure E-4. OTDR trace simulation of the effect of multiple bend losses for deliberately gross individual bend losses for a 1 ns FWHM pulse width.

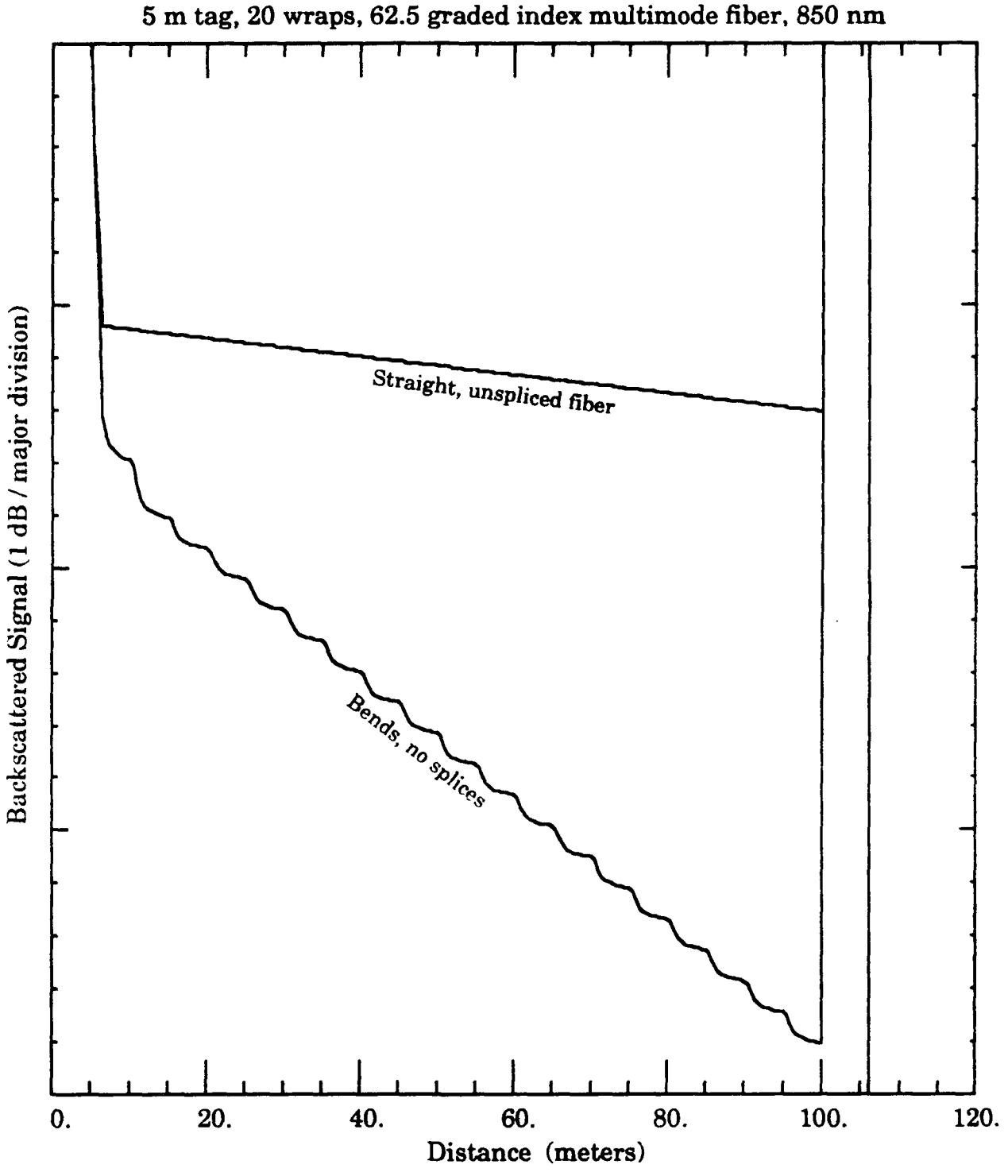

Figure E-5. OTDR trace simulation of the effect of multiple bend losses for deliberately gross individual bend losses for a 10 ns FWHM pulse width.

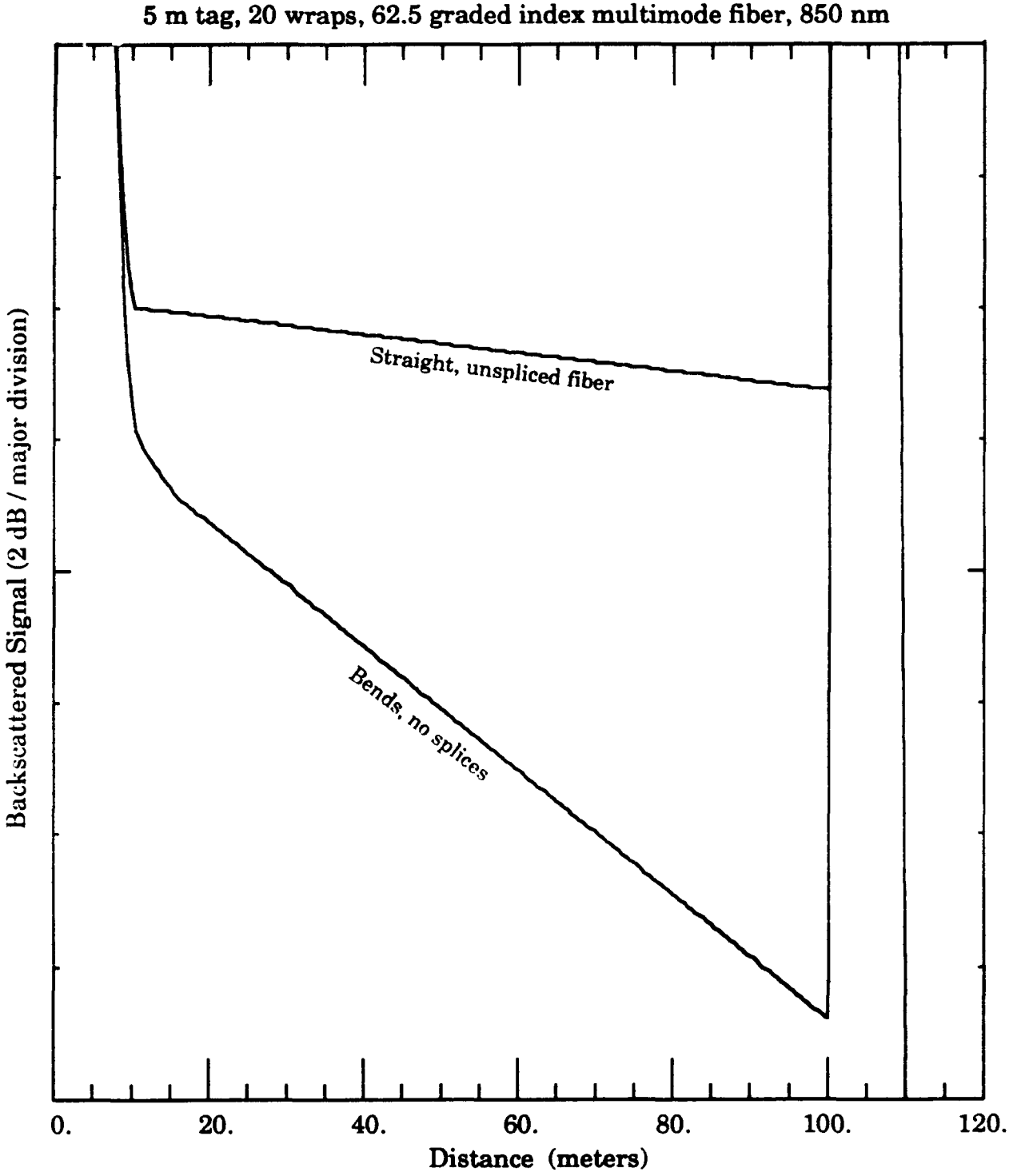

Figure E-6. OTDR trace simulation of the effect of multiple bend losses for deliberately gross individual bend losses for a 50 ns FWHM pulse width.

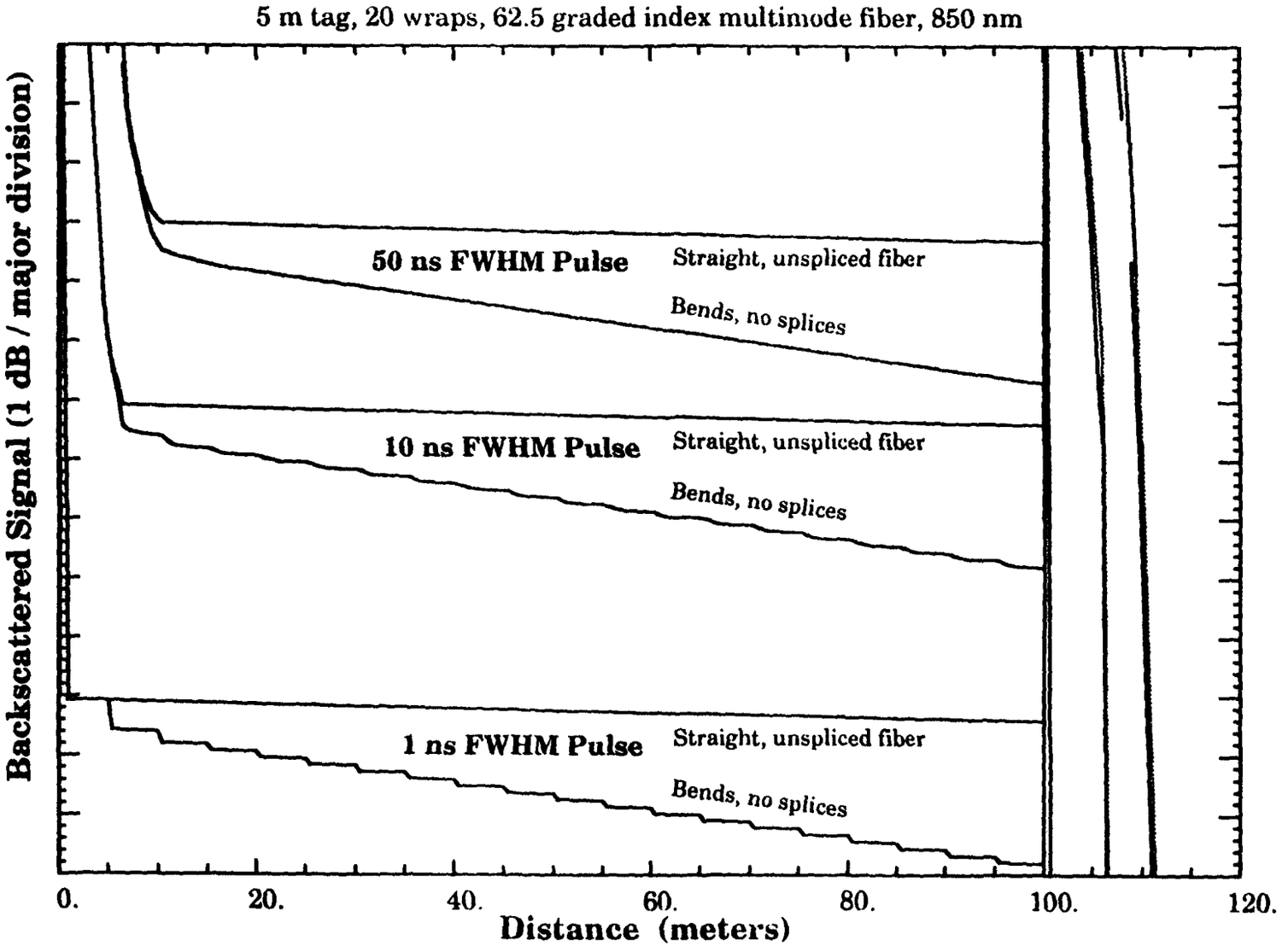

Figure E-7 OTDR trace simulation of the effect of multiple bend losses for deliberately gross individual bend losses for three different pulse widths.

Figure E-8 is a bar chart of more realistic bend losses for the actual bend radius (1 inch) used in the laboratory prototype MWG SLOTS design based on analysis of actual Antel board OTDR traces in a MWG tag loop mockup.

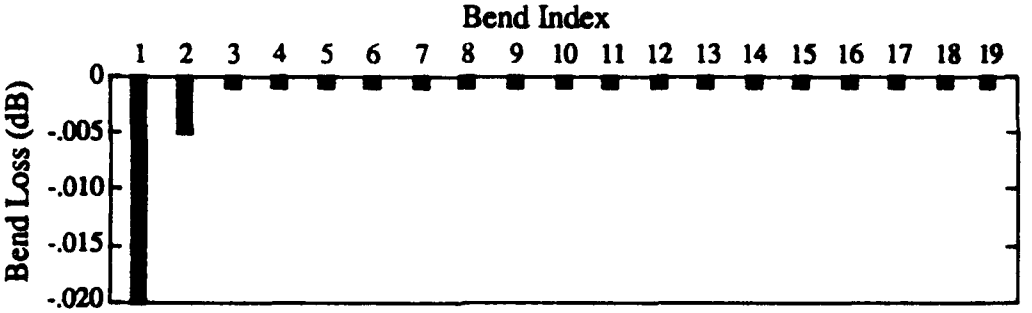

Figure E-8. More realistic bend losses used in the second round of simulations.

Figure E-9 is the histogram and associated ogive of fusion splice loss as measured by Sakamoto,[2] et. al. An ogive is a piecewise linear fit to the cumulative relative distribution function representing the data. The Sakamoto data are the only published statistical data on splice losses that has been found. Also, the splice losses in the Sakamoto distribution are large enough to be useful for displaying the cumulative effects of splices on the OTDR trace.

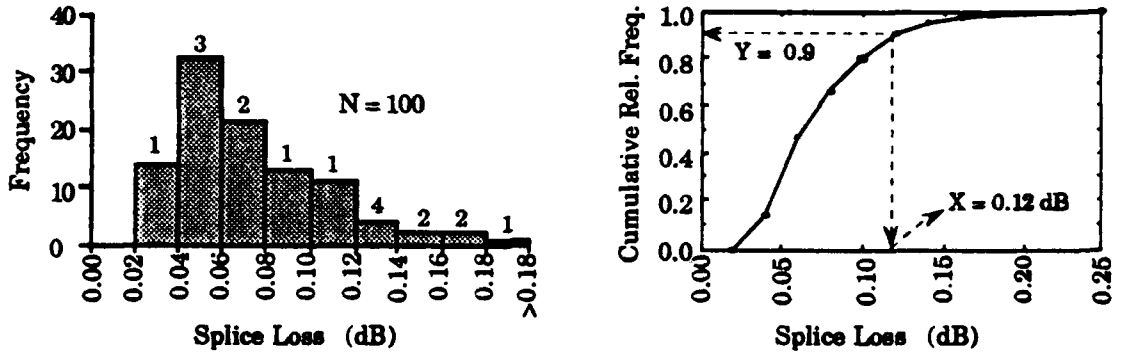

Figure E-9. The splice loss distribution measured by Sakamoto, et.al., and its associated ogive.

Figures E-10 through E-12 plot the OTDR traces predicted by equation E-12 and E-14 for three different pulse widths, using the bend losses specified in figure E-8 and inserting random loss values weighted to be consistent with the

---

[2] Sakamoto, K., T. Miyajiri, H. Kakuzen, M. Hirai, N. Uchida, "The Automatic Splicing Machine Employing Electric Arc Fusion," Proc. 4th Eur. Conf. Opt. Comm., p.296, September 1978.

Sakamoto distribution. Each trace uses the same set of splices for ease of comparison. Figure E-13 displays these traces in lower resolution on the same plot so that the relative amplitudes, resulting from differences in total backscattered power due to pulse width differences for a constant peak amplitude laser source, can be compared. The random losses were generated by drawing a random number from the uniform distribution on the interval (0,1) and "inverting" the ogive of the Sakamoto distribution to find the loss X corresponding to Y. The dashed lines in figure E-9 illustrate an example where Y = 0.9 is drawn at random from the uniform distribution and "inverted" to a splice loss of X = 0.12 dB.

Note that with the more realistic bend losses, the traces for the fiber with bends (gray lines) are nearly indistinguishable from the traces for straight fibers (solid lines). Furthermore, the traces for the fiber with splices are quite distinct from both the other trace types. These simulation results are consistent with findings for traces generated by the Antel OTDR board on actual fibers with and without bends. The overall conclusion of this work regarding the effect of bends is that *losses for bends at the tag design bending radius can be ignored in the verification procedure.*

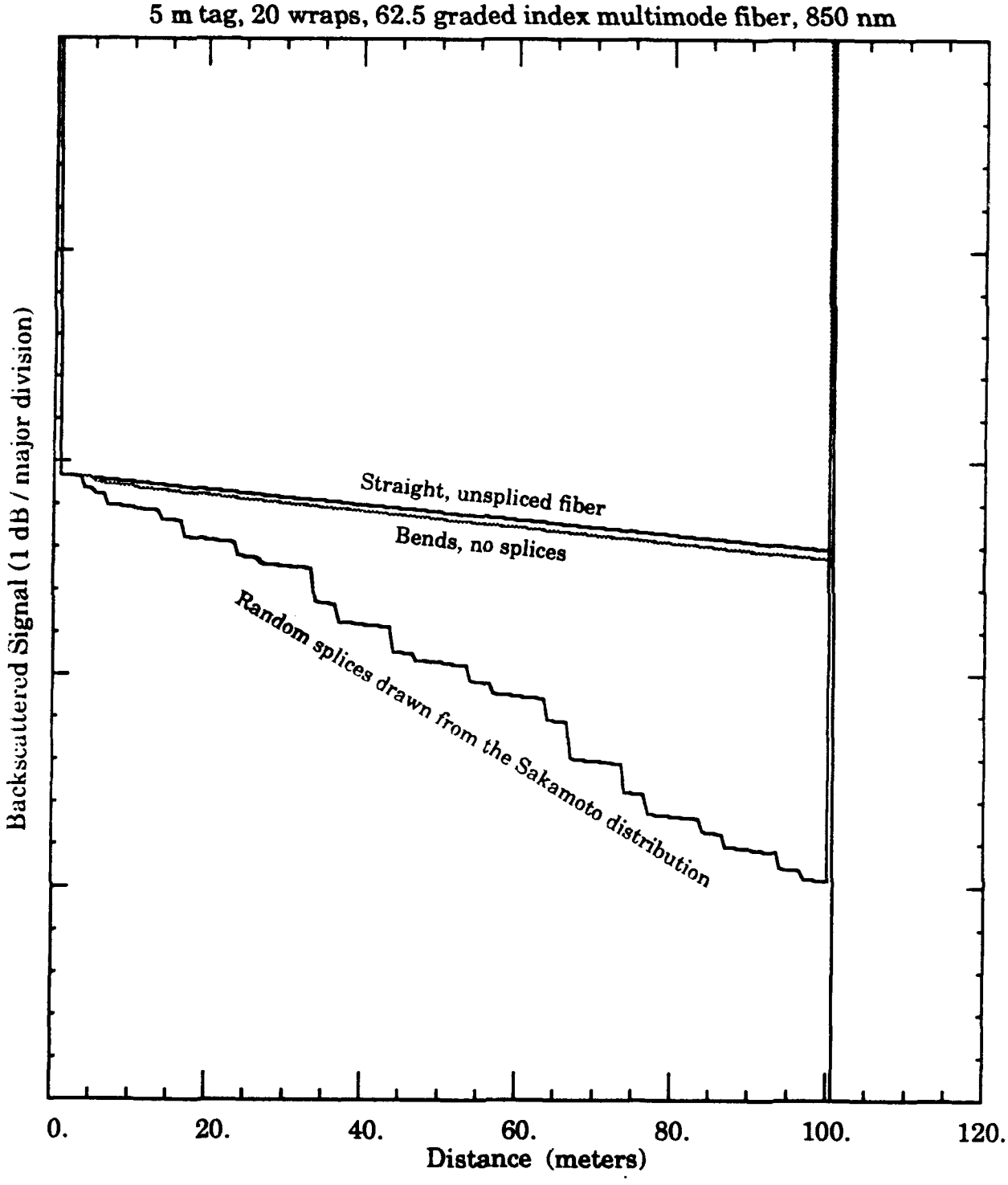

Figure E-10. OTDR trace simulation of the effect of splice losses based on the Sakamoto splice loss distribution for a 1 ns FWHM pulse width.

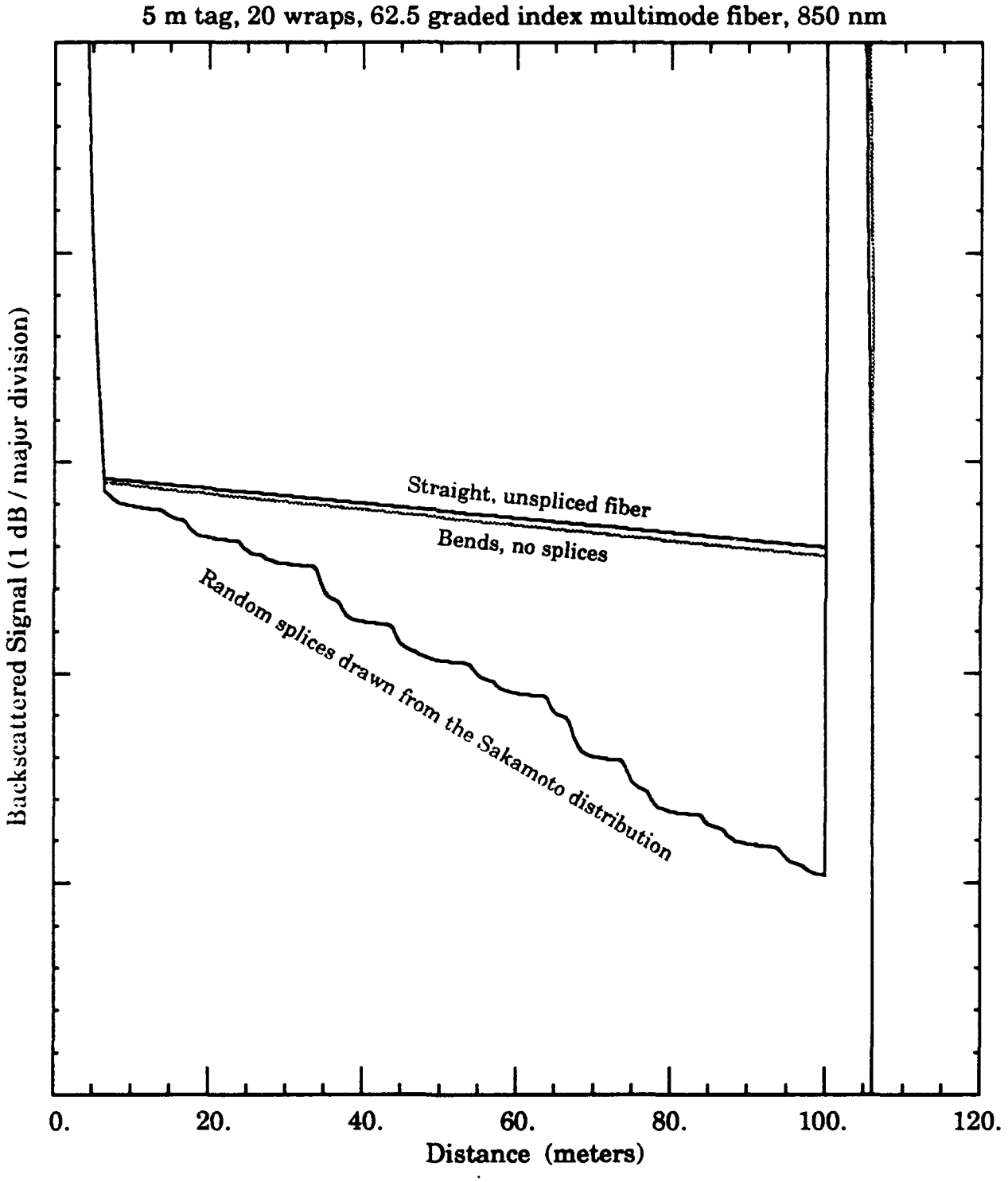

Figure E-11. OTDR trace simulation of the effect of splice losses based on the Sakamoto splice loss distribution for a 10 ns FWHM pulse width.

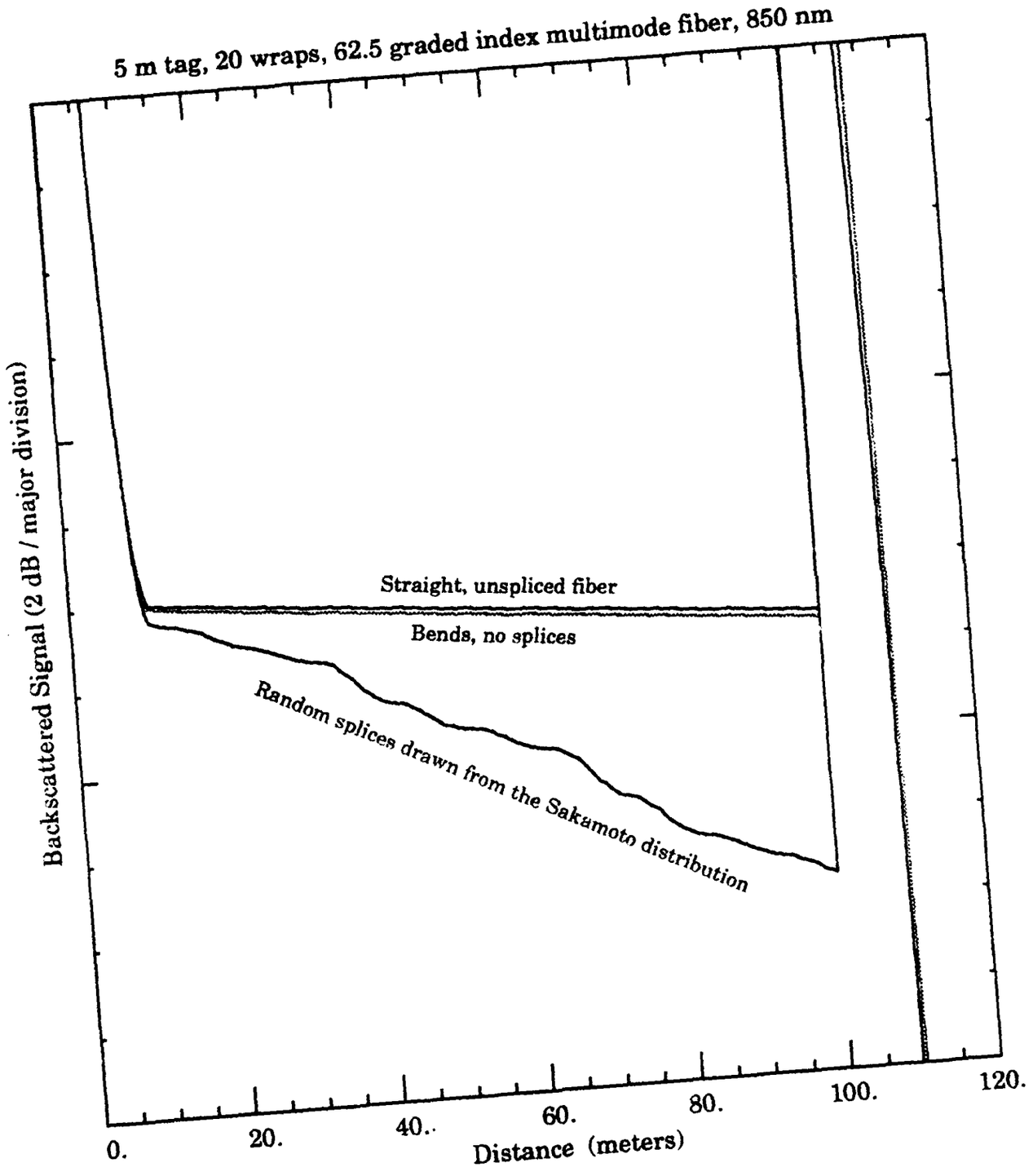

Figure E-12. OTDR trace simulation of the effect of splice losses based on the Sakamoto splice loss distribution for a 50 ns FWHM pulse width.

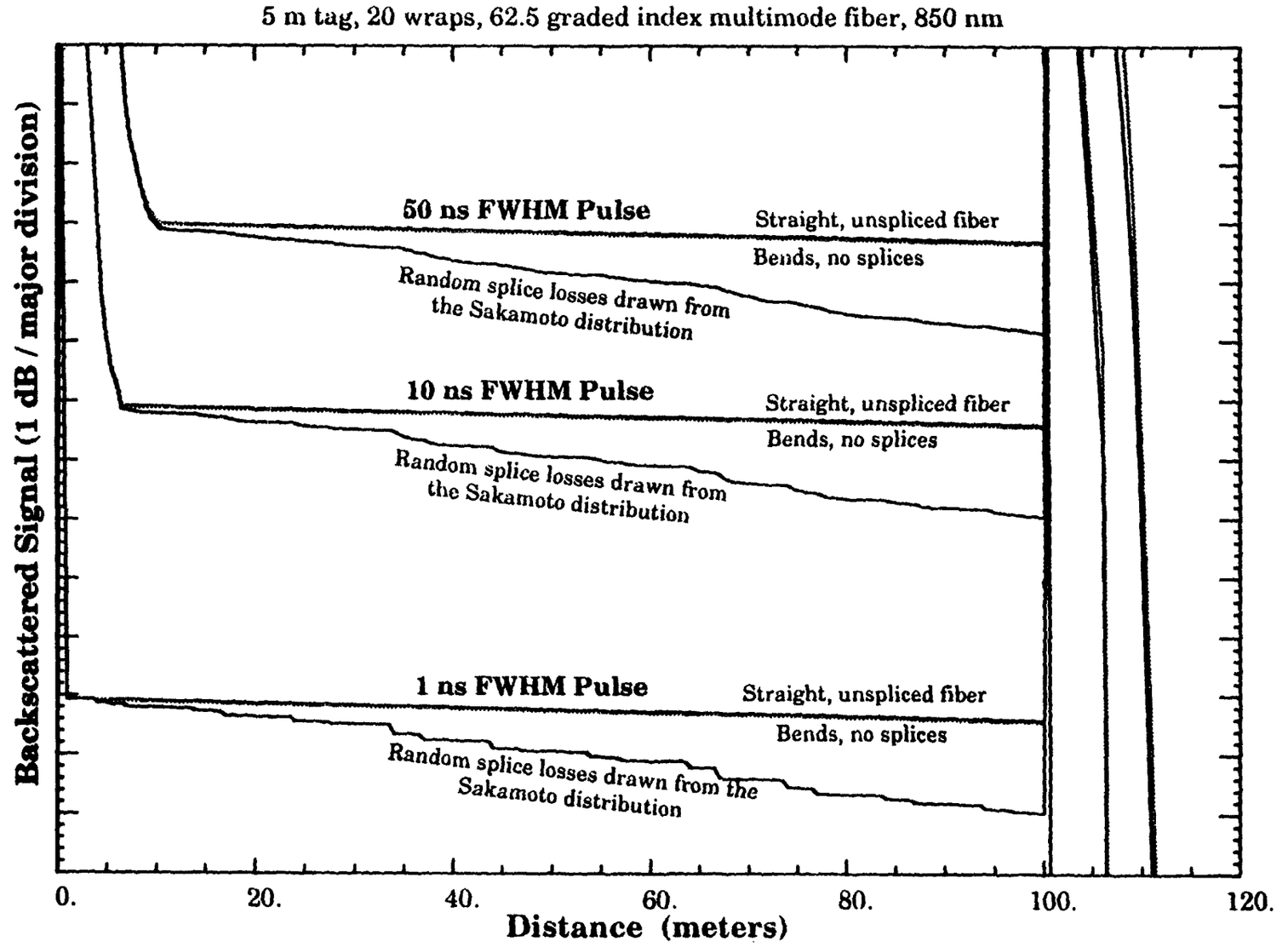

Figure E-13. OTDR trace simulation of the effect of splice losses based on the Sakamoto splice loss distribution for three different pulse widths.

The Sakamoto paper describes the quality of fusion splices achievable in 1978, but is not representative of the state of the art in fusion splicing today. Unfortunately, no recent publications of splice quality could be found. However, BDM gained access to and was able to generate numerous splices using the Fujikura FSM-20CS fusion splicer, which is arguably the finest splicing machine available. The fiber cleaving device recommended by Fujikura to obtain the highest quality results was also obtained and used. After and initial training period, twenty-two fusion splices of excellent quality were made by BDM in series at roughly 12 meter intervals on a single, 62.5/125 graded index multimode glass optical fiber. The cumulative loss on the fiber was recorded after each splice using the Antel OTDR board. These splices had typical throughput losses of about 0.02 dB or less, with the worst splice being 0.07 dB. Figure E-14 shows OTDR trace overlays from the Antel OTDR board of the optical fiber before and after splicing with the Fujikura machine. These experimental results agree qualitatively with the theoretical results presented up to this point, and demonstrate that a spliced fiber is easily distinguishable from an unspliced fiber using the Antel OTDR board with even only a few of the highest quality splices attainable.

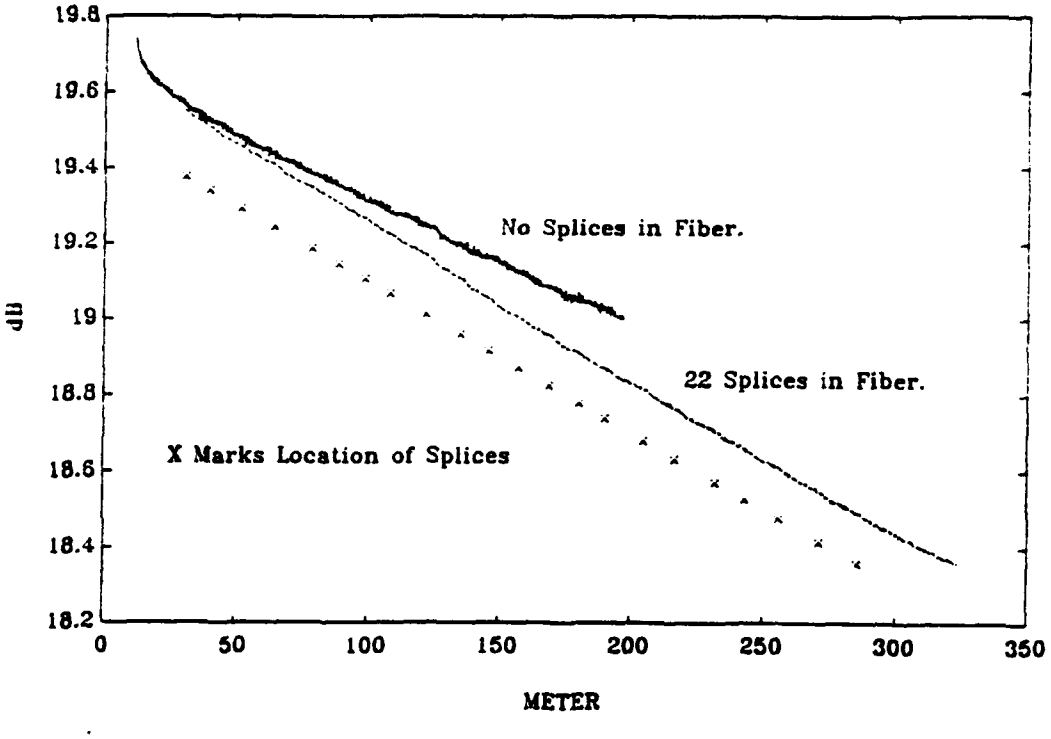

Figure E-14. Comparison of Antel OTDR traces on an optical fiber before and after splicing multiple times with the Fujikura splicing machine.

E.4 CONCLUSIONS.

A body of theory has been developed to analyze the effect of multiple splices and bends in a single optical fiber as it would be configured in the MWG SLOTS tag/seal. Simulations based on measured bend loss data show that bend losses in the MWG SLOTS design contribute negligibly to the shape of the OTDR trace. Model simulations using both demonstration and measured splice loss data show that even if losses from individual splices cannot be distinguished (i.e., the backscatter event associated with each splice is negligible *and* individual losses from each splice are below the resolution of the OTDR trace as distinguishable events), the cumulative loss from many splices results in easily recognized slope differences in the Rayleigh backscatter floor. Direct OTDR measurements on a multiply spiced fiber with splices of the the finest quality attainable corroborate the theoretical basis for MWG SLOTS tamper detectability and firmly establish confidence in the MWG SLOTS tamper detection concept.

APPENDIX F
CREATIVE TASK FINAL REPORT - INNOVATIVE TAGS

F.1 EXECUTIVE SUMMARY

The Creative Task had as its charter to survey technologies for viable tags and seals as alternatives to those being pursued at the DOE national laboratories. This report provides technical detail for most of the major elements of the Creative Task activities since the report of January 31, 1991 (Technical Report BDM/ABQ-91-0072-TR). In addition, section F.2 gives an overall, historical summary of the Creative Task activities under the BDM Tagging RDT&E contract. Two major elements of the Creative Task activities are not included here in any technical detail. These are the Secure Loop Inspectable Tag/Seal (SLITS) and the Passive Tamper Indicating Loop Seal (PTILS), which was called Secure Loop Optical Tag/Seal (SLOTS) in its early stages. These two concepts were originated under the Creative Task, but they showed such early promise that they were transitioned to development through industrial prototypes. They, together with the associated industrial prototype development of the Universal Videographic Reader (UR), are described in detail elsewhere.

The major elements of the Creative Task covered in this appendix are:

(1) The Read-at-Home Tag/Seal concept
(2) The Scanning Electromagnetic/Acoustical Measurement (SEAM) intrinsic signature concept
(3) The Magnetostrictively Interrogated Loop Seal (MILS) concept
(4) An investigation of nonlinearities and other means of enhancing tamper detection in optical fiber-based loop seals
(5) The Fourier optics intrinsic signature concept
(6) The null field concept for loop seals.

Some of these activities had reached a definitive conclusion at the time of the Creative Task stop-work order, and others were still in progress at that time. The remainder of this executive summary will briefly characterize each of these

major elements, the principal conclusions available at the time of the stop-work, and any recommendations for further work that seems promising.

The Read-at-Home tag/seal concept is basically that of dispensing with complex tag reading (for identification) and seal inspection (for tamper indication) in place at on-site inspection time. This would ease the load on the on-site inspection team by doing away with the need for complex inspection equipment and procedures. Instead, the tag/seal would be removed from the TLI during inspection, with only minimal inspection to ensure that the process of removal did not obscure possible evidence of tampering; another tag/seal would immediately be applied to replace the removed tag/seal; and finally, the removed tag/seal would be subjected to extensive inspection for identity and tamper indication in an at-home laboratory. We carried out considerable analysis and laboratory experimentation on possible designs that would meet the requirements for a read-at-home tag/seal. A composite reflective-particle (RP) signature type was identified as being most suitable, and mylar RP material was tentatively identified to solve problems found with micaceous hematite in the read-at-home application. We developed an agenda of further development work that would be required to bring this read-at-home concept to the industrial prototype stage. It is our judgment that development to the industrial prototype can be done with relatively low risk. Thus, if the read-at-home approach is determined to be desirable by the treaty verification community, we recommend that this work be continued to industrial prototype and initial operational test and evaluation (IOT&E).

The SEAM intrinsic tag concept proposes to make use of near-field properties of 3 cm microwave radiation from a small aperture to achieve near millimeter resolution of small scale variations of dielectric constant in the structure of a potential treaty limited item (TLI) as an intrinsic signature of the TLI. This SEAM probe extends several millimeters into the material of the TLI, so that the signature is not limited to just the surface region where it can be counterfeited more easily. (The use of near-field radiation at optical frequencies to achieve optical microscopy with sub-wavelength resolution has been under very active development in the last several years.) Using equipment already available in our laboratory, plus a custom-built microwave cavity with aperture and a commercial audio power amplifier and speaker as means of modulating the

separation distance between the cavity aperture and the sample under test, we assembled a bread-board SEAM system and examined several different types of laboratory mockup samples, as well as a sample of Peacekeeper motor bottle with EPM covering. The results of these early studies clearly demonstrated the capacity of the bread-board SEAM system to sense the kinds of small scale variations of dielectric constant that might be expected in the fabrication of some classes of TLI. These results are sufficiently promising that we recommend further work be pursued on the use of SEAM to read intrinsic signatures of certain classes of TLI. This further work should include the development of a laboratory prototype SEAM system. All of the electronics (except for the microwave cavity, which is relatively inexpensive) and most of the mechanical components are expected to be commercial off-the-shelf items, so that the laboratory prototype development is low risk. The further work should also include an extensive survey of potential TLIs to ascertain the degree to which unique intrinsic SEAM signatures occur, their sensitivity to field conditions (including alignment and other variations), and their difficulty of counterfeiting or other spoofing.

The MILS loop concept makes use of the fact that in wires (called "a-wires") of certain amorphous magnetostrictive materials there are only a few large ferromagnetic domains. Magnetostrictive traveling waves, associated with the traveling wall of reversal between magnetic domains, can be induced in these wires by applying a magnetic field (say, by an auxiliary winding of ordinary wire around the length of the a-wire) and triggering the magnetostrictive wave from one end (the transmitting end). If the a-wire is undisturbed from its pristine condition, then the magnetostrictive wave induces a large pulse in a pickup coil at the other end (the receiving end) by the so-called "Barkhausen coupling," after a characteristic delay following initiation of the wave at the first end. On the other hand, if the a-wire has been altered by splicing or other significant damage, the magnetic domain wall propagation ceases entirely at the point of damage, and no signal is induced at the pickup coil at the receiving end. Thus, the MILS loop is generically a passive tamper-indicating loop seal. We carried out laboratory experiments that demonstrated the magnetostrictive inspection of a-wires in both pristine and spliced form. We were not able to splice the a-wires so that they could pass the magnetostrictive inspection after splicing. These results show that

MILS has considerable promise, and we recommend that it be considered for further development.

The study of nonlinearities and other means of enhancing tamper detection in optical fiber-based loop seals began as an investigation into whether nonlinearity in optical fiber materials might be exploitable as a means of enhancing splice detection in the PTILS/SLOTS system (i.e., inspecting a fiber optic loop with an optical time domain reflectometer, OTDR), in case the state of art of fiber splicing should advance to the point that detectability of splices might fall below the capability of usual OTDR reading. Analysis and a survey of available optical fiber materials concluded that there are presently no commercially available optical fiber materials having large enough nonlinear properties that nonlinearity effects could be detected with field-usable OTDR instruments. The survey of optical materials did reveal several promising directions for further work. First, we became aware of some specialty optical fiber being developed at Pacific Northwest Laboratory which has high promise for tamper resistance and detection. We strongly recommend further development of this material for use in a PTILS system in order to evaluate it as a potential alternative to the polymer (PMMA) in the present PTILS design. (This material is not known to have significant nonlinearity.) Second, three other lines of investigation were identified that have some promise, and should be pursued further to see whether they may be applicable to treaty verification. The first of these is the recent invention of optical materials with very high nonlinearities. Very high concentration erbium-doped silica fiber has been developed for use in optical fiber laser amplifiers, and this material is likely to be available for evaluation in a PTILS system soon. In addition, CuCl "quantum dot" doped glass material has been developed recently which has the highest known nonlinearity so far. It has not yet been prepared in optical fiber form, but if it can be prepared in fiber form, it should be evaluated for possible PTILS application. The second line of investigation identified is that of using a twin-core fiber in place of the present single-core fiber of PTILS. With twin-core fiber, an adversary would have a much more difficult task in creating undetectable splices, because of difficulties in alignment of both cores, and in addition, there is the possibility of exploiting interference between light passed through the two cores to detect sub-micron discrepancies in length caused by splicing. The third line of investigation is that of exploiting mode-conversion by splices as a means of detecting splices.

The Fourier optics intrinsic tag concept proposed to make use of interference in the image of a portion of a TLI when illuminated with coherent light as an intrinsic signature for the TLI. Proof-of-concept measurements, however, revealed that the proposed signature was dominated by purely surface features of the target area. The conclusion, therefore, is that this concept is not viable for tagging applications, because, on the one hand, limitation of the signature to strictly the surface makes the signature too vulnerable to counterfeiting, and, on the other hand, localization to the surface also makes the signature too vulnerable to environmental degradation.

Finally, another novel concept for loop seals arose during the work that led to MILS. The null-field loop concept uses a bundle of many (small) wires into a cable used as a loop about the TLI. With certain configurations of currents driven through the individual wires during inspection, the resulting magnetic field produced around the cable by the currents should be very small; if a splice is made without sufficient care to match all wires exactly across the splice, then the magnetic field produced at inspection can exceed the installed low field value and thus produce evidence of a tamper. Enough analysis was done on this task to indicate that it is possible to detect such splices. However, many questions remain to be resolved, particularly on means to inhibit proper reconnection of individual wires in a splice. It would be useful to analyze this concept further.

F.2 SUMMARY OF INNOVATIVE TAGS ACTIVITIES.

The "Creative Task" was performed under the Innovative Tags Technical Instructions (TI90-10, July 17, 1990 and its amendments and TI91-15, March 1, 1991 and its replacement TI91-15, May 7, 1991). The purpose of the Creative Task was to survey technologies for viable tags and seals as alternatives to those being pursued in the DOE national laboratories. These survey efforts included invention of tagging concepts, analysis of the physical principles involved, and system engineering feasibility analysis. BDM staff from a variety of scientific and engineering disciplines were used to create concepts and perform internal Red Teaming of the concepts. Many ideas were considered and assessed. Few survived the internal BDM Red Teaming process.

The innovative tags work began with the authorization of TI90-10. The innovative tags work was in a creative mode exclusively until after a briefing of Col. Davie and others from the DNA/OPAC office on January 16, 1991. There was some proof-of-concept laboratory work, but no formal prototype development during this first phase of the innovative tags work. Most of the very early concepts died during the laboratory studies. This early work was documented to DNA in an Initial Report on Innovative Tags in August and Interim Reports in October 1990 and January 1991. The schedule for the Innovative Tags work is shown in figure F-1.

Toward the end of the Fall 1990, two loop tag/seal concepts emerged as primary candidates for prototype development. These were the Secure Loop Inspectable Tag/Seal (SLITS) and the Secure Loop Optical Tag/Seal (SLOTS). Much later SLOTS was renamed as the Passive Tamper Indicating Loop Seal (PTILS). Both SLITS and PTILS were developed through laboratory prototype and then industrial prototype stages. SLITS was Red Teamed by Idaho National Engineering Laboratories. The industrial prototype designs for both SLITS and PTILS are depicted in figures F-2 and F-3.

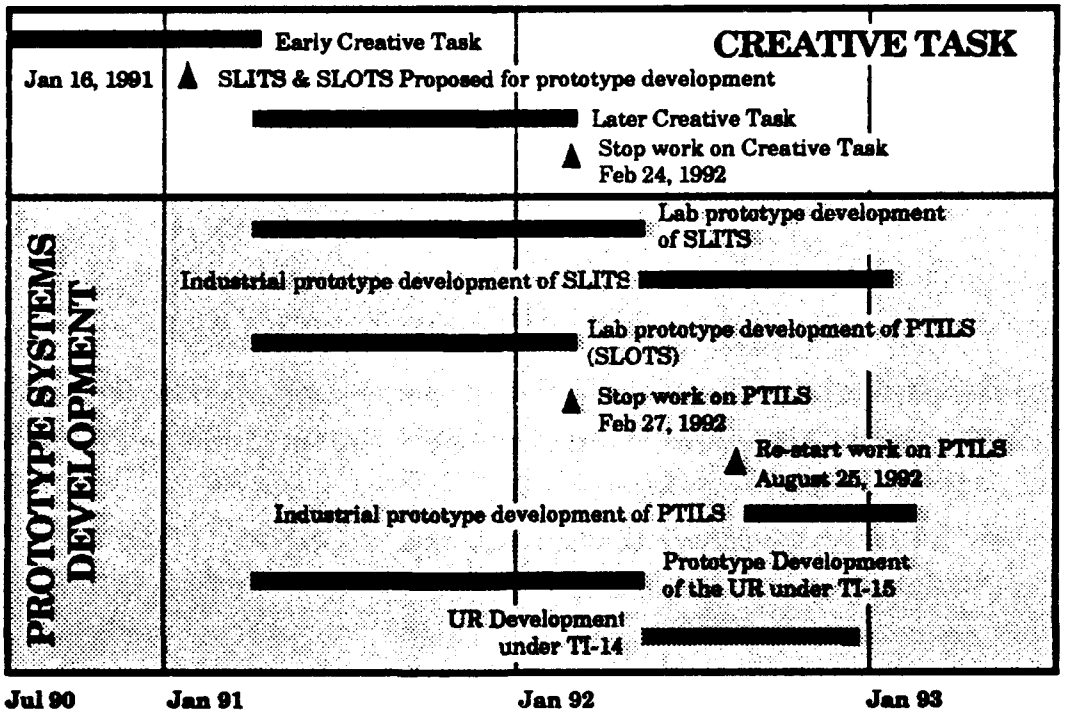

Figure F-1. BDM innovative tags schedule.

Following the issuance of TI91-15 in March 1991 for the laboratory prototype developments of SLITS and SLOTS, the Creative Task was also continued in the pursuit of other innovative tag or seal concepts. Additional concepts were created and proof-of-concept analysis and laboratory measurements were performed for some of them. Many status briefings were given on the Creative Task, particularly to Lt.Col. John Sharples, COTR for Tagging. The Creative Task efforts ended with a stop work instruction on February 24, 1992.

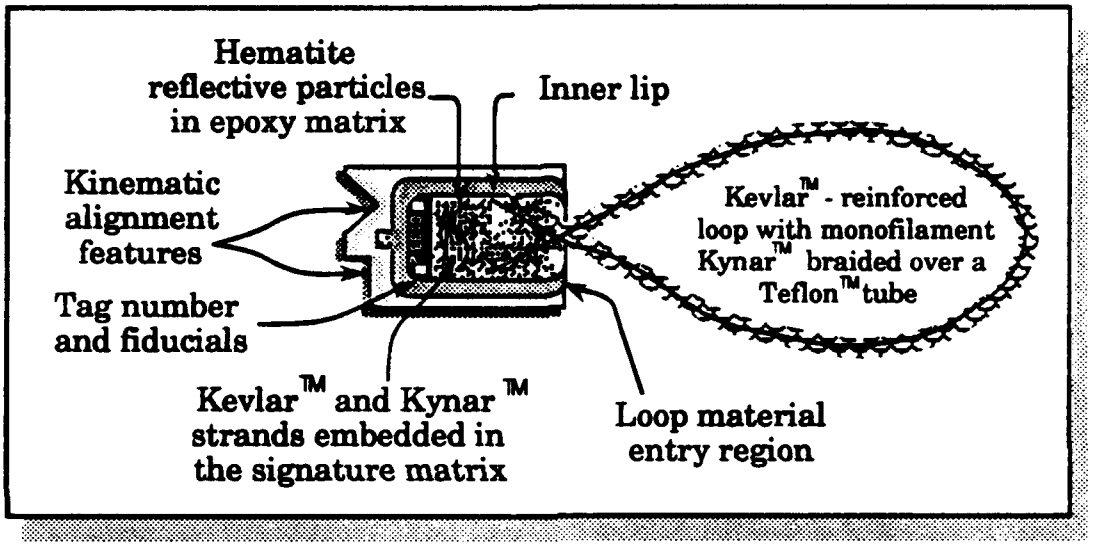

Figure F-2. Industrial prototype SLITS design.

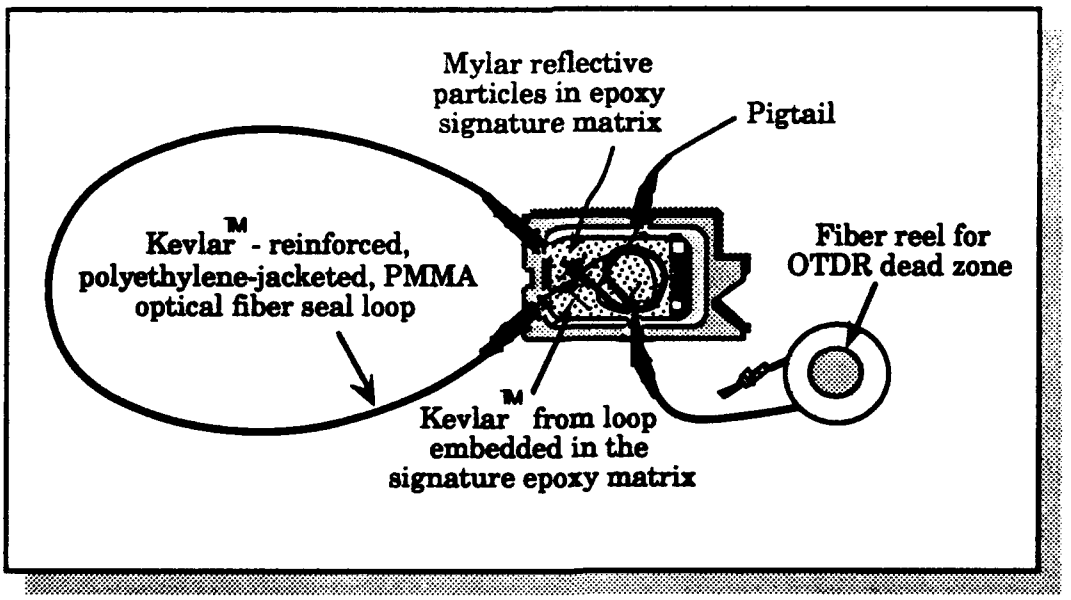

Figure F-3. Industrial prototype PTILS design.

F.3 CHANGES IN VERIFICATION REQUIREMENTS.

One reason that so few Creative Task concepts survived for prototype development was the set of constraints imposed by the bilateral START Treaty. Under the START ground rules, relatively few, very high value assets of a well-known adversary were being considered for tagging for arms control verification. Tagging and inspection of operational, deployed systems were possible. Tags could be fielded for years with few inspections per year. Therefore, the demands on tags for this purpose were severe. Due to relations that existed between the U.S. and the Soviet Union at the time, there were serious operational constraints for the inspection procedures and application of tags. Both the U.S. and the USSR wanted nonintrusive verification. These START constraints indicated the following requirements:

- very demanding signature requirements
  - uniqueness, non-counterfeitability, repeatability
  - environmental robustness
- strong tamper detectability
  - positive determination on-site and low probability of false call
- limitations on data collection capability
  - only data necessary for verification could be recorded
  - all data had to be shared, including tag construction
  - no active (powered) tags or seals in the field
  - minimal computer capability in the field
- operational effectiveness of the tagged item should not be impaired

These constraints eliminated from consideration any active system, such as electronic identification devices or active fiber optic systems. Designs that might be perceived as an antenna were of concern to the National Security Agency. In addition to these START-driven constraints, BDM imposed on its assessments operational simplicity and use of as much commercial-off-the-shelf (COTS) implementation as possible.

In the time frame since the inception of the Tagging contract, the scenarios for arms control verification changed. A "New World Order" exists. There is no USSR and, in its place, there are unstable CIS economies. There is an

unstable third world and multilateral participation in arms control negotiations. For verification of treaties and agreements other than START (e.g., CWC, BDA, non-proliferation, dismantlement and destruction of non-deployed systems), many of the START constraints are relaxed. In general, a much larger number of individually less valuable assets must be controlled. Shorter-term tag or seal deployment may be required. Operational deployment of tags and seals in more severe environments is possible. Requirements different from those for START become more important. Examples of the requirements in the New World Order include:

- rapid installation of tags and seals
- rapid readings
- smaller, more lightweight reading equipment
- very low cost, operationally simple technologies for tags, seals, and reading systems

Had these requirements been recognized earlier, the suite of tags and seals pursued under the Creative Task effort may have been very different. Many radically new concepts were proposed by BDM internally in the waning months of the contract that were not formally part of the Creative Task effort (since the Creative Task work had ended a year earlier), but which would be responsive to the new requirements.

F.4 RESULTS OF THE CREATIVE TASK.

The outcomes of the Innovative Tags work include three operational industrial prototype systems and several technologies that have shown high potential for positive proof-of-concept. The three industrial prototype systems and their status are:

- SLITS - Industrial Prototype available
  - Red Teamed: adversarial attacks easily detected upon inspection
  - very low cost using injection-molded joints: (< $10 each, including loop material, joint, protective pouch, and signature material)
  - loop materials are commercial-off-the-shelf (COTS)
  - simple modifications would improve operational ease

- PTILS - Industrial Prototype available
  - provides robust tamper resistance and objective splice detection
  - relatively low cost: (< $100 each)
  - loop material is COTS
  - needs further environmental and operational testing
  - needs Red Teaming

- UR - Industrial Prototype available
  - can read any signature that can be recorded with videographic imaging (RPT, SLITS, PTILS, etc.)
  - microcomputer is interchangeable: laptop computer or ruggedized computer versions can be assembled
  - implements a software "blinker" feature for tamper detection
  - supports a video microscope feature for documentation

The three industrial prototype systems are covered in section 4 of the Tagging RDT&E Draft Final Report, BDM/ABQ-93-0012-TR, and will not be discussed further here.

Other outcomes of the Creative Task included the invention and assessment of additional concepts that hold promise as tags. These concepts were assessed late in the Creative Task. There was not time on the Tagging contract before the stop work for the Creative Task to complete all of the assessments nor to do any prototype development of the potentially winning concepts. The promising concepts include:

- the Scanning Electromagnetic/Acoustic Measurement (SEAM), an intrinsic tag concept;
- the Magnetostrictively Interrogated Loop Seal (MILS), a candidate loop technology that may provide very robust, objective "binary" tamper detection in the loop;
- read-at-home tag/seals, tags that do not require the use of a reader in the field at all, but offer very robust signature repeatability and tamper detection;
- nonlinear and other specialty optical fibers.

All of these promising technologies are reported in more detail in this Creative Task Report.

Many other concepts were considered and assessed under the Creative Task work. These are listed in figure F-4 and reasons for their rejection or "shelving" for later consideration are also listed. Items covered before December 30, 1990, are discussed in the January 31, 1991, report (BDM/ABQ-91-0072-TR). Some items covered since then are discussed in the present report.

Concept	Type of Tag	Assessment
• Optical Interference and Diffraction Techniques - holography - Fourier optics imaging - diffraction grating strip loop	Intrinsic or Adhered	These techniques are so sensitive that they do not offer stable signatures because of contaminants and material changes.
• Acoustic Interference	Loop	Unstable due to temperature and pressure variations.
• Differential Pressure tubes	Loop	Cannot hold the differential pressure reliably for years.
• Binary chemical - "scratch and sniff"	Loop or Adhered	Technology not COTS. Unstable at high temperature.
• Special ropes and inspection with a fiberscope	Loop	20 micron resolution available. 10 meter inspection would require unreasonable time.
• Nonlinear Optical Fibers	Loop	Requires more optical power to drive the nonlinear effects than can be obtained from a laser diode
• Low-loss Coaxial Cables	Loop	Measurements showed that tamper detection was indecisive.
• Early Consideration of Electronic Identification Devices (EIDs)	Adhered or Loop	Concerns of intelligence agencies eliminated EIDs from BDM consideration for START.
• Smart skins	Adhered or Loop	Ordinarily an active (powered) system; therefore, unacceptable for START.
• Tamper tape	Adhered	None with unique signature available in this COTS technology; therefore, unacceptable for START.
• Hollow fiber optic cables	Loop	Needs a long wavelength, laser light source that is difficult to obtain in any fieldable configuration.
• Resistance Network Cables	Loop	Inadequate sensitivity to solder splicing.
• Other signatures	NA	None found that had any advantage over RP.

Figure F-4. List of other concepts assessed.

F.5 OVERVIEW OF THIS APPENDIX.

In section F.6, we will discuss the read-at-home tags. The basic concept of a tag that would require no reader in the field was proposed by Dr. Buddy Swingle who was in OUSD(A) at the time. It must be possible with a read-at-home tag to create the signature temporarily before taking the tag to the field for deployment, and then recreate the same signature permanently in the field. The tag is then routinely or randomly removed for identification and tamper detection in a home laboratory. Section F.12 includes a discussion of the Scanning Electromagnetic/ Acoustic Measurement (SEAM) intrinsic tag concept. SEAM could, for example, be used to obtain a unique signature from a composite material skin of a missile. The Magnetostrictively Interrogated Loop Seal (MILS) technology is discussed in section F.17. MILS offers a strong potential of providing definitive, objective detection of cut-and-splice loop tampering with simple instrumentation in the field. An analysis of nonlinear and other specialty optical fibers is provided in section F.22. These fibers were considered for loop tags and seals as candidates that could provide great difficulty to an adversary who would covertly cut-and-splice a loop tag/seal.

Section F.26 includes a discussion of an attempt to obtain an intrinsic signature using Fourier optical techniques. As with other technologies using visible light wavelengths, the Fourier optics technology was determined to have severe problems with stable, repeatable signatures. Also the penetration of composite materials like fiberglass-epoxy was limited and light was multiple-scattered inside the material in ways that introduced much confusion into the reflected signal. A preliminary null field loop concept is discussed in section F.31. Section F.34 includes a discussion of lessons learned and conclusions from the Creative Task work.

F.6 READ-AT-HOME TAG/SEALS.

The concept of a read-at-home tag/seal or a tag/seal that required no reader in the field was first suggested by Dr. Buddy Swingle of OUSD(A). This tag/seal would be routinely removed and replaced during a verification inspection. Therefore, its cost must be small. This concept offers the following benefits:

(1) The highest confidence of any loop tag/seal (because of very high technology capability to detect tampering in a well-equipped, at-home laboratory)
(2) Quick and easy inspection procedures
(3) Minimal equipment and data transport
(4) Compatibility with the Universal videographic Reader system
(5) Long-term reliability at very low cost.

The read-at-home tag seal was conceived as a system that could be deployed in the field without requiring a field reader, thus reducing logistics requirements. The read-at-home tag developed here is based on a composite reflective particle signature, where some percentage of the composite signature resides on each half of the tag. Only preliminary work on the read-at-home concept was performed prior to the stop work on February 24, 1992.

Several experiments were performed to study the properties of a composite tag and a limited number of tags were fabricated. The best tag was fabricated using a polycarbonate SLITS joint block for the two halves of the tag. Kevlar rope was used for the loop for initial tests due to its ease of use.

F.7 SYSTEM DESCRIPTION.

The read-at-home tag concept is based on a reflective particle (RP) signature that is fabricated and read in a controlled laboratory environment, and installed in the field with no need to read the tag in the field. This reduces the amount of hardware required in the field, and reduces the time required to install the tag.

BDM has considered several different types of read-at-home tags. They may be broken into two general families; the composite signature tags, and the dual independent signature tags. Both families share the common general feature of having a re-entrant topology of the mating surfaces between the two halves. The re-entrant surface increases tag security by avoiding a single separation plane that might be cut to separate the two halves in a tamper attempt. For the family of composite tags, the RP signature is formed by the overlay of the two tag halves, with each half of the tag contributing some percentage of the overall signature. Ideally, each half of the tag would contribute some portion to the composite signature. The optimum contribution from each half of the tag most likely lies within the range from 50/50% to 20/80%, although further investigation is required to determine the ideal mix. This type of tag requires that the two halves of the tag have some mechanism for ensuring that the alignment of the two halves is repeatable so that the two halves have the same alignment in the field after they are bonded that they had in the laboratory where they were temporarily assembled for the initial reading. The family of dual independent signature tags employs independent signatures formed in each half of the seal block. Each half of the seal block has complementary mating surfaces with multiple metal film layers between the seal block halves to detect any tampering. The advantage of this type of tag is that precise alignment of the two seal block halves is not required. An example of this concept is shown in figure F-5.

Development of the composite signature read-at-home tag system was pursued since it was felt that it was both a more secure system and potentially a less expensive tag than the dual independent signature concept. There are several different configurations for a composite read-at-home tag. The "Popsicle Tag" concept is shown in figure F-6. It utilizes a female base with an RP matrix located as shown, and a male plug with RP matrix that slips inside the base. A kinematic alignment system is incorporated in the mating surfaces of the two halves of the tag to ensure repeatable alignment of the composite RP signature. Implementation of another concept of a composite read-at-home tag is shown in figure F-7. The kinematic alignment of this tag uses three alignment hemispheres with mating cavities. A larger hemisphere is located in the center of the tag to eliminate a straight cutting plane through the center of the tag. The kinematic alignment features also have the effect of making the mating surface re-entrant as desired. The parts of the RP signature are formed on the surfaces of

each half of the seal block. A read-at-home tag made and studied with a SLITS joint is shown in figure F-8.

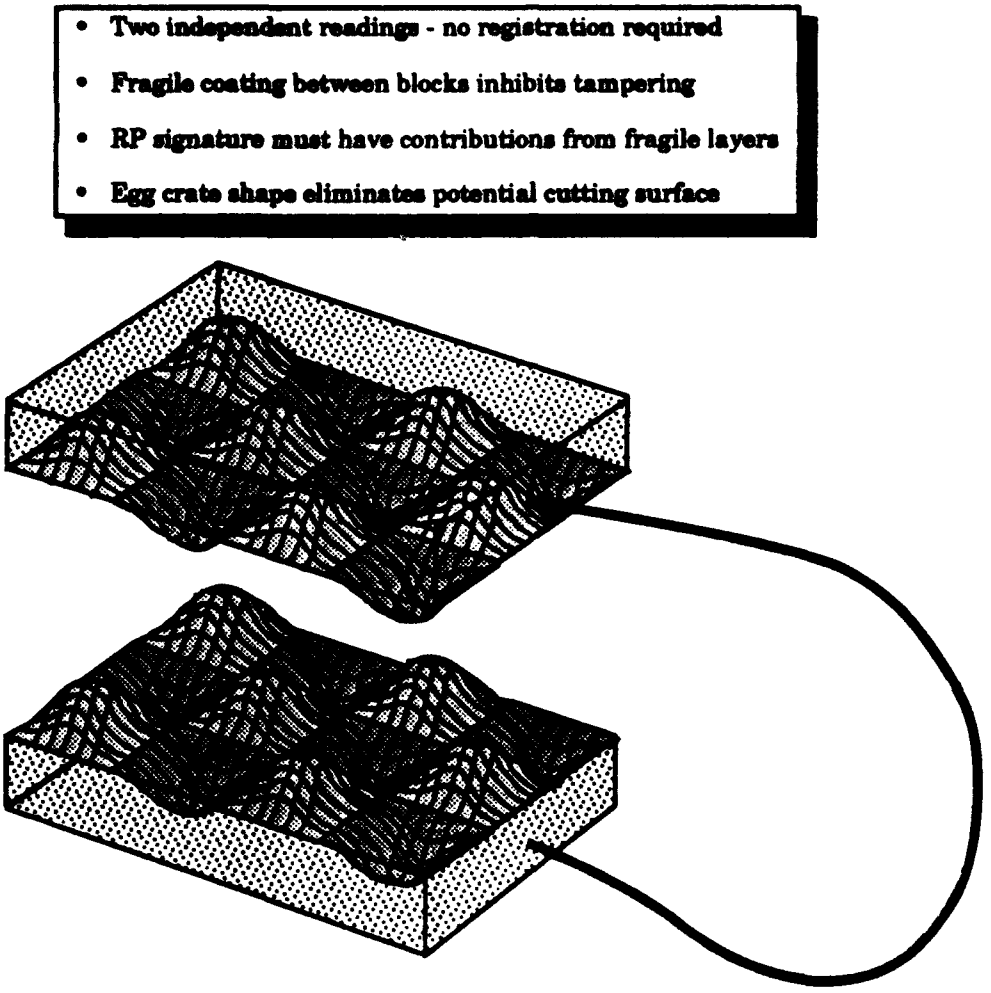

Figure F-5. Dual independent signature egg crate read-at-home tag/seal.

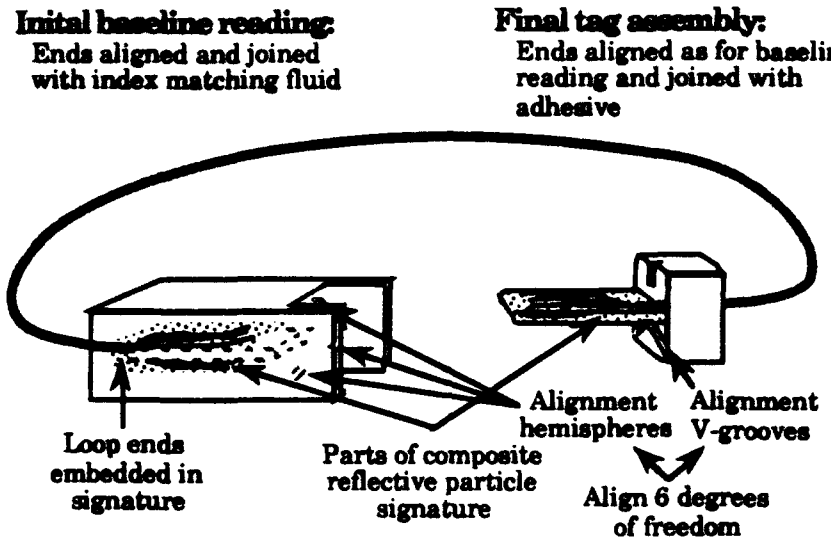

Figure F-6. Composite signature popsicle read-at-home tag/seal.

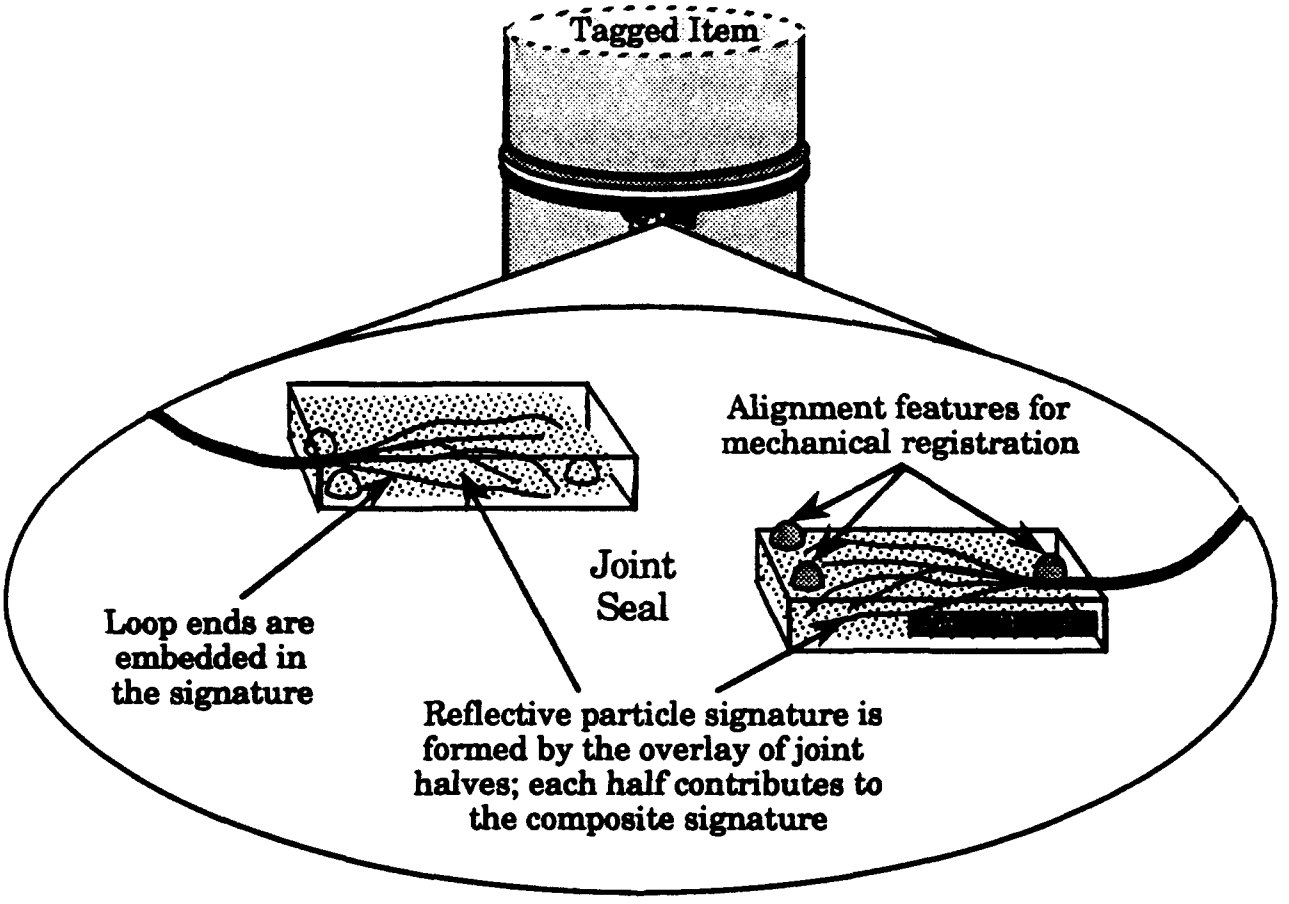

Figure F-7. Application of a read-at-home tag/seal.

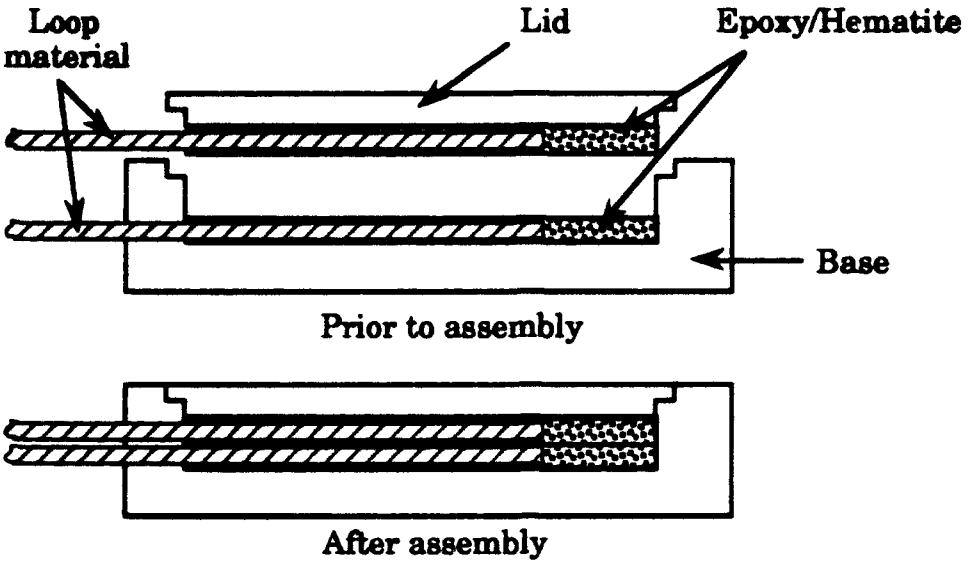

Figure F-8. SLITS modified as a read-at-home tag/seal.

The tag shown in figure F-8 utilizes the SLITS joint block, and relies on a tight fit between the lid and base to ensure repeatable registration of the composite signature. Since the making of re-entrant mating surfaces seems rather straightforward, this study concentrated only on the more pressing question of making approximately equal contributions to the composite signature from the top and bottom parts of the tag block.

F.8 PROCESS EMPLOYED.

The most successful read-at-home tag that was fabricated in the lab utilized a SLITS seal block. The process that was used to fabricate the laboratory prototype is essentially the same as the process that would be used in production, except that assembly jigs or molds would be used to eliminate some of the steps. The fabrication process that was used in the laboratory is as follows:

(1) Lay one end of the rope loop in the base.
(2) Prepare a mixture of epoxy and hematite and pour this mixture into the bottom of the base to encapsulate the end of the rope.
(3) Lay a 0.030 inch thick Teflon shim on top of the epoxy-hematite mixture and press the lid into the base. The Teflon shim provides a flat surface to the epoxy mixture and also prevents the lid from sticking to the epoxy. The shim also provides room for the epoxy mixture that will be bonded to the lid, and for the adhesive that will be

used to bond the top and bottom epoxy-hematite tags. To properly align the hematite crystals for maximum reflection, invert the base so that the planar surfaces of the hematite will tend to settle toward the Teflon shim.

(4) After the epoxy is cured, remove the lid and the Teflon shim from the base.

(5) Place a 0.005 inch thick Teflon shim into the base, and apply a mold release agent to the inner portions of the base. The Teflon shim will provide room for the adhesive used to bond the top and bottom parts.

(6) Lay the other end of the rope loop in the base on top of the Teflon.

(7) Mix an additional batch of epoxy and hematite and pour it into the base as before.

(8) Press the lid into the base and cure the epoxy.

(9) Remove the lid from the base and remove the Teflon sheet. The tag is now complete, except for reading the signature.

The deployment process is as follows:

(1) Assemble the read-at-home tag in the laboratory using a non-curing non-adhesive substance with index-matching optical properties similar to the adhesive that will be used to bond the tag in the field.

(2) Place the tag into the reader to record its signature.

(3) Remove the tag from the reader, clean all traces of the index matching material from the tag, and transport to the field.

(4) Assemble the tag in the specified location using adhesive. No reading is required.

(5) To verify that no tampering has occurred, it is necessary to remove the read-at-home tag from the item and replace it with another read-at-home tag. The removed read-at-home tag is returned to the laboratory and read with the reader, and its signature is compared with the original signature.

F.9 DESIGN EVOLUTION.

The purpose of the read-at-home tag is to provide an easily deployable high security tag. Design constraints for the read-at-home tag are as follows:

(1) The overall dimensions of the completed system should be within the allowable envelope of the reader jig.
(2) The joint between the base and the lid should be configured so that it would be impossible to split the base and lid apart on a single plane and not intersect either the base, lid, or either RP portion of the signature.
(3) The composite RP material should be located midway between the top of the lid and the bottom of the base. This will allow the signature to be read from the top and the bottom.
(4) The composite thickness of the RP material should be relatively close to 0.10" thick to provide a good 3-D RP signature without becoming obscured by too thick a layer of epoxy and hematite.
(5) Since the read-at-home tag will not be read in the field, a method of repeatably aligning the top and bottom RP must be incorporated into the read-at-home tag design to ensure that the initial composite RP signature is the same as the signature that would be read in the field after the read-at-home tag is installed and bonded.

A series of experiments were performed to determine how to develop a repeatable composite RP signature. The results of these experiments are reported in this section.

The first read-at-home tag utilized a kinematic alignment approach, as shown in figure F-7. Alignment hemispheres were imbedded in one half of the tag and matching depressions were located in the other half of the tag. A layer of hematite/epoxy mixture was applied to each half of the tag with a loop end embedded in the epoxy, and the two halves were pressed together with a mold release between the two halves. After the epoxy was cured, the two halves were separated and cleaned.

The results of this trial were not acceptable for a variety of reasons. The first and probably most important issue was that the contribution to the composite RP signature was dominated by the top half of the tag. This was due to the density of the hematite within the epoxy, the positioning of the loop ends within the hematite/epoxy mix that partially obscured the lower RP signature, and the

position of the alignment spheres. Also, the mold release used between the two halves of the tag reduced the optical clarity of the surface finish.

Another issue that became apparent from this test was that the hematite crystals tend to settle to the bottom of the epoxy with their flat faces aligning with the surface in contact with the epoxy. The result is that there are more reflective planes aligned with the bottom surface, as shown in figure F-9, than toward the top surface.

To determine a more appropriate method of generating a composite RP signature, a series of experiments were performed to study these effects and the effects of using other reflective materials.

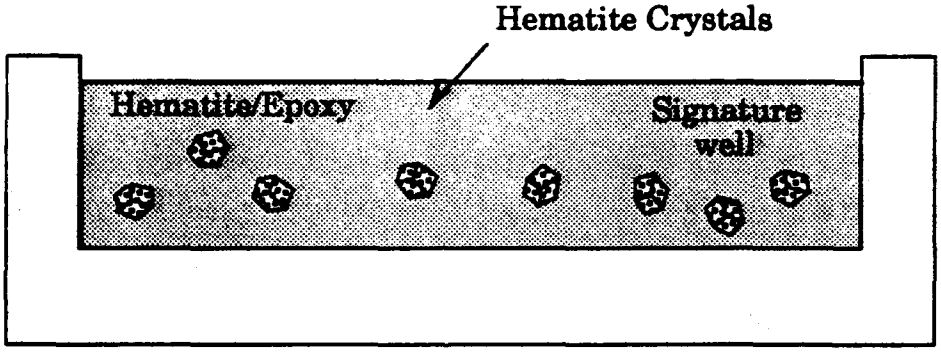

Figure F-9. Distribution of reflective hematite particles in signature.

A well was developed to facilitate the fabrication of RP test pieces. Test pieces were fabricated with several different densities of hematite and epoxy, and thin aluminum oxide film coated mylar (glitter) and epoxy. A jig consisting of two sheets of 1/4" plastic sheet was developed to allow the test pieces to be easily handled and manipulated. The results from these experiments are as follows:

(1) To improve the RP contribution from both halves of the tag, it is desirable to form each half of the tag so that the hematite particles are oriented with their flat reflective faces all facing the same direction. Since the hematite particles tend to sink in the epoxy and align their flat reflective faces with the bottom surface, best results were obtained when the tags were oriented during the curing process with the "active" face toward the bottom.

(2) The thin film coated mylar remains well suspended and more randomly oriented in the epoxy during the curing process. This allows more flexibility during fabrication since it is not necessary to take special actions to align the RP material. The mylar RP provides very bright reflections.

Based on these experiments, additional tags were fabricated using a SLITS type joint block. The SLITS body relies on a tight fit between the lid and base to provide repeatable registration between the upper and lower RP tags. The procedure for fabricating a SLITS-type read-at-home tag was listed earlier.

The initial correlation (in the hematite-loaded RP tag) using the correlation algorithm for the tag was 90. On taking the tag apart and reassembling it, the correlation decreased slightly from the previous reading, and after four successive disassemble/reassemble cycles it had dropped to 85. Since the tag would be disassembled and reassembled only once during standard practice, the correlation should remain well within acceptable standards. If the hematite-loaded lid is placed in a clear (no hematite) polycarbonate base, the correlation of just the lid drops to 70-75, showing that a significant portion of the composite signature is due to the base portion. A correlation score of 65 or more is passing for read-in-the field RP tags, so this high correlation for half a tag might be worrisome even for read-at-home tags. However, the mylar-loaded tags show only a correlation score of about 50 for similar half-tag experiments. This is another demonstration of the improvement brought about by the use of mylar reflective particles.

All of these correlation data were gathered without any index matching material between the two halves of the tag. In addition, the tag was never glued together, so these correlation results are inconclusive. One issue that needs to be answered through additional testing includes the effects of gluing the two RP halves together. Air bubbles and inclusions will form. The amount of air bubbles and inclusions that will adversely affect the composite RP signature must be determined. Also, methods of reducing or eliminating these defects must be investigated.

F.10 FINAL STATUS/AVAILABILITY.

Due to cancellation of task, the read-at-home tag/seals are not fully developed and are not available for use. Additional testing and development are required to complete the read-at-home tag. An agenda for further study is as follows:

(1) The required particle density to achieve a 50 percent contribution to the composite RP signature needs to be determined. It may be that the particle density for the bottom RP needs to be greater than the top particle density, due to the presence of the loop ends.

(2) The best type of particle or particle mix needs to be determined. Since the mylar particles tend to remain suspended in the epoxy during the fabrication process, they may be more appropriate for this application, or perhaps a mixture of hematite and mylar would result in a better tag. Mylar is also more transparent and can produce a transmissive color signature.

(3) The long-term aging effects on the mylar particles must be determined. If there is any degradation or change in the reflective characteristics of the mylar particles, this must be determined before they are adopted. Sandia National Laboratories has already accepted mylar as an RP material.

(4) The most appropriate alignment mechanism should be identified. It appears that a tight fit between the two halves of the seal block will provide satisfactory alignment, but there may be other configurations that should be examined.

(5) Noise tolerance from air bubbles and dust particles must be determined. When the tag is installed in the field, there could be dust or air bubbles trapped between the two halves of the tag or in the adhesive used to bond the tag. This could be a very significant issue since the air bubbles could contribute to the composite signature, lowering the correlation between the original reading in the lab and the final reading taken when the tag is removed from the tagged object and returned to the lab.

(6) The optimum joint surface curvature to defeat cutting must be determined.

(7) Seal geometry needs study. How small can one end of the tag be and still produce an acceptable composite signature. This is significant since there are applications where one end of the loop would need to be threaded through a small opening. Minimizing one half of the tag would increase the number of applications for this tag.

F.11 LESSONS LEARNED.

For micaceous hematite as the reflective particles in the composite read-at-home tag signature, it appears necessary to carefully orient the read-at-home tag during fabrication so as to properly align the hematite crystals for maximum reflective particle contribution.

F.12 SCANNING ELECTROMAGNETIC/ACOUSTICAL MEASUREMENT (SEAM)TAG CONCEPT.

The scanning electromagnetic/acoustical measurement (SEAM) method is fundamentally an electromagnetic probe that may detect minute imperfections in a non-conducting material, such as a plastic or a largely non-metallic composite. (The sample may contain localized pieces of metals or other conductors, just so long as they do not dominate the entire target area to be scanned.) If these imperfections have a distinct pattern, then SEAM could provide an unique identification of the material. If this material were a non-removable part of some treaty limited item (TLI) such as a missile, then SEAM could provide an intrinsic tag for this TLI.

This report describes a feasibility study to determine the effectiveness of SEAM as a tag. First we summarize the principle of operation. Then we describe the measurement system used for this feasibility study. Next we describe measurements obtained to determine the detectability of imperfections in non-conducting materials. In the summary discussion of these experiments, we point toward the need for some further experimentation. Finally we describe preliminary ideas for a prototype system assembled largely from commercial off-the-shelf items as the next step in development toward making SEAM into a practical field instrument.

F.13 PRINCIPLE OF OPERATION.

F.13.1 Overview.

Figure F-10 shows a notional description of the SEAM principle of operation. Major components include the microwave system and the test sample mechanical support system.

The mechanical support system positions the test sample surface close to the aperture of the microwave cavity probe. In this way, electromagnetic energy can interact with a local volume of the test material close to the cavity aperture. The amount of interaction depends on material composition and density which can change throughout the material due to manufacturing imperfections such as air-bubbles, etc. The amount of interaction influences the probe response.

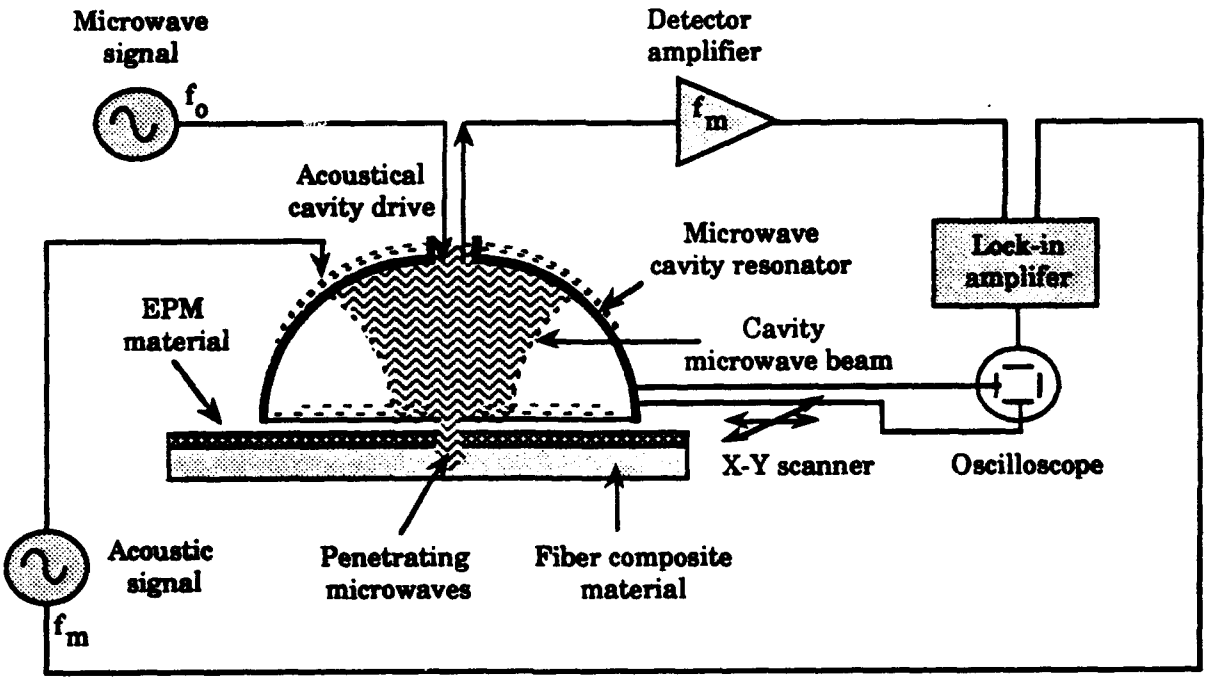

Figure F-10. Scanning electromagnetic/acoustic measurement (SEAM) tag concept.

The support system varies the separation distance between the cavity aperture and the sample surface. The amount of electromagnetic interaction also depends on separation distance. Thus modulating (vibrating) the separation

distance by a known amount and at a fixed frequency, f_m, will cause the probe response to vary with the same fixed frequency, f_m. This induced fluctuation in probe response is necessary to separate the material interaction component from the total microwave system response. The vibration frequency f_m is in the acoustic range, which is the reason for the term "acoustic" in the SEAM acronym.

The support system also scans the probe aperture across the sample surface to develop a two dimensional map of the amount of electromagnetic interaction versus position. If the map is unique to a given material sample, then one has an intrinsic tag.

The microwave system has three major components, a source, a cavity with a small aperture used to illuminate the material sample, and a microwave receiver.

The source produces a low amplitude signal of frequency, f_0. This signal is fed to a microwave cavity with a small aperture used to illuminate the test material.

The higher the source frequency, the smaller is the cavity and the cavity aperture size. A frequency of 10 GHz produces convenient results. For f_0=10 GHz, one has a wavelength of λ=3 cm. A high performance hemispherical cavity needs a diameter equal to several wavelengths so that diameters of 10-20 cm are required. A 10-20 cm cavity size is small enough to provide convenient physical handling and access to material samples. An aperture located on the flat side of the hemispherical cavity can be as small as 0.02-0.05 l or 0.6-1.5 mm. Since lateral spatial resolution will be proportional to aperture size, then material resolutions in the vicinity of 1 mm are expected. On the other hand, attenuation of the microwave radiation in the sample material is determined by the wavelength, so that variations in the material deeper than the size of the lateral resolution distance can be sensed.

The material information is contained in the signal reflected from the cavity and observed by the microwave receiver. If the test sample is vibrated at a frequency of f_m, then the reflected signal has power at frequencies of f_0 and $f_0 \pm$

f_m. A detector or mixer will convert a fraction of the power in the offset frequencies to a frequency of f_m which is monitored by the receiver.

These concepts are illustrated in an alternate way in figure F-11 which portrays the hardware, an equivalent circuit and the resulting image. The equivalent circuit shows that varying the aperture-material separation distance causes a variation of the termination impedance of the microwave circuit. Variation of the termination impedance ΔZ produces a corresponding variation in the reflected power, ΔP. ΔP is proportional to the material properties so that a two dimensional map of ΔP, an image as produced by the receiver, provides a potential intrinsic tag signature of the material.

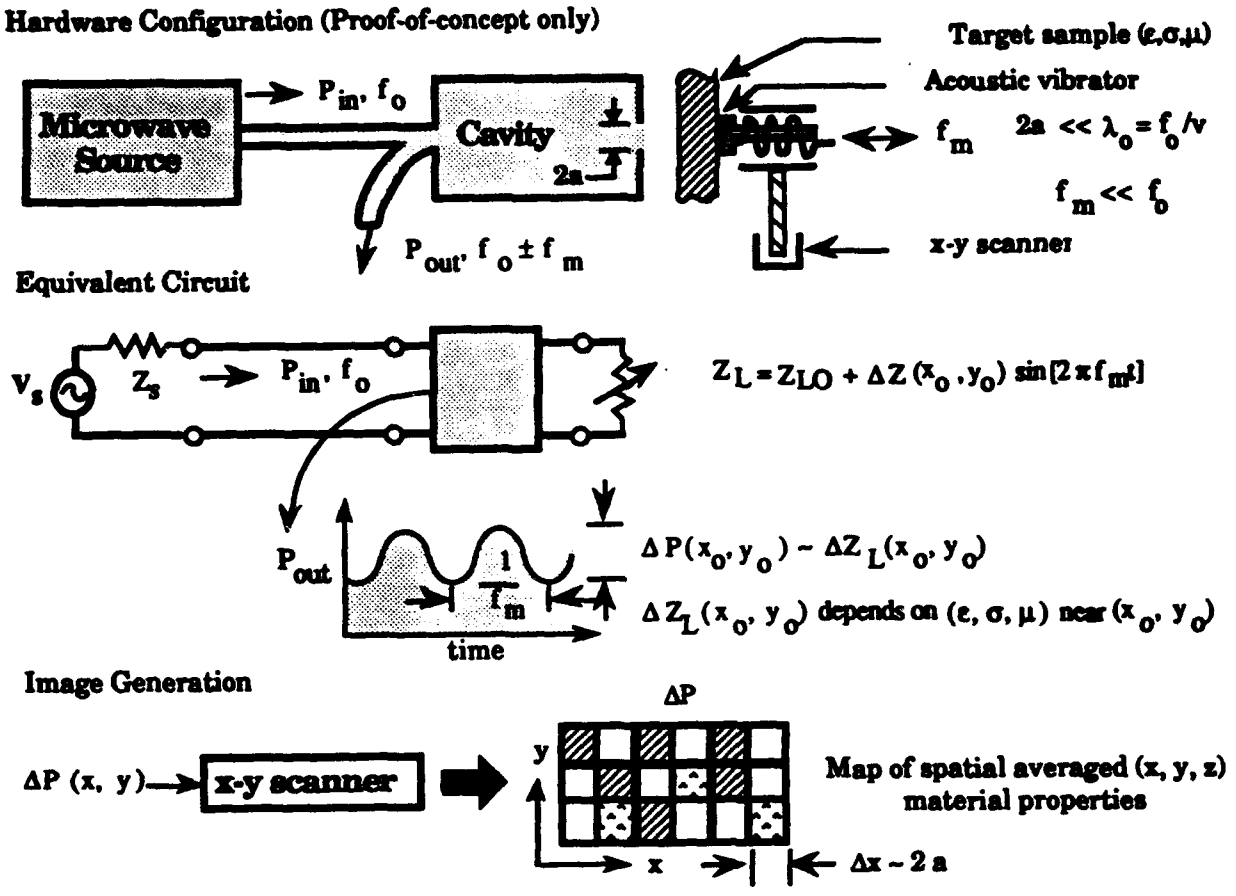

Figure F-11. SEAM produces a scan of target material properties.

The major advantage of SEAM over other microwave or optical probe techniques is that one obtains test sample spatial resolution at a fraction of a operating system wavelength. Classical imaging systems including microscopes and synthetic aperture radar (SAR) probe their targets in the far-field regime, and thus produce images whose resolution is about one wavelength or larger. The SEAM advantage arises from probing its target in the near-field regime, and is useful because it exploits the material penetration depth available at longer wavelengths while preserving the resolution usually available only at much shorter wavelengths. Thus one can map the volumetric properties of a non-conducting material close to its surface that would be opaque at optical frequencies and would have poor (inadequate) contrast with a X-ray transmission imaging system.

F.13.2 Previous Work on SEAM.

The SEAM concept was first reported by Ash and Nicholls (1972) in a paper entitled "Super-resolution Aperture Scanning Microscope." Figure F-12 summarizes some of the key measurements. In one experiment, they deposited a thin metal film on a glass substrate, so that this sample contained a high spatial contrast in dielectric properties between the metal and glass. The film formed the letters "UCL." Figure F-12 shows that their SEAM instrument was able to image the letters whose size was 1/15 inch (2 mm) with an aperture diameter as small as 1/60 inch (0.5 mm). In a second experiment, they prepared a dielectric sample consisting of Perspex (polymethyl-methacrylate (PMMA), relative dielectric constant of e_r=2.58) and polythene (polyethylene, e_r=2.28), thus giving a low spatial contrast in this sample's dielectric properties. Their measurements reproduced in figure F-12 show that SEAM could distinguish these relatively similar (in dielectric constant) materials.

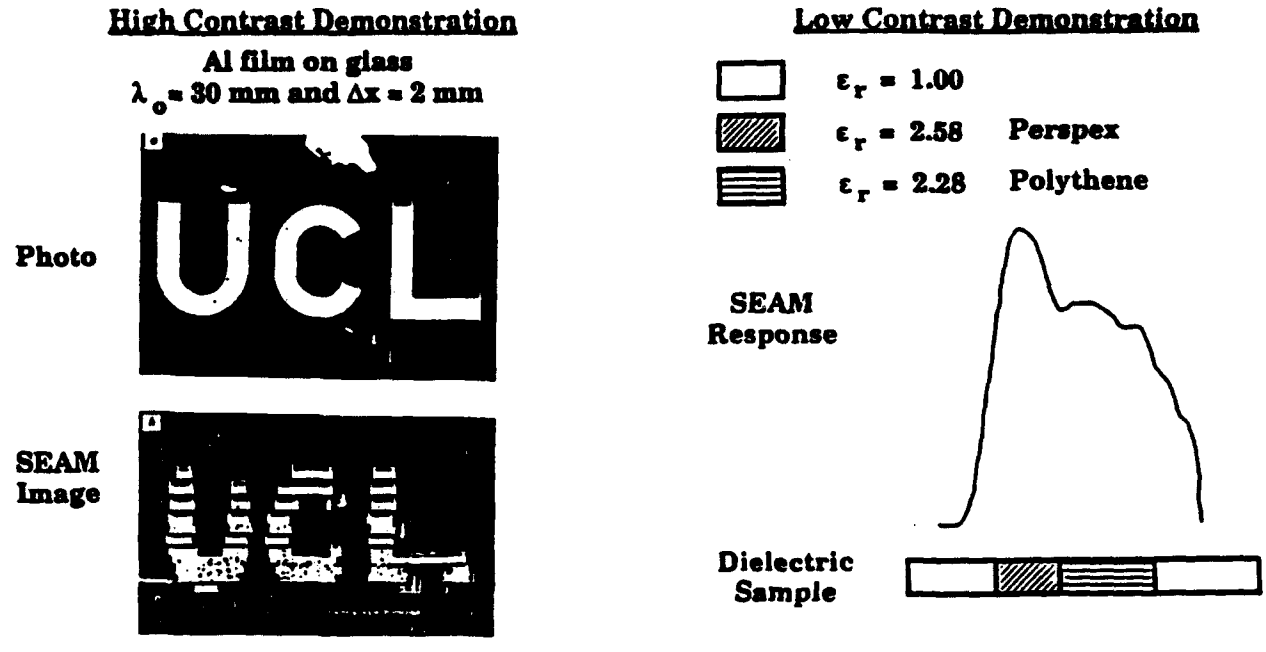

Figure F-12. Ash and Nicholls demonstrated SEAM feasibility.

The original idea to utilize near-field optics to overcome diffraction limitations in microscopy was due to Synge (1928). Recently this idea has seen considerable development at optical wavelengths (Lewis et al., 1984, Reddick et al., 1989, and Betzig et al., 1991), and a photon scanning microscope which works on similar near-field principles is now commercially available (see, e.g., Murday, 1992).

F.13.3 Quantitative Model of SEAM.

F.13.3.1 Microwave Components. We developed a quantitative model of the SEAM instrument in order to optimize performance. The model is based on the standard ABCD transmission matrices that relate voltage and current at either end of a microwave system (see Collin (1966)). Each component in the system has a separate ABCD matrix, and the performance of a chain of components is given by the matrix multiplication of the chain of separate ABCD matrices.

Figure F-13 illustrates the concept. Here a source is connected to a microwave cavity through a length of cable or wave guide. This cable is characterized by its length, propagation constant γ_1, and characteristic impedance Z_1. The cavity is simply modeled as a section of transmission line terminated at each end with the relatively low impedance of a small aperture (without the aperture, the impedance would be identically zero corresponding to a short circuit). The cavity transmission line has its length, D, propagation constant, γ_0, and characteristic impedance, Z_0. The aperture impedance is represented by a small inductance given by

$$L = \mu_o \left(\frac{8}{3\pi}\right) r_o^3 / \omega_o^2$$

Figure F-13 also shows expressions for the input impedance to the cavity, Z_{in}, the reflection coefficient ρ, and the reflected power. At resonance, the input impedance is maximized and takes the simple form

$$Z_{in}^{max}(\omega_o) = Z_1^2(\omega_o)/4R_s(\omega_o)$$
$$R_s(\omega_o) = \sqrt{\pi \mu_o f_o / \sigma}$$
$$Z_1(\omega_o) = j\omega_o L_1$$

where L_1 is the inductance of the entrance aperture, σ is the conductivity of cavity structure ($\sigma \approx 5 \times 10^7$ mhos/meter for good metals such as aluminum, copper or silver), and $\omega_0 = 2\pi f_0$ where f_0 is the cavity resonant frequency. Figure F-14 shows a plot of input impedance versus entrance aperture radius, r_0. Note in this example that an impedance of 50 ohms is obtained with r_0=2.06 mm.

Equivalent Circuit

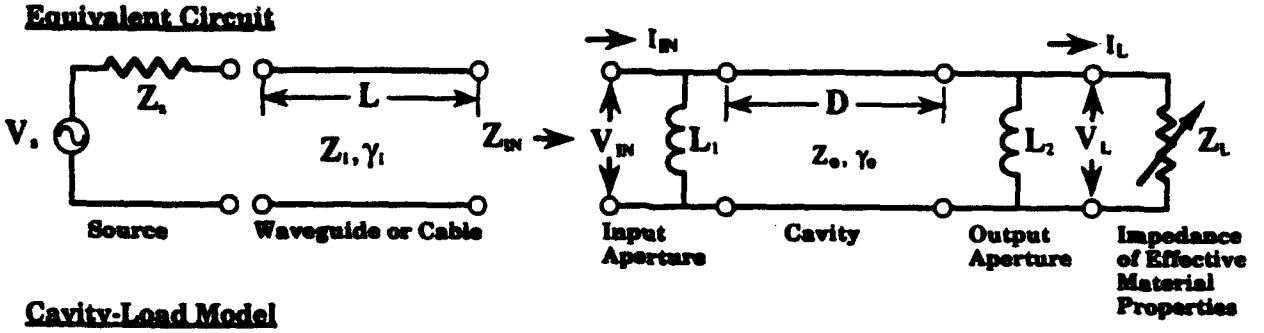

Cavity-Load Model

$$\begin{bmatrix} V_{IN} \\ I_{IN} \end{bmatrix} = \begin{bmatrix} A & C \\ B & D \end{bmatrix} \begin{bmatrix} V_L \\ V_L/Z_L \end{bmatrix}$$

$$\begin{bmatrix} A & B \\ C & D \end{bmatrix} = \begin{bmatrix} 1 & 0 \\ (j\omega L_1)^{-1} & 1 \end{bmatrix} \begin{bmatrix} C & (jz_0)S \\ \left(\frac{j}{z_0}\right)S & C \end{bmatrix} \begin{bmatrix} 1 & 0 \\ (j\omega L_2)^{-1} & 1 \end{bmatrix}$$

$C = \cos\ \theta$
$S = \sin\ \theta$
$\theta = \gamma_0 D$
$\gamma_0 = \frac{\omega}{v}$
$v = 3\times10^8$

Reflected Power Versus Z_L

$$P_{out} = \rho^2 P_{in} \qquad \rho = \frac{(Z_{in} - Z_1)}{(Z_{in} + Z_1)} \qquad Z_{in} = \frac{(AZ_0 + B)}{(CZ_0 + D)}$$

Figure F-13. SEAM system model.

Figure F-14 also shows an example of the change in reflected power due to a change in relative dielectric constant of the material being tested. Expressions for this change in reflected power, $\Delta P/P_{in}$, are shown below

$$\Delta P / P_{in} = (\Delta\rho)^2$$

$$\rho = \frac{Z_{in} - Z_s}{Z_{in} + Z_s}$$

$$\Delta\rho = \frac{d\rho}{dZ_{in}} \Delta Z_{in}$$

$$= \frac{2 Z_s}{(Z_{in} + Z_s)^2} \Delta Z_{in}$$

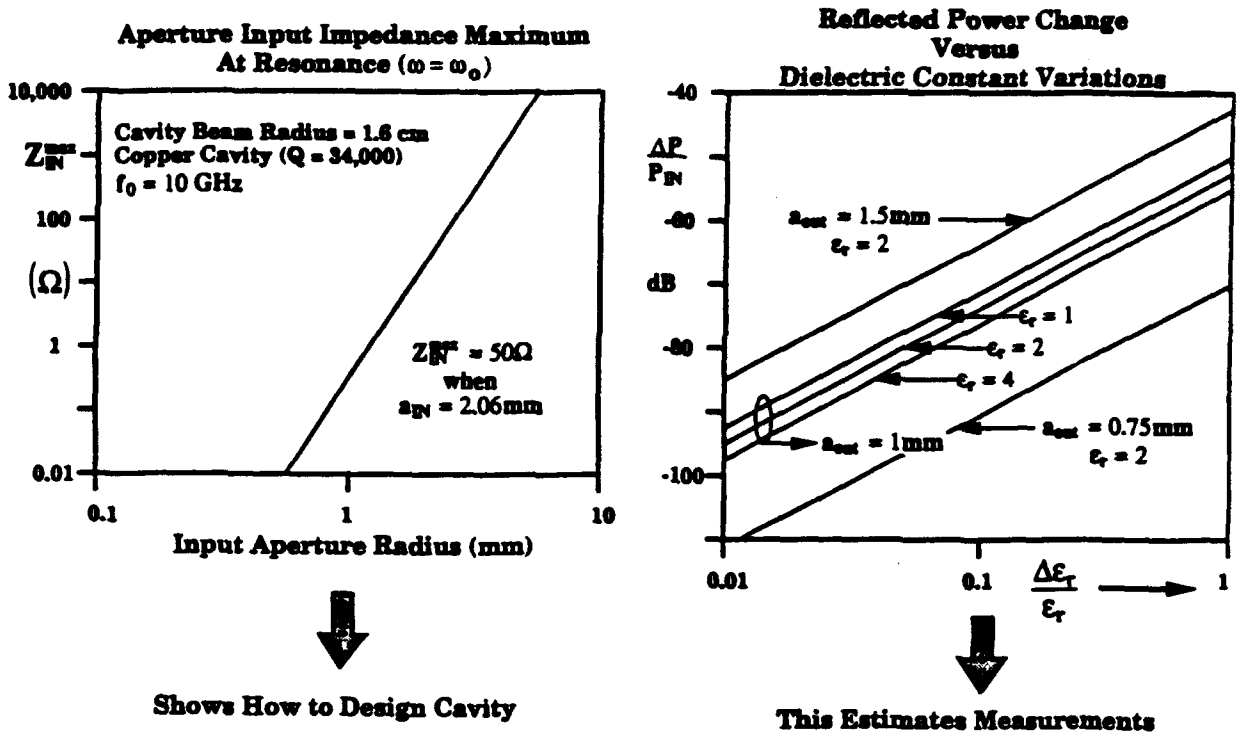

Figure F-14. SEAM model predicts responses for assumed material impedance.

where Z_s is the source impedance and ΔZ_{in} is the change in cavity input impedance due to a change in dielectric constant, $\Delta\varepsilon$, by the output or exit aperture near the test material.

Near resonance, the input impedance is given by

$$Z_{in} = \frac{Z_{in}^{max}}{1 + j(\alpha + \delta / \Delta\omega)}$$

$$\Delta\omega = \omega_o / 2Q$$

$$Q = n \frac{\pi}{8} \frac{\eta}{R_s}$$

where α is the fractional amount that the source is tuned away from cavity resonance (typically, α~1), δ is shift in cavity resonance due to the presence of a dielectric near the output aperture, Q is the cavity quality factor, $\eta=120\pi$ ohms, and n is the multiple of the fundamental cavity resonance (typically, n=5-10).

The cavity resonance shift is related to the cavity terminating impedance, Z_T, as shown below. Note $Z_T=Z_2Z_L/(Z_2+Z_L)$ where Z_2 is the inductive impedance of the output aperture and Z_L is the impedance of the external dielectric material.

$$(\omega_o+\delta)L/c = n\pi$$
$$\delta L/c \approx Z_T/\eta$$
$$\delta = Z_T/\mu_o L$$

The expression for the change in input impedance can be written as

$$\Delta Z_{in} = \frac{dZ_{in}}{d\delta}\frac{d\delta}{dZ_L}\Delta Z_L$$

$$\left|\frac{dZ_{in}}{d\delta}\right| \approx \frac{Z_{in}^{max}}{1+\alpha^2}\frac{1}{\Delta\omega}$$

$$\frac{d\delta}{dZ_L} = \frac{d\delta}{dZ_T}\frac{dZ_T}{dZ_L}$$

$$= \frac{1}{\mu_o L}\frac{Z_2^2}{(Z_2+Z_L)^2}$$

$$\approx \frac{1}{\mu_o L}\left(\frac{Z_2}{Z_L}\right)^2$$

$$\Delta Z_L = \frac{dZ_L}{d\varepsilon_r}\frac{d\varepsilon_r}{d\Delta\varepsilon_r}\Delta\varepsilon_r$$

$$\approx -\frac{1}{2}\frac{\eta}{(\varepsilon_r)^{3/2}}\Delta\varepsilon_r$$

$$\approx -\frac{1}{2}Z_L\frac{\Delta\varepsilon_r}{\varepsilon_r}$$

$$\Delta Z_{in} \approx -\frac{1}{2}\frac{Z_{in}^{max}}{1+\alpha^2}\frac{Z_L}{\Delta\omega\mu_o L}\left(\frac{Z_2}{Z_L}\right)^2\frac{\Delta\varepsilon_r}{\varepsilon_r}$$

Figure F-14 shows typical results for this reflected power. For example, a 10 per cent change in relative dielectric constant, $\Delta\varepsilon_r/\varepsilon_r$, produces about a -60 dB change in relative power for an output radius of 1.5 mm and ε_r=2. A combination of directional coupler isolation and mixer/detector isolation will be required to achieve at least 60 dB isolation between incident and reflected power.

F.13.3.2 Test Sample Impedance. The material to be tested or characterized presents an effective impedance to the microwave cavity as shown in figure F-13. Details of the calculation are given in the attachment. A summary is given here.

The key relationship is that between the energy stored in the field external to the aperture and the field at the aperture surface. The external energy depends on the summation (integration) of energy densities throughout the material sample and the surrounding space. These energy densities, in turn, depend on the local constitutive properties of the material under test.

The aperture fields can be described in terms of the effective electric and magnetic dipoles. Due to the cavity mode configurations, only the magnetic dipole is excited at the aperture. This dipole term depends on the local magnetic field. Thus, the impedance is given by

$$Z_L = W_T/a^2|H_A|^2,$$

where W_T is the external energy, H_A is the magnetic field that would be present at the aperture location in the cavity if the aperture were not present, and a is the aperture radius. (Note that in the presentation and discussion of the experimental results, it is more convenient to describe the aperture in terms of its diameter rather than its radius.) The attachment describes the detail of the external field energy calculations that are key to this estimate.

F.13.3.3 Mechanical Acoustic Vibrator. Design of the mechanical support system for the test material samples requires some estimate of the change in aperture-material separation distance and the size of vibrator needed to achieve this variable distance as a function of frequency, f_m, and material sample weight. Criteria are developed in the following paragraphs.

Fields near an electrically small aperture decay as $(2a/r)^3$ where a is the aperture radius and r is distance from the aperture. Thus moving from 1 to 2 aperture diameters would decrease field strength by a factor of 8. In a qualitative sense, one surmises that the aperture/material separation distance must be moved about 1 aperture diameter to achieve significant changes in the impedance associated with the external materials.

An acoustic speaker is a readily available vibrator that can be used to evaluate the SEAM concepts. Speaker requirements are estimated from the following analysis.

A speaker is an electrical motor that exerts a force given by $f_{SP} = (BL)_{eff}\, i_{SP}$. The speaker current can be obtained from the specified speaker impedance, R_{SP}, and speaker power, P_{SP}, as $i_{SP} = \sqrt{P_{SP} / R_{SP}}$ The magnet strength term, $(BL)_{eff}$, is readily determined by noting the DC current needed to deflect (move) a known weight by the maximum possible amount. The resulting formula is $(BL)_{eff}$ = ma / I where a is the acceleration of gravity (a ≈ 9.81 m/s^2) , m is the known mass (kg) and I is the required current.

The relation among force, sample mass and vibration frequency is found by the following. Let the speaker cone displacement and acceleration be given by

$$x = x_o \sin \omega_o t$$

$$a = -\omega_o^2 x_o \sin \omega_o t$$

Equating mechanical and electrical force terms, one finds

$$(BL)_{eff} \sqrt{P_{SP} / R_{SP}} = (m_o + \Delta m) x_o \omega_o^2$$

where m_O is the mass of the speaker cone (given in speaker specifications) and Δm is the added test sample mass.

As an example, consider the performance available from the speaker used in the SEAM feasibility experiments. A Phase Linear PL S800 speaker was used. Specifications included: P_{SP} =100 watts; R_{SP}=4 ohms; and m_O=17.5 grams. Laboratory measurements yielded $(BL)_{eff}$≈5 Tesla-meters. Calculations of the displacement distance versus sample mass are shown in figure F-15.

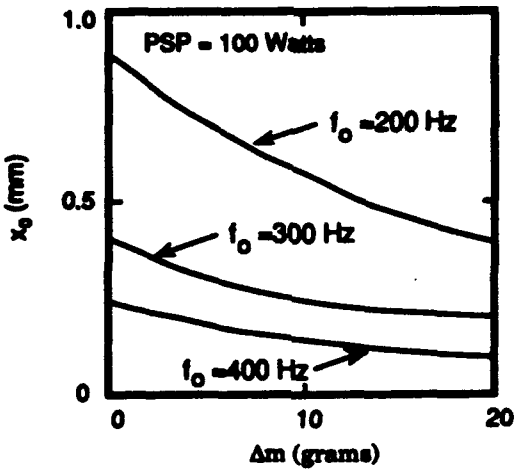

Figure F-15. Maximum cone deflection versus sample weight for PL S800.

F.14 MEASUREMENT SYSTEM.

Measurements were made with the instrumentation seen in figure F-16. The 20.3 cm diameter hemispherical cavity was fabricated from aluminum stock at a local machine shop. The inner cavity surface was copper plated to reduce losses. The Phase Linear speaker and the Majestic audio amplifier were purchased from a local audio components store. The rest of the equipment was available from BDM laboratory equipment.

Figure F-17 shows a measurement of the cavity input reflection coefficient versus frequency. The cavity resonates when the reflection is minimized. Inspection of these data shows two very sharp resonances at about 10.99 GHz. Cavity Qs were estimated from these data to be 39,200 and 47,800. SEAM system sensitivity is proportional to Q, and these values will provide acceptable performance.

After some experimentation, we settled on a set of test conditions. The HP4192 replaced the HP204D to obtain a frequency stability better than 1 Hz. The generator was tuned to 275 Hz, and the HP3577A receiver was set to a 1 Hz bandwidth.

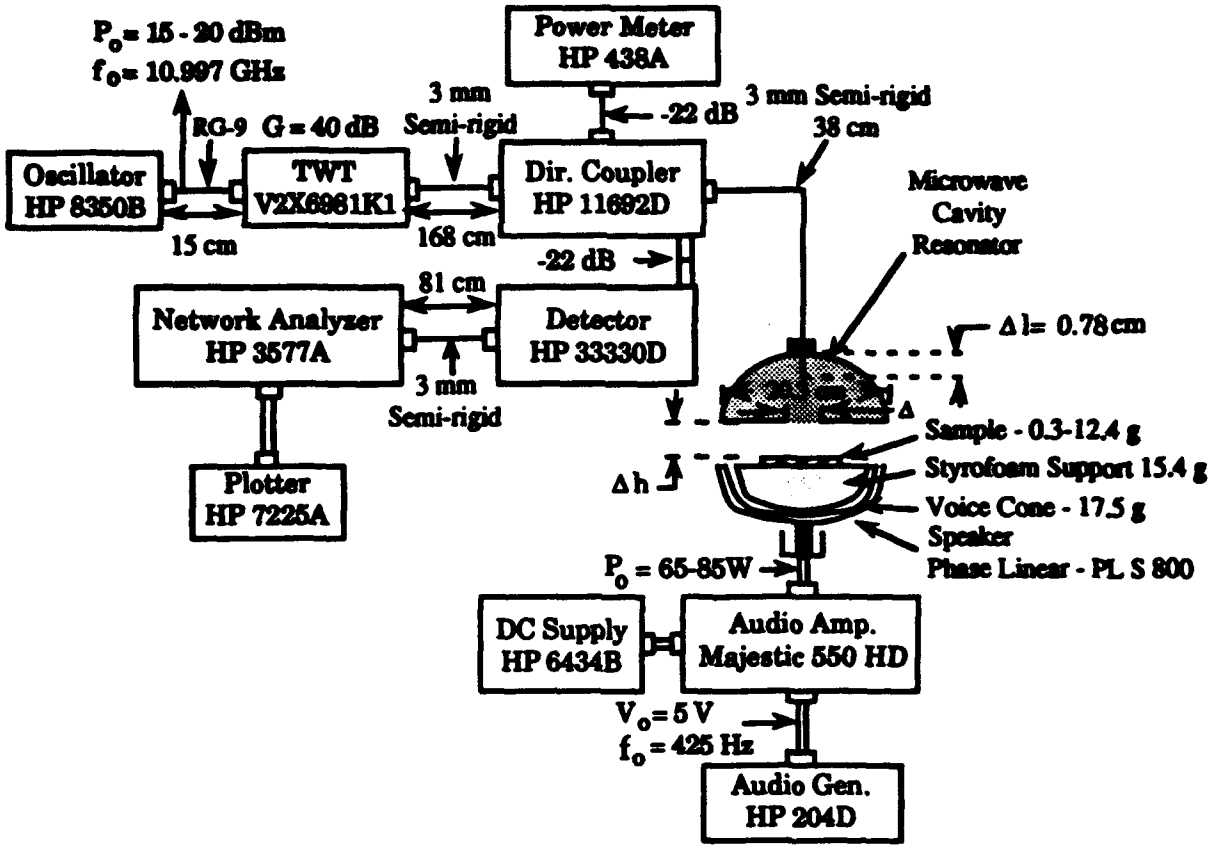

Figure F-16. SEAM experimental configuration.

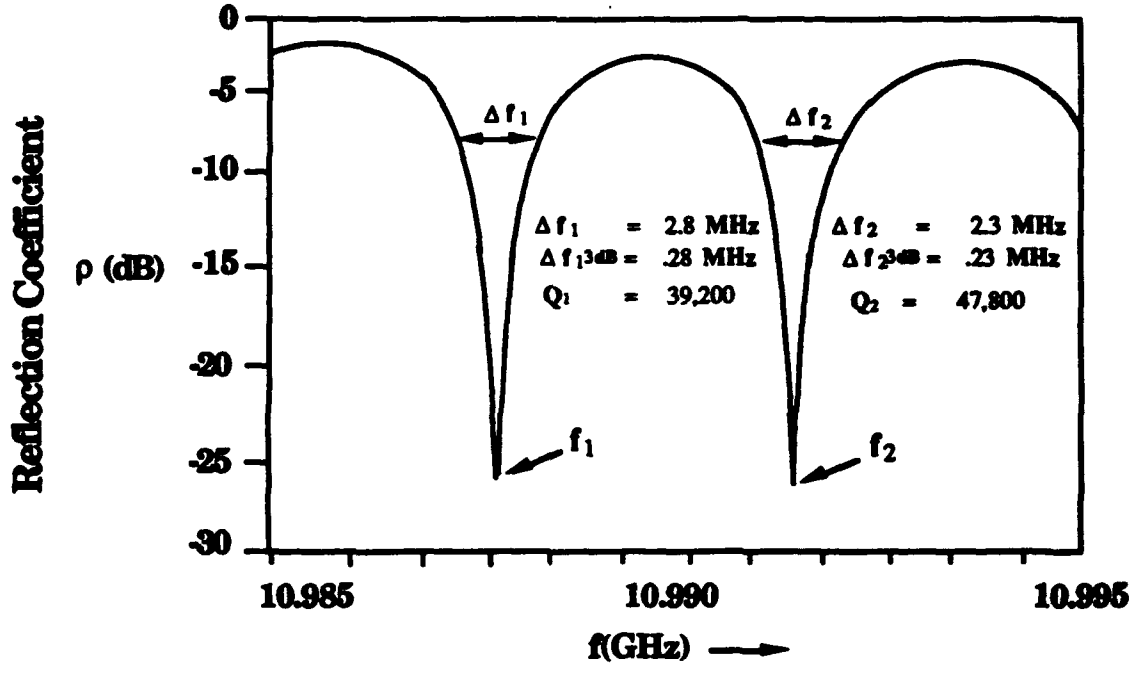

Figure F-17. SEAM cavity response.

Data were taken in a scan traverse over a material sample as a series of measurements at several (typically 3 to 8) discrete scan points arranged in a linear path over the test sample at a nominally constant height above the sample. The scan points are termed "material data points" in the displays presented in section F.15 to emphasize their dependence on the material properties of the sample. Several–typically 5–measurements were taken at each scan point location in the scan over the test sample. These repeated readings at each location were used to obtain the sample mean and sample standard deviation error bars which are shown in the displays of data for each scan over a test sample. These displays show relative power in dB versus location in the scan, where the zero reference for reflected power is taken to be the average (mean) of the means at all scan points in the scan.

F.15 MEASUREMENTS.

F.15.1 Overview.

A series of measurements were taken to characterize SEAM system performance. Four types of samples were used: (1) parallel copper strips laid on a glass substrate; (2) layered fiberglass with holes drilled beneath parallel to the surface; (3) glass and PMMA plastic strips laid on a polystyrene foam substrate; (4) and a sample section of the Peacekeeper motor bottle covered with its environmental protection material (EPM). The first sample type shows the greatest SEAM response contrast between the various component materials in the sample (copper, a conductor, and glass, a dielectric) The second sample type shows SEAM contrast due to large voids in the sample. The third sample type shows SEAM contrast due to relatively small localized inhomogeneities in the material's dielectric constant. And the fourth sample type provides a real-world sample of arms control interest, to examine whether detectable response contrast can be obtained with such items using SEAM.

F.15.2 Copper-on-Glass Samples.

Figure F-18 is a representative drawing of the copper-on-glass sample showing the relative scan point locations. The samples consist of parallel strips of copper of width a laid on a glass substrate and separated by bare glass strips of

width *b*; a given sample is characterized as a "*a* x *b* sample", where *a* and *b* are replaced by the actual strip width of the sample. A sample scan is a series of measurements of reflected power at indicated locations along a linear path across the sample. At each location, several repeated readings (typically, n = 5) are made to obtain the mean reflected power and an estimate of the random error (as sample standard deviation error bars) at that point. Most results displayed for scans across samples are in dB, using as a reference level the mean over the scan locations of the mean reflected power at each location.

The range of variation in scans over different samples can be seen by considering the change of the reflected power, ΔP, in terms of the ratio of the received signal when the aperture is over the copper versus that when the aperture over the glass. With a 1.5 mm cavity aperture, scanning a distance of 12.7 mm laterally and at a height Δh = 1 mm above the substrate, a 1 mm x 1 mm copper-on-glass sample produces a 0.1 dB change; a 2 mm x 2 mm copper-on-glass produces a 2.26 dB change; and a 2 mm x 4 mm copper-on-glass produces a 3 dB change.

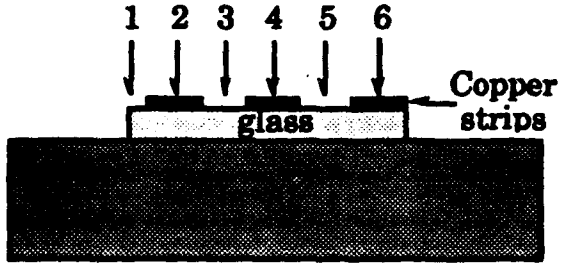

Figure F-18. High contrast sample – copper strips on glass.

Figure F-19 is the result of a three-point scan over a 2 mm x 2 mm copper-on-glass sample with a 1 mm aperture at a standoff height of Δh = 1 mm. Data point 1 is with the aperture over the glass, near the edge where the glass drops away to the polystyrene foam block which interfaces the sample to the speaker. Data point 2 location is with the aperture over the middle of the 2 mm wide copper strip. Data point 3 has the aperture over middle of the glass strip between two copper strips. Five power readings (n=5) were made at each location to obtain the

mean for the location, and the means for the three locations were averaged to obtain the graph mean of ΔP = -53.089 dBm which was used as the reference level in figure F-19 The results in figure F-19 demonstrate that the SEAM technique can easily provide a spatial resolution between the copper and glass. At the third data point, where the aperture is located midway between two copper strips, the reflected power has not quite returned to the low value of point 1, which is an indication that the size of the dipole radiated at the aperture is large enough to be influenced by the copper 0.5 mm beyond the edge of the aperture both left and right.

Figures F-20 and F-21 display data obtained from scanning the 2 mm x 2 mm sample with a 1.5 mm aperture. The difference between the two scans is that the sample was rotated 180° in the apparatus between the two scans, in order to test the reversibility of the procedure. The two scans differ because the sample holder surface for this item was not exactly parallel to the path traversed by the scan. The sample holder had tilt of approximately a 0.15 mm dip over a 12.5 mm traverse (a 0.68° tilt), so that Δh changed during the scans from the nominal 1.0 mm to 1.15 mm. This is a clear indication of the affects of signal power changes related to $1/(\Delta h)^2$.

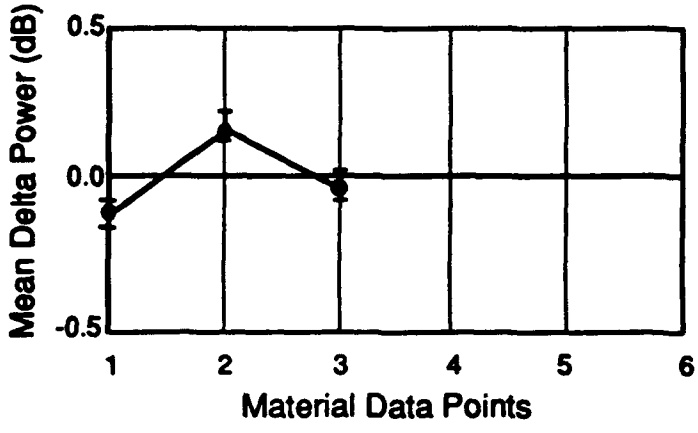

Figure F-19. Scan across a 2 mm x 2 mm copper-on-glass sample aperture =1 mm, standoff = 1 mm).

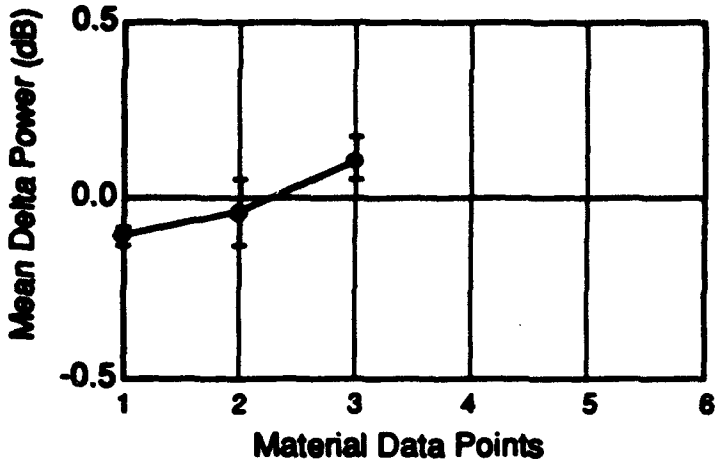

Figure F-20. Scan across a 2 mm x 2 mm copper-on-glass sample (aperture =1.5 mm, standoff = 1 mm).

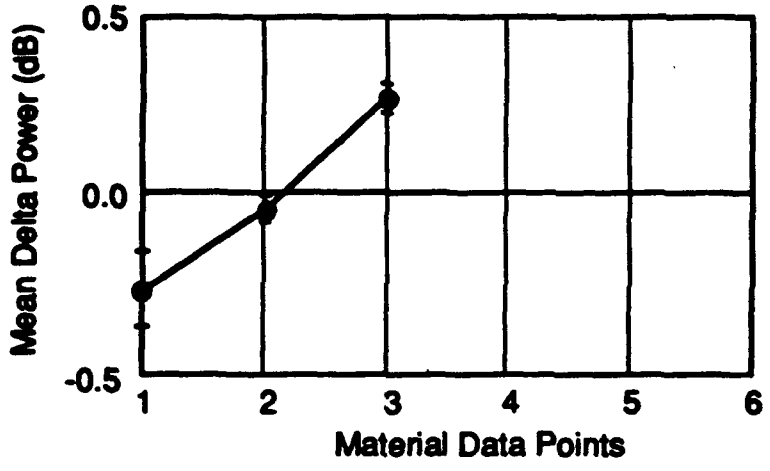

Figure F-21. Scan of 2 mm x 2 mm copper strips on glass, sample rotated 180° (aperture =1.5 mm, standoff = 1 mm).

F.15.3 Layered Fiberglass Sample with Buried Void.

Figure F-22 represents the layered fiberglass sample showing the aperture locations relative to the data points. Figure F-23 shows a typical result with data obtained by scanning layered fiberglass (6.35 mm total thickness), with the individual layers of fiberglass averaging about 1 mm thick, an aperture of 1.0 mm, and a nominal Δh of 1 mm. The 0 reference (mean value) is -58.377 dBm. Five measurements were obtained at each location (n = 5), with the four data point means used to obtain the 0 reference. Once again, the sample holder was

measured during post testing investigation and was found to be beveled with 0.12 mm tilt over a 12.5 mm traverse (0.54°). Figure F-24, a composite of two runs and eight measurements, differs slightly from figure F-23. These differences are likely due to uncertainties of about 0.5 mm in the repeatability of the lateral

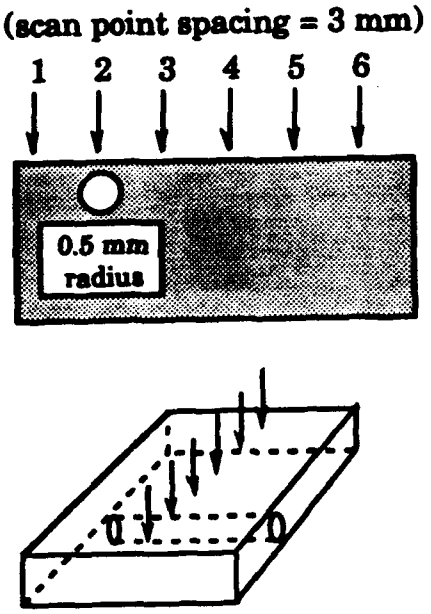

Figure F-22. Fiberglass sample with buried void.

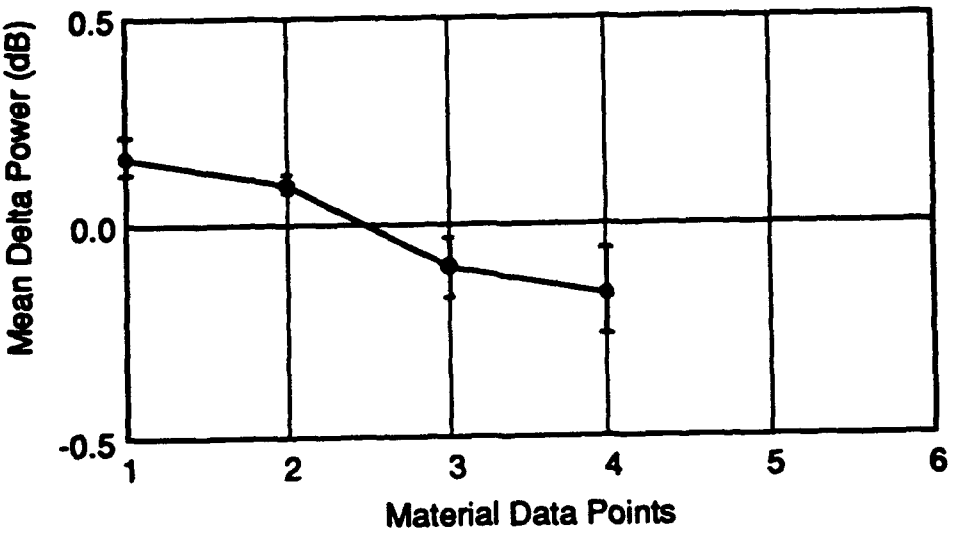

Figure F-23. Scan of layered fiberglass with buried void (aperture =1 mm, standoff = 1 mm).

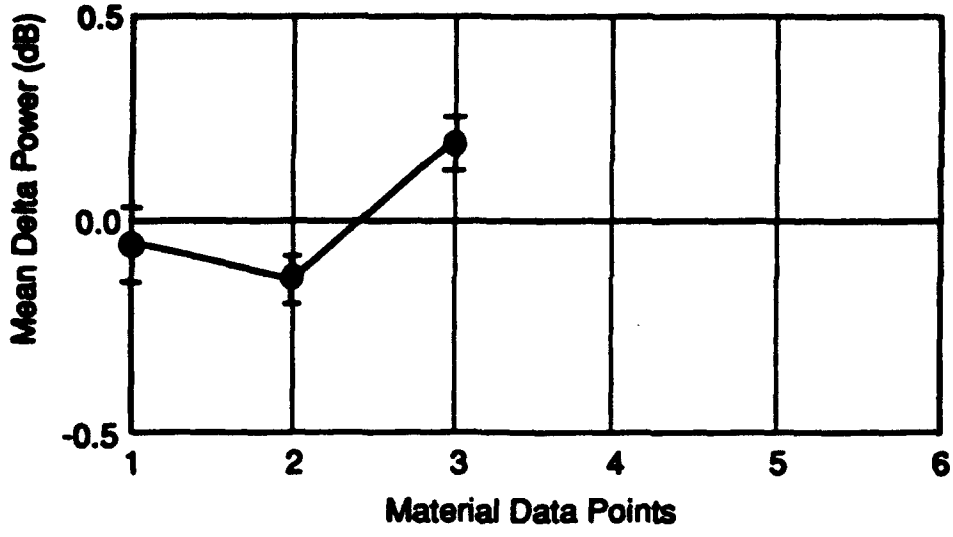

Figure F-24. Scan of layered fiberglass (aperture =1 mm, standoff = 1 mm).

alignment of the scan traverse over our sample. Data point 1 has the aperture aligned at a position over the material located midway between the edge of the material and the centerline of a 1.0 mm diameter hole bored parallel to the surface and centered 1.0 mm below the surface. Data point 2 has the aperture aligned over the center line of the 1.0 mm hole. Data point 3 has the aperture located over the solid substrate 3 mm beyond the centerline of the hole. The layered material provides a definite signal feature representative of contour of the material. The 0 reference (-58.803 dBm) is obtained from the three data points. For this sample, there was no measurable tilt of the sample with respect to the scan path, the plot contains no slope bias due to sample tilt. During post testing investigation, it was verified that the sample was level. The layered fiberglass material thickness changes were obtained by using a 6X microscope and making measurements with the microscope micropositioners.

F.15.4 Glass and Plastic (PMMA) on Polystyrene Foam.

The glass and PMMA samples were 1 mm thick and 2 mm wide in the direction of the scan traverse; they were 10 mm or longer in the direction perpendicular to the scan traverse. The standoff distance from the aperture to the top of the glass or PMMA samples was Δh=1 mm, or 2 mm above the polystyrene

foam substrate. Figure F-25 is a representative drawing of the sample showing the scan location data points. A 1.5 mm aperture was used to obtain figure F-26 with n=5 data items. The 0 reference (-51.023 dBm) is obtained from the mean of the three scan data points. The data reflect only marginal deviations between the plastic and glass. However, when compared to the data obtained with a 1 mm aperture (figure F-27), the deviations become more apparent. The results for the larger size aperture show an effect of the extended size of its dipole sampling some of the dielectric materials on either side to the center of the aperture, which keeps the contrast in the response lower than it is with a smaller aperture. With the smaller size aperture, repeatable measurements (figure F-27) with much more pronounced contrast in the observed reflected power. The general downward trend is a result of a bevel in the sample holder, - 0.1 mm tilt in a 12.5 mm traverse (0.45°), which results in Δh changing from 1.0 mm to 1.1 mm. Here five measurements per location were taken at three locations to obtain a zero reference of -54.85 dBm.

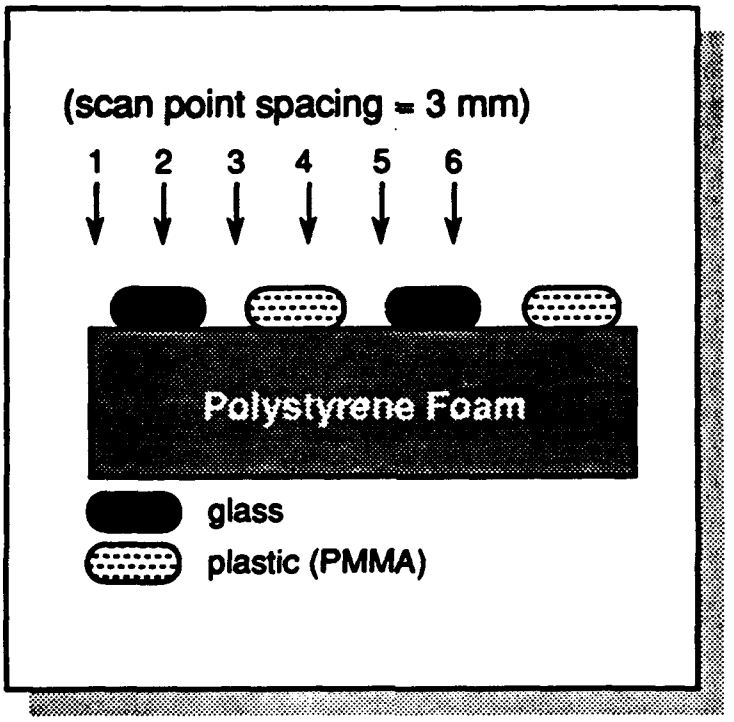

Figure F-25. Low contrast sample, glass and plastic (PMMA) on polystyrene foam.

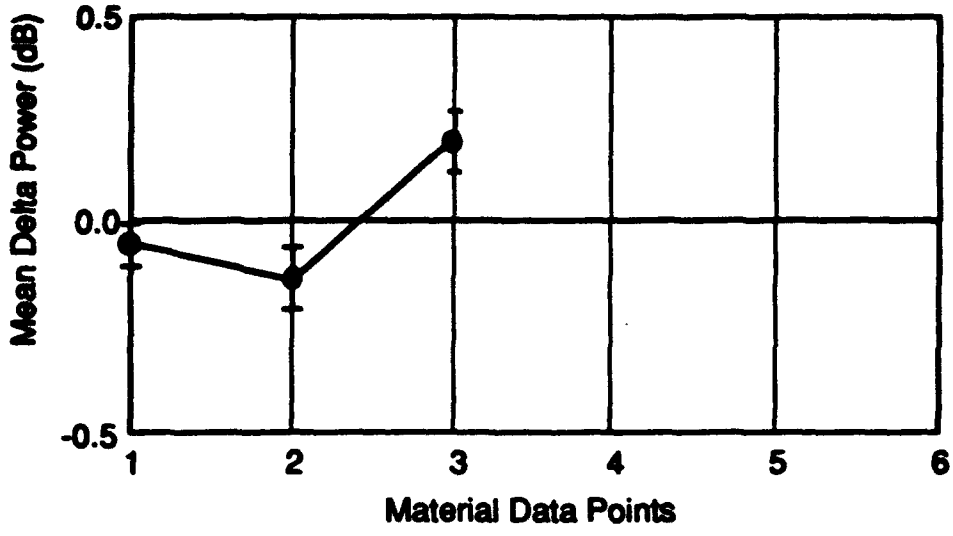

Figure F-26. Scan of glass and PMMA samples on polystyrene foam (aperture =1.5 mm, standoff = 1 mm).

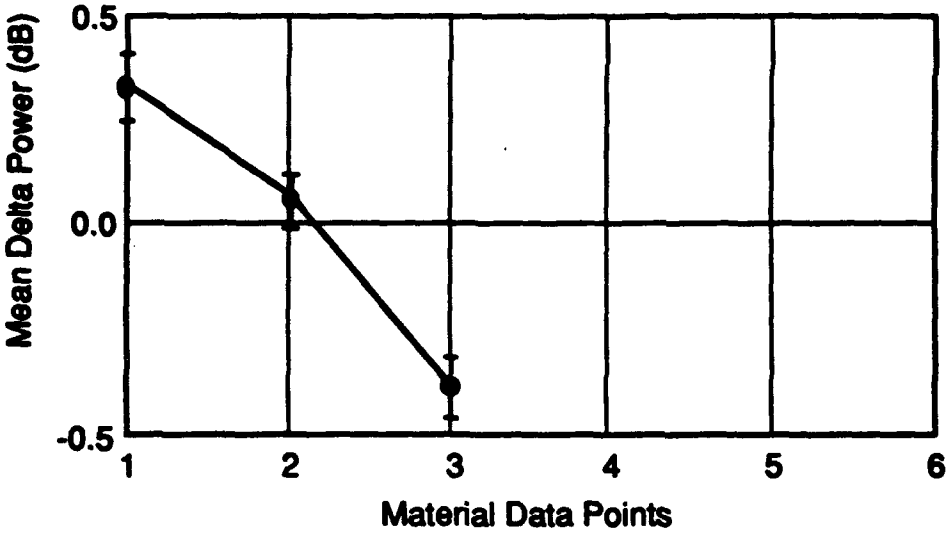

Figure F-27. Scan of glass and PMMA samples on polystyrene foam with smaller aperture (aperture =1 mm, standoff = 1 mm).

F.15.5 Peacekeeper Motor Bottle Sample.

Figure F-28 is a representative drawing showing the data point locations relative to the Peacekeeper motor bottle material. The final experiment consists of scanning a piece of a motor bottle with the EPM attached. Viewing the material with the unaided eye revealed readily apparent variations in thickness and boundary. The largest variability is the variation in the thickness of the adhesive layer between the EPM and the motor bottle wall. The adhesive varies in thickness along the surface by as much as 0.5 mm (0.020 in.). The various layers of the motor bottle wall have slightly smaller variations in observable thickness. Figures F-29 and F-30 show typical SEAM results with 1 mm and 1.5 mm apertures, respectively. Five measurements at each of eight locations were made.

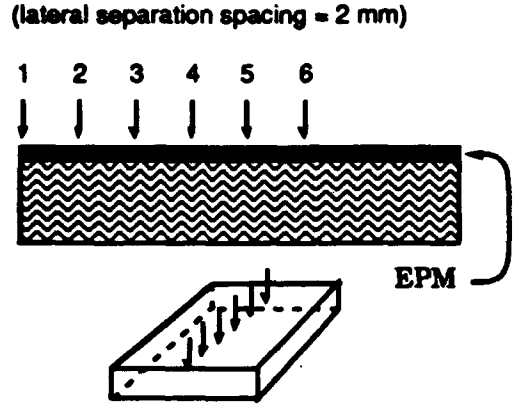

Figure F-28. Sampling locations on Peacekeeper motor bottle material.

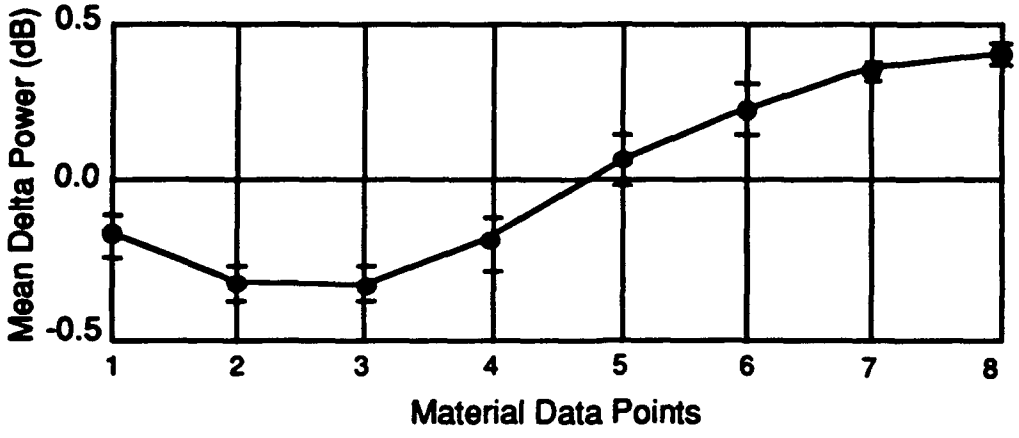

Figure F-29. Scan of Peacekeeper motor bottle material (aperture =1 mm, standoff = 1 mm).

The EPM made the set-up difficult and resulted in Δh changing slightly along the scan path (tilt of 0.075 mm in 12.5 mm traverse or a tilt angle of 0.34°). Consequently, in both figures there is an upward data trend that may be attributed to changes in Δh. Despite this overall upward trend, large enough local power variations occurred to map an intrinsic characteristic of the sample.

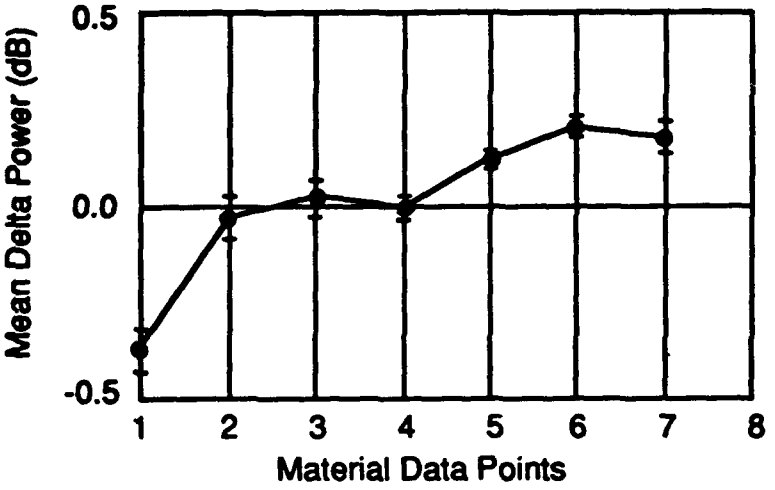

Figure F-30. Scan of Peacekeeper motor bottle material, with larger aperture (aperture =1.5 mm, standoff = 1 mm).

F.15.6 Summary of Results.

F.15.6.1 Copper on Glass. The random data spread at each scan point, defined as two standard deviations (the top to bottom span of the error bars), was about 0.1 dB. The contrast , or relative change, between the aperture being centered over a copper strip and the aperture being over glass midway between two copper strips is about 0.2 dB for the 1 mm diameter aperture and 0.3 dB for the 1.5 mm aperture. The optimum aperture size appears to involve a trade-off between sensitivity and spatial resolution. A larger aperture provides a larger response signal, or better sensitivity, while the smaller aperture yields more abrupt changes in response versus spatial position. The data were sensitive to sample placement and deviations from constancy in Δh. We observed that a 0.7° tilt in the sample holder produced a systematic 0.3 dB drift in the measured response over a scan traverse.

F.15.6.2 Layered Fiberglass with Buried Void. The random data spread for this sample was 0.15 dB, while the contrast between the aperture being over homogeneous material and the aperture being over the buried void was about 0.3 dB. Sensitivity to sample alignment and deviations from constant Δh was similar to that observed in the copper-on-glass sample.

F.15.6.3 Glass and PMMA on Polystyrene Foam. Random data spreads were in the 0.1 to 0.15 dB range. The contrast between the aperture being over glass versus the aperture being over the polystyrene foam between the glass and PMMA elements was about 0.35 dB for the 1.5 mm aperture, and 0.50 dB for the 1 mm aperture. This case thus shows a clear superiority of a smaller aperture, while the copper-on-glass case was more ambiguous.

F.15.6.4 Peacekeeper Motor Bottle with EPM. The smaller aperture, 1 mm, provides about 0.2 dB change in the point-to-point scan, while the random data spread was also about 0.2 dB. The larger aperture, 1.5 mm, reduced the size of both the point-to-point variation and the random data spread. Since in the present study only one sample was measured, one cannot say with assurance whether these *point-to-point* variations in signal amount to a unique signature for such items.

F.15.6.5 Evaluation. Experiments show that material inhomogeneities are measurable with a SEAM system in the laboratory. The random data spread using our setup assembled from available laboratory storeroom equipment was 0.1 - 0.15 dB. This spread could be reduced significantly by optimized choice of components. For example, the use of a phase-locked-loop receiver, which is readily available on the current instrumentation market but which was not in our laboratory inventory for use in the present series of experiments, would greatly reduce the random noise level and thus the random data spread. The present results indicate that more care should be given to sample alignment and registration, in order to get more repeatable results. Additional measurements are needed to characterize minimum detectable material differences, and to survey whether representative types of TLIs have sufficiently unique variations as to serve as signatures for individual items. In addition, more measurements are needed to validate the prediction models.

F.16 PRELIMINARY IDEAS FOR A PROTOTYPE SEAM SYSTEM.

F.16.1 Introduction.

The measurement system used in the feasibility study reported here was assembled out of components available in BDM's laboratory inventory and otherwise uncommitted to other projects. This system was adequate to indicate that SEAM has potential capability for intrinsic tagging in treaty verification applications. However, this system is not optimal in terms of the capability of equipment that is available in the current commercial off-the-shelf (COTS) market. For example, the RF receiver component was not optimized for signal-to-noise ratio; phase-locked-loop (PLL) receivers on the current COTS market can greatly reduce the noise to signal ratio. In addition, this feasibility study moved the sample both in the audio frequency modulation and in the scan traverse and kept the cavity stationary. In an application to treaty verification, the cavity would have to be moved relative to a stationary TLI. Thus, the next stage of development of SEAM as an intrinsic tag reader system would require a prototype system which has significantly lower noise and a cavity support system that moves the cavity relative to the inspected sample. This subsection presents some preliminary ideas for such a prototype system. Of necessity it is not complete, since some of the missing detail would have to be a product of further development.

F.16.2 Requirements.

The prototype SEAM system should have some attention given to a design for use in a non-permanent, non-benign environment. That is, the system should support field activities and the environment encountered during mobile on-site inspections. This would require the system to be readily field-transportable by one or two individuals and be capable of being set-up and calibrated very quickly. A calibration would be required to ensure accurate results and the calibration results would become a part of the inspection report. Similarly, the system would require means of taking and storing baseline signatures for the TLIs and for taking inspection signatures and comparing them with the baseline signature. Therefore, the system should provide immediate hard (permanent) copies of the calibration test results and of the signature reading and comparison results.

F.16.3 Top-Level Equipment Requirements.

The equipment necessary to support the requirements would include an RF source (f_0 signal generator and amplifier), a directional coupler or circulator, the cavity, an RF receiver, the cavity support mechanism (including the audio frequency (AF) drive and scan traverse subsystems), and means to record calibration and signature data and to compare baseline and inspection signatures. The cabling is a made-to-order part of this system, but it can be obtained at competitive prices from companies such as Belden or Andrews.

F.16.4 Equipment Listing.

The following commercial off-the-shelf items (see table F-1) have been identified which could be assembled into an prototype system:

Table F-1. Major components of prototype SEAM system.

Component	Manufacturer	Model
RF Source and PLL Receiver	Watkins Johnson	WJ Mini-Series model
Circulator	Narda Microwave	Model CGS-8018
Cavity	Allied Plastic Eng., Inc	Custom requirements
Support (incorporates AF source and cavity shaker)	Mayco, Inc.	Several models available
Controller for Support and Positioner	Reliance Electric Co.	X Series programmable controller
Positioner	Pacific Precision Labs.	TransLine Dual Axis ST-TL1414
Power Supply	Best Power Technology	X Series FERRUPS

F.16.5 Equipment Logistics.

The equipment listed above could readily be made to fit into two custom design carrying cases, such as those manufactured by Anvil Corporation.

Figure F-31 is a block diagram of the system and figure F-32 is a conceptual drawing of the packaging.

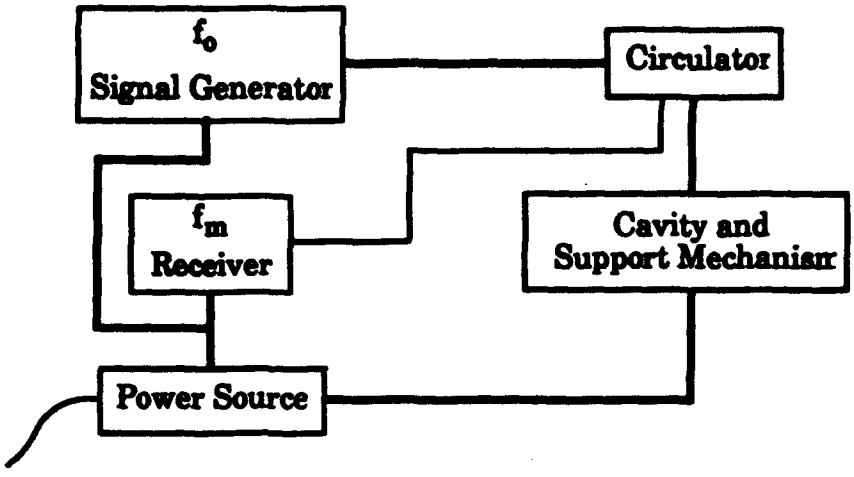

Figure F-31. SEAM system conceptual block diagram.

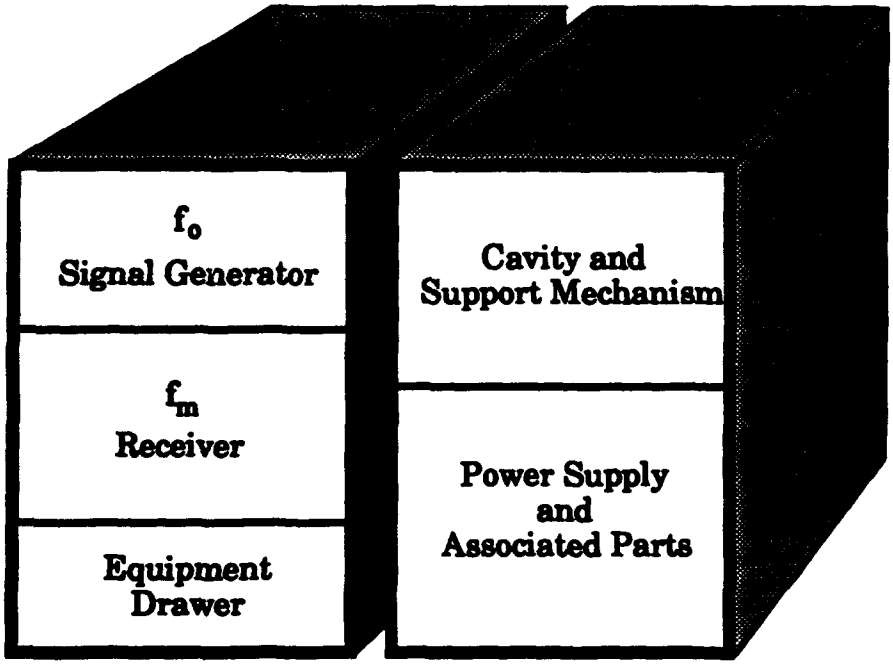

Figure F-32. Conceptual SEAM packaging.

F.17 THE MAGNETOSTRICTIVELY INSPECTED LOOP SEAL (MILS).

One of the technologies explored during this effort was the use of magnetostrictive wires or ribbons as possible tag/seals. Magnetostrictive materials change their dimensions slightly during the application of a magnetic field, and it is possible that this effect might be used to obtain acoustic or electrical signatures which may indicate both tag uniqueness and adversarial tampering. The motivation for this research sprang from the historic use of arrays of magnetostrictive wires for ion detection in spark chambers. Development of these materials has progressed greatly in the last decade. Magnetostrictive ribbons and wires of high quality and exact specifications are available commercially. The Metglas Products division of Allied Signal Inc. (Parsippany, NJ) produces or distributes several kinds of magnetostrictive materials. Most of these materials are made of amorphous (noncrystalline) glassy metals. They are routinely used for magnetic shielding, magnetostrictive delay lines, distance sensors, vibration and stress sensors, identification markers, digitizing tablet sensors, small transformer windings, and so forth. Small samples of both ribbon and wire were obtained from Allied Signal. The magnetostrictive ribbons were found to be easily spliced, while the magnetostrictive wires were found to be very difficult to solder together. Therefore, attention was focused on the magnetostrictive wires, which are produced by Unitika Ltd. of Japan. The wire samples investigated are Unitika's iron-base "Sency" wires, type AF-10. They have a diameter of 125 μm (microns), and are composed of $Fe_{81}B_{14}Si_4C_1$ and $Fe_{77.5}Si_{7.5}B_{15}$. These amorphous magnetostrictive wires, called a-wires for short, are produced by ejecting molten alloy against the inside wall of a rotating drum coated with a cooling fluid, which rapidly solidifies the wires. These a-wires have a high resistance per unit length (on the order of 150 Ω per meter), which helps to reduce eddy-current losses for some applications.

F.18 BARKHAUSEN EFFECT.

The Barkhausen effect occurs when a ferromagnetic material is magnetized. A typical B-H (hysteresis) curve for a normal magnetic material appears in figure F-33. The magnetic properties of the material are responsible for the shift of magnetic induction (B) with applied external magnetic field (H). Over the steep parts of the curve, local magnetic domains can suddenly change in

both size or magnetization orientation. These small, discontinuous changes in the domains, some of which are indicated in the figure, constitute the Barkhausen effect. This effect is very pronounced in magnetostrictive materials, in which just a few domains can occupy the entire wire. In certain amorphous magnetostrictive wires, the vertical portions of the hysteresis loop are formed by just one or two major domain reversals, or "Large Barkhausen Jumps" (Mohri et. al.,1984), as indicated in figure F-34.

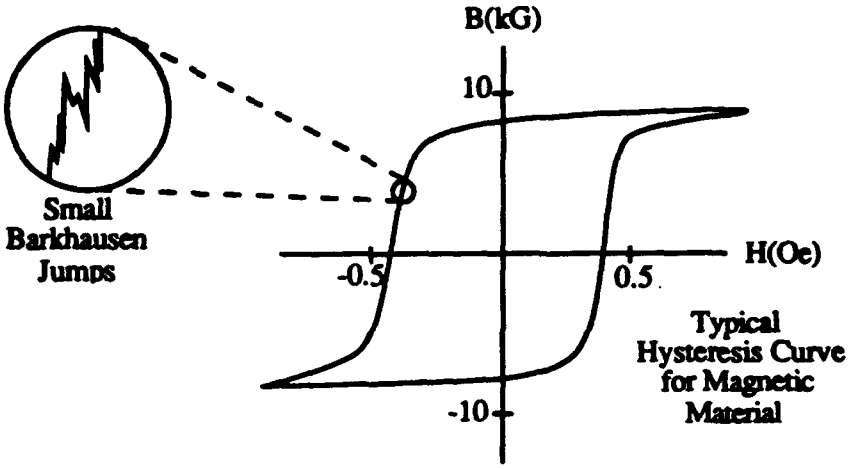

Figure F-33. Hysteresis curve and the small Barkhausen effect for typical magnetic material.

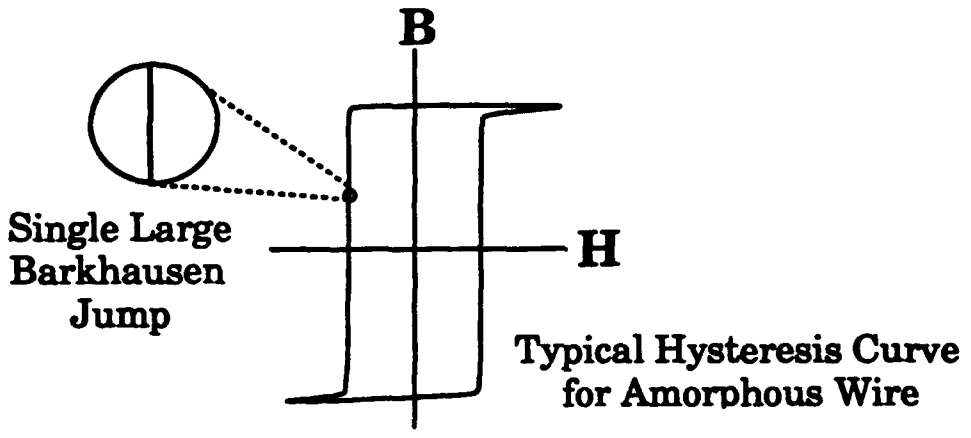

Figure F-34. Hysteresis curve and the large Barkhausen effect for magnetostrictive amorphous wire.

If an amorphous magnetostrictive wire (a-wire) is exposed to an external magnetic field, and a small pickup coil is placed around the a-wire, a Barkhausen-effect voltage will appear across the terminals of the pickup coil as the domain wall propagates through the coil. The magnitude of this voltage is approximately (Mohri et al., 1985):

$$V_B = \pi D^2 N N_w M_s B_s \cos(\theta) (H^* - H_0) / \beta ,$$

where D is the diameter of the inner core of the a-wire (typically about 110 μm), N the number of turns of the pickup coil, N_w the number of domain walls propagating along the wire through the coil (the domains are assumed to be circular disk-shaped), M_s is the saturation magnetization, B_s is the saturation flux density, θ is the average angle of the magnetization vector with respect to the wire axis, H^* is the critical field for flux reversal domain nucleation, H_0 is the critical field of domain propagation, and β is the eddy current damping coefficient. The propagation of a domain wall down the axis of an a-wire is shown in figure F-35. In the figure, the entire wire consists of just two domains, labeled "North" and "South." As the domain wall moves down the wire, portions of the "North" domain flip polarity and become part of the "South" domain. The propagation of domain walls depends on many factors (including wire composition and size, and the strength of the applied magnetic field). The velocities of the domain boundaries are typically in the acoustic range (100 to 400 meters per second). Through the phenomenon of magnetostriction, the propagating domain boundaries are coincident with magnetoelastic waves.

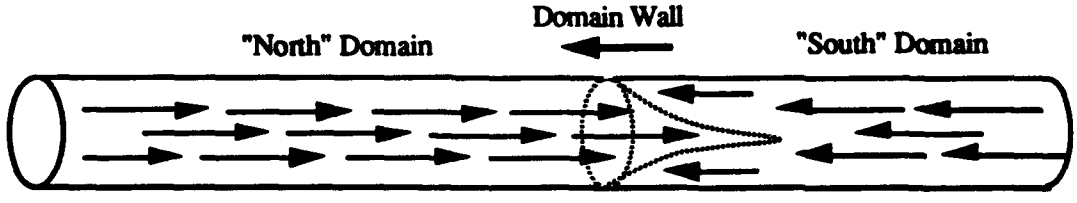

Figure F-35. Propagation of a domain wall in an amorphous wire.

An a-wire subjected to a suitable external magnetic field will possess just a few domains instead of several domains, as would be the case for conventional materials. If the external field is uniform, and is raised above the critical value, domain walls will spontaneously nucleate and begin propagating from both ends of the wire toward the center of the wire. Magnetoelastic waves from just one end

of the wire can be obtained by adding a small driving field to the main external field at that end of the wire. This is accomplished by using a long coil for the main external field, and including a small driving coil (connected in series with the main coil) at the desired end of the a-wire. The enhanced local field ensures that domain nucleation will occur only at the end of the wire near the drive coil.

The propagation of magnetic domains is a surface effect rather than a volume effect, and depends critically on the uniform composition and shape of the amorphous material. *If an a-wire is damaged, spliced, or even bent too sharply, magnetic domain wall propagation ceases entirely at the point of damage.* That is, the "magnetic and mechanical uniformity of the wire is of utmost importance with respect to large Barkhausen discontinuities" (Sixtus and Tonks, 1931).

F.19 MEASUREMENT OF THE BARKHAUSEN JUMPS IN A-WIRE.

Measurements on a-wires provided by Allied Signal and by Unitika Ltd. were performed at the BDM laboratory in Albuquerque. The design of the experiment is indicated in figure F-36. An amorphous wire was placed inside a main coil that was a meter long, with about 8 turns per centimeter. A small drive coil having about 20 turns per centimeter was wired in series with the main coil. Both coils were driven with a square wave of 3 volts amplitude, and a frequency of 60 Hertz. This produced domain nucleation and magnetoelastic propagation of domain walls along the wire. A small pickup coil (having a total of about 700 turns for high sensitivity) was used to detect the Barkhausen effect; this coil was connected to a Tektronix oscilloscope with time-delay capability. The response of the pickup coil was composed of two parts. The first part was an early-time, sharp-peaked response which was determined to be caused by coupling from the main and driving coils to the pickup coil; this early-time "Coil Coupling" response occurred whether or not the amorphous wire was placed inside the main coil, and is therefore completely independent of the properties of the amorphous wires. The second part of the response was delayed by about 250 μsec from the first, and was *very* dependent on the presence and condition of the a-wire. This late-time "Barkhausen Coupling" was found to be on the order of 150 millivolts for undamaged and unspliced a-wires. When the a-wire was removed from the main coil, the Barkhausen coupling vanished entirely. *In addition, when the a-wire was spliced and re-inserted into the main coil, so that the pickup coil surrounded*

a section of the a-wire as before, but a splice existed between drive and pickup coils, the Barkhausen coupling vanished entirely. **The splice was made carefully, and the connection was good electrically; however, the presence of the splice apparently inhibited the propagation of magnetic domains totally and completely. The measurements for both normal and spliced amorphous wires appear in figure F-37.**

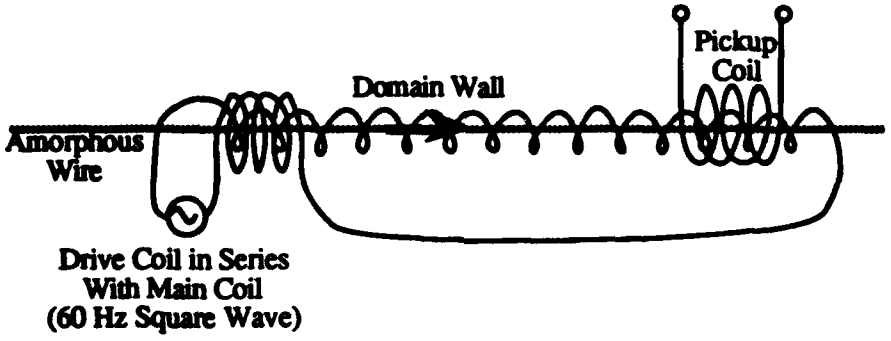

Figure F-36. Setup for measurement of Barkhausen effect at BDM laboratory.

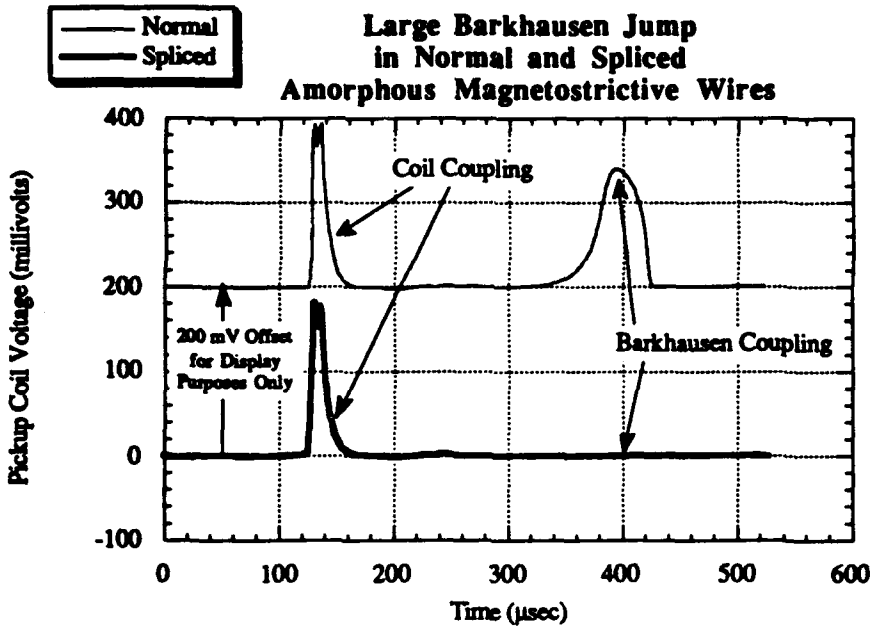

Figure F-37. BDM laboratory measurement of Barkhausen effect for normal and spliced amorphous wires.

F.20 MAGNETOSTRICTIVE TAG/SEAL.

Since propagation of magnetic domain walls in amorphous magnetostrictive wires is severely inhibited by damage to the surface of the wires (such as may be caused by splicing or bending), it appears that these wires may provide a way to seal a TLI to a given unique identification tag. Although the a-wires do not provide a unique signature themselves, they can be locked to a tag connector (such as the box containing a reflective particle tag). Any tampering done to the seal (i.e. the a-wire) can hypothetically be detected via measurements of the Barkhausen effect. A schematic of one possible implementation of a tag/seal for treaty verification is shown in figure F-38.

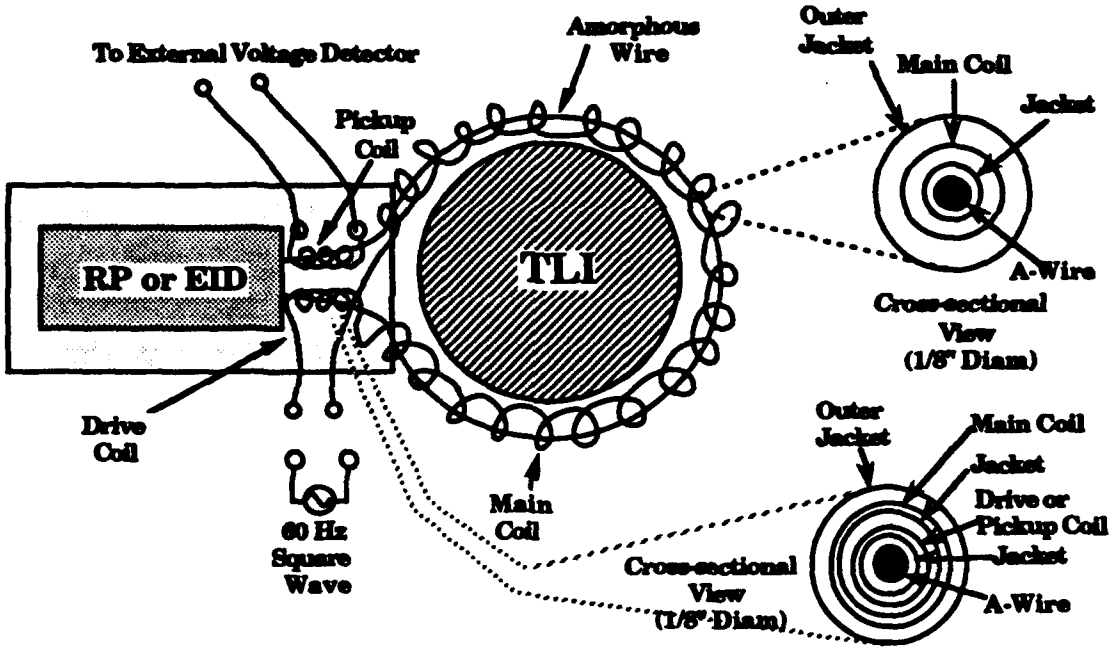

Figure F-38. One possible implementation of a tagging seal utilizing the large Barkhausen effect in amorphous wire.

F.21 SUMMARY AND RECOMMENDATIONS.

Although the experimental studies of the properties of the magnetostrictive materials were too limited to permit a complete assessment of their usefulness as

loops for tag/seals, these materials may indeed turn out to be very useful for some tamper-detection tagging applications. It appears that magnetostrictive materials provide a way to test with confidence whether or not a tagging seal has been compromised. Of course, many technical issues remain to be resolved, but the basic technologies are *well developed, easily implemented,* and *commercially available.* It is strongly recommended that this technique be given further study.

F.22 NONLINEAR OPTICAL FIBER AND OTHER MEANS TO INCREASE THE TAMPER-DETECTION SECURITY OF SLOTS/PTILS.

The work covered by this report had as its principal goal the identification of concepts and development of means for improving the detection of attempts at tampering (via splicing) with the optical fiber loop of the Passive Tamper Indicating Loop Seal (PTILS), or its other name the Secure Loop Optical Tag/Seal (SLOTS).

It must be made clear at the outset that the currently-developed PTILS was not at risk of compromise. Developmental testing of PTILS (based on short-haul communications grade polymer fiber) showed that current state-of-the-art splices are clearly detectable with the optical time-domain reflectometers (OTDR) identified for use as field inspection instruments.

On the other hand, there are substantial technological incentives toward improving the current state-of-the-art in optical fiber splicing, driven by the needs of the communications industries. In addition, there are incentives arising from the desire of adversaries to defeat the purposes of tags and seals. Substantial resources might be dedicated to technological means of defeating tags and seals. Hence, there is some long-term technical risk that the state-of-the-art for optical fiber splicing could be advanced eventually to the point that the currently-developed PTILS tamper detection technology might not be capable of detecting tamper attempts at a sufficiently high level of confidence. It is to mitigate this technical risk that the work described here was undertaken.

In addition to the principal goal, a secondary goal was to seek means for making use of the OTDR-in-a-slot (Antel board) in the Universal videographic

Reader (UR) in PTILS. This would reduce the number of pieces and weight of on-site inspection equipment.

BDM undertook a search for potential phenomena, materials, and fiber configurations that might support these goals, and did evaluations of candidate items identified in this search. The search used several guidelines, including the following:

(1) New approaches identified in phenomena and materials must be available in optical fiber configurations for use in the loop of PTILS.

(2) The PTILS configuration resulting from new approaches identified must be inspectable by relatively simple on-site equipment. It is preferable that the currently identified OTDR equipment would serve, with little or no change.

(3) Samples of optical fiber representative of new approaches must be obtainable for developmental PTILS testing with no extraordinary costs. The PTILS development effort could not undertake the cost burden of commissioning fabrication of materials and fiber. It was planned to take advantage of availability of attractively featured fiber wherever it could be found. If developmental testing proves its usefulness for PTILS, attractively featured fiber that was available only in experimental lots would be required to have the potential of reasonable cost production.

(4) Because PTILS configurations and instrumentation were based on multimode fiber, the search for new fiber configurations was biased toward similar characteristics. The bias toward multimode fiber was compelling. The larger fibers are more easily handled, the connectors are less sensitive and expensive, and PTILS instrumentation uses multimode components.

(5) The search for new approaches and the evaluations of those identified occurred in a short timeframe. Consequently, the search and evaluations were of necessity kept rather tightly focused and limited. A

consequence of such limitation was that approaches that might have great potential, but would require greater development time, were not considered. Detailed analysis was also restricted for the same reasons.

The search for new approaches with enhanced tamper detection involved nonlinear optical effects (NLOE), specialty optical fibers, and potential exploitation of complex fiber configurations. The following sections contain more detail of these topics.

F.23 SEARCH FOR NONLINEAR EFFECTS AND MATERIALS FOR USE IN PTILS.

The arena of NLOE is a very rich one, with a great deal of research and development activity going on in the application of NLOE to communications and to the prospect of optical compu ation. The books listed in the References are useful for background and details on NLOE and optical fibers. A major effort covered by this report was to (1) evaluate the potential for NLOE enhancing splice detection with an OTDR; (2) search for optical fiber materials with enhanced nonlinear properties and potential suppliers of such fiber; and (3) attempt to identify other NLOE that could be used to simplify splice detection in PTILS.

Before going into the details of this work, it is useful to give a brief survey of some of the nonlinear optics fundamentals. The book by Butcher and Cotter (1990) provides a good overview of NLOE fundamentals. Nonlinear optical effects arise from a polarization response $\vec{P}$ of an optical material to the electric field $\vec{E}$ of a light wave that has contributions proportional not only to the first power of $\vec{E}$ but also to the second and third powers of $\vec{E}$ as follows:

$$\vec{P} = \varepsilon_0 [\overleftrightarrow{\chi}^{(1)} \cdot \vec{E} + \overleftrightarrow{\chi}^{(2)} : \vec{E}\vec{E} + \overleftrightarrow{\chi}^{(3)} \vdots \vec{E}\vec{E}\vec{E}]$$

The linear susceptibility $\chi^{(1)}$ gives rise to the usual refractive index n_0. (The zero subscript is added to this electric field independent quantity in anticipation of the appearance of a nonlinear contribution to the total refractive index that is proportional to the square of the electric field.)

The second-order susceptibility $\chi^{(2)}$ gives rise to such phenomena as second harmonic generation (frequency doubling). However, because it is present only in those media that lack inversion symmetry (especially certain complex crystals), it is not likely to be significant in most optical fibers because of the amorphous structure of glasses and randomly polymerized plastics. It is possible to induce a second-order susceptibility into optical fibers of some materials by the process of "poling." Poling is heat treatment in the presence of a strong applied electric field. This adds an extra processing step, and in many materials such as polymers, the poling is susceptible to degradation by fairly low environmental temperatures such as might be experienced by PTILS in the field. For such reasons, materials having second-order susceptibility were not pursued.

For the purposes of PTILS, the most useful nonlinearity is that embodied in the third-order susceptibility $\chi^{(3)}$. We analyze the light wave electric fields into frequency components of angular frequency ω ($\omega = \pm 2\pi f$, where f is the cyclic frequency in Hz), where the negative frequencies indicate complex conjugate electric field amplitudes. Then the polarization response in general is at a frequency which is the sum of up to three different frequencies appearing in the applied electric fields as follows:

$$P_i^{(3)}(\omega_a) = \varepsilon_o \chi_{ijkl}^{(3)}(-\omega_a; \omega_b, \omega_c, \omega_d) E_j(\omega_b) E_k(\omega_c) E_l(\omega_d)$$

where the frequency ω_a and the wavevector k_a of the output wave are related to the frequencies and wavevectors of the input waves as follows:

$$\omega_a = \omega_b + \omega_c + \omega_d \quad \text{(energy conservation)},$$

and

$$\vec{k}_a = \vec{k}_b + \vec{k}_c + \vec{k}_d \quad \text{(phase matching)}$$

where the wavevector magnitude is related to the vacuum wavelength λ_0 as

$$k = 2\pi/\lambda_0.$$

Here i, j, k, and l denote x, y, and z direction components of the $\vec{E}$ and $\vec{P}$ fields. For complex crystal structures, the $\chi^{(3)}$ tensor has many independent components.

But for the amorphous materials of most optical fibers, the materials are largely isotropic and there are only three independent parameters as follows:

$$\chi_{xxxx},\ \chi_{xyxy},\ \chi_{xxyy},\ \chi_{xyyx} \neq 0$$

$$\chi_{xxxx} = \chi_{xyxy} + \chi_{xxyy} + \chi_{xyyx}$$

} 3 independent parameters,

and usually the scalar $\chi^{(3)}$ denotes the following particular tensor component

$$\chi^{(3)} = \chi_{xxxx} = \chi_{1111}.$$

(Note that in the above, the x and y stand for any of the x, y, and z directions; that is, $\chi_{yyyy} = \chi_{xxxx}$, $\chi_{yzyz} = \chi_{xyxy}$, etc.)

Even with the limitations on $\chi^{(3)}$ for isotropic materials, we can see that there is a rather rich variety of effects that can be obtained by suitable choices of electric field frequencies and orientation of electric fields. Several examples are the following:

Third-Harmonic Generation (THG):

$$\omega_b = \omega_c = \omega_d = \omega \Rightarrow \omega_a = 3\,\omega$$

DC-Field Induced Second Harmonic Generation (DCFISH):

$$\omega_b = 0 \text{ (DC field)},\ \omega_c = \omega_d = \omega;\ \Rightarrow \omega_a = 2\,\omega.$$

Nonlinear Refractive Index Contribution, n_2:

$$\omega_b = -\,\omega_c = \omega_d = \omega \Rightarrow \omega_a = \omega$$

and

$$P_i^{(3)} = \varepsilon_o \frac{3}{4} \chi_{iiii}(-\omega;\ \omega,\ -\omega,\ \omega) \left|E_i(\omega)\right|^2 E_i(\omega)$$

where

$\left|E_i(\omega)\right|^2 \propto I(\omega)$, the intensity

$$\mathrm{Re}[\,\chi_{iiii}(-\omega;\,\omega,\,-\omega,\,\omega)] \propto n_2(\omega)$$

and the total refractive index at frequency ω is

$$n(\omega) = n_0(\omega) + n_2(\omega)\, I(\omega)$$

The nonlinear refractive index effect is the one we follow in most of this analysis of nonlinear effects for PTILS. The effects which involve significant changes of light wave frequencies, such as the THG and DCFISH effects, would require inspection equipment with much greater spectral bandwidth and capability of spectral analysis than would be justified for on-site inspection.

To demonstrate the range of nonlinear refractive indices that was observed, table F-2 gives a selection including as a baseline the standard optical fiber materials of silica and polymethyl methacrylate (PMMA). Note that the n_2 tabulated here is the coefficient for intensity, as opposed to the coefficients for $|E_{max}|^2$ or for $\langle |E(t)|^2 \rangle$, as are frequently reported in the literature.

Table F-2 also includes several recently reported materials exhibiting considerably enhanced nonlinearity, including three with very large values. These very large values were found under very unusual conditions: (1) the "DAN" crystal fiber was only 4 mm long; (2) the 514 nm wavelength used for determining n_2 for the Er-doped silica bi-core fiber was a resonance line or very close to it for the Er ion system; and (3) the determination of n_2 was reported only for the spectral region very close to the Z_3 exciton resonance of the CuCl material used in the doping of the glass. Thus the two largest values of n_2 correspond to resonant, or near resonant, wavelengths, where the attenuation to be expected could also be large. Most of the very large values have been reported in the research literature only very recently, and little has been learned about how far significant enhancements of n_2 persist away from the resonant regions where the attenuation would be more moderate. This question was pursued with the researchers that published the high values of n_2, but no definitive results have been received.

Table F-2. Selected values of the nonlinear refractive index coefficient n_2.

Material	Reference	Wavelength (μm)	n_2 (10^{-12} m^{2}W^{-1})	Attenuation (m^{-1})	n_o	Notes
Lucite (probably PMMA)	Smith (1986)	1.064	0.77		1.49	Derived from data by Moran (1975).
Silica	Kuzyk (1991) (quoting Stolen (1978))	0.51	0.27	2.3×10^{-3}		
Lead glass	Kuzyk (1991) (quoting Newhouse (1990))	1.06	2.2	0.46		
ISQ/PMMA	Kuzyk (1991)	1.3	40.8	4.6		Fiber
BSQ/PMMA	Kuzyk (1991)	1.3	87.7	4.6		No fiber.
Azo dye attached to acrylate and copolymerized with PMMA	Matsumoto (1987)	2.05 (in) 0.65 (out)	90 (est.)			Thin film measurement for THG, yielding $\chi^{(3)}$ = 1.25 x 10^{-12} esu at 25.9 mol-percent azo dye in copolymer. n_2 estimated from $\chi^{(3)}$ value and n_o = 1.49 (PMMA).
DANS [4-dialkylamino-4'-nitro-stilbene]	Marques (1991)	1.064	70 ± 10		1.616 TE 1.624 TM	Thin film. Nonresonant effect.
DAN2 [4-dialkylamino-4'-nitro-diphenyl-butadiene]	Marques (1991)	1.064	190 ± 10		1.623 TE 1.618 TM	Thin film. Nonresonant effect.
DAN [4-(N,N-dimethylamino)-3-acetaminonitro benzene]	Yamashita (1990)	0.835	5.2×10^{3}		1.778	Single crystal of DAN in flint glass capillary; crystal length 3.9 mm; crystal diameter 4.6 μm.
Er-doped silica	Betts (1991)	0.514	$6.9 \pm 1.5 \times 10^{4}$			Twin core fiber, one core doped; no coupling between cores. Probable resonant effect.
CuCl-doped borosilicate glass	Justus (1990)	0.370 to 0.388	4×10^{7}			Thin film. CuCl microcrystallites (av. 4.4 nm diameter) dispersed in glass; 0.5% CuCl by weight. Resonant effect (Bulk Z_3 exciton peak at 0.384 μm).

References for table F-2:

Betts, R. A., Tjugiarto, T., Xue, Y. L., and Chu, P. L. (1991) IEEE J. Quantum Electron., **27**, 908-913.

Justus, B. L., Seaver, M. E., Ruller, J. A., and Campillo, A. J. (1990) Appl. Phys. Lett., **57**, 1381-1383.

Kuzyk, M. B., Paek, U. C., and Dirk, C. W. (1991) Appl. Phys. Lett., **59**, 902-904.

Marques, M. B., Assanto, G., Stegeman, G., Moehlmann, G. R., Erdhuisen, E. W. P., and Horsthuis, W. H. G. (1991) Appl. Phys. Lett., **58**, 2613-2615.

Matsumoto, S., Kubodera, K., Kurihara, T., and Kaino, T. (1987) Appl. Phys. Lett., **51**, 1-2.

Moran, M. J., She, C.-Y., and Carman, R. L. (1975) IEEE J. Quantum Electron., **11**, 259-263.

Newhouse, M. A., Weidman, D. L., and Hall, D. W. (1990) Opt. Lett., **15**, 1185-1187.

Smith, W. L. (1986) Handbook of Laser Science and Technology, **Vol. 3**, Section 1.3, ed. M. J. Weber. Boca Raton, FL: CRC Press.

Stolen, R. H., and Lin, C. (1978) Phys. Rev. A, **17**, 1448-1453.

Yamashita, M., Torizuka, K., and Uemiya, T. (1990) Appl. Phys. Lett., **57**, 1301-1303.

It should also be noted that the attenuation constant for the ISQ and BSQ doped PMMA is very large (20 dB/m), so that it will be hard to maintain a significant NLOE in such materials over a significant distance. However, Kuzyk et.al., (1991) project that they may be able to reduce the attenuation by at least a factor of ten, while also increasing n_2 by a factor of ten.

The value of n_2 estimated for the azo dye attached to an acrylate/methyl-methacrylate copolymer uses the 3rd order susceptibility, $\chi(-3\omega;\omega,\omega,\omega)$, reported from a third harmonic generation (THG) experiment, and assumes for purpose of the estimate that its value is approximately that for $\chi(-\omega;\omega,-\omega,\omega)$ (for the n_2 effect). This is a rough approximation; therefore, the value for n_2 for this material in table F-2 is only good for an order of magnitude estimate. The value of n_0 used was that of PMMA.

F.23.1 Evaluation of Potential Nonlinear Enhancement of OTDR Splice Detection.

The first task undertaken was to evaluate the potential for NLOE to enhance splice detection with an OTDR. The backscattering from a splice in optical fiber is a complex phenomenon in detail because of the cylindrical geometry of the core/clad system, the breaking of cylindrical symmetry by the lateral and angular misalignments at a splice, and the potential effects of multiple reflection interference between the two adjacent faces of the fibers being joined at the splice. (Fusion splicing of silica fiber is missing the multiple reflection complication, but has complications of its own.)

A first step in the evaluation is to consider the Fresnel reflection at the planar interface between two optical media such as that of the core material and that of air or an "index-matching" medium. Consideration of this simple case will determine whether more complex analysis is required.

F.23.1.1 Nonlinear Effects in Fresnel Reflection at an Interface. Reflection and transmission at a planar interface between two optical media are characterized by the Fresnel equations. Since an OTDR is currently used in PTILS inspection, the primary interest here is in the reflection. Therefore, focus is given to the reflectance equations. For plane waves of light in medium 1 (refractive index n_1) incident at the angle θ_i to the interface with medium 2 (refractive index n_2),

where the transmitted wave emerges in medium 2 at the angle θ_t, the Fresnel equations for the ratio of reflected electric field amplitude, $R_{\parallel,\perp}$, to incident electric field amplitude, $A_{\parallel,\perp}$, are given by

$$\frac{R_\parallel}{A_\parallel} = \frac{n_2 \cos\theta_i - n_1 \cos\theta_t}{n_2 \cos\theta_i + n_1 \cos\theta_t}$$

and

$$\frac{R_\perp}{A_\perp} = \frac{n_1 \cos\theta_i - n_2 \cos\theta_t}{n_1 \cos\theta_i + n_2 \cos\theta_t}$$

where θ_t is given in terms of θ_i, n_1, and n_2 by Snell's Law:

$$n_1 \sin\theta_i = n_2 \sin\theta_t$$

The $\parallel$ refers to the electric field components parallel to the plane of incidence, and $\perp$ refers to components perpendicular to the incidence plane.

The reflectances (the relative reflected intensities), $R_{\parallel,\perp}$, for the two polarizations are the square magnitude of the respective ratios $R_{\parallel,\perp}/A_{\parallel,\perp}$. For normal incidence, the distinction between the two polarizations disappears, and the reflectance takes the simple form

$$R = \frac{(n_1 - n_2)^2}{(n_1 + n_2)^2}$$

The approximation of normal incidence is a good approximation for our purposes, because even for fiber of fairly large numerical aperture, say 0.5, the weakly guided modes of the fiber with a refractive index of, say 1.5, will be incident on a cleaved end with angles less than 20°.

Since many relations in optics have historically been based on linear response (e.g., intensity independence of the refractive index), the derivation of Snell's law of refraction and Fresnel's laws of reflection at a planar interface between two dielectrics was carefully reconsidered to make sure that they are not

limited by any implied assumption of linear response in their foundation. The conclusion is that, so long as the incident, reflected, and transmitted waves are *straight-crested plane* waves (i.e., the spatial dependence of these waves is that of plane waves in the form of $\exp(i\, n\, \mathbf{k}\cdot\mathbf{r})$, where $n = n_0 + n_2 I$ and $k = 2\pi/\lambda_0$), then Snell's law and Fresnel's laws follow from fundamental principles, with the refractive indices appearing in them being the total refractive index $n = n_0 + n_2 I$ for the respective media.

F.23.1.2 Evaluation of the Potential for Splice Detection via Nonlinear Effects in Reflection. The next step is to estimate whether NLOE can be detected in Fresnel reflection such as might appear in a butt joint splice with reasonable care to fill the gap with index-matching fluid. Again, we take the approximation of normal incidence, and consider the interface between a nonlinear fiber core material (medium A) having $n_2 = 100 \times 10^{-19}$ m^2/W (slightly more nonlinear than the BSQ/PMMA material in table F-2) and a linear material (medium B). The key part of the normal reflectance R is the difference in the refractive indices for the two media joined at the interface:

$$\Delta n = n_A - n_B = \Delta n_0 + \Delta n_2$$

where

$$\Delta n_0 = n_{0A} - n_{0B} \quad \text{and}$$
$$\Delta n_2 = (n_{2A} - n_{2B})\, I$$

The full set of Cargille Series A refractive index liquids (Cargille (1991)) is something of an industry standard of index matching fluids for laboratory work. In this set there is a 0.002 step in refractive index between adjacent liquids. Assume that the linear refractive indices can be matched to the precision of one such step; we take $\Delta n_0 = 0.002$.

We look for the intensity that would give a nonlinear contribution to the refractive index difference of the same size: $\Delta n_2 = 0.002$. Define the intensity that gives this Δn_2 as $I_{.002}$:

$$I_{.002} = \frac{0.002}{n_{2A} - n_{2B}}$$

Now, with our nominal nonlinear core material, $n_{2A} = 100 \times 10^{-19}$ m^2/W, and a linear adjacent material, $n_{2B} = 0$, we find that $I_{.002} = 2 \times 10^{14}$ W/m^2 = 200 W/μm^2. A 62.5 μm diameter fiber core has a cross section of 3.07×10^3 μm^2, and a 240 μm diameter fiber core (representative of the PMMA in current PTILS) has a cross section of 4.5×10^4 μm^2; thus, an input intensity of $I_{.002}$ = 200 W/μm^2 corresponds roughly to input powers of 600 kW and 9 MW, respectively.

To give some perspective to these powers, consider the following points:

(1) Byron and Pitt (1985) cite as an example of upper limits of power transmission through optical fiber a report of 400 W CW transmitted over meter-lengths for robotic welding applications. (The fiber diameter was not given by them.) Their own work demonstrates that in a 50 μm core, GeO_2-doped silica fiber at 1.06 μm wavelength, the output power at 1.06 μm tends to saturate at 100 to 200 W for fiber lengths of a few hundred meters or more, even though the input power continued up to nearly 1 kW. Raman scattering appeared to be the predominant mechanism shifting the input power out of the 1.06 μm band into mainly longer wavelengths.

(2) In the BDM work on PTILS, damage was observed in 500 μm core PMMA fiber at fluences slightly above 0.25 J/cm^2 with 530 nm pulses of 7 ns length; this corresponds roughly to a peak intensity of 0.36 W/μm^2. (There was no indication in the OTDR signal of nonlinearity in the PMMA fiber or the index-matching fluid as the input power increased up to the onset of noticeable permanent damage in the PMMA fiber.)

(3) The sources in the Antel and Optoelectronics OTDRs planned for PTILS, input less than 0.1 W into the fibers under test.

Thus, we conclude that NLOE can be a significant source of Fresnel reflection enhancement only when n_2 can be much larger than 100×10^{-19} m^2/W. Whether this can be achieved for our purposes remains to be investigated. The resonant or near resonant n_2 for Er-doped silica and CuCl-doped borosilicate glass in table F-2 are respectively 690 and 400,000 times greater than the nominal value we considered in the previous paragraphs. The Er-doped silica at the

reported doping levels may not offer enough n_2 enhancement even at its resonant value to get the $I_{.002}$ value down to a feasible level. The resonant value of n_2 for the CuCl-doped glass can get the input power down to 1.5 to 23 W for the two nominal PTILS fiber sizes, but the question is whether the accompanying attenuation due to the resonance will reduce the available power at a potential splice site too much. BDM pursued with the authors of the CuCl-doped glass work the question of the expected persistence of the n_2 enhancement into the spectral regions of interest to PTILS, and the expected attenuation there, but had not received a definitive answer by this writing.

The smallness of the nonlinear enhancement of Fresnel reflection at a splice can be understood from the point of view that the effect of the nonlinear properties here is small because it is being produced in a very small interaction volume. The interface is smaller in the direction of propagation than the light wavelength itself. On the other hand, for phenomena that arise from large interaction volumes, such as the entire length of the fiber, the cumulative nonlinear effect can be significant.

F.23.2 Search for Nonlinearity-enhanced Optical Fiber Materials and Sources of Supply.

The search for nonlinearity-enhanced optical fiber materials and sources of samples for use in PTILS developmental testing took a three-pronged approach, with considerable interactions between the first two prongs.

F.23.2.1 Literature Search. The literature search was kept as focused as possible on concerns that are likely applicable to the PTILS development. Since there is an enormous global-wide activity in nonlinear optical effects because of their economic potential in the areas of communication and high-speed, high-density optical computing, a general mechanized database literature search would generate a very large volume of items that would swamp our limited resources to evaluate. Instead, an approach that can be termed "key journals/key laboratories" was used.

Most of the important work on nonlinear optical fiber and related issues appears in a rather small number of journals, and from the relevant papers

appearing in them, key laboratories and collaborative researcher groups can be identified. The top half dozen journals appear to be Applied Physics Letters, Optics Letters, Journal of Lightwave Technology, Electronics Letters, Journal of the Optical Society of America B, and Physical Review B. Perusal of recent journal issues and recent volume indices, identified most of the key articles contributing to table F-2, and the remaining key articles came from referral by contact with key researchers.

F.23.2.2 Leading Researcher Search. A number of leading researchers were contacted by phone, FAX, and other correspondence. They were identified by a number of means. Chief among these were the following: prior acquaintance with them and their work in relevant optical research, authorship of key articles identified in the literature search, and referrals from other key researchers previously contacted. Persons contacted were asked about potential nonlinear fiber optic materials, potential sources of supply (at least for the small quantities needed for PTILS evaluation), and for suggestions of other people and organizations that it might be useful to contact.

One result of this search to date that can be summarized briefly is that no source of supply for nonlinear-enhanced optical fiber at acceptable cost for PTILS development was identified. Several university-based laboratories were identified who could fabricate nonlinear fiber on a custom basis, but at estimated costs of $20,000 to $100,000 per batch, which is too high for the PTILS development.

F.23.2.3 Supplier Search. In addition to the requests for referrals to potential sources of supply made in the leading researcher search and the follow-up of contacts they suggested, a systematic survey was made of all 18 companies listed as sources of supply of polymer optical fiber in a leading industry guide, the annual *Technology and Industry Reference* (December 25, 1991) published by *Lasers & Optronics.*

Not all the companies contacted responded to our inquiry. Of those that did respond, none could supply nonlinearity-enhanced optical fiber. The conclusion from this search is that while some of these companies may be willing to fabricate nonlinearity-enhanced fiber once a market has been identified for it, they are not

currently doing innovative R&D on nonlinear optical fiber, at least to the extent that they might have experimental lots of nonlinear fiber for evaluation purposes.

F.23.3 Consideration of Nonlinear Effects for Enhanced Tamper Detection.

F.23.3.1 General Considerations. The work of Betts et.al., (1991) cited in table F-2 for the Er-doped silica fiber offers some inspiration both for exploitation of nonlinear phenomena and for a fiber form more difficult to splice than current silica fiber. Their results were obtained with a twin core fiber, with one silica core undoped and the other doped at 300 ppm with erbium. They observed the intensity-dependent positions of the two-source interference fringes from the light exiting the downstream end of the fiber. Figure F-39 depicts this arrangement. The laser source beam was focused to illuminate both cores simultaneously; at the exit end of the fiber the emerging beams from the two cores spread until they overlapped and interfered. The interference fringes were observed at a distance D from the exit end of the fiber. Betts et.al., were able to measure phase shifts roughly proportional to fiberlength and input power at input powers of as low as 0.3 mW. At this power level, they obtained a phase shift of 1.2 radian in a fiber length of 2 m. At higher input power levels, the phase shift began to saturate in power, but continued roughly proportional to fiber length. At 4.5 mW, the 2 m fiber's phase shift had saturated to a value of about 5.3 radians. The saturation in power level arises because of the resonant population of excited states and excited state absorption.

Betts, et.al. did not report a full characterization of their fiber (no report of dimensions of the cores or of the separation between cores), but did assert that there was no light transfer between the cores for lengths of up to 20 m. However, the cores were very likely single-mode so as to simplify the interference conditions, and by the method of fabrication described in an earlier paper, the cores are rather elliptical in cross section.

The more complex structure of a twin-core fiber such as this has a potential for making undetectable splices more difficult. In principle, each core in the fiber could be examined separately with an OTDR so that more care must be exerted to align a splice. If the spacing between the cores and propagation parameters of

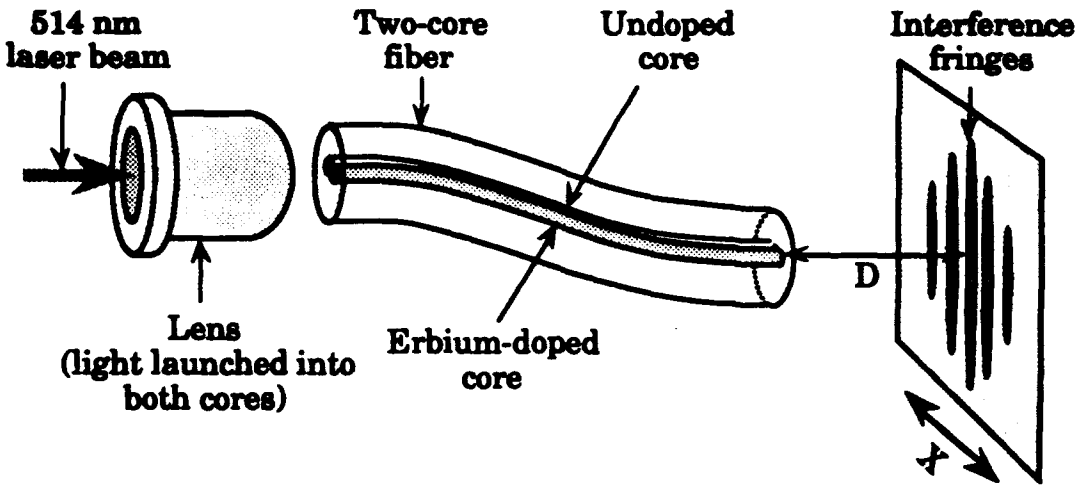

Figure F-39. Experimental setup to measure fringe shift due to nonlinear refractive index (after R. A. Betts, et.al., IEEE J. Quantum Electron. 27(4), (1991), 908).

the cores were close to the condition for inter-core coupling in the PTILS length, then a splicer would have to take care to maintain the lack of coupling, because a test for isolation between cores could be part of the inspection. The highly elliptical cores are birefringent, so that a splicer would have to take care to maintain this property, because a test for coupling between polarizations could be made a part of the inspection.

The interferometric properties of a twin-core fiber with one core linear and the other nonlinear may also offer some potential for splice detection. Even at low intensities (i.e., in the linear regime for both cores), a splicer would have to take care that a splice did not change the differential optical path between the two cores by more than a small fraction of a wavelength, or the fringe shift might be detected at inspection. For example, if the inspection instrument used light of 820 nm, a difference in path of 0.41 μm (a differential phase shift between the two cores of π radians) would shift the dark interference fringes into the place of the bright fringes. Consequently, a splicer would have to balance the optical path lengths in the two cores so that after the splice there would not be a difference of more than, say, about 0.2 μm path length between the two cores. Shorter wavelengths in the inspection instrument would make this test more difficult for a splice to pass.

The pattern of fringe shift as the intensity is increased may offer an additional potential for detecting subtle splices by serving as a signature. If conditions were feasible for a reflection-mode approach, this could be seen as an input power dependent modulation of the Fresnel reflection from the far end of the fiber. The input power could be varied by using an adjustable neutral density filter in the light path between the laser and the input end of the fiber. Care would have to be taken to assure that the reflected light exiting from the input ends of the two fibers is brought together so that the interference condition is obtained. Similar considerations would apply in a transmission-mode approach. (Note: The above discussion of interferometric properties does not require the assumption that the two core path lengths would be equalized in an installed PTILS; it *would* be necessary to record some sort of path length difference baseline on the PTILS at installation.)

It should be noted that this discussion concerning potential use of interferometric aspects is still somewhat speculative. It requires more assessment for feasibility. How to establish an interferometric baseline for a PTILS at installation and the effects of environment on the interferometric properties for an intact PTILS are key concerns to be investigated. If the twin core fiber has very low loss, it might be possible to run the inspection in a reflection-mode, because the reflection of light from the open end of the fiber will be about 3 to 4 percent (equivalent to an attenuation of the input light of 14 to 15 dB, apart from attenuation of light along the length of the fiber.) For more lossy fiber, the inspection would have to be run in a transmission-mode, depicted in figure F-39, or else the free end of the fiber cores would have to be mirrored so that almost all light incident on the end will be reflected.

For the non-interferometric properties (i.e., inspection of each of the twin cores individually), it remains to be determined how much of the tests might be accomplished with the addition of custom optical attachments to the presently planned OTDR. Mirroring of the free end of the fiber cores, mentioned in the previous paragraph, might have adverse effects on the use of OTDR measurements on individual cores because of the strength of the end-reflected would be 14 to 15 dB greater than encountered in usual uses of OTDRs.

F.23.3.2 Specific Considerations. The possibility of NLOE coupled with interferometric phenomena as an extension to PTILS testing directs our interest next to the question of what lengths of fiber are required to get a significant effect of NLOE in interference. For this purpose, define the π-phase length parameter l_π as the length of fiber required to get a difference of π radians in phase between a linear core and a nonlinear core of the same linear refractive index. This length would result in the shift of a bright fringe into the position previously occupied by a dark fringe. It depends explicitly on wavelength and has an implicit wavelength dependence contained in n_2. It also depends on the intensity. We will neglect resonant effects in the following discussion. Refer to Betts et.al., for the much more complex case of resonant effects. In the presence of attenuation, l_π has an implicit definition as given in the following development.

The intensity at point z is given in terms of the intensity I_0 at z = 0 by

$$I(z) = I_0 e^{-\alpha z}$$

The phase change in length dz due to the nonlinear component of refractive index is 2π times the ratio of the change in optical path length to the vacuum wavelength λ_0:

$$d\phi(z) = 2\pi \frac{n_2 I(z)\, dz}{\lambda_0}$$

Thus, the phase change of π due to the nonlinear component of refractive index is given by

$$\pi = \int_0^{\pi} d\phi(z) = 2\pi \frac{n_2 I_0}{\lambda_0} \int_0^{l_\pi} e^{-\alpha z}\, dz$$

$$= 2\pi \frac{n_2 I_0}{\lambda_0} L_\pi$$

where we have introduced the effective π-phase length L_π

$$L_\pi = \frac{1}{\alpha}(1 - e^{-\alpha l_\pi}) = \frac{\lambda_0}{n_2 I_0} \qquad \text{(F-1)}$$

Note that for vanishing attenuation ($\alpha \to 0$), L_π and l_π are identical. More generally, we compute L_π by the last member of equation (F-1), and then determine l_π as follows:

$$l_\pi = -\frac{1}{\alpha}\log(1 - \alpha L_\pi) \qquad \text{(F-2)}$$

Note that equation (F-2) implies a constraint on attenuation and L_π, because the argument of the logarithm must be positive; thus, we must have L_π bounded as follows:

$$L_\pi < \frac{1}{\alpha}$$

One meaning of this constraint is that if the attenuation is too large, then the intensity cannot be kept large enough to produce an additional phase shift of π radians due to the nonlinear effect.

For purposes of a first estimate, we focus on evaluation of just L_π, thereby ignoring attenuation for the moment. This is a rough approximation for materials with attenuations as large as that of the doped PMMA of Kuzyk et.al., (1991). But it allows a quick survey for suitability, and any material having a reasonably small value in this survey could then be more carefully assessed for the impact of attenuation. For many of the materials listed in table F-2, the associated attenuation coefficient was not reported along with the report of n_2; additional research will be necessary before l_π can also be determined for them. Also, for purposes of this quick estimate, we have sometimes ignored the effects of dispersion by using a value of n_2 at a wavelength significantly different from that at which the n_2 value was measured. Except possibly in the case of resonance NLOE (e.g., in the Er-doped silica), this is a much less gross approximation than neglecting attenuation. We also have assumed that the intensity is uniform

across the cross section of the fiber and that it is just the input power divided by the cross sectional area of the core.

For a nominal input power of 100 mW (approximately twice the power coupled into the fiber by the Optoelectronics OFM-series OTDR), table F-3 gives estimates for L_π for several materials, several wavelengths, and several core diameters. The "KPD Projection" is for a hypothesized material that Kuzyk et.al.,(1991) speculate that they can make with n_2 increased by a factor of 10 and with attenuation reduced by a factor of 10.

Table F-3. Estimates of the effective π-phase length L_π arising from n_2.

Material	n_2 (10^{-19} m^2/W)	Core Diameter (μm)	I ($W/\mu m^2$)	$(2n_2I)^{-1}$ (wavelength)	Source Wavelength (μm)	L_π (m)
Silica (Kuzyk 1991)	0.27	62.5	3.26×10^{-5}	5.7×10^{11}	0.680	390×10^3
PMMA (neat) (Smith 1986)	0.77	240	2.21×10^{-6}	2.9×10^{12}	0.680	2000×10^3
PMMA/ 1% BSQ (Kuzyk 1991)	41	240	2.21×10^{-6}	5.5×10^{10}	0.680	37×10^3
					1.300	72×10^3
PMMA/ 2% BSQ (Kuzyk 1991)	88	240	2.21×10^{-6}	2.6×10^{10}	0.680	17×10^3
		24	2.21×10^{-4}	2.6×10^8	0.680	170
					1.300	330
PMMA/ "KPD projection" (Kuzyk 1991)	410	240	2.21×10^{-6}	5.5×10^9	1.300	7.2×10^3
		24	2.21×10^{-4}	5.5×10^7		72
Er-doped silica (300 ppm) (Betts 1991)	6.9×10^4	62.5	3.26×10^{-5}	2.2×10^6	0.514	1.1
CuCl-doped borosilicate glass (Justus 1990)	4×10^7	62.5	3.26×10^{-5}	3.8×10^3	0.400	1.5×10^{-3}

References for table F-3:

Betts, R. A., Tjugiarto, T., Xue, Y. L., and Chu, P. L. (1991) IEEE J. Quantum Electron., **27**, 908-913.

Justus, B. L., Seaver, M. E., Ruller, J. A., and Campillo, A. J. (1990) Appl. Phys. Lett., **57**, 1381-1383.

Kuzyk, M. B., Paek, U. C., and Dirk, C. W. (1991) Appl. Phys. Lett., **59**, 902-904.

Smith, W. L. (1986) Handbook of Laser Science and Technology, Vol. 3, Section 1.3, ed. M. J. Weber. Boca Raton, FL: CRC Press.

The estimates in table F-3 indicate that the basic core materials (silica and PMMA) are not very favorable. Some of the nonlinear materials are worthy of further examination, particularly the Er-doped silica and the CuCl-doped glass. Even though the effective π-phase length differs from the actual π-phase length (which may not exist in fiber with high enough loss), the fact that Betts et.al., did observe significant power-dependent phase shifts indicates that, even in the resonant regimes these highly nonlinear materials can be used to exhibit power-dependent phase shifts.

F.24 CONSIDERATION OF OTHER MEANS OF ENHANCING PTILS TAMPER DETECTION.

F.24.1 Specialty Fibers with Intrinsic Tamper Resistance.

Late in the period covered by this report we were able to make contact with the group working on "secure fibers" at the Department of Energy's Battelle Pacific Northwest Laboratory. The specialty fibers they have been developing show considerable promise for application to PTILS. The nonlinear optical properties of the PNL materials are not yet known, so the potential application does not depend on such properties.

The PNL fibers are a lithium alumino-silicate glass core coated with a silicone polymer as the clad. The glass material has its composition adjusted and nucleating agents added so that the glass, after the process of drawing (from the melt) and adding the polymer clad, is on the verge of devitrification. Tamper resistance is contributed to in several ways in this system. In the PNL composition designs intended at the time of the stop-work order on the Creative Task, there were to be already some needle-shaped (acicular) micro-crystallites present in the as-drawn fiber, which would prevent good cleaves of the core of the fiber, and so inhibit high quality splices. (Since the end of the Creative Task, PNL's design compositions have moved slightly farther away from the verge of devitrification so the acicular crystals do not form in the as-drawn fiber; this was done to increase the light transmission through the fiber.) The original soft polymer clad also acts to inhibit high quality splices. It does not strip well, and when the fiber is cleaved through the clad, it tends to smear and contaminate the glass end. The same effect occurs under polishing actions. (Since the end of the

Creative Task, PNL has done some work with harder polymer clad materials in order to reduce water infiltration through the clad and thus increase the corrosion resistance of the fiber. This evolution has reduced somewhat the tamper-resistance contributed by the clad.) Finally and most strongly, the glass will devitrify to the point of opacity under attempts to heat it to a melting point to attempt a fusion splice (as depicted in figure F-40), thus ensuring the detection of such a splice with an OTDR. Also, the polymer clad is not compatible with such heating.

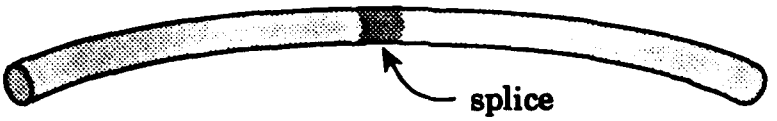

Figure F-40. Devitrification of PNL optical fiber at fusion splice.

The tamper resistant properties of such fibers indicate that it would be useful to pursue a collaborative effort with PNL to determine the feasibility of applying such fiber to PTILS. Some of the points to be pursued further are the following:

(1) Can the fibers' attenuation be made low enough to be compatible with the PTILS inspection instruments (OTDRs)? This implicitly involves an assessment of optical properties of the fibers at the operating wavelength(s) for the OTDRs.

(2) Can the use of this fiber in a single-wrap configuration make it possible to use the OTDR hosted in the Universal Videographic Reader computer (the Antel OTDR board), thereby making the separate OTDR unit unnecessary?

(3) Are the fibers' long term environmental responses compatible with the PTILS environmental requirements?

(4) In view of the tamper-resistant features of the fibers, can connections be made to them that are adequate for the purposes of PTILS?

(5) What kinds of coating/jacketing are necessary to protect the soft polymer clad, and how can it be applied?

(6) What life-cycle costs are to be expected for adoption of such fiber for the PTILS application?

F.24.2 Splice Sensitive Effects Detectable by Other Than Simple OTDR Measurements.

Mode conversion in multimode fibers has some attraction as a possible phenomenon for detecting high quality splices. For example, Ikeda et.al., (1977) examined the mode conversion for a very high quality splice (less than 0.01 dB loss). The tested splice was obtained by careful cleaving silica fibers, verifying by electron microscopy the perfection of the cleaved ends, alignment of the fiber ends at the splice with a 3D micromanipulator, and use of an index-matching fluid. When light of very close to an equilibrium mode distribution (assured by a long lead-in fiber wound on a small drum) was incident on this splice, although there was very little light power loss in the transmitted beam, about 11 percent of the power was redistributed from the lower order modes into the higher order modes. This mode conversion was most apparent when the exit power was analyzed by exit angle.

All analysis and experiments found were concerned with mode conversion in the transmitted beam, rather than in the reflected beam. Consequently, it is not immediately known whether significant mode conversion by a splice can be seen in reflection. However, there is at least one situation in which it is obvious that mode conversion would occur in reflection due to a splice. In the communications arena, reflections from joints sometimes cause concern because of interference with sources and processors. In such cases, the joints are formed by cleaving the fibers at a slight angle, so that most of the reflected light is redirected into lossy modes. If the angle is made too large, one can redirect all the reflected light into lossy modes so that there is negligible reflection, but that comes at the cost of substantial increase in the transmission loss, which could be seen by an OTDR as a significant drop of the Rayleigh floor beyond the joint. In a multimode fiber the slight angle cleave would definitely promote some of the incident power of the lower modes into the higher order modes.

If further research determines that mode conversion by a splice can be seen easily in reflection, then it may be possible to use an OTDR (with feasible modification) to inspect a optical fiber loop using the mode conversion effect. For example, one might devise a "single-mode fiber array (SMFA) mode test" inspection head to connect the OTDR to the fiber under test. This head might use a central single-mode fiber to inject the source light into the fiber under test on its axis, and one or more single-mode fibers at constant lateral displacement off the axis to collect the back-scattered light and convey it to the detector. While this arrangement is not a pure mode analyzer such as that described by Ikeda et.al., (1977), the central fiber would tend to excite the low order modes preferentially, and the laterally displaced receiving fibers would tend to collect the higher order modes preferentially.

If the SMFA inspection head arrangement proves feasible, an OTDR could locate a splice according to the time-delay at which the higher modes are received in increased strength. If this arrangement should not be feasible, it may still be possible to insert a proper mode analyzer into the light path of an OTDR and still get the splice location. In a regular reflection-mode inspection, however, one needs to keep in mind that on the return path there are joints (e.g., the OTDR bulkhead connector) that can also contribute mode conversion. Thus, one necessary point to clarify in developmental work would be to determine whether the mode conversion effects due to adversarial splices can be detected in the presence of mode conversion due to legitimate joints in reflection-mode. Another point to be explored is whether mode conversion arising from the physical configuration of the optical fiber in a PTILS could reduce the detectability of mode conversion due to adversarial splices. For example, any tight coil of a lead-in section of fiber such as that intended to keep the dead zone of the PTILS connector within the protected volume of the tag block can be expected to give some mode conversion, and the magnitude of this would have to be evaluated in development testing.

The transmission-mode use of mode conversion is more attractive by avoiding two-way passes through unavoidable joints and by virtue of the known mode conversion in transmission. However, it requires instrumental access to both ends of the fiber and different instrumentation from the kind currently employed for PTILS. Some of the questions mentioned above in connection with

reflection-mode use of mode conversion will also have to be settled for a transmission-mode use.

F.25 CONCLUSIONS.

In the preceding sections, BDM efforts at identifying means of improving the detection of adversarial splices in PTILS have been discussed. Based on the findings discussed, the following further work is recommended:

(1) The development for the PTILS application of the tamper-resistant specialty glass optical fiber developed by PNL appears to be most attractive. Much of the development work for the material is already done, the PNL development group and their management are interested in a collaboration with the DNA PTILS effort, and there appears to be a good prospect for a successful outcome near-term. In addition, use of this type of fiber may open up the possibility of using the OTDR hosted in the Universal Reader unit, thereby simplifying the on-site inspection equipment requirements. It is strongly recommended that this line of development be continued.

(2) The potential use of more complex configuration optical fiber such as the twin core fiber configuration of Betts et.al., (1991) looks attractive, because such configurations increase the complexity of adversarial splicing substantially and offer increased opportunities for detection, while still keeping OTDR-type inspections. The added features of the use of a nonlinear core and of interferometric inspection may prove useful also. It is recommended that the feasibility of twin-core fiber be investigated further, particularly if Betts et.al., (1991) can provide samples of fiber for evaluation.

(3) While the potential use of other highly nonlinear optical fiber for improving the tamper detection of PTILS is interesting and may have some long-term prospects of success, it does not appear for the near-term that the sources of supply for such fiber and on-site instrumentation for PTILS use are mature enough to support intensive efforts for the current DNA tasks. Further inquiries to NLOE

researchers can be made with little effort. It is recommended that these researchers be contacted.

(4) The mode conversion effects of splices looks interesting, because their use would not involve any change of the tag/seals themselves from current designs. Further investigation will be required to assess whether such effects can enhance the detectability of adversarial splices in PTILS configurations and environments, and whether the instrumentation to provide such detection can be obtained by acceptable modifications to current PTILS instrumentation. Additional feasibility study of this approach is recommended.

F.26 FOURIER OPTICAL INTRINSIC SIGNATURE.

The Fourier optical concept is an example of an intrinsic tag. The concept is to use optical features of the materials of a treaty-limited item to provide its unique identity. The hope is to be able to obtain scattered or reflected light from below the surface of the material, since return from only the surface might offer an adversary the opportunity to counterfeit the surface features, and thereby the identity of the item. Also, surface-only intrinsic signatures are susceptible to environmental degradation and increased probability of false indication of tamper. Only a low level-of-effort was expended on the Fourier work because the outcome of the first stage of proof-of-concept analysis was that it was not likely to provide an acceptable level of security. The Fourier optical tag work was performed during May 1991.

The concept of Fourier optics is fundamental in image formation from optical components such as a lens, particularly when coherent light is used to illuminate the object. Propagation of light from a point source in the front focal plane of a converging lens and through the lens produces a plane wave behind the lens. Therefore, propagation of coherent light from a complex object, composed of many point sources, and through a lens results in the interference pattern (Fraunhofer diffraction) in the back focal plane. This diffraction image is the Fourier transform image of the object. These concepts are depicted in figure F-41.

Ideally, the Fourier optical image would provide detailed information of the optical features of a material, including its subsurface features. Initially perceived advantages of the Fourier optical intrinsic signature include:

(1) Operationally simplicity
(2) Minimal intrusiveness
(3) Potential robustness against counterfeiting
(4) Potential unique, high-resolution information about material structural detail
(5) Potential robustness against environmental degradation
(6) Micron resolution (due to the use of visible light wavelengths)
(7) Inexpensive production costs.

Perceived disadvantages include: (1) surface features are potentially counterfeitable, (2) appropriate resolution must be proven (too much resolution could result in too much sensitivity to extraneous information), and (3) environmental degradation (e.g., dust, grease, moisture) could be a problem (including possible moisture condensation in voids around glass fibers).

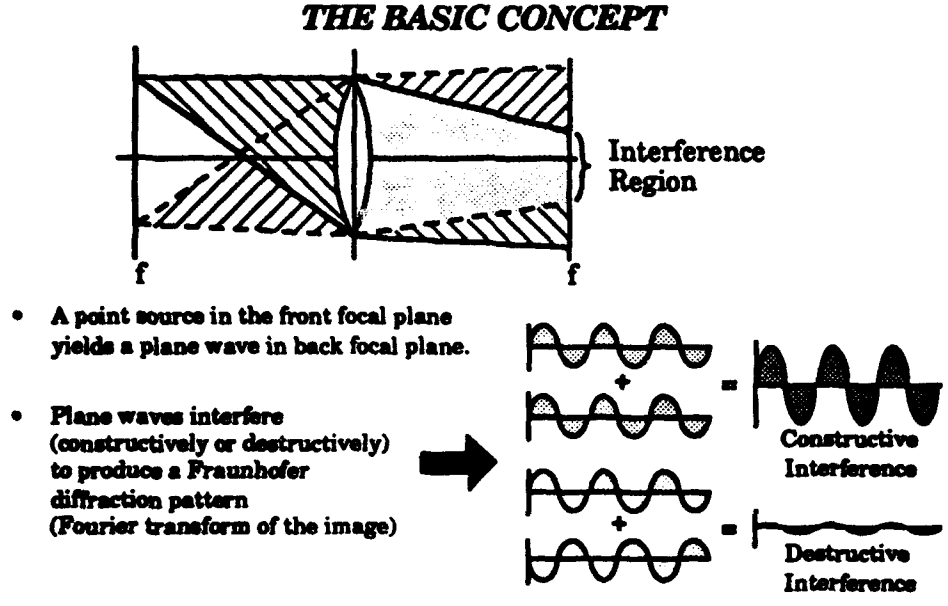

Figure F-41. Fourier transforms with a lens.

The Fourier optical imaging method takes advantage of the Fourier transform concept in mathematics. Physically, an optical system produces an image that is the Fourier transform of the original object that is being examined. A very simple example of this phenomenon is shown in figure F-42. Here a small aperture or pinhole is illuminated uniformly with parallel light and the lens forms the Fourier transform or the Fraunhofer diffraction pattern on a screen.

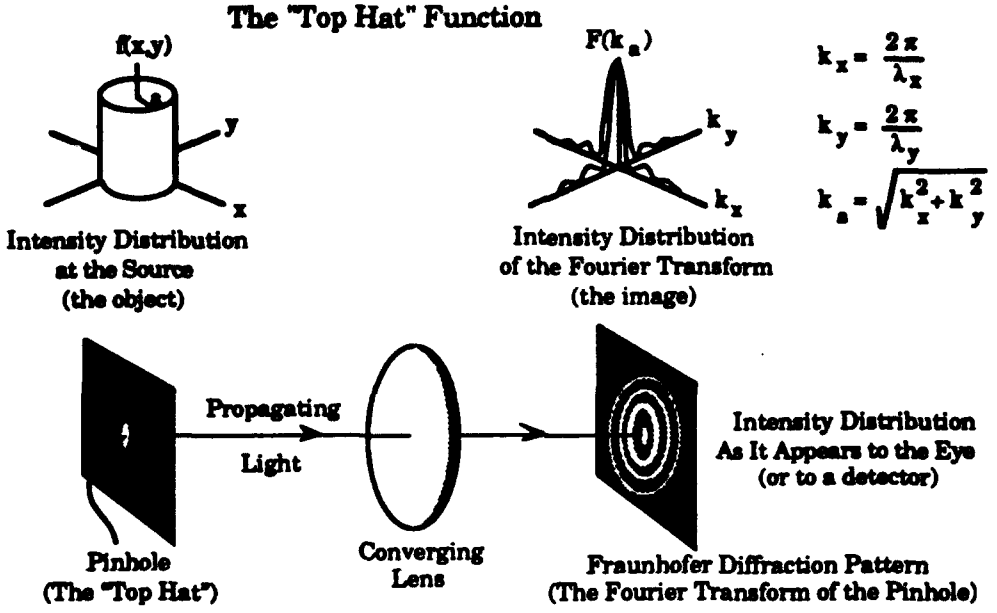

Figure F-42. A simple illustration of how a Fourier transform happens.

F.27 SYSTEM DESCRIPTION.

A prototype system was not developed because of the results of proof-of-concept measurements. At the time of this work, the arms control treaty verification scenario that drove the development of tags and seals was START. The proof-of-concept measurements showed that only surface features of the materials examined determined the Fourier images obtained. However, if a scenario exists where surface information is adequate and potential environmental degradation of a signature can be controlled, a possible Fourier optical imaging system is represented in figure F-43.

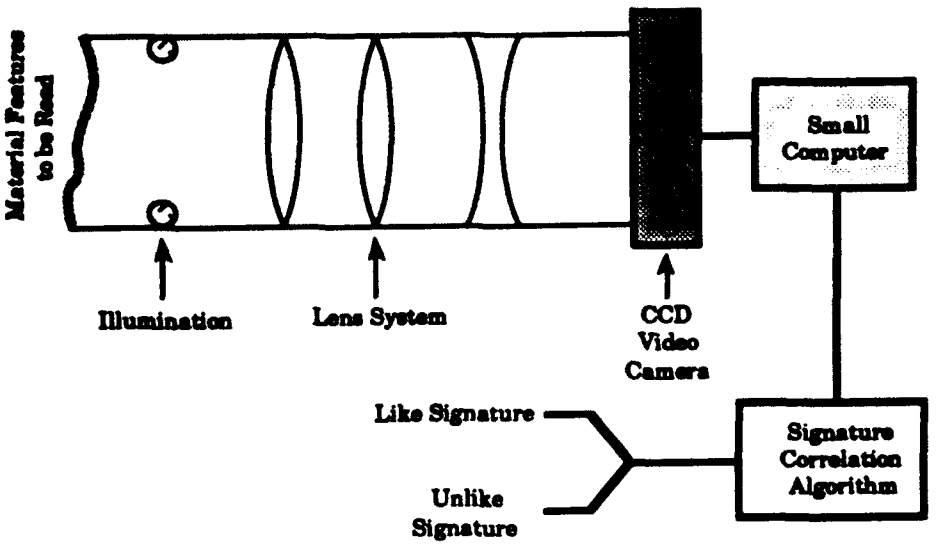

Figure F-43. Conceptual Fourier optical imaging system design.

F.28 PROCESS EMPLOYED.

Similar to the simple pinhole case illustrated in figure F-42, more complex objects can be examined with simple optical systems and a Fourier transform or Fraunhofer diffraction pattern is produced in the image plane. Conceivably, the skin material of a missile that is treaty-limited could produce a unique Fourier image. However, in order to assure non-counterfeitability, it was extremely desirable for START purposes to be able to gain information in the image from material features below the surface. Therefore, the laboratory proof-of-concept measurements had among their objectives finding Fourier image features that arose from subsurface features. The material chosen for proof-of-concept sample measurements was fiberglass-epoxy composite missile skin.

A set of progressive laboratory measurement steps was planned for proof-of-concept. The planned set of measurements are depicted in figure F-44.

The measurement procedure was designed to check that Fourier transform images were obtained for known geometry objects and then proceed to the more complex structures existing in the fiberglass/epoxy composite. The eventual goal was to obtain Fourier images that were adequately sensitive to the internal structure of the composite materials.

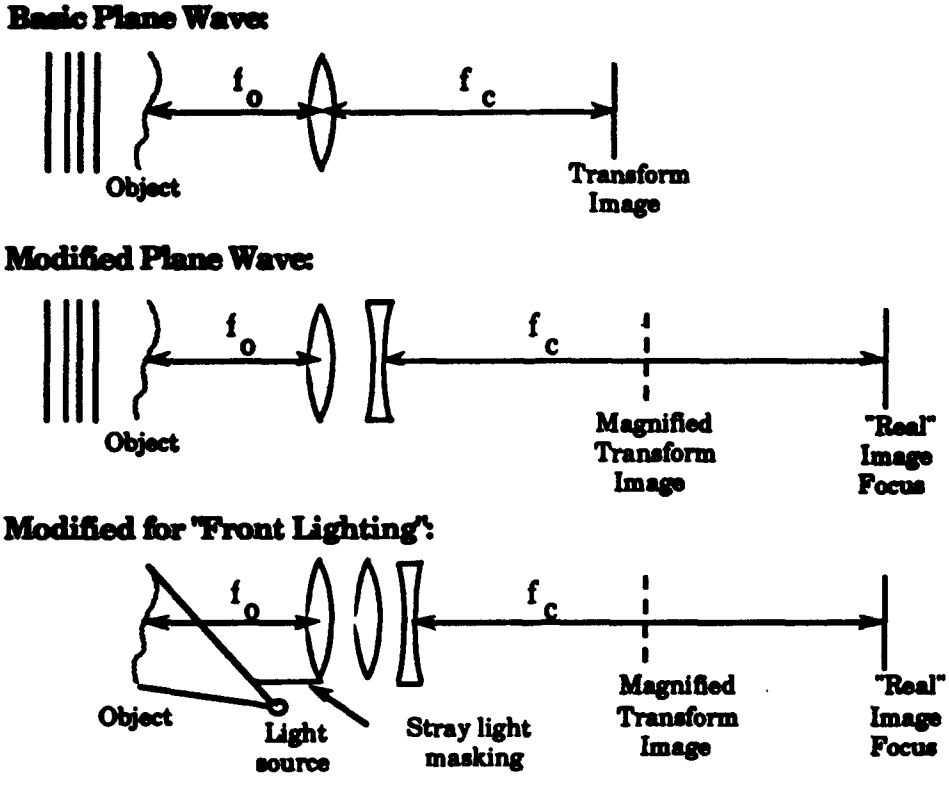

Figure F-44. Steps of measurement sophistication.

The test plan included the following steps:

(1) measure the Fourier images of known object geometries,
(2) measure the Fourier images of real materials,
(3) quantify monochromatic coherent vs. white light differences,
(4) determine practical resolution achievable,
(5) determine resolution required,
(6) perform industry search for existing apparatus,
(7) construct a correlation algorithm and equipment,
(8) test new and degraded real surfaces

Expected diffraction patterns were obtained for the following cases:

- monochromatic (single wavelength) backlighting of a known pattern.
- white light (polychromatic) backlighting of a known pattern,
- monochromatic laser (coherent) front-lighted known pattern,
- white light front-lighted known pattern.

These measurements all used apertures, high-resolution geometrical transmission patterns, or high-resolution geometrical reflection patterns.

Following these Fourier pattern measurements from relatively simple geometrical patterns, measurements were made of reflection Fourier patterns from the fiberglass/epoxy composite missile material samples. These measurements used both coherent and incoherent light from a laser and other sources. The results were unsatisfactory. The Fourier patterns were difficult to obtain repeatability because of alignment problems. Further, it was demonstrated that the patterns obtained were primarily from surface reflections and the detailed random complexity subsurface features in the composite material, such as the random lay of glass fibers in the epoxy, caused uncontrollable scattering of light that introduced noise into the Fourier image.

Upon these determinations, the Fourier optical intrinsic tag concept was not pursued further, due to requirements for START verification.

F.29 FINAL STATUS/AVAILABILITY.

A Fourier optical intrinsic tag system is unavailable. The decision to drop this concept was based on the need in high asset arms control of unique, non-counterfeitable, repeatable signatures from subsurface features.

F.30 LESSONS LEARNED.

Some signature methods, such as the visible light Fourier images, yield too much resolution. The extreme resolution results in sensitivity to extraneous information that may not be controllable.

F.31 NULL FIELD LOOP.

The null field loop, another concept for loop seal/tags was originated during the exploratory phase that led to the Magnetostrictively Interrogated Loop Seal (MILS). This was not developed to the same level as MILS. The null field loop uses cancellation of magnetic fields around an array of conductors for tamper detection. If this type of array is designed so that a very small or null field is obtained when a specific configuration of currents is introduced into the conductors at inspection time, then tampering may be detected simply by measurement of a magnetic field above a threshold (null) value as apart of the inspection procedure.

The concept presented in this section is preliminary; only analysis was performed, and total system definition of the suggested tag was not carried out in detail. The null-field tag looks quite promising, but a number of questions remain, including construction of a device for measurement of the fields, and termination of the conductor array to prevent its use as an inadvertent antenna.

F.32 NULL-FIELD LOOP SEAL/TAGS.

The null-field loop seal/tag is a device which utilizes cancellation of magnetic fields around an array of conductors for tamper detection. If this type of array is designed so that a very small or null field is obtained when certain currents are introduced into the conductors, then tampering may be detected simply by measurement of a magnetic field above a threshold (null) value. This idea was not taken through laboratory tests, but the preliminary analyses described below indicated that it may have potential use if developed further. The array of wires could be used to encircle the tagged item, and the ends of the network could be locked into a tamper-proof connector which itself contains a unique tag for the controlled item. The purpose of the conductor array would thus be to seal the unique connector to the tagged item, and to provide evidence of tampering.

F.32.1 Analysis and Models.

The magnetic fields surrounding a long bundle of current-carrying thin wires depend strongly on the configuration of the wires. The configuration is determined by both the direction of the currents and the distribution of the wires within the bundle. For this effort, the magnetic fields around long arrays of 16 wires were studied. Figure F-45 shows this array, for which the wires are placed in a 4 by 4 arrangement.

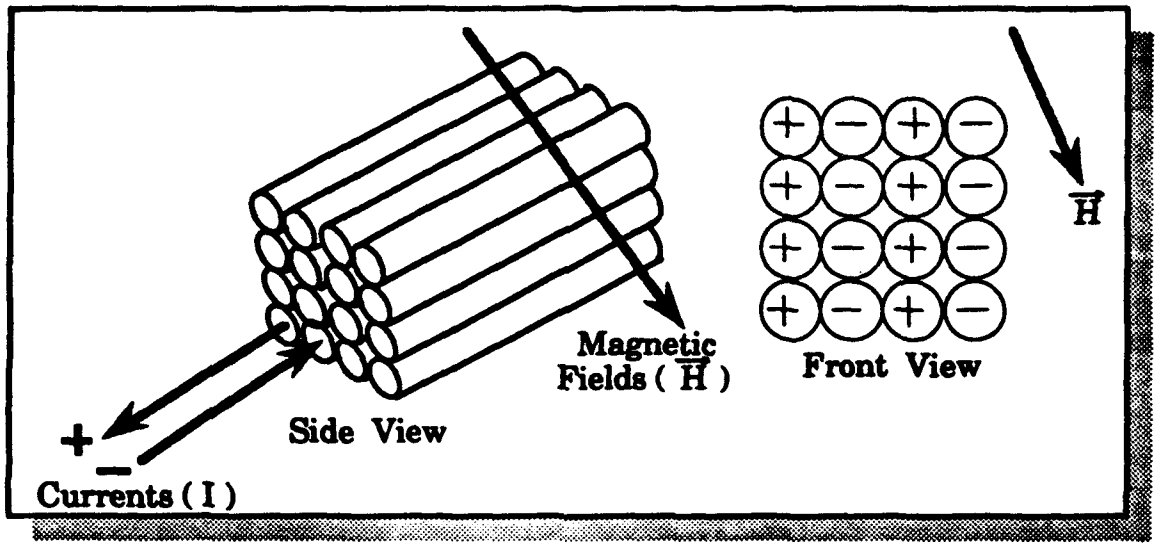

Figure F-45. A 4x4 array of current carrying wires.

The magnetic field around a very long straight wire is given by

$$H = \frac{I_w}{2\pi r},$$

where I_w is the current in the wire, and r is the perpendicular distance from the wire to the field point. If the wire runs along the z axis, and an (x,y) coordinate system is used to describe the field plane as shown in figure F-46, then the distance r is given by $\sqrt{(\Delta x^2 + \Delta y^2)}$, where $\Delta x = x_f - x_w$, $\Delta y = y_f - y_w$, the field point location is (x_f , y_f), and the wire location is (x_w , y_w). The x and y components of the magnetic field can then be expressed as:

$$H_x = \frac{-I_w \Delta y}{2\pi r^2}, \quad H_y = \frac{I_w \Delta x}{2\pi r^2}.$$

Simple summations of the above expressions over the 16 wires produce the net fields at any desired field point. Results for five different wire configurations are presented in section F.32.2.

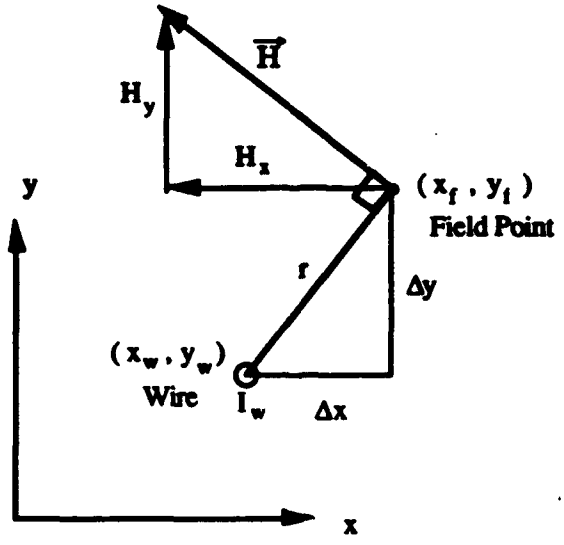

Figure F-46. Geometry for magnetic field calculation for a single wire.

F.32.2 Results.

The magnetic fields for several different configurations were developed and analyzed. For most of these configurations, the spacing between the centers of adjacent wires was set as 1 mm; one configuration used a spacing of 2 mm. For all simulations, the currents in each wire were set at 1 ampere. Total fields were calculated on a 21 by 21 grid of field points spaced 1 cm apart, for a total area of 20 cm by 20 cm. In the first configuration studied, the currents are unidirectional (running in the same direction); the fields for this case appear in figure F-47. The second configuration is described as bipolar; the top 8 currents run opposite to the bottom 8 currents. The fields for the bipolar case are shown in figure F-48. For the staggered configuration, alternating columns (each column having four wires) are used; the results for this case are displayed in figure F-49. The checkerboard configuration consists of an array in which the current directions alternate horizontally and vertically with every wire; this is shown in figure F-50. All of the wire arrays for figures F-47 through F-50 have 1 mm wire separations. The fields for a checkerboard configuration with 2 mm wire spacing are given in

figure F-51. The average and peak fields (in amps per meter) for all 5 cases are listed in table F-4. The peak fields are reported for the field point closest to (but still outside) the wire array, which is a distance of about 1.41 cm from the center of the array.

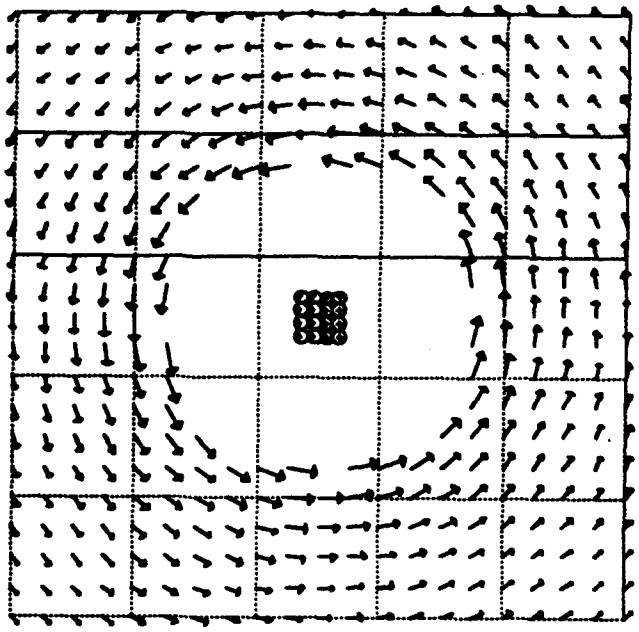

Figure F-47. Unidirectional current array with 1 mm separation.

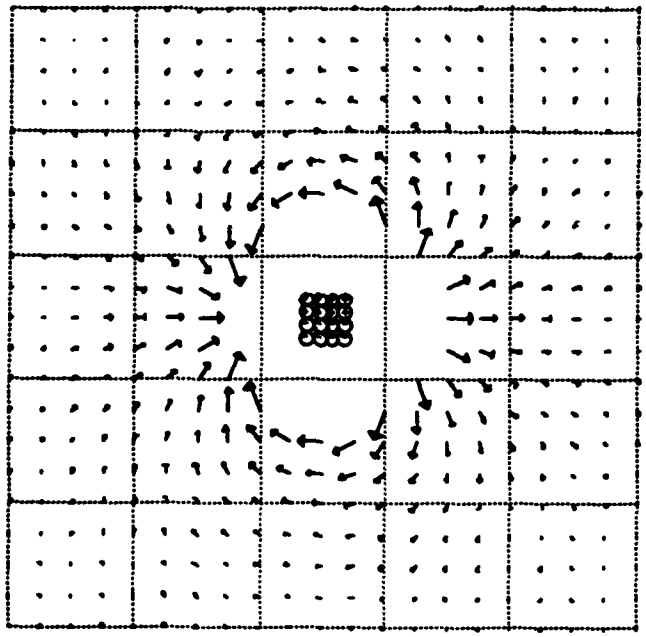

Figure F-48. Bipolar current array with 1 mm separation.

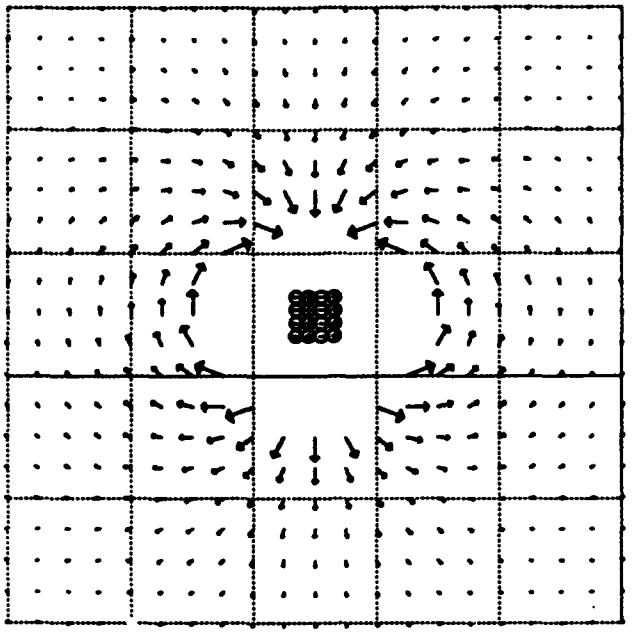

Figure F-49. Staggered current array with 1 mm separation.

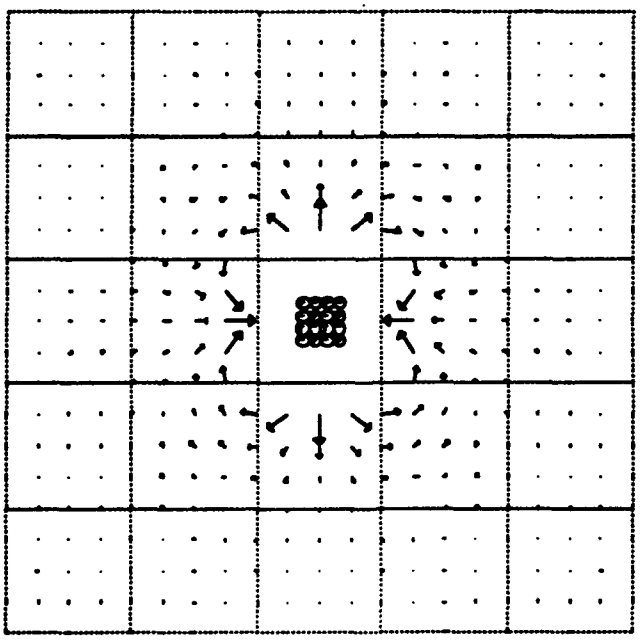

Figure F-50. Checkerboard current array with 1 mm separation.

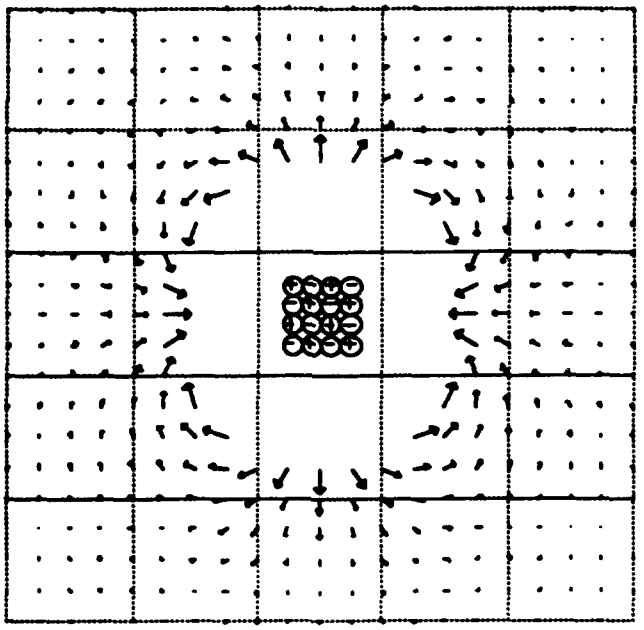

Figure F-51. Checkerboard current array with 2 mm separation.

Table F-4. Average and peak fields for various current configurations.

CONFIGURATION	AVERAGE FIELD (A/m)	PEAK FIELD (A/m)
UNIDIRECTIONAL 1 mm	34	180
BIPOLAR 1 mm	0.68	12.7
STAGGERED 1 mm	0.34	6.4
CHECKERBOARD 1 mm	0.01	0.45
CHECKERBOARD 2 mm	0.04	1.84

The unidirectional case produces the largest fields, as is to be expected. It has been included mainly as a point of departure for the more complex configurations. For all other cases, balanced currents (equal numbers and amounts, in opposite directions) are assumed. As the configuration is changed from bipolar to staggered, both peak and average fields are reduced by a factor of 2. The peak fields for the checkerboard case (at 1 mm wire spacings) are more than a factor of 14 lower than those for the staggered case, and almost 30 times lower than those for the bipolar case. The average fields for the checkerboard case (again at 1 mm wire spacings) are 34 times lower than those for the staggered case, and 68 times lower than those for the bipolar case. These comparisons

show that changing the configuration of the current-carrying wire arrays has a very strong effect on the local magnetic fields of the wires, on the level of 1 to 2 orders of magnitude.

Comparing the 1 mm and 2 mm wire spacings for the lowest-field (checkerboard) configuration, it is evident that increasing the wire spacing by a factor of 2 leads to a factor of 4 change in the magnetic fields. Thus, even if the configuration of wire current directions is maintained during alteration of the array (splicing or tampering), localized changes in wire separation may be easily detectable.

F.33 SUMMARY AND RECOMMENDATIONS.

For a tagging application of the null-field concept, it may be feasible to use an array of hundreds or thousands of very fine wires, perhaps imbedded in a glue matrix to make tampering more difficult. Whatever configuration is adopted, it must be complex enough that it could not be repaired after splicing within a reasonable amount of time, or without evidence of obvious damage. Figure F-52 shows one possible implementation of this concept, wherein the array of conductors is bundled and placed around the tagged or sealed item, and a field detector ("mouse") is run along the length of the tag loop. The mouse, with supporting hardware and software, might be designed to respond to magnetic fields above a given threshold (null) value. Alternatively, the detector could be designed to detect changes in the magnetic field with respect to length ($\partial H/\partial z$) such as would be caused by bends, kinks, or discontinuities in the bundled array.

The sensitivity of the null-field approach looks quite promising, but a number of issues must be addressed before its development can proceed. These include construction of a mouse device for measurement of the fields, complexity of the wire configuration for prevention of wire-by-wire splicing, means for ensuring that the configuration of wires will be maintained along their length (possibly with a glue matrix), types of unique connectors which can be used to seal the device, design of a peak detector for red-light/green-light determination of tag integrity, termination of the conductor array to prevent its use as an inadvertent antenna, and others.

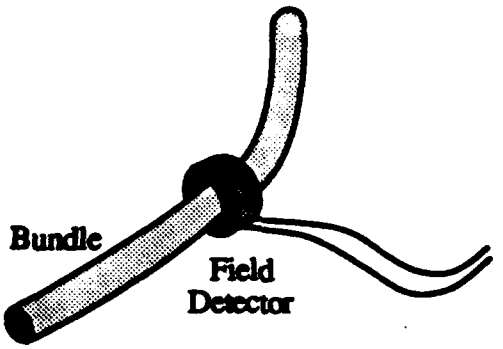

Figure F-52. Null-field array with a movable field detector (mouse).

F.34 OVERALL CREATIVE TASK LESSONS LEARNED AND CONCLUSIONS.

Throughout the work on the Creative Task, it was clear that such activities were very productive in identifying new tag and seal concepts appropriate for consideration as alternatives for treaty verification technologies. To obtain such productivity, it is necessary to have certain ingredients in the effort, including:

(1) A group of people representing a broad range of scientific and engineering disciplines
(2) Intensive mini-Red Teaming of all concepts proposed, including:
    (a) A "critical mass" of people so that intensive debate can ensue
    (b) Thorough analysis of the physical principles involved
    (c) Analysis of how the concept will be operationally employed
    (d) Adequate engineering design work to assess concept feasibility
    (e) A strong orientation toward delivery of functional systems.

The productivity of the creative process is indicated by the fact that three industrial prototype systems (SLITS, PTILS, and the UR) came from this effort. The SLITS system (the only one Red Teamed) survived well the Red Team adversarial work. That is, all adversarial attacks were readily detected upon inspection by minimally-trained inspectors. This outcome was the result of strong debate during development on material choices and design features that would frustrate covert adversarial actions, in the sense that the actions could be detected. All three of the prototype systems have survived well during functional, operational, and environmental tests that have been performed.

Further, several other rather promising concepts were identified that passed through preliminary analysis and/or proof-of-concept demonstration. These have been discussed in this report and, as discussed, some of these "winners" deserve more proof-of-concept investigations, and where warranted, prototype development.

BDM learned that early interaction with end-users and other interested agencies is critical in order to understand real operational needs and requirements, as well as to gain an appreciation of field environments experienced by verification systems. And finally, as one would expect, it was observed during the Innovative Tags work that learning was progressive. The staff became much more aware of the operational needs of verification and more knowledgeable of the various technologies as investigations proceeded. This experience led to more rapid assessment and creation of new ideas later in the Tagging program.

F.35 CONCLUSIONS.

The creative process can be of benefit to the government in developing arms control verification systems and other technologies. With direct input from intended users, appropriate verification inspection support systems can be and were developed. These included low cost and simple, but robust technologies, taking maximum advantage of COTS equipment. This inventive and developmental philosophy resulted in products and systems of high maintainability that are operationally attractive (user-friendly). And these technologies were delivered to the government on a timely schedule.

A major conclusion of the work on Tagging is that one technology cannot meet all the needs for verification of compliance across all treaties. Several technologies are needed. Continuing development of verification systems is prudent in order to be ready when the need arises. Such readiness will give representatives much more meaningful options during negotiation of treaties and agreements. It is important that the representatives and their technical advisors be thoroughly briefed on what options are, and are not, available.

APPENDIX F (Attachment 1)
MATHEMATICAL DETAIL:
MATERIAL EQUIVALENT CIRCUIT FOR THE SEAM SYSTEM.

This attachment presents mathematical detail for the material equivalent circuit response equations of the SEAM system discussed in section F.12.

We begin by treating the aperture as a dipole source. Configuration and Laplace representation of the dipole electric and magnetic fields are

$$E(r,s) = -\frac{1}{\varepsilon}\nabla \times \left[P(s) \times \nabla G(r,s)\right] + s\mu M(s) \times \nabla G(r,s)$$

$$H(r,s) = -sP(s) \times \nabla G(r,s) - \nabla \times \left[M(s) \times \nabla G(r,s)\right]$$

where

$$G(r,s) = \frac{e^{-\gamma r}}{4\pi r}$$

$$\nabla G(r,s) = \frac{e^{-\gamma r}}{4\pi r^2}(1 + \gamma r)\hat{e}_r$$

with $\gamma = jk = s/c$ and $k = \omega/c$. In the above equations P(s) and M(s) are the electric and magnetic dipole moments. The SEAM cavity modes are configured such that P(s) = 0. Consequently, we specialize to the magnetic dipole case and decompose into spherical coordinates

$$M(s) = M(s)\left[\cos\theta\hat{e}_r - \sin\theta\hat{e}_\theta\right]$$

$$E(r,s) = -s\mu M(s)\frac{e^{-\gamma r}}{4\pi r^2}(1 + \gamma r)\sin\theta\hat{e}_\varphi$$

$$H(r,s) = \frac{M(s)\,e^{-\gamma r}}{4\pi r^3}\left[2(1 + \gamma r)\cos\theta\,\hat{e}_r + \left(1 + \gamma r + \gamma^2 r^2\right)\sin\theta\,\hat{e}_\theta\right]$$

Near-field mode SEAM operation requires

$$\frac{\Delta\omega}{\omega_0} \approx \frac{W_h^D - W_e^D}{W_{cav}} \geq \frac{1}{Q_{cav}}$$

where $\Delta\omega$ is the fractional cavity bandwidth, ω_0 the SEAM RF frequency, W_{cav} the total electromagnetic energy in the cavity, Q_{cav} is the cavity quality factor, and

W_h^D, W_e^D are the electric and magnetic energies of the dipole in the presence(absence) of the material sample.

The next task is to obtain expressions for the above energies. We begin with the basic expressions

$$W_E = Re\left[\frac{1}{4}\int_v' \mathbf{E} \bullet \mathbf{D}^* \, dV\right]$$

$$W_H = Re\left[\frac{1}{4}\int_v' \mathbf{H} \bullet \mathbf{H}^* \, dV\right]$$

where D is the electric displacement and the asterisk denotes complex conjugation. Using the approximation that ε and μ are real scalars, we can write the dipole energy densities as

$$w_E^D = \frac{\mu M(s) M^*(s)}{64\pi^2}\left[\frac{k^4}{r^2}\sin^2\theta + \frac{k^2}{r^4}\sin^2\theta\right]$$

$$w_H^D = \frac{\mu M(s) M^*(s)}{64\pi^2}\left[\frac{k^4}{r^2}\sin^2\theta + \frac{k^2}{r^4}(4 - 5\sin^2\theta) + \frac{1}{r^6}(4 - 3\sin^2\theta)\right]$$

The difference $w_H^D - w_E^D$ is

$$w_H^D - w_E^D = \frac{\mu M(s) M^*(s)}{64\pi^2}\left[\frac{k^2}{r^4}(4 - 6\sin^2\theta) + \frac{1}{r^6}(4 - 3\sin^2\theta)\right] \qquad \text{(F-3)}$$

We will not be dealing with magnetic media so $\mu = \mu_0$; also $k^2 = \varepsilon_r k_0^2$ where k_0 is the vacuum wavenumber. Equation (F-3) then becomes

$$\Delta w = w_H^D - w_E^D = \frac{\mu M(s) M^*(s)}{64\pi^2}\left[\frac{\varepsilon_r k_0^2}{r^4}(4 - 6\sin^2\theta) + \frac{1}{r^6}(4 - 3\sin^2\theta)\right] \qquad \text{(F-4)}$$

Now we must apply equation (F-4) to a specific geometry in order to continue with development of the model. The configuration of interest is shown in figure F-53.

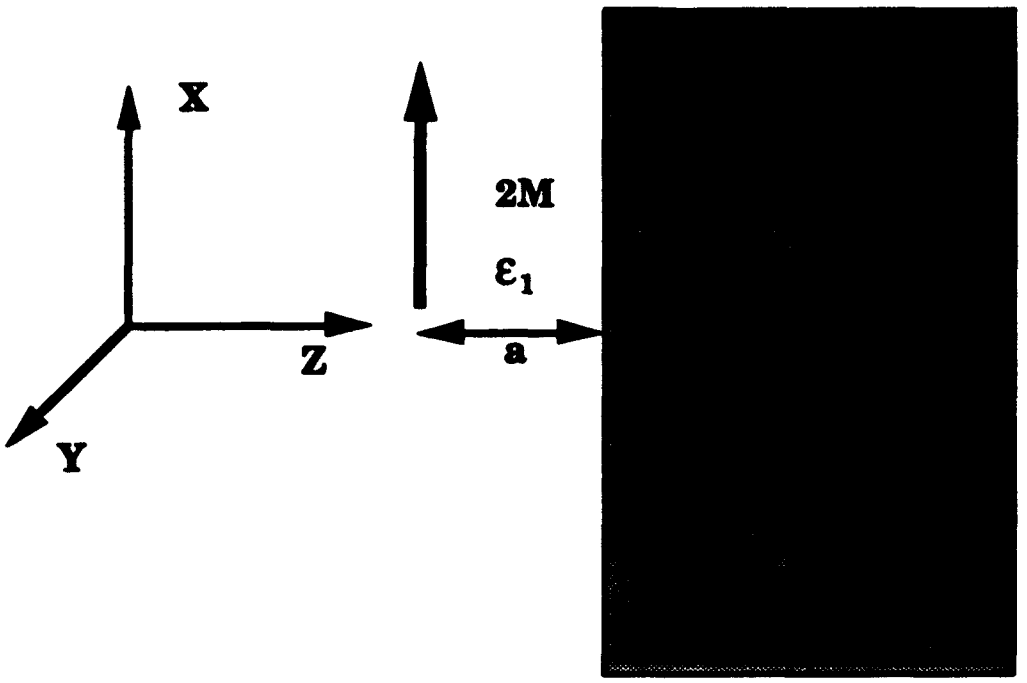

Figure F-53. Material Response Geometry Model

Computation of ΔW, the change in energy, for the geometry shown above is performed with image theory in a manner analogous to that used to calculate the electrostatic potential of a point charge situated in a similar arrangement. Switching to cartesian coordinates and noting that $\sin\theta = z/r$, we have

$$\Delta w = \frac{\mu M(s) M^*(s)}{64\pi^2}\left[\frac{\varepsilon_r k_0^2}{r^4}\left(4 - 6\frac{z^2}{r^2}\right) + \frac{1}{r^6}\left(4 - 3\frac{z^2}{r^2}\right)\right]$$

or

$$\Delta w = \frac{\mu M(s) M^*(s)}{64\pi^2}\left[\frac{\varepsilon_r k_0^2}{[x^2 + y^2 + z^2]^2}\left(4 - 6\frac{z^2}{[x^2 + y^2 + z^2]}\right) + \frac{1}{[x^2 + y^2 + z^2]^3}\left(4 - 3\frac{z^2}{[x^2 + y^2 + z^2]}\right)\right]$$

We next construct a reflection coefficient

$$\Gamma_1 = \frac{\varepsilon_2 - \varepsilon_1}{\varepsilon_2 + \varepsilon_1}$$

so that it is possible to write an expression for the energy density change in the region $0 \le z \le a$

$$\Delta w_1 = \frac{\mu M(s) M^*(s)}{64\pi^2}\left[\frac{\varepsilon_r k_0^2}{\left[x^2+y^2+z^2\right]^2}\left(4-6\frac{z^2}{\left[x^2+y^2+z^2\right]}\right)+\frac{1}{\left[x^2+y^2+z^2\right]^3}\left(4-3\frac{z^2}{\left[x^2+y^2+z^2\right]}\right)\right]$$
$$-\Gamma_1\left[\frac{\varepsilon_r k_0^2}{\left[x^2+y^2+(2a-z)^2\right]^2}\left(4-6\frac{z^2}{\left[x^2+y^2+(2a-z)^2\right]}\right)+\frac{1}{\left[x^2+y^2+(2a-z)^2\right]^3}\left(4-3\frac{z^2}{\left[x^2+y^2+(2a-z)^2\right]}\right)\right]$$

(F-5)

A similar equation can be constructed for the region $a \le z$,

$$\Delta w_2 = \frac{\mu M(s) M^*(s)(1-\Gamma_1)}{64\pi^2}\left[\frac{\varepsilon_r k_0^2}{\left[x^2+y^2+z^2\right]^2}\left(4-6\frac{z^2}{\left[x^2+y^2+z^2\right]}\right)+\frac{1}{\left[x^2+y^2+z^2\right]^3}\left(4-3\frac{z^2}{\left[x^2+y^2+z^2\right]}\right)\right]$$

(F-6)

The energy difference in each region is found by integrating equations (F-5) and (F-6) over the appropriate volumes. Consequently

$$\Delta W_1 = \int_{-\infty}^{\infty}\int_{-\infty}^{\infty}\int_{0}^{\infty} \Delta w_1 \, dx \, dy \, dz \qquad \text{(F-7)}$$

$$\Delta W_2 = \int_{-\infty}^{\infty}\int_{-\infty}^{\infty}\int_{a}^{\infty} \Delta w_2 \, dx \, dy \, dz \qquad \text{(F-8)}$$

There are eight separate integrals to perform in equation (F-7) and four to do in equation (F-8). Except for the first four integrals in equation (F-7), all of the integrals in the above expressions can be evaluated directly or as Mellin transforms. The first four integrals in equation (F-7) can be separated into divergent and finite pieces by introduction of a cutoff parameter. We set the cutoff parameter equal to the aperture radius, r_o, then equate the sum of the remaining divergent integrals to the self interaction energy of the aperture equivalent dipole source, i.e.

$$F(s)[I_1 + I_2 + I_3 + I_4] = \frac{4}{3}\mu_o r_0^3 H_i(s) H_i^*(s)$$

where

$$F(s) = \frac{\mu_o M(s) M^*(s)}{64\pi^2}$$

$$I_1 = 32\,\pi\,\varepsilon_r\,k_o^2 \int_0^{\infty}\int_0^{\infty} \frac{\rho\,d\rho\,dz}{[\rho^2+z^2]^2}$$

$$I_2 = -\,48\,\pi\,\varepsilon_r\,k_o^2 \int_0^{\infty}\int_0^{\infty} \frac{\rho\,z^2\,d\rho\,dz}{[\rho^2+z^2]^3}$$

$$I_3 = 32\,\pi \int_0^{\infty}\int_0^{\infty} \frac{\rho\,d\rho\,dz}{[\rho^2+z^2]^3}$$

$$I_4 = -\,24\,\pi \int_0^{\infty}\int_0^{\infty} \frac{\rho\,z^2\,d\rho\,dz}{[\rho^2+z^2]^4}$$

H_t (s) is the complex total (short circuit) magnetic field at the aperture location in the resonator, and, symmetry in the x,y directions has been used to simplify the integrations. This is a physical prescription for renormalizing, or removing, the divergences. No rigorous derivation, in a mathematical sense, has been done.

Setting

$$U_s(s) = \frac{4}{3}\,\mu_o\,r_o^3\,H_t(s)\,H_t^*(s)$$

we can write the final result for ΔW_1 as

$$\Delta W_1 = U_s(s) + F(s)\left\{ \frac{10\pi\varepsilon_r k_o^2}{r_o}\,\mathrm{Tan}^{-1}\left(\frac{a}{r_o}\right) - \frac{13\pi^2\varepsilon_r k_o^2}{4r_o} \right.$$

$$+\frac{6\pi\varepsilon_r k_o^2 a}{[r_o^2+a^2]} - \frac{3\pi\varepsilon_r k_o^2}{2r_o} + \frac{7\pi}{2r_o^3}\,\mathrm{Tan}^{-1}\left(\frac{a}{r_o}\right) + \frac{4\pi a}{r_o^2[r_o^2+a^2]}$$

$$\left. -\frac{7\pi^2}{8r_o^3} - \frac{9\pi}{4r_o^3} + \frac{\pi a}{[r_o^2+a^2]^2} - \frac{6\pi\varepsilon_r k_o^2 \Gamma_1}{a} - \frac{1089\pi\Gamma_1}{60a^3} \right\}$$

The integrals for ΔW_2 can be done exactly. The result is

$$\Delta W_2 = F(s)\left\{ \frac{4\pi\varepsilon_r k_o^2}{a}\left(1-\Gamma_1\right) + \frac{4\pi}{3a^3}\left(1-\Gamma_1\right) \right\}$$

The total response detected by modulating the aperture/sample separation distance is determined from

$$\frac{\Delta W_1 + \Delta W_2}{W_{cav}} = \frac{\Delta W_T}{W_{cav}}$$

The cavity energy is given by

$$W_{cav} = \frac{\mu_o \pi w_0^2 D H_i^2}{32}$$

where w_0 is the cavity TM mode radial scale length and D is the centerline cavity length.

It is instructive to examine the limits of ΔW_T with respect to a. In the limit a -> ∞, ΔW_2 vanishes and

$$\Delta W_1 = U_s(s) + F(s)\left\{\frac{7\pi^2\varepsilon_r k_o^2}{4r_o} + \frac{7\pi^2}{8r_o^3} - \frac{3\pi\varepsilon_r k_o^2}{2r_o} - \frac{9\pi}{4r_o^3}\right\} \qquad \text{(F-9)}$$

Equation (F-9) divided by W_{cav} provides a lower bound on the sample induced de-tuning response. Another limit of interest is a-> r_o. This limit yields the following expressions for ΔW_1 and ΔW_2

$$\Delta W_1 = U_s(s) + F(s)\left\{\frac{3\pi\varepsilon_r k_o^2}{2r_o} - \frac{3\pi^2\varepsilon_r k_o^2}{4r_o} - \frac{6\pi\varepsilon_r k_o^2\Gamma_1}{r_o} - \frac{1089\pi\Gamma_1}{60r_o^3}\right\}$$

$$\Delta W_2 = F(s)\left\{\frac{4\pi\varepsilon_r k_o^2}{r_o}(1 - \Gamma_1) + \frac{4\pi}{3r_o^3}(1 - \Gamma_1)\right\}$$

Summing these two equations and dividing by W_{cav} provides an upper bound on the sample induced de-tuning response consistent with the limitations imposed by the renormalization scheme.

APPENDIX F - REFERENCES

Agrawal, G. P., Nonlinear Fiber Optics, Academic Press, San Diego, 1989.

Allard, F. C., (ed.), Fiber Optics Handbook for Engineers and Scientists, McGraw-Hill, New York, 1990.

Ash, E. A., and Nicholls, G., Nature, "Super-resolution aperture scanning microscope", vol. 237, 1972, pp. 510-512.

Betts, R. A., Tjugiarto, T., Xue Y. L., and Chu, P. L., "Nonlinear refractive index in erbium doped optical fiber: Theory and experiment", IEEE J. Quantum Electron.,Vol. 27, No. 4, 1991, pp. 908-913.

Betzig, E., Trautman, J. K., Harris, T. D., Weiner, J. S., and Kostelak, R. L., Science, "Breaking the diffraction barrier: Optical microscopy on a nanometer scale", vol. 251, 1991, pp. 1468-1470.

Born, M., and Wolf,E., Principles of Optics, Sixth Edition, Pergamon Press, Oxford, 1980.

Boyd, R. W., Nonlinear Optics, Academic Press, San Diego, 1992.

Bryon, K. C., and Pitt, G. D., "Limits to power transmission in optical fibres", Electron. Lett., Vol. 21, No. 19, 1985, pp. 850-852.

Butcher, P. N., and Cotter, D., The Elements of Nonlinear Optics, Cambridge University Press, Cambridge, 1990.

Cargille Laboratories, Inc., R. P., (55 Commerce Road, Cedar Grove, NJ 07009; 201/239-6633), Price List RI-PL-1167 (1 November 1991).

Collin, R. E., Foundations for Microwave Engineering, McGraw-Hill Book Co., New York, 1966.

Ikeda, M., Murakami, Y., and Kitayama, K., "Mode scrambler for optical fibers", Appl. Opt., Vol. 16, No.4, 1977, pp. 1045-1049.

Justus, B. L., Seaver, M. E., Ruller J. A., and Campillo, "Excitonic optical nonlinearity in quantum-confined CuCl-doped borosilicate glass", Appl. Phys. Lett., Vol. 57, No. 14, 1990, pp. 1381-1383.

Kuzyk, M. G., Paek, U. C., and Dirk, C. W., "Guest-host polymer fibers for nonlinear optics", Appl. Phys. Lett., Vol. 59, No. 8, 1991, pp. 902-904.

Lewis, A., Issacson, M., Harootunian, A., and Muray, A., "Development of a 500 Å spatial resolution light microscope. I. Light is efficiently transmitted through 1/16 diameter aperture", Ultramicroscopy, vol. 13, 1984, pp. 227-231.

Marques, M. B., Assanto, G., Stegeman, G., Moehlmann, G. R., Erdhuisen, E. W. P., and Horsthuis, W. H. G., "Large, nonresonant, intensity dependent refractive index of 4-dialkylamino-4'-nitro-diphenyl-polyene side chain polymers in waveguides", Appl. Phys. Lett., Vol. 58, 1991, pp. 2613-2615.

Matsumoto, S.,, Kubodera, K., Kurihara, T., and Kaino, T., "Nonlinear optical properties of an azo dye attached polymer", Appl. Phys. Lett.,Vol. 51, No. 1, 1987,pp. 1-2.

Mohri, K., Humphrey, F. B., Yamasaki, J., and Kinoshita, F., "Large Barkhausen Effect and Matteucci Effect in Amorphous Magnetostrictive Wires for Pulse Generator Elements", IEEE Trans. Magnetics, vol. MAG-21, pp. 2017-2019, 1985.

Mohri, K., Humphrey, F. B., Yamasaki, J., and Okamura, K., "Jitter-less Pulse Generator Elements Using Amorphous Bistable Wires", IEEE Trans. Magnetics, vol. MAG-20, pp. 1409-1411, 1984.

Moran, M. J., She, C.-Y., and Carman, R. L., "Interferometric measurements of the nonlinear refractive-index coefficient relative to CS2 in laser-system-related materials", IEEE J. Quantum Electron., Vol. 11, No. 6, 1975, pp. 259-263.

Murday, J. S., "Nanometer science and technology", in APS News, vol. 1, no. 3, 1992, Physics News in 1991 Supplement, pp. 71-74.

Newhouse, M. A., Weidman, D. L., and Hall, D. W., "Enhanced-nonlinearity single-mode lead silicate optical fiber", Opt. Lett., Vol. 15, No. 21, 1990, pp. 1185-1187.

Personick, S. D., Fiber Optics - Technology and Applications, Plenum Press, New York, 1985.

Prasad, P. N., and Williams, D. J., Introduction to Nonlinear Optical Effects in Molecules and Polymers, John Wiley and Sons, New York, 1991.

Reddick, R. C., Warmack, R. J., and Ferrell, T. L., "New form of scanning optical microscope", Phys. Rev. B, vol. 39, 1989, pp. 767-770.

Saleh, B. E. A., and Teich, M. E., Fundamentals of Photonics, John Wiley and Sons, New York, 1991.

Sixtus, K. J., and Tonks, L., "Propagation of Large Barkhausen Discontinuities", Phys. Rev., vol. 37, pp. 930-958, 1931.

Smith, W. L., "Article 1.3 Nonlinear refractive index", in Handbook of Laser Science and Technology, Vol. 3, ed. by M. J. Weber, CRC Press, Boca Raton, FL, 1986, pp 259-281, Table 1.3.6.

Stolen, R. H., and Lin, C., "Self-phase-modulation in silica optical fibers", Phys. Rev., Vol. A17, No. 4, 1978, pp. 1448-1453.

Synge, E. H., "A suggested method for extending microscopic resolution into the ultra-microscopic region", Phil. Mag., series 7, vol. 6, 1928, pp. 356-362.

Yamashita, M., Torizuka, K., and Uemiya, T., "Femtosecond-response, highly third-order nonlinear 4-(N, N-dimethylamino)-3-acetamidonitrobenzene crystal cored fiber", Appl. Phys. Lett., Vol. 57, No.13, 1990, pp. 1301-1303.

APPENDIX G
UTILITY PROGRAMS USED FOR BLINK COMPARATOR PROCESS

A number of utility programs are associated with the Universal Reader system (version 5.2) to assist in running a "blink" comparison of tag images. LTEST is used to control Read Head lighting (needed for the BLINK program). HTSTFID extracts "raw" image data from Universal Reader files. FILEGRAB will capture a "raw" image directly from the Universal Reader Camera into a user named file. BLINK compares a "raw" recorded image to a "live" image. ARCBLINK compares two recorded "raw" images. BLINK1 will compare a file in Universal Reader format to a live image and BLINK2 will compare two images in Universal Reader format. Another utility useful for quick checkout of the Universal Reader camera is called GRAB which initializes the camera and frame grabber. The reason for having different "blink" programs for "raw" files and Universal Reader files is that there may be times when ("raw") images of things other than standard tags are to be compared.

Note: The difference between the "raw" and Universal reader formats is the presence of header information preceding, and 20 "extracted" images following, the 484 x 512 "preview" image in the latter. The "raw (preview)" images in both cases are 512 pixels in the X direction and 484 in the Y direction. The Universal Reader Camera records each pixel with a resolution of 256 shades of gray giving 1 byte per pixel. The total file size for a "raw" image should be 247,808 bytes. The total file size for a Universal Reader format file should be 498,619 bytes.

Note: It is assumed in the following descriptions that the Utility programs, data files, BGI files, and the User, are all in the same directory. Path names are omitted for simplicity. The symbol <CR> is the carriage return (Enter Key).

G.1 LTEST.

Utility to turn LEDs on/off in the Universal Reader Read Head. When the program executes, it will ask the user to press the GO button (switch #1) on the Universal Reader system Read Head, then will display an interactive menu of

user options. The program will terminate when the ESC key is pressed. This utility is not required when using the BLINK1 utility.

Note: When comparing a "live" image to a file preview image, turn on lights 1, 6, 11, and 16.

To invoke the program at the DOS prompt enter:

LTEST <CR>

G.2 HTSTFID.

Utility to display Universal Reader data files on color monitor and/or to extract, and write to disk, raw "image" files for use in the BLINK or ARCBLINK software. Plot images are "false color" mappings of gray-scale images. This program is just a tool, and its behavior is determined by the answers to questions. If no plots are requested then it is assumed that the (first) preview image and not any of the extracted images is requested. If one wishes (in this version of HTSTFID) to write a "RAW" version of one of the 20 extracted images in the UR data file, the plot must be requested of the image first (this builds the 2500 "extracted" points into a 484 x 512 image with the remaining points zero (dark) filled. This utility is not required when using either the BLINK1 or BLINK2 utilities.

To invoke the program at the DOS prompt enter:

HTSTFID input_filename <CR>

Note: This program requires a VGA color monitor and the VGAEGA.BGI file in the same directory the program is run from. The program will ask a series of questions related to plot options and to extraction of a raw file.

Example:

C:> HTSTFID 00100004.1SE <CR>

.

(File header information displayed here)

.

.

Plot first image in file (Y/N): N <CR>

Plot a Raw image (Y/N): N <CR>

Plot an Extracted image (Y/N): N <CR>

Do you want to write this image as a 'raw' file?: Y <CR>

Enter Filename: 00100004.RAW <CR>

C:>

G.3 FILEGRAB.

Utility to "grab" a single video image from the UR Read Head and write a "raw" data file.

To invoke the program at the DOS prompt enter:

FILEGRAB output_filename <CR>

G.4 BLINK.

Utility to "blink" two images on a video monitor. One image will be from a "raw" image file and the other a "live" video image from the UR Read Head.

To invoke the program at the DOS prompt enter:

BLINK input_filename <CR>

Note: This program runs "forever" unless the user enters the CRTL-BREAK key. After a few seconds, the program will stop blinking the video monitor and ask if the user wishes to abort the program. Answer "Y" to terminate or "N" to continue.

G.5 ARCBLINK.

Utility to "blink" two "raw" data file images on a video monitor.

To invoke the program at the DOS prompt enter:

ARCBLINK input_filename1 input_filename2 <CR>

Note: This program runs "forever" unless the user enters the CRTL-BREAK key. After a few seconds, the program will stop blinking the video monitor and ask if the user wishes to abort the program. Answer "Y" to terminate or "N" to continue.

G.6 BLINK1.

Utility to "blink" two images on a video monitor. One image will be from a Universal Reader image file and the other a "live" video image from the UR Read Head. When the program starts, it will try to turn off all LED lights in the read head then turn on the preview lights (1, 6, 11, 16) so that the "live" image may be compared with the preview image from the file.

To invoke the program at the DOS prompt enter:

BLINK1 input_filename <CR>

Note: This program runs "forever" unless the user enters the CRTL-BREAK key. After a few seconds, the program will stop blinking the video monitor and ask if the user wishes to abort the program. Answer "Y" to terminate or "N" to continue.

G.7 BLINK2.

Utility to "blink" two Universal Reader data file images (usually a reference and inspection image) on a video monitor.

To invoke the program at the DOS prompt enter:

BLINK2 input_filename1 input_filename2 <CR>

Note: This program runs "forever" unless the user enters the CRTL-BREAK key. After a few seconds, the program will stop blinking the video monitor and ask if the user wishes to abort the program. Answer "Y" to terminate or "N"to continue.

G.8 GRAB.

Utility to initialize the Universal Reader Camera, acquire a high resolution image, place the camera and frame-grabber in "live" mode, and store the image in a file named E:IMAGE.DAT. This utility is used primarily to check out the camera (i.e. set it in "live" mode) rather than to acquire data. If drive E is not defined on the computer system, an error message will occur, but the camera will already be initialized.

To invoke the program at the DOS prompt enter:

GRAB <CR>

Notes:

1. Example procedure - Run the Universal Reader software (UR52) to record a baseline image of a tag. Then at a later date use UR52 to capture another reading of the same tag. Run the HTSTFID program to extract and record "raw" data images from both the baseline and newer reading for that tag. Run ARCBLINK to compare the two images. For instance, UR52 might create a baseline

such as 00120000.2SE and a reading file 00120001.2SE. Then the following general steps could follow:

a. UR52
   (creating 00120000.2SE)
b. UR52
   (creating 00120001.2SE)
c. HTSTFID 00120000.2SE
   (creating file 00120000.RAW)
d. HTSTFID 00120001.2SE
   (creating file 00120001.RAW)
e. ARCBLINK 00120000.RAW 00120001.RAW

2. Example procedure - Run LTEST to set up the LEDs in the UR Read Head as needed, then FILEGRAB to acquire a "raw" image of the tag, then after some change is made to the tag, place the tag in the UR Read Head and use BLINK to compare the recorded and live images. General steps would be:

   a. LTEST
      (setting up LEDs as desired)
   b. FILEGRAB TAG1.RAW
   c. BLINK TAG1.RAW

3. Example procedure - Run UR52 to record a baseline image of the tag. At a later date use LTEST to set up the Read Head LEDs to the same light pattern as the UR52 software used, (for example, the preview image recorded by the UR52 program would have lights 1, 6, 11, 16 on) then run FILEGRAB to record a "raw" image of the tag. Use HTSTFID to extract the "raw" image from the UR52 data file and run ARCBLINK to compare the two images. General steps would be:

   a. UR52
      (creating 00190000.1SE)
   b. LTEST
      (setting up LEDs as desired)

c. FILEGRAB 00190001.RAW
d. HTSTFID 00190000.1SE
(creating 00190000.RAW)
e. ARCBLINK 00190000.RAW 00190001.RAW

4. Example procedure - Run UR52 to record a baseline image of the tag. At a later date use UR52 to acquire another image of the same tag. Then run BLINK2 to compare the two images. General steps would be:

a. UR52
(creating 00190000.1SE)
b. UR52
(creating 00190001.1SE)
c. BLINK2 00190000.1SE 00190001.1SE

5. Example procedure - Run UR52 to record a baseline image of the tag. At a later date use BLINK1 to compare a "live" image (using Universal Reader Camera) to the baseline. General steps would be:

a. UR52
(creating 00190000.1SE)
b. BLINK1 00190000.1SE

6. Filenames used in the above examples are arbitrary conventions. The interaction with the programs is simplified since they are question and/or menu driven and this is not a true operator's guide, just notes to assist someone using these utilities as tools.

DISTRIBUTION LIST

DNA-TR-93-69-V2

DEPARTMENT OF DEFENSE

ASSISTANT SECRETARY OF DEFENSE
INTERNATIONAL SECURITY POLICY
ATTN: VERIFICATIONS POLICY

DEFENSE INTELLIGENCE AGENCY
ATTN: DB
ATTN: DI-5
ATTN: DIW-4
ATTN: DT
ATTN: PAM-1D

DEFENSE NUCLEAR AGENCY
ATTN: DFRA JOAN MA PIERRE
ATTN: NASF
ATTN: OPAC CATHY MONTIE
5 CY ATTN: OPAC LT COL BLANCHETTE
ATTN: OPNA
2 CY ATTN: TITL

DEFENSE SYSTEMS SUPPORT ORGANIZATION
ATTN: C-332
ATTN: JNGO

DEFENSE TECHNICAL INFORMATION CENTER
2 CY ATTN: DTIC/OC

FIELD COMMAND DEFENSE NUCLEAR AGENCY
10 CY ATTN: FCPRC
ATTN: FCTO

OASD
ATTN: BRIG GEN JOHNSON
ATTN: MS BUCKLEY
ATTN: USD/P

OFFICE OF THE GENERAL COUNSEL
3 CY ATTN: MR HADAD

ON-SITE INSPECTION AGENCY
ATTN: COL GILBERT

OUSD ACQUISITION
ATTN: DR J FREEDMAN
ATTN: L MINICHIELLO
ATTN: M EVANS

U S EUROPEAN COMMAND/ECJ2-T
ATTN: ECJ-3
ATTN: ECJ2-T

DEPARTMENT OF THE ARMY

ARMY RESEARCH LABORATORIES
ATTN: TECH LIB

DEP CH OF STAFF FOR OPS & PLANS
ATTN: DAMO-SWN

U S ARMY BALLISTIC RESEARCH LAB
ATTN: SLCBR-SS-T

U S ARMY CONCEPTS ANALYSIS AGENCY
ATTN: TECHNICAL INFO CENTER

U S ARMY MATERIAL COMMAND
ATTN: AMCAN-CN COL NIKAI

U S ARMY NUCLEAR & CHEMICAL AGENCY
ATTN: MONA-NU DR D BASH

U S ARMY WAR COLLEGE
ATTN: LIBRARY

US ARMY MATERIEL SYS ANALYSIS ACTVY
ATTN: AMXSY-CR

USA CML & BIOLOGICAL DEFENSE AGENCY
ATTN: AMSCB-TC MR COLBURN

DEPARTMENT OF THE NAVY

NAVAL AIR FORCE
ATTN: COMMANDER

NAVAL AIR FORCE
ATTN: COMMANDER

NAVAL POSTGRADUATE SCHOOL
ATTN: CODE 52 LIBRARY

NAVAL RESEARCH LABORATORY
ATTN: CODE 5227 RESEARCH REPORT

NAVAL SURFACE FORCE
ATTN: COMMANDER

NAVAL TECHNICAL INTELLIGENCE CTR
ATTN: NTIC-DA30

NAWCWPNSDIV DETACHMENT
ATTN: CLASSIFIED LIBRARY

OFFICE OF CHIEF OF NAVAL OPERATIONS
ATTN: NUC AFFAIRS & INT'L NEGOT BR

DEPARTMENT OF THE AIR FORCE

AFIS/INT
ATTN: INT

AIR FORCE CTR FOR STUDIES & ANALYSIS
ATTN: AFSAA/SAI

AIR UNIVERSITY LIBRARY
ATTN: AUL-LSE

DEPUTY CHIEF OF STAFF FOR PLANS & OPERS
ATTN: AFXOOSS
ATTN: AFXOXI COL ENGSTROM

DEPARTMENT OF ENERGY

ARGONNE NATIONAL LABORTORY
ATTN: DR A DEVOLPI

BROOKHAVEN NATIONAL LABORATORY
ATTN: DR J INDUSI

EG&G IDAHO INC
ATTN: DR J JONES